

# Northumbria Research Link

Citation: Leach, Mark (2005) A new method for holographic measurement of microwave antenna radiation patterns. Doctoral thesis, Northumbria University.

This version was downloaded from Northumbria Research Link:  
<https://nrl.northumbria.ac.uk/id/eprint/15778/>

Northumbria University has developed Northumbria Research Link (NRL) to enable users to access the University's research output. Copyright © and moral rights for items on NRL are retained by the individual author(s) and/or other copyright owners. Single copies of full items can be reproduced, displayed or performed, and given to third parties in any format or medium for personal research or study, educational, or not-for-profit purposes without prior permission or charge, provided the authors, title and full bibliographic details are given, as well as a hyperlink and/or URL to the original metadata page. The content must not be changed in any way. Full items must not be sold commercially in any format or medium without formal permission of the copyright holder. The full policy is available online: <http://nrl.northumbria.ac.uk/policies.html>

Some theses deposited to NRL up to and including 2006 were digitised by the British Library and made available online through the [EThOS e-thesis online service](#). These records were added to NRL to maintain a central record of the University's research theses, as well as still appearing through the British Library's service. For more information about Northumbria University research theses, please visit [University Library Online](#).

# Northumbria Research Link

Citation: Leach, Mark (2005) A new method for holographic measurement of microwave antenna radiation patterns. Doctoral thesis, Northumbria University.

This version was downloaded from Northumbria Research Link:  
<http://nrl.northumbria.ac.uk/id/eprint/15778/>

Northumbria University has developed Northumbria Research Link (NRL) to enable users to access the University's research output. Copyright © and moral rights for items on NRL are retained by the individual author(s) and/or other copyright owners. Single copies of full items can be reproduced, displayed or performed, and given to third parties in any format or medium for personal research or study, educational, or not-for-profit purposes without prior permission or charge, provided the authors, title and full bibliographic details are given, as well as a hyperlink and/or URL to the original metadata page. The content must not be changed in any way. Full items must not be sold commercially in any format or medium without formal permission of the copyright holder. The full policy is available online: <http://nrl.northumbria.ac.uk/policies.html>

Some theses deposited to NRL up to and including 2006 were digitised by the British Library and made available online through the [EThOS e-thesis online service](#). These records were added to NRL to maintain a central record of the University's research theses, as well as still appearing through the British Library's service. For more information about Northumbria University research theses, please visit [University Library Online](#).

**A New Method For Holographic Measurement Of  
Microwave Antenna Radiation Patterns**

Mark Leach

A thesis submitted for fulfilment of the requirements  
of Northumbria University for the degree of  
Doctor of Philosophy

Research undertaken in the School of  
Engineering and Technology

January 2005

# ABSTRACT

The rate at which new communications technologies are being developed has been immense and will continue to intensify for the foreseeable future. This evolution is fuelled by the desire to meet the wants and needs of the global community, by developing devices able to offer ever-increasing functionality, with greater complexity. To achieve this designers are forced to move to higher and higher frequencies.

The antenna, as one of the fundamental building blocks of any radiated wave system, and as such, must develop along with the evolution of the communication system be it for, mobile, satellite or point to point systems. Antenna designers need to be able to test antenna, to ensure they exhibit the characteristics to which they were designed. Antenna test becomes progressively more difficult and costly as both, the operating frequency and the size of the antenna increase, especially for the measurement of the antenna Far-Field radiation pattern. Either the distance over which the measurement must be made becomes unfeasibly large or expensive measurement equipment is required to attain the phase component of the antenna field, where traditional methods for measuring close to the antenna are applied.

Techniques have been developed to eliminate the need for the expensive phase measurement at reduced distances. Specifically of interest in this thesis, is the optical process of Off-Axis holography. The process allows phase information to be retained in a scalar measurement by use of a phase coherent known reference source. The reference desired reference source is a plane wave, which although possible at optical

frequencies with the use of lasers is problematic at microwave frequencies. To date the plane wave characteristic required has been approximated using conventional radiating elements, which degrades the quality of the recorded holographic image.

This thesis proposes a novel implementation of the Off-Axis hologram system, for application in the microwave frequency region. The novel system developed here addresses the problem of generating the desired plane wave characteristic. The conventional radiating element used to provide the near plane wave reference is replaced by a synthetic equivalent, which allows the magnitude and phase of the reference beam to be directly controlled at every measurement location required.

Practical verification of the novel system proposed has been performed, with comparisons made between the results obtained from the novel technique and standard techniques used in industry. The comparisons show that the novel implementation is valid and able to provide good repeatable results.

# TABLE OF CONTENTS

ABSTRACT .....	ii
TABLE OF CONTENTS .....	iv
LISTS OF FIGURES AND TABLES.....	viii
ACKNOWLEDGEMENTS.....	xiii
DECLARATION.....	xiv
GLOSSARY OF ACRONYMS.....	xv
GLOSSARY OF SYMBOLS.....	xvi
CHAPTER 1 INTRODUCTION .....	1
1.1 Research Background.....	1
1.2 Outline of Work.....	3
1.3 Aims and Objectives .....	5
1.4 Chapter Outline .....	7
1.5 Original Contribution.....	8
1.6 Published Works .....	9
CHAPTER 2 ANTENNA RADIATION PATTERNS AND MEASUREMENT RANGES .....	11
2.1 Introduction .....	11
2.2 Antenna Radiation Patterns .....	12
2.3 The Far-Field Test Range .....	14
2.4 The Compact Antenna Test Range .....	17
2.5 The Near-Field Range .....	19
2.6 Intensity Only Near-Field Ranges.....	24
2.6.1 Holographic Near-Field imaging.....	24
2.6.2 Iterative phase retrieval.....	26
2.7 Summary.....	28
CHAPTER 3 NEAR-FIELD FAR-FIELD TRANSFORM THEORY AND MEASUREMENT.....	30
3.1 Introduction .....	30
3.2 Introduction to Near-Field Measurement Theory.....	31
3.3 The Plane Wave Spectrum & Near-Field Far-Field Evaluation .....	31
3.4 Sampling in the Near-Field.....	34
3.5 The Fast Fourier Transform .....	37
3.6 Aperture Imaging .....	38
3.7 Physical Error Sources .....	39
3.7.1 Probe field .....	39
3.7.2 Probe positioning errors .....	41
3.7.3 Data set truncation.....	42
3.7.4 Instrumentation and equipment error.....	45
3.7.5 Environmental errors .....	45
3.8 Near-Field Far Field Simulation .....	47

3.9	Summary.....	53
CHAPTER 4 HOLOGRAPHY AND THE USE OF HOLOGRAMS .....		55
4.1	Introduction .....	55
4.2	Optical Holography.....	56
4.3	Indirect Holography.....	57
4.3.1	The In-Line hologram .....	57
4.3.2	The Off-Axis hologram.....	61
4.4	Microwave Holography.....	67
4.4.1	Object imaging .....	69
4.4.2	Holographic antennas.....	69
4.4.3	Total field recovery .....	70
4.5	Improving The Quality Of The Recorded Hologram .....	74
4.5.1	The non-planar reference beam .....	74
4.5.2	The relative magnitude of image terms.....	75
4.5.3	Mathematical removal of the auto-correlation terms .....	77
4.6	Summary.....	77
CHAPTER 5 INDIRECT HOLOGRAPHIC MICROWAVE ANTENNA RADIATION PATTERN MEASUREMENT .....		79
5.1	Introduction .....	79
5.2	Microwave Antenna Radiation Pattern Measurement Using Indirect Holography .....	80
5.3	Antenna Measurement Using In-Line Holograms.....	83
5.3.1	In-Line hologram recording for antenna Near-Field measurement.....	83
5.3.2	In-Line hologram simulation for antenna Near-Field measurement.....	84
5.4	Antenna Measurement Using Off-Axis Holograms .....	87
5.4.1	Off-Axis hologram recording for antenna Near-Field measurement.....	88
5.4.2	Off-Axis hologram simulation for antenna Near-Field measurement.....	90
5.4.3	Acquiring the Far-Field radiation pattern from the Off-Axis hologram.....	93
5.4.4	Acquiring planar Near-Field distribution and the antenna aperture distribution from the Off-Axis hologram .....	94
5.5	Locating Faults In The Aperture Field.....	97
5.6	Sampling and Processing Intensity Data .....	99
5.7	Sources of Error .....	101
5.8	Summary.....	102
CHAPTER 6 NOVEL OFF-AXIS HOLOGRAM APPROACH FOR INDIRECT NEAR-FIELD ANTENNA MEASUREMENT.....		103
6.1	Introduction .....	103
6.2	Synthetic Reference Off-Axis Hologram Generation .....	104
6.2.1	Proposed Off-Axis hologram antenna measurement system - overview.....	104

6.2.2	Measurement methodology .....	107
6.2.3	Advantages of proposed technique.....	108
6.3	Verification Of Proposed Off-Axis Reference Synthesis.....	109
6.3.1	Design of a one-dimensional measurement system .....	110
6.3.2	Selection of test antenna .....	111
6.3.3	Verification methodology and measurement parameters .....	114
6.4	One-Dimensional Measurements.....	117
6.4.1	Indirect holography – intensity only measurement .....	117
6.4.2	Direct holography – complex Near-Field measurement .....	121
6.4.3	One-dimensional scan results - discussions and comparisons .....	123
6.5	System Error Sources .....	127
6.6	System Limitations.....	131
6.6.1	Mathematical and spectral restrictions .....	131
6.6.2	Physical restrictions .....	132
6.7	Summary .....	134
CHAPTER 7 TWO-DIMENSIONAL INDIRECT HOLOGRAPHIC SCANNING SYSTEM.....		136
7.1	Introduction .....	136
7.2	Synthesising A Two-Dimensional Off-Axis Reference .....	137
7.3	Two-Dimensional Off-Axis Hologram Simulation.....	138
7.4	Two-Dimensional Measurements .....	144
7.4.1	Direct Far-Field measurements .....	146
7.4.2	Indirect holography – two-dimensions.....	147
7.4.3	Direct holography – two-dimensions.....	154
7.5	Result Comparisons and Discussions .....	158
7.5.1	Far-Field comparison.....	158
7.5.2	Complex Near-Field comparisons and discussions .....	161
7.5.3	Complex aperture field comparison and discussion .....	165
7.6	System Error Sources .....	167
7.7	Summary.....	169
CHAPTER 8 THE NOVEL INDIRECT HOLOGRAPHIC RANGE – 'SLOW WAVE' INTERFERENCE.....		172
8.1	Introduction .....	172
8.2	Over Sampling to Increase Spectral Width.....	173
8.3	Experimental Design and Parameter Definition .....	181
8.3.1	Antenna properties and Far-Field measurement.....	181
8.3.2	Measurement parameters .....	183
8.4	Simulation Of Reduced Sample Spacing For Pyramidal Horn.....	186
8.5	Practical Measurement Of Pyramidal Horn Using Reduced Sample Spacing .....	193
8.5.1	Indirect holographic measurement of medium gain pyramidal horn antenna (sampling criteria 1) .....	194
8.5.2	Indirect holographic measurement of medium gain pyramidal horn antenna (sampling criteria 2) .....	196
8.5.3	Direct holographic measurement of medium gain pyramidal horn antenna.....	199

8.5.4	Comparison of pyramidal horn Far-Field patterns .....	200
8.6	System Limitations.....	202
8.7	Summary.....	203
CHAPTER 9 CONCLUSIONS & FURTHER WORK.....		206
9.1	Conclusions .....	206
9.2	Further Work .....	211
9.2.1	System development .....	211
9.2.2	Microwave imaging.....	214
REFERENCES.....		216

# LISTS OF FIGURES AND TABLES

## Figures

Figure 2.1 The Field Regions Of An Antenna .....	13
Figure 2.2 Features Of An Antenna Radiation Pattern .....	14
Figure 2.3 A Simple Direct Far-Field Test Range .....	15
Figure 2.4 A Simple Compact Antenna Test Range .....	18
Figure 2.5 The Five Scanning Surfaces Used For Antenna Near-Field Measurement (a) Planar (b) Cylindrical (c) Spherical (d) Plane-Polar and (e) Bi-Polar.....	21
Figure 2.6 A Typical Planar Near-Field Test Range.....	22
Figure 2.7 Iterative Phase Retrieval Test Range .....	27
Figure 3.1 Planar Near-Field Scanning Surface.....	36
Figure 3.2 Probe Field Effects On Planar Measurements.....	40
Figure 3.3 Valid Angle Of The Far-Field Obtained By Planar Scanning.....	44
Figure 3.4 (a) Magnitude And (b) Phase Of A $32\lambda$ Uniform Aperture Distribution And Its Near-Field Calculated At $Z_0 = 5\lambda$ .....	50
Figure 3.5 Plane Wave Spectrum Magnitude Normalised to Maximum Magnitude...	50
Figure 3.6 Simulated Far-Field Radiation Pattern Calculated From A Truncated Near-Field Distribution Formed At $5\lambda$ From A $32\lambda$ Aperture With Uniform Illumination .....	51
Figure 3.7 Original And Reconstructed Aperture Distributions (a) Magnitude Normalised To Unity and (b) Phase Normalised To 0.....	52
Figure 4.1 In-Line/Gabor Hologram Generation .....	58
Figure 4.2 Image Reconstruction From An In-Line/Gabor Hologram .....	60
Figure 4.3 Generating An Off-Axis Hologram.....	62
Figure 4.4 Image Reconstruction From An Off-Axis Hologram .....	62
Figure 4.5 Angular Frequency Spectrum Of An Off-Axis Hologram .....	65
Figure 4.6 Arrangement For Microwave In-Line Hologram Recording.....	72
Figure 4.7 Arrangement For Microwave Off-Axis Hologram Recording .....	73
Figure 4.8 Comparison Of Off-Axis Hologram Spectrums With Varying Magnitudes Of Reference Beam Relative To The Object Beam Normalised To The Maximum Magnitude.....	76
Figure 5.1 Equipment Employed By Bennett For Off-Axis Hologram Formation For Microwave Antenna, Intensity Only, Near-Field Testing [1] .....	81
Figure 5.2 Near-Field In-Line Holographic Antenna Measurement System.....	83
Figure 5.3 In-Line Hologram/Intensity Pattern Formed By The Near-Field Of A $32\lambda$ Aperture With Uniform Distribution And Reference Exhibiting Uniform Magnitude And Phase .....	85
Figure 5.4 Spectral Plots Of The Intensity Components Of An In-Line Hologram (5.2) , (5.3) and (5.4)/(5.5) Normalised To The Maximum Magnitude.....	86
Figure 5.5 Spectrum Of An In-Line Hologram Normalised To The Maximum Magnitude .....	87
Figure 5.6 Basic Near-Field Off-Axis Indirect Holographic Antenna Measurement System.....	88
Figure 5.7 Typical Spectrum Of An Off-Axis Hologram.....	90

Figure 5.8 Off-Axis Hologram/Intensity Pattern Formed By The Near-Field Of A $32\lambda$ Aperture With Uniform Distribution And A Reference Exhibiting Uniform Magnitude At An Angle Of $45^\circ$ .....	91
Figure 5.9 Spectral Plots Of The Intensity Components Of An Off-Axis Hologram (5.7) - (5.10) Normalised To The Maximum Magnitude.....	92
Figure 5.10 Spectrum Of An Off-Axis Hologram Normalised To The Maximum Magnitude .....	92
Figure 5.11 Simulated Far-Field Radiation Patterns For A $32\lambda$ Uniformly Illuminated Aperture Using Direct and Indirect holographic Techniques.....	94
Figure 5.12 Comparison Of A Simulated Complex Near-Field For A $32\lambda$ Uniformly Illuminated Aperture And The Complex Near-Field Reconstruction From Intensity Only Samples And Application Of Indirect Holographic Theory (a) Magnitude And (b) Phase.....	95
Figure 5.13 Comparison Of Initial Aperture Distribution and Reconstructed Aperture Distribution Through Simulation Of The Indirect Holographic Technique (a) Magnitude And (b) Phase .....	96
Figure 5.14 Comparison Of Far-Fields Obtained Through Simulation Of The Indirect Holographic Method For A $32\lambda$ Cosine Distribution With And Without A Nulled Region .....	97
Figure 5.15 Comparison Of Reconstructed Aperture Distributions For An Initial Aperture With And Without A Nulled Region Through Simulation Of The Indirect Holographic Technique (a) Magnitude Centrally Normalised To Unity And (b) Phase Centrally Normalised To 0 .....	98
Figure 6.1 Proposed New System For Indirect Holographic Imaging Of Microwave Antenna Radiation Patterns.....	105
Figure 6.2 Photographs Of One-Dimensional Indirect Holographic Measurement System .....	111
Figure 6.3 Equivalent One-Dimensional Current Source For (a) A Rectangular Aperture Distribution and (b) A circular Aperture .....	115
Figure 6.4 Intensity Patterns Measured For Andrews Parabolic Dish With $\Delta x = \lambda/2$ and $\theta_{xI} = 120^\circ$ .....	119
Figure 6.5 Spectrum Of Measured Intensity Pattern In Figure 6.4 Normalised to Maximum Magnitude.....	120
Figure 6.6 PWS Filtered From Spectrum The Spectrum In Figure 6.5 .....	121
Figure 6.7 Measured Complex Near-Field Data (a) Magnitude And (b) Phase .....	122
Figure 6.8 Near-Field Far-Field Transform Of Direct Holographic Measurements..	123
Figure 6.9 Comparison Of One-Dimensional Directly and Indirectly Obtained PWS's .....	124
Figure 6.10 Comparison Of Measured Near-Field And Near-Field Calculated Via The Indirect Holographic Method (a) Magnitude And (b) Phase .....	125
Figure 6.11 Comparison Of Beam-Limited Spectral Near-Field And Near-Field Calculated Via The Indirect Holographic Method (a) Magnitude And (b) Phase.....	126
Figure 6.12 Far-Field Radiation Pattern Of Open Ended Waveguide Probe.....	130
Figure 6.13 Three Combinations Of Reference Wave Phase Shift For Two-Dimensional Indirect Holographic Scanning (a) Phase Shift In X Only (b) Phase Shift In Y Only And (c) Phase Shift In X and Y .....	133
Figure 7.1 Implementation Of The Three Possible Phase Gradients using $120^\circ$ .....	137
Figure 7.2 Two-Dimensional Aperture Distribution Mode $TE_{10}$ .....	139

Figure 7.3 Two-Dimensional Near-Field Distribution At $Z_0=5\lambda$ For A $32\lambda \times 32\lambda$ Rectangular Aperture With Mode $TE_{10}$ .....	140
Figure 7.4 Simulated Intensity Pattern Between The Near-Field Of Figure 7.3 And A Reference Wave With $120^\circ$ Phase Gradient In The $x$ -axis (a) Two-Dimensional plot, (b) Cut Through Centre Of The $y$ -axis And (c) Cut Through Centre Of The $x$ -axis .....	141
Figure 7.5 Two-Dimensional Intensity Pattern Spectral Distribution With Phase Shift In $x$ -axis Only (a) Surface Plot And (b) Contour Plot.....	142
Figure 7.6 Two Dimensional Intensity Pattern Spectral Distributions With (a) $y$ Only And (b) $x$ And $y$ Phase Shifts.....	142
Figure 7.7 Far-Field For A $32\lambda \times 32\lambda$ Aperture With $TE_{10}$ Mode Distribution Simulated Using Indirect Holography (a) Two-Dimensional Plot, (b) Principal H-Plane Cut And (c) Principal E-Plane Cut.....	143
Figure 7.8 Photograph Of Two-Dimensional Positioning System.....	145
Figure 7.9 Photographs Of Parabolic Dish Aperture (a) With And (b) Without Its Radome Cover.....	146
Figure 7.10 Far-Field Measurement Of The Parabolic Dish (a) The Principal H-Plane And (b) The Principal E-Plane At 12.7 GHz By Andrews Corp. ....	147
Figure 7.11 Measured Two-Dimensional Intensity Pattern For Parabolic Dish With $\Delta x=\lambda/2$ , $\Delta y=\lambda/2$ and $\theta_{xI}=120^\circ$ (a) Surface Plot Of Measured Data, (b) Contour Plot Of Measured Data, (c) Cut Through Centre Of The $x$ -Axis And (d) Cut Through Centre Of The $y$ -axis .....	149
Figure 7.12 Measured Two-Dimensional Intensity Pattern Spectral Distribution (a) Surface Plot And (b) Contour Plot.....	150
Figure 7.13 Far-Field Radiation Pattern From Intensity Only Measurements (a) Two-Dimensional Surface Plot, (b) Principal E-Plane Cut And (c) Principal H-Plane Cut .....	151
Figure 7.14 Indirectly Measured Near-Field Magnitude (a) Surface Plot, (b) Contour Plot And Near-Field Phase (c) Surface Plot, (d) Contour Plot.....	152
Figure 7.15 Aperture Distribution From Indirectly Measurements Magnitude (a) Surface Plot (b) Contour Plot And Phase (c) Surface Plot (d) Contour Plot .....	153
Figure 7.16 Measured Near-Field Magnitude (a) Surface Plot (b) Contour Plot And Phase (c) Surface Plot (d) Contour Plot .....	155
Figure 7.17 Far-Field Radiation Pattern From Two-Dimensional Complex Field Measurement (a) Two-Dimensional Surface Plot, (b) Principal E-Plane Cut And (c) Principal H-Plane Cut .....	156
Figure 7.18 Aperture Distribution From Two-dimensional Complex Near-Field Measurements Magnitude (a) Surface Plot (b) Contour Plot And Phase (c) Surface Plot (d) Contour Plot .....	157
Figure 7.19 Comparison Of Parabolic Dish Far-Fields From Indirect/Direct Holography And Direct Far-Field Measurement .....	159
Figure 7.20 Comparison Of Parabolic Dish Complex Near-Field Obtained From Indirect Holography And From Direct Complex Near-Field Measurements (a) Magnitude Across Centre Of The $y$ -axis (b) Phase Across Centre Of The $y$ -axis (c) Magnitude Across Centre Of The $x$ -axis (d) Phase Across Centre Of The $x$ -axis .....	163
Figure 7.21 Comparison Of Parabolic Dish Complex Near-Field Obtained From Indirect Holography And From Beam-Limited (Spectrally Filtered) Direct Complex Near-Field Measurements (a) Magnitude Across Centre Of The $y$ -axis	

(b) Phase Across Centre Of The $y$ -axis (c) Magnitude Across Centre Of The $x$ -axis (d) Phase Across Centre Of The $x$ -axis .....	164
Figure 7.22 Comparison Of Parabolic Dish Complex Aperture Field Obtained From Indirect Holography And From Beam-Limited (Spectrally Filtered) Direct Complex Near-Field Measurements (a) Magnitude Across Centre Of The $y$ -axis (b) Phase Across Centre Of The $y$ -axis (c) Magnitude Across Centre Of The $x$ -axis (d) Phase Across Centre Of The $x$ -axis .....	166
Figure 8.1 Spectral Distribution Of An Intensity Pattern Generated By The Near-Field Of A Uniformly Illuminated $32\lambda$ Aperture And Plane Reference Beam At $90^\circ$ With $\lambda/2$ Sample Spacing Normalised To The Maximum Magnitude .....	174
Figure 8.2 Spectral Distribution Of An Intensity Pattern Generated By The Near-Field Of A Uniformly Illuminated $32\lambda$ Aperture And Plane Reference Beam At $90^\circ$ With $\lambda/4$ Sample Spacing Normalised To The Maximum Magnitude .....	175
Figure 8.3 Off-Axis Intensity Pattern Spectral Distribution For Minimal Sample Spacing.....	178
Figure 8.4 Angular Spectrum For $\lambda/4$ Sampled Data With Reference Beam Increment at $135^\circ$ Normalised To Maximum Magnitude .....	179
Figure 8.5 Direct Far-Field Measurement Of Pyramidal Horn At 10 GHz .....	182
Figure 8.6 Simulated Flann 16240 Pyramidal Horn $TE_{10}$ Aperture Illumination (a) Magnitude And (b) Phase .....	186
Figure 8.7 Flann 16240 Pyramidal Horn Near-Field Magnitude Distribution For (a) Sampling Criteria 1 $\Delta x = \Delta y = \lambda/2$ And (b) Sampling Criteria 2 $\Delta x = \lambda/6$ $\Delta y = \lambda/3$ Calculated From The Aperture Distribution In Figure 8.6.....	187
Figure 8.8 Intensity Patterns Formed Between Simulated Near-Field Of Figure 8.7 And A Reference Wave With $\theta_{XI} = 120^\circ$ For (a) Sampling Criteria 1 $\Delta x = \Delta y = \lambda/2$ And (b) Sampling Criteria 2 $\Delta x = \lambda/6$ $\Delta y = \lambda/3$ .....	187
Figure 8.9 Spectral Distribution Of Figure 8.8(a) Sampling Criteria 1 As (a) Contour Plot And (b) Cut Through The Centre Of The $y$ -axis.....	188
Figure 8.10 Spectral Distribution Of Figure 8.8(b) Sampling Criteria 2 As (a) Contour Plot And (b) Cut Through The Centre Of The $y$ -axis.....	188
Figure 8.11 Simulated Far-Field Radiation Pattern Of Pyramidal Horn Obtained Using Sampling Criteria 2.....	189
Figure 8.12 Comparison Of Pyramidal Horn Far-Field Principal (a) E-Plane And (b) H-Plane Produced Through Simulation Using Fresnel Integrals And Direct/Indirect Holography For Sampling Criteria 2 .....	190
Figure 8.13 Comparison Of Initial Aperture Illumination and Reconstructed Aperture Field From Indirect Holographic Processing Using $\lambda/6$ Sample Spacing (a) Magnitude Across Centre Of The $x$ -axis (b) Phase Across Centre Of The $x$ -axis (c) Magnitude Across Centre Of The $y$ -axis (d) Phase Across Centre Of The $y$ -axis.....	192
Figure 8.14 Measured Two-Dimensional Intensity Pattern For Pyramidal Horn For Sampling Criteria 1 $\Delta x = \Delta y = \lambda/2$ and $\theta_{XI} = 120^\circ$ (a) Surface Plot Of Measured Data, (b) Cut Through Centre Of The $x$ -Axis And (c) Cut Through Centre Of The $y$ -axis .....	195
Figure 8.15 Spectral Distribution Of Intensity Pattern In Figure 8.14 Using Sampling Criteria 1 (a) Contour Plot And (b) Cut Through The Centre Of The $y$ -axis.....	195

Figure 8.16 Measured Two-Dimensional Intensity Pattern For Pyramidal Horn For Sampling Criteria 2 $\Delta x = \lambda/6$ $\Delta y = \lambda/3$ and $\theta_{XI} = 120^\circ$ (a) Surface Plot Of Measured Data, (b) Cut Through Centre Of The $x$ -Axis And (c) Cut Through Centre Of The $y$ -axis.....	197
Figure 8.17 Spectral Distribution Of Intensity Pattern In Figure 8.14 Using Sampling Criteria 2 (a) Contour Plot And (b) Cut Through The Centre Of The $y$ -axis.....	198
Figure 8.18 Far-Field From Pyramidal Horn Sampling Criteria 2.....	198
Figure 8.19 Measured Complex Near-Field Magnitude (a) Surface Plot, (b) Contour Plot And Phase (c) Surface Plot And (d) Contour Plot.....	199
Figure 8.20 Far-Field Radiation Pattern Of Pyramidal Horn Obtained From Complex Near-Field Measurements .....	200
Figure 8.21 Comparison Of Far-Fields Of Pyramidal Horn In The Principal (a) H-Plane And (b) E-Plane Obtained Using Direct Far-Field Measurement, Direct Holographic Measurement And Indirect Holographic Measurement Using Sampling Criteria 2.....	201

## Tables

Table 6.1 Antenna Properties.....	112
Table 6.2 Measurement Parameters For Initial One-Dimensional Scanning System Verification .....	116
Table 6.3 Phase Shifter Settings at 12.7 GHz.....	118
Table 7.1 Comparison Of Theoretical And Simulated Beam Properties For A $32\lambda \times 32\lambda$ Aperture With $TE_{10}$ Distribution .....	144
Table 8.1 Measurement Parameters Used For Pyramidal Horn.....	185
Table 8.2 Phase Shifter Settings At 10 GHz.....	193

# ACKNOWLEDGEMENTS

First and foremost, I would like to thank my Principle Supervisor Dr. David Smith, for all of his time, effort, support, suggestions and patience during throughout the entirety of this research work. Without his valuable contributions and insights this work would not have been possible. I will be forever indebted to him.

I would also like to thank other members of the academic team at Northumbria University, especially Dr Sean Danaher for always providing me with an outlet for my frustrations and Prof. Alistair Sambell as my second supervisor, maintaining interest and offering support.

To the German placement student contingent including Peter Tittes, Egon and Andreas Kellner, their work on developing the positioning system used in this work was critical to the success of the project and for that I am in their debt.

To my co-researchers Chatchai Supitaksakul, Yu Jian, Shit Fun Ooi, Chong Ng, Mahesh Menon, Wisit Loedhammacakra, Ezzeddin Gheblawi, Farok Azmat and Razali Ngah to name but a few, thank you for your unfaltering support and encouragement, without which I would have left long before the end.

Finally, to my family and Robert Burke goes the utmost gratitude and thanks for without whom, I would have never made it this far.

# DECLARATION

I hereby declare that this thesis is entirely my own work and has not been submitted in support of an application of another degree or qualification of this or any other university, institute of learning or industrial organisation

Signature:

Name: Mark Leach

Date: 30/9/04

# GLOSSARY OF ACRONYMS

AUT .....	Antenna Under Test
CATR.....	Compact Antenna Test Range
CW .....	Continuous Wave
DC .....	Direct Current
DFT .....	Discrete Fourier Transform
FNBW .....	First Null Beamwidth
FFT .....	Fast Fourier Transform
FT .....	Fourier Transform
GHz .....	Gigahertz
GPIB.....	General Purpose Interface Bus
RF.....	Radio Frequency
HPBW .....	Half Power Beamwidth
IFT .....	Inverse Fourier Transform
PC.....	Personal Computer
PWS .....	Plane Wave Spectrum
SCATR.....	Semi-Compact Antenna Test Range
SNBW .....	Second Null Beamwidth
SPCR.....	Single Plane Collimating Range
THz.....	Terahertz
VNA .....	Vector Network Analyser

# GLOSSARY OF SYMBOLS

Symbol	Definition
$A(\mathbf{k})$ .....	Electric plane wave vector magnitude
$A(k_X, k_Y)$ .....	Plane wave spectrum
$A_{AUT}(k_X, k_Y)$ .....	Antenna plane wave spectrum
$A_{MNF}(k_X, k_Y)$ .....	Measured plane wave spectrum
$A_P(k_X, k_Y)$ .....	Probe plane wave spectrum
$A_X$ .....	Dimension of antenna aperture in $x$ axes
$A_Y$ .....	Dimension of antenna aperture in $y$ axes
$D$ .....	Largest antenna dimension in meters
$D1$ .....	Measured data set one
$D2$ .....	Measured data set two
$D3$ .....	Measured data set three
$D4$ .....	Measured data set four
$E(\mathbf{k})$ .....	Electric field plane wave vector
$E(x, y, z)$ .....	Electric field vectors on a plane
$E_{FF}(\theta, \phi)$ .....	Radiating electric field vector in right-handed spherical co-ordinate system
$E_R(x, y)$ .....	Electric field of reference wave over a plane
$E_O(x, y)$ .....	Electric field of object wave over a plane $x, y$
$g$ .....	Incremental variable for $k_X$ axes
$h$ .....	Incremental variable for $k_Y$ axes
$I_{IL}(x, y)$ .....	Intensity of interference for an in-line hologram over a plane $x, y$
$IL1(k_X, k_Y)$ .....	Fourier transform of component one of an in-line hologram
$IL2(k_X, k_Y)$ .....	Fourier transform of component two of an in-line hologram

$IL3(k_x, k_y)$ .....	Fourier transform of component three of an in-line hologram
$IL4(k_x, k_y)$ .....	Fourier transform of component four of an in-line hologram
$INF_{IL}(x, y)$ .....	In-line intensity formed in the antenna Near-Field over a plane $x, y$
$I_{OA}(x, y)$ .....	Intensity of interference for an off-axis hologram over a plane $x, y$
$\mathbf{k}$ .....	Wave vector
$k_0$ .....	Wavenumber in rads/meter
$k_{OBJ}$ .....	Spectral extent of the object component
$k_X$ .....	wave vector $x$ component
$k_Y$ .....	wave vector $y$ component
$k_Z$ .....	wave vector $z$ components
$k_{XAUTMAX}$ .....	Maximum non-negligible spectral width of the antenna beam in $k_X$ direction
$k_{YAUTMAX}$ .....	Maximum non-negligible spectral width of the antenna beam in $k_Y$ direction
$k_{XMAX}$ .....	Maximum spatial frequency of Fourier Transform in $k_X$ axes
$k_{YMAX}$ .....	Maximum spatial frequency of Fourier Transform in $k_Y$ axes
$k_{XR}$ .....	Spectral value of reference intercept angle in $x$ axes
$k_{YR}$ .....	Spectral value of reference intercept angle in $y$ axes
$k_{XV}$ .....	Valid spectral beamwidth in $k_X$ axes
$k_{YV}$ .....	Valid spectral beamwidth in $k_Y$ axes
$l$ .....	Integer defining the power of 2 data set length for the FFT
$N_X$ .....	Number of elements in $x$ axes
$N_Y$ .....	Number of elements in $y$ axes
$O(x, y)$ .....	Object field magnitude over a plane $x, y$

$o(k_x, k_y)$ .....	Object spectral distribution
$OA1(k_x, k_y)$ .....	Fourier transform of component one of an off-axis hologram
$OA2(k_x, k_y)$ .....	Fourier transform of component two of an off-axis hologram
$OA3(k_x, k_y)$ .....	Fourier transform of component three of an off-axis hologram
$OA4(k_x, k_y)$ .....	Fourier transform of component four of an off-axis hologram
$R$ .....	Reference wave magnitude
$\mathbf{r}$ .....	Position vector to any co-ordinate $x, y, z$
$s$ .....	Incremental variable for $x$ axes
$S_X$ .....	Scanning window width in the $x$ axes
$S_Y$ .....	Scanning window width in the $y$ axes
$S_{XMIN}$ .....	Minimum Near-Field width for a given valid angle
$t$ .....	Incremental variable for $y$ axes
$T_{F1}(k_x, k_y)$ .....	Fourier transform of component one of an Off-Axis hologram illuminated by the reference wave
$T_{F2}(k_x, k_y)$ .....	Fourier transform of component two of an Off-Axis hologram illuminated by the reference wave
$T_{F3}(k_x, k_y)$ .....	Fourier transform of component three of an Off-Axis hologram illuminated by the reference wave
$T_{F4}(k_x, k_y)$ .....	Fourier transform of component one to four of an Off-Axis hologram illuminated by the reference wave
$T_{IL}(x, y)$ .....	Transmitted wave for an in-line hologram illuminated by the reference wave over a plane $x, y$
$T_{OA}(x, y)$ .....	Transmitted wave for an off-axis hologram illuminated by the reference wave over a plane $x, y$
$Var$ .....	Average variation of data sets
$Var_I$ .....	Intensity data variation
$Var_{NF}$ .....	Complex Field data variation
$W$ .....	Simplification of argument of <i>sinc</i> function

$x$	$x$ component of a right-handed Cartesian co-ordinate system
$xa$	$x$ -axis of aperture plane spaced at $\Delta x$
$xs$	$x$ -axis of sampling plane spaced at $\Delta x$
$Xa$	Width of aperture in $x$ axes
$X_{MAX}$	Maximum width in $x$ axes
$y$	$y$ component of a right-handed Cartesian co-ordinate system
$ya$	$y$ -axis of aperture plane spaced at $\Delta y$
$ys$	$y$ -axis of sampling plane spaced at $\Delta y$
$Y_{MAX}$	Maximum width in $y$ -axes
$z$	$z$ component of a right-handed Cartesian co-ordinate system
$Z_0$	Distance from antenna under test to scanning plane in meters
$Z_{FF}$	<i>Distance to Antenna Far-Field</i>
$Z_L$	Distance between two sampling planes used in iterative phase retrieval
$Z_{MIN}$	Minimum distance to Near-Field sampling window
$\lambda$	Freespace wavelength in meters
$\Delta k_x$	Spatial frequency sample spacing in $k_x$ axes
$\Delta k_y$	Spatial frequency sample spacing in $k_y$ axes
$\Delta x$	Sample spacing in $x$ axes
$\Delta y$	Sample spacing in $y$ axes
$\Delta x_{BL}$	Maximum sample spacing for beam-limited spectrums in $k_x$ axes
$\Delta y_{BL}$	Maximum sample spacing for beam-limited spectrums in $k_y$ axes
$\theta$	Angular vector component in $z$ - $x$ axis
$\phi$	Angular vector component in $y$ - $x$ axis

$\theta_{XAUTMAX}$ .....	Maximum non-negligible angular width of the antenna beam in plane $\phi = 0$
$\theta_{YAUTMAX}$ .....	Maximum non-negligible angular width of the antenna beam in plane $\phi = \pi/2$
$\theta_{XBL}$ .....	Angle of beam-limiting in $x$ axes of the sampling window
$\theta_{YBL}$ .....	Angle of beam-limiting in $y$ axes of the sampling window
$\theta_{XBW}$ .....	Maximum valid beamwidth in $x$ axes
$\theta_{YBW}$ .....	Maximum valid beamwidth in $y$ axes
$\theta_{XI}$ .....	Reference wave phase gradient in $x$ axes
$\theta_{YI}$ .....	Reference wave phase gradient in $y$ axes
$\theta_{XR}$ .....	Angle at which reference wave intercepts the hologram in $x$ axes
$\theta_{YR}$ .....	Angle at which reference wave intercepts the hologram in $y$ axes
$\theta_{XRMIN}$ .....	Minimum intercept angle for physical separation of hologram components
$\theta_{XV}$ .....	Maximum valid angle in $x$ axes
$\theta_{YV}$ .....	Maximum valid angle in $y$ axes
$\phi_{NF}(x,y)$ .....	Antenna phase over a plane $x, y$
$\phi_O(x,y)$ .....	Object field phase over a plane $x, y$

# CHAPTER 1 INTRODUCTION

## 1.1 Research Background

The antenna is one of the key building blocks in any radiated wave system. The increase in these applications over the last few decades has been vast, spanning areas from mobile communication and satellite technology to radar and scanning techniques. The demand for faster and more complex functionality in these technologies is continuous and is met by increasing system bandwidths this results in higher transmission frequencies requiring the design and development of new Radio Frequency (RF) components such as antenna. Along with the development of new antennas it is necessary that the antenna test procedures and verification methods used to measure antenna characteristics, such as their angular power distribution (Far-Field radiation pattern), gain and directivity, are continuously reviewed and improved to provide the most accurate and cost effective test solutions.

Testing is performed to ensure that an antenna selected for use in a system exhibits the properties desired by the system designer. In general, antenna measurements consist of the recording of the electric field component radiated by the antenna, with a suitable field probe. The magnetic field component could also be measured since one component is deducible from the knowledge of the other. The electric field component is commonly chosen since electric field probes offer better sensitivity and are generally more convenient.

Antenna design becomes more complex as operating frequencies increase. In tandem with this, the test processes and methodologies that must be used are more complex and costly to the point at which they are either unacceptably inaccurate due to noise, or very expensive. For this reason there is much interest in the development of new methods for the testing of antenna aimed at reducing cost.

Focussing on the measurement of the antenna radiation pattern (or Far-Field), the inadequacy of traditional Far-Field ranges for the test of high frequency or large antenna due to the distance at which the measurements must be made, of the order of several kilometres, is readily acknowledged amongst academics and engineers. Much research into the development of test ranges that can be used to take measurements closer to the antenna has been carried out, starting around the mid 1900's. Two main branches of reduced range test facilities evolved as a result of the research; these are the Near-Field range and the Compact range. Both of these are expensive in terms of the time it takes to test the antenna and the cost of the equipment required, which increases with antenna size and frequency of operation. Both of these ranges offer advantages dependant the type of antenna being measured, though it is the variety of Near-Field ranges that provides the most versatility in terms of its applicability to low medium and high gain antenna.

To facilitate the application of Near-Field theory it is required that measurements of both field magnitude and phase are made. Unlike direct Far-Field measurement or Compact range techniques where only magnitude is measured; Near-Field range measurements require a Vector Network Analyser (VNA) to obtain the phase information. The high cost of a VNA makes the use of Near-Field ranges very

expensive, especially at high frequencies, in the Terahertz (THz) region phase cannot be measured directly due to the limitations of the equipment. The desire to use the Near-Field range but minimising the cost, ultimately led to the development of methods, which required only a scalar measurement, thus no longer requiring the expensive VNA. Two Near-Field range methodologies were devised to accomplish the reduction to a scalar measurement, one of these is based on the optical technique of holography adapted for microwave antenna measurement in the early 1970's by Bennett [1], and the other relies on adaptive algorithms to derive the phase from an initial guess and scalar measurement. It is the Near-Field range coupled with the holographic technique on which this research work is concentrated.

Developed at optical frequencies, holography allows the relative phase information of waves to be recorded, encoded within an intensity only data set. A direct application of the theory used in optics can be applied at microwave frequencies, though due to hologram generation requirements some of the valid assumptions at optical frequencies cannot be held true in the microwave region. This work aims to develop novel methods, for the generation of microwave holograms that adhere to the assumptions made in the optical domain, this will be explained later.

## **1.2 Outline of Work**

The University of Northumbria has a small anechoic environment, which can be used to perform the Far-Field measurement of relatively small antenna at distances of up to  $\approx 1.5$  m. There is no permanent system for the measurement of antenna radiation patterns at reduced distances and no previous work in microwave holography has been carried out.

This work is based around the development of a measurement system capable of attaining antenna radiation patterns at reduced distances from the acquisition of intensity only data. The foundation of the system is the indirect holographic Near-Field technique devised over the past few decades. However, the manner in which the system is adapted will differ considerably to that previously utilised, to account for inconsistencies that the direct application of optical theory has in the microwave region.

Holograms are widely used in optics as a way of capturing phase information contained in an optical wavefront. A hologram is a two-dimensional recording of a scattered signal capable of reproducing a three-dimensional image of the object that produced the scatter meaning that the phase information has been attained in the recording process. An indirect hologram is a manner of recording a hologram without directly measuring phase. In optics all holograms are indirectly obtained, as phase cannot be measured therefore the two terms hologram and indirect hologram are synonymous. In the microwave region phase can be measured and so it is necessary to distinguish between direct and indirect holograms.

In general, an indirect hologram is physically formed in free space as the interference pattern formed over a two-dimensional surface by two coherent waves, a scattered wave of which it is desired to acquire the magnitude and phase information and a coherent planar reference wave. The planar reference wave is usually at an angle (Off-Axis) to the recording plane and as such exhibits a uniform magnitude and linear phase variation over the hologram. At optical frequencies the plane waves can be achieved using a laser, however at microwave frequencies a transmitted beam cannot

be assumed to be planar due to the relative wavelengths and therefore the reference generated for optical holograms cannot be replicated for indirect microwave holograms.

In the optical region hologram is generally recorded on a photosensitive medium, however a microwave hologram is generally recorded as a set of probed field measurements, though photosensitive media have been used in certain situations.

It is proposed here that the reference used to generate the microwave hologram should not be a transmitted wave, rather a bounded wave controllable using waveguide components. Instead of forming an intensity pattern in free space the intensity at individual points will be formed and collected over a scanning plane allowing the reference amplitude and phase to be controlled at each sample point.

The novel indirect holographic system proposed and constructed as part of this thesis shows that it is possible to generate a bounded Off-Axis reference wave allowing the production of indirect holograms from which antenna fields can be obtained. This will be validated by measurements made using industry standard techniques and through mathematical simulations.

### **1.3 Aims and Objectives**

The main aim of this research work is to develop a new indirect holographic technique for the determination of antenna radiation patterns and imaging antenna fields at microwave frequencies. This main aim is expressed in terms of seven objectives in order to provide a structured approach to the research:

1. To develop a theoretical basis for indirect holography and determine its limitations, by means of researching previous work and the current status of other ongoing works in similar areas: Chapters 2, 3, 4, 5 and 8.
2. To develop computer programmes in order to demonstrate the validity of this technique for the production of Far-Field radiation patterns of microwave antenna with standard illuminations using intensity patterns: Chapters 3, 5 and 8.
3. To further develop computer programmes to demonstrate the validity of this technique for the reconstruction of antenna aperture fields in both amplitude and phase from intensity patterns: Chapters 3, 5 and 8.
4. To develop an experimental system for producing microwave holographic intensity patterns with a synthesised Off-Axis reference wave and utilise this system for antenna radiation pattern measurement: Chapters 6, 7 and 8.
5. To develop programs for reconstructing antenna Far-Field radiation patterns and antenna aperture field distributions from measured intensity patterns: Chapters 6, 7 and 8.
6. To compare the results obtained using the novel indirect holographic approach with results obtained in a traditional manner using either a vector network analyser or direct Far-Field measurement: Chapters 6, 7 and 8.
7. To critically analyse the results and provide suggestions for improvement: Chapters 6, 7, 8 and 9.

## 1.4 Chapter Outline

Chapter 2 – Presents an overview of antenna radiation pattern characteristics and field regions, followed by a review of the techniques currently used in industry to measure microwave antenna radiation patterns.

Chapter 3 – Outlines Near-Field measurement theory in terms of the Near-Field to Far-Field transform, which is an integral part of the indirect holographic technique to be developed in concurrent chapters. Simulations are used to show how the method works and the problems and limitations associated with the technique are highlighted.

Chapter 4 – Introduction to holography in its more familiar form, as an optical technique. Microwave holography is discussed generally including current applications. The problems relating to the generation of microwave holograms are brought to light.

Chapter 5 – A review of the application of indirect holography to the intensity only Near-Field measurement of microwave antenna is provided. Simulations are presented showing how intensity patterns calculated for standard antenna illuminations can be processed to acquire the radiation characteristics of an antenna.

Chapter 6 – A novel method for the generation of microwave Off-Axis holograms is presented, and an initial one-dimensional practical system is constructed. Measured data is collected for a parabolic dish antenna. The processed data is then compared with measurements made using other standard techniques to show that the novel system is valid.

Chapter 7 – An automated two-dimensional system is developed to produce holographic intensity patterns for antenna measurement and data is collected for a parabolic dish antenna. The processed two-dimensional data is then compared with measurements made using other standard techniques.

Chapter 8 – The generation of a ‘slow-wave’ reference wave using the novel range, not possible using traditional techniques, allows the indirect holographic method to be applied to more types of antenna. This is demonstrated through both simulation and through practical measurement of a medium gain pyramidal horn.

Chapter 9 – Provides a summary of the conclusions that have been made during the course of the work and presents ideas for the further development of the novel antenna measurement system and highlights some of the other potential areas to which the application of this idea may be advantageous.

## **1.5 Original Contribution**

This research work is based in the area of microwave antenna radiation pattern measurement. The motivation behind this work is the continuous drive to attain microwave antenna radiation patterns in a more controlled and compact environment whilst maintaining cost effectiveness. The application of the holographic principle has been successfully used to provide a measurement range with these issues in mind, however improvements to the manner in which this methodology is applied are the focus of this research.

This research brings about further development of the optical holographic principle in the microwave domain, as applied to total field recovery required in antenna Near-Field measurement. The problem under consideration is the need to produce a plane wave with a controllable linear phase gradient over a large plane measurement surface. An approximation to the plane wave is currently made using a radiating element, however no conventional microwave-radiating element is able to provide the desired plane wave condition.

A technique for synthesising a plane wave with variable linear phase shift that can be used to form a holographic intensity pattern has been developed. The system developed provides a compact solution to the problem that can be readily adapted into any existing Near-Field system and eliminate the need for a VNA.

## 1.6 Published Works

The following is a list of publications arising as a direct result of the work carried out in this thesis:

- D. Smith, M. Leach, A. J. Sambell, 'An Indirect Holographic Method for Determining Antenna Radiation Patterns and Imaging Antenna Fields', *IEEE Int. Symp. Of Antennas and Propagation Soc.*, San Antonio Texas US, Conf. Publ. Vol.3, 2002, pp. 706-709.
- D. Smith and M. Leach, '3D Imaging Of Antenna Fields From Electronically Synthesised Scalar Intensity Patterns', *Asia-Pacific Conference On Applied Electromagnetics*, APACE-03, Kuala Lumpur Malaysia, Conf. Publ. Vol. 1, Aug. 2003, pp. 50-53.

- D. Smith, M. Leach, A. J. Sambell, 'Microwave Indirect Holographic Imaging using an Adaptation of Optical Techniques', *IEEE Microwave and Wireless Components Letters*, Vol. 13, No. 9, Sept. 2003, pp. 379-381.
- D. Smith and M. Leach, '3D Imaging of Antenna Fields and Metal Objects Using a New Indirect Holographic Technique', *Int. Conf. On Electromagnetics for Advanced Applications*, ICEAA-03, Torino Italy, Sept. 2003, pp. 711-714.
- D. Smith, M. Leach, S. S. Dlay, W. L. Woo, 'A Novel Technique for the Determination of the Radiation Patterns of Medium Gain Antennas from Scalar Intensity Patterns', *6th Int. Sym. On Antennas, Propagation and Electromagnetic Theory*, ISAPE-03, Beijing China, Oct. 2003, pp. 373-376.
- D. Smith, M. Leach and A. Kellner, 'Indirect Holographic Imaging Of Antennas Using An Electronically Synthesised Slow-Wave', *IEEE Int. Symp. Antennas And Propagation Soc.*, Monterey California, June 2004, pp. 703-706.
- D. Smith, M. Leach, M. Elsdon and S. J. Foti, 'Using Invisible Region Wave Vectors For Determining The Properties Of Microwave Antennas And Imaging Fields', *4<sup>th</sup> Int. Symp. On Communication Systems, Networks And Digital Signal Processing*, CSNDSP-04, Newcastle UK, July 2004, pp. 248-251.
- D. Smith, M. Leach, M. Elsdon and S. J. Foti, 'Imaging Of Concealed Objects From Scalar Microwave Holograms', *RF and Microwaves Conf.*, RFM-04 Malaysia, Oct. 2004, pp. 127-131.
- D. Smith, M. Leach, M. Elsdon and S. J. Foti, 'Holographic Reconstruction of Dish Antenna Measurements', *Int. Symp. On Antennas*, JINA-04, Nice France, Nov. 2004, pp. 308-309.

# CHAPTER 2 ANTENNA RADIATION PATTERNS AND MEASUREMENT RANGES

## 2.1 Introduction

The purpose of this chapter is to present a general overview of antenna fields and measurement processes. This is a necessary point of departure as it provides evidence for the motivation behind the research work while offering a useful insight into the research area as a whole.

The concept of the antenna radiation pattern is described along with the antenna field regions in section 2.2. The field regions are shown to control the type of measurements that must be used in order to attain the desired antenna radiation pattern. Once these initial concepts regarding antenna fields have been explained, an examination of the types of measurement range that are currently used to obtain the antenna radiation pattern is made. First in section 2.3 the traditional direct Far-Field recording technique is discussed this is followed by the reduced range measurement techniques in sections 2.4-2.6. Emphasis in this chapter is given to the methods not being employed in the remainder of this research, which are dealt with in detail in subsequent chapters.

The general information contained in this chapter can be found in most antenna textbooks, the main text used throughout this thesis as a source of standard theory is '*Antenna Theory Design and Analysis 2<sup>nd</sup> Ed, by C. A. Balanis*' [2].

## 2.2 Antenna Radiation Patterns

The space around an antenna can be subdivided into three regions classified by the characteristics that the radiation emitted by the antenna exhibits within that region. The regions are: the 'Reactive Near-Field region', the 'Radiating Near-Field (or Fresnel) region' and the 'Radiating Far-Field (or Fraunhofer) region', each extends over a certain range of distances from the antenna. Mathematical expressions for the region boundaries have been formulated in the past based on the dimensions of the antenna and the frequency of operation, however there is no immediate distinction in the radiation pattern as the distance at which it is observed crosses these formulated boundaries. Rather they are just accepted distances, and exist in order to aid antenna designers and users to know something of the behaviour of an antenna at a given distance [3].

The measurement of antenna patterns is most commonly associated with the necessity to obtain the antenna Far-Field radiation pattern since this is the normal operating region of the antenna. In some circumstances it is also desired or even necessary to obtain field distributions within other regions closer to the antenna, for example when there have been manufacturing errors and the measured Far-Field is not as expected in comparison to its design and modelling. For example, observation of the field over the aperture of an antenna can provide detection of any faulty elements on the aperture.

The Far-Field region of an antenna is defined as "that region of the field of an antenna where the angular field distribution is essentially independent of the distance from the antenna". The distance to this point in the radiating field of the antenna can be found as a function of the antenna size and frequency of operation.

As inferred previously by the region names, the Near-Field of an antenna can be separated into two sectors. Firstly, the area closest to the antenna is the Reactive Near-Field, here the radiation is said to be reactive as there is a high degree of coupling between the field and the antenna. The effect of this coupling is to cause waves to be produced, which do not propagate more than a few wavelengths beyond the antenna and therefore are not present in the Far-Field; these are generally termed as evanescent waves. The second sector is the Radiating Near-Field, located between the Reactive Near-Field and the Far-Field. The relative magnitude of the propagating wavefront in this region changes with distance and therefore the field is said to be complex. In short until the wavefront reaches the Far-Field the antenna pattern can be considered to be forming. Generally accepted distances from the antenna to the boundaries of these regions are as shown in Figure 2.1, of particular interest is the distance to the Far-Field [2]-[4]:

$$Z_{FF} = \frac{2 \cdot D^2}{\lambda}, \quad (2.1)$$

where  $D$  is the largest dimension of the antenna and  $\lambda$  the wavelength of operation.

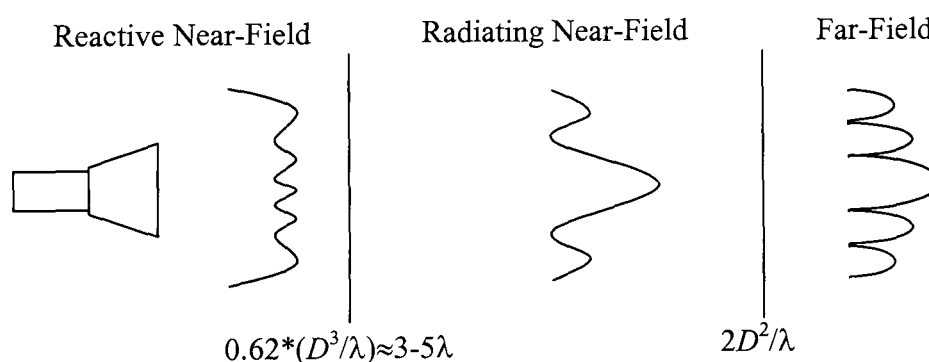


**Figure 2.1 The Field Regions Of An Antenna**

As seen in Figure 2.1 and (2.1), the formulae used to define the boundaries are based on the physical size of the antenna and the frequency of operation. In terms of the Far-Field, it is most notable that as the largest dimension of the antenna increases then the

distance to the Far-Field increases proportional to its square. The distance to the Far-Field also increases proportional to the frequency. These boundary approximations assume that the value  $D > \lambda$ , where it is not, then the distance to the Far-Field is assumed to be negligible and the extents of the Near-Field regions almost zero.

An example of the Far-Field radiation pattern of a directive antenna is shown in Figure 2.2 with its significant features highlighted: the half power beamwidth the various null beamwidth's and the relative levels of the side lobes to the maximum of the major lobe.

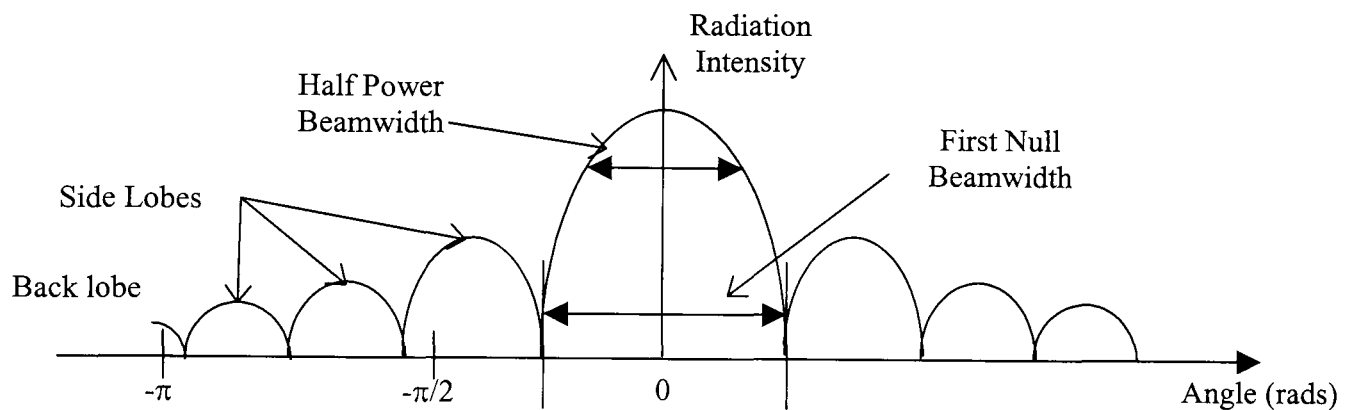
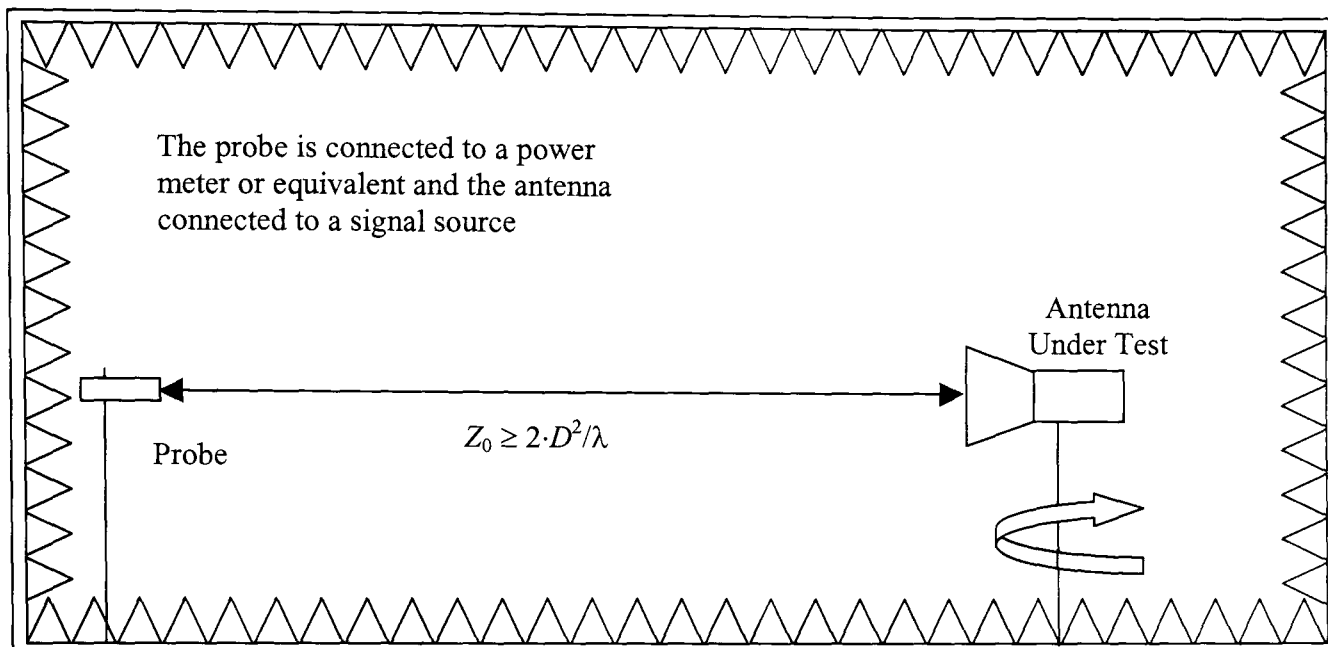


Figure 2.2 Features Of An Antenna Radiation Pattern

### 2.3 The Far-Field Test Range

The most straightforward way to obtain the Far-Field radiation pattern of an antenna is through its direct measurement on a Far-Field test range. The measurement itself is a recording of relative power as the Antenna Under Test (AUT) it is rotated about its axis. The distance between the probe and the AUT ( $Z_0$ ) should be at least the distance to the AUT Far-Field given as (2.1). Either the probe or the AUT can be used as the transmitter or receiver, as through reciprocity this would lead to the same result [2]. A basic Far-Field test range is shown in Figure 2.3.



**Figure 2.3 A Simple Direct Far-Field Test Range**

These ranges exist in both anechoic, but more commonly non-anechoic environments. An anechoic environment is clearly preferable, as it provides shielding from outside sources and prevents reflections of the AUT field from surrounding elements. It is the distance over which the measurements must be taken that dictates whether or not an anechoic environment is practical. For high frequency/large antenna the distance to  $Z_{FF}$  can be of the order of 10's-1000's of meters or even more for which the construction of anechoic chambers is not feasible. Non-anechoic environments can result in high levels of noise contamination.

If the AUT is used as the receiver in the measurement (as is common practice), its aperture must be illuminated by a plane wave while the relative power received as the antenna is rotated about its axis is recorded. This requires that the illuminating element be located in the AUT Far-Field. If the AUT is used as the transmitter then the power received by the field probe is recorded as the AUT is rotated about its axis. This also requires that the probe is located in the Far-Field of the AUT.

Various approaches have been developed such as slant ranges, elevated ranges and reflection ranges. All of these ranges have been developed with the premise of accounting for reflections from the most likely contributor over the large distances involved i.e. the ground. If the range in Figure 2.3 were outdoor and stretched over 10's of meters, then the pattern received by the probe would be contaminated mainly by a reflection from the ground appearing at the probe location. The 'Elevation' range [2] was developed to overcome this problem using the AUT as the receiver located in an elevated position in relation to the antenna used for illumination. The illuminating antenna needs to be directive so that there is little, if any, of the radiated energy directed towards the ground. However, it must also provide the AUT with plane wave illumination in order for the AUT to appear to be receiving in its Far-Field mode as it is rotated and the relative received power recorded with angle. The planarity of the wave achieved in this manner is dependant on the size of the AUT that needs to be illuminated and the distance at which the antenna pair can be placed.

The 'Slant' range [5], still requires that the AUT be operated in its receiving mode and be mounted in an elevated position in relation to the illuminating antenna. Unlike the Elevated range the illuminating antenna is not narrow beam in order to avoid reflections from the ground, here ground reflections are harnessed by placing the antenna very close to the ground. This utilises the ground as an extended section of the illuminating antenna and is arranged such that the reflections combine with the direct radiation to create a plane wave front for the AUT.

Other methods of producing a plane wave illumination to the AUT, without suffering reflections from the ground or the surroundings have been utilised, such as reflection

ranges. These must be designed very carefully as they rely on causing constructive and destructive interference from known reflection sources to effectively cancel them out leaving the desired plane wave [6]. Where distances are unfeasibly large for such a range to be constructed satellites have been used to provide the illumination [7]. This obviously generates its own set of problems such as noise contamination from other transmitting sources. A useful guide to Far-Field antenna test procedures is the *IEEE* standard from 1979 [8].

The major drawbacks of all of these techniques are the large distances required to perform the measurements over and the background noise, which cannot be controlled in an outdoors environment. Even though good results are obtained when using these ranges, they are highly expensive in terms of space requirements, which are constantly increasing along with the development of higher frequency applications and larger antenna. They also require the AUT to be relocated to the range in order to be measured, which for very large antenna is not always practical or even possible. These were the main driving forces behind the movement to reduced range techniques. The two main solutions developed are the Compact Range and the Near-Field Range, both in common use in industry today.

## **2.4 The Compact Antenna Test Range**

R. C. Johnson pioneered the Compact Antenna Test Range (CATR) in the 1950's [9]. The idea behind the range is reasonably straightforward; the aim is to produce a plane wave wide enough to fully illuminate an AUT in receiving mode. Recording the power received by rotating the AUT about its axis then provides the desired antenna Far-Field radiation pattern, as the antenna appears to be receiving in its Far-Field. The

simplest method of creating this plane wave zone or test zone is using a parabolic reflector with a small feed element as shown in Figure 2.4. Other similar systems utilise more than one reflector to produce a higher quality plane wave region. Many varieties of compact range exist including, the Semi-Compact Antenna Test Range (SCATR), introduced by Farhat [10], where only a partial parabolic reflector is used along with mathematical transformations. Also the Single-Plane Collimating Range (SPCR) where rather than creating a plane wave region a cylindrical wave is used to illuminate the AUT and mathematical expansions are used to extrapolate the AUT Far-Field.

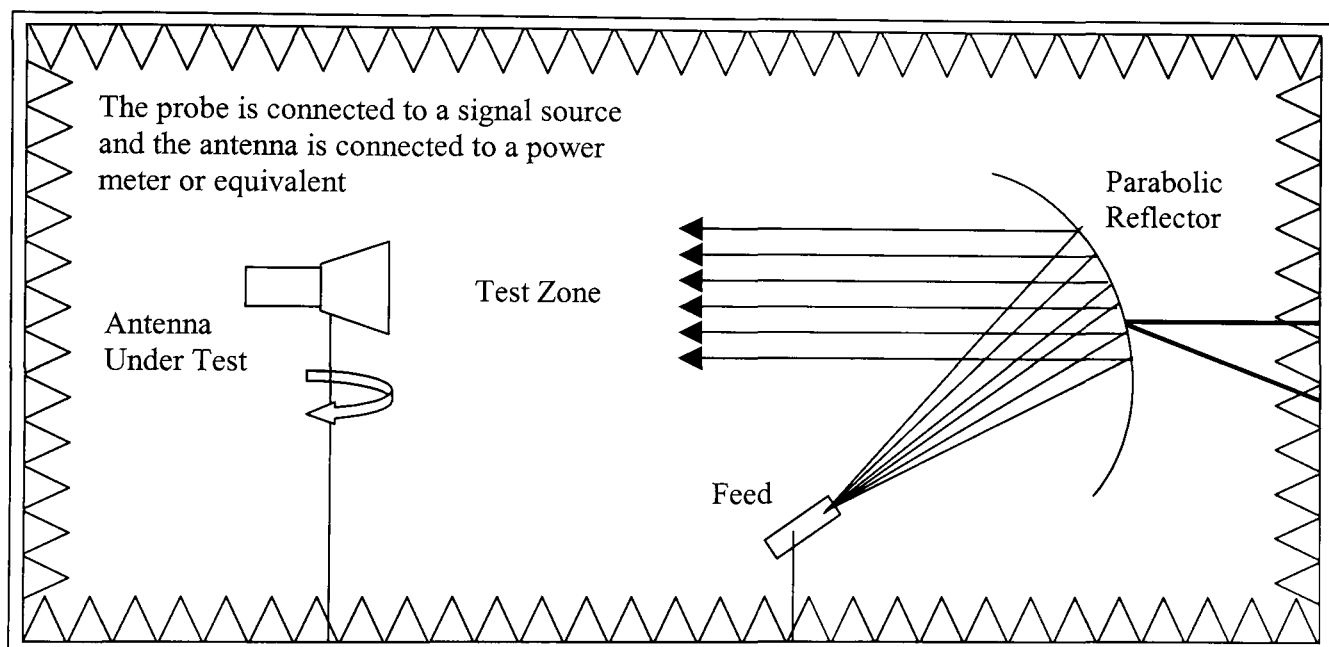


**Figure 2.4 A Simple Compact Antenna Test Range**

Observation of the manner in which the plane wave region/test zone is generated, makes the main limitations of the compact range immediately apparent. Three key problems that need to be avoided are, aperture blockage, where the feed element blocks or causes interference in part of the wave reflected by the parabola, direct radiation from the feed to the AUT and diffraction from the edges of the reflector or none perfect manufacture of the reflector causing none plane reflections to occur in the test zone. The diffraction effects increase with frequency; various mechanisms

have been employed to reduce this problem, such as curved or serrated edges on the reflectors designed to diffract the parts of the wave hitting the edges of the reflector away from the plane wave/test region [2].

The fabrication of large parabolic reflectors is very difficult and also feeding the large reflector from a suitable source becomes more difficult at higher frequencies. Despite these limitations, the compact range is still a highly utilised method, receiving continued attention in its development as an antenna metrology tool operating at frequencies up into the high millimetre wave bands [11].

Continuing developments in CR design are concerned with the improvement of the planarity of the wave generated in the so-called quiet zone, considering the edge reflections and feed arrangements for the increasing operating frequencies of AUT's. Further information is available in the following references [12], [13]

## **2.5 The Near-Field Range**

The Near-Field Range is versatile with many configurations having been developed to allow antenna of any type to be handled. As this range type comprises one of the fundamental parts of the research, only a brief introduction and history is given here, the mathematical and practical details are discussed in Chapter 3.

The initial catalyst to the Near-Field test range was provided in 1950 by H. G. Booker and P. C. Clemmow [14] who showed that given any rectangular two-dimensional aperture distribution, the Fourier Transform (FT) could be used to express the field at all points in front of that plane as the superposition of an angular spectrum of plane

waves. The result of this, with respect to antenna measurements, was that if the complex field of an antenna was known over an aperture then the Far-Field could be found as a set of monochromatic plane waves radiating away from it, though this could only be applied to highly directional antenna, where energy is radiated along one axis.

Brown [15] realised the potential for adapting this to the Near-Field measurement of antenna in the late 50's. In 1961 Brown and Jull [16] showed how the method could be extended for use with not only directional antenna but also for omni-directional antenna by developing a cylindrical system where measurements were taken over a cylinder that enclosed the antenna rather than a rectangular plane in front of the antenna. The essence of this method is that the expansion of the radiated field is in terms of a series of cylindrical modes. A Fourier analysis of the measured Near-Field generates the amplitudes and phases of these modes, and the radiation pattern is obtained as a Fourier series containing these amplitudes and phases. The movement to a spherical scanning surface where the wave expansions are in terms of spherical waves was suggested, though the process was considered too computationally demanding, as calculations at that time were performed using a desktop calculator.

The effect of the probes directional field on both planar and cylindrical Near-Field measurements was also considered by Brown and Jull, who argued that correction was required which until then had been thought negligible and was ignored. A detailed analysis of probe correction was not addressed until 1963, by D. M. Kerns [17], [18].

In 1970 Jensen [19], devised the mathematical process required for the treatment of measurements made on a spherical surface. The mathematical computation involved here was far more rigorous than that of either the planar or cylindrical expansions. At the time the computational power to perform the required calculations was still not available. In 1975 Wacker [20] presented some work exploiting orthogonalities in the data, reducing the level of computation and making the process possible.

The drive for reduced scanning time and data reduction led to the development of more scanning surfaces including plane-polar and bi-polar (See Figure 2.5). These surfaces although restricted, like the planar method to the measurement of directive antenna, utilise scanning systems and co-ordinates that allow a reduction in data collection and they are mechanically more accurate in comparison to the planar technique. This work is concerned with only the planar measurement method and so the discussion shall remain there, however references regarding the other measurement surfaces are offered to provide further information [2], [21], [22].

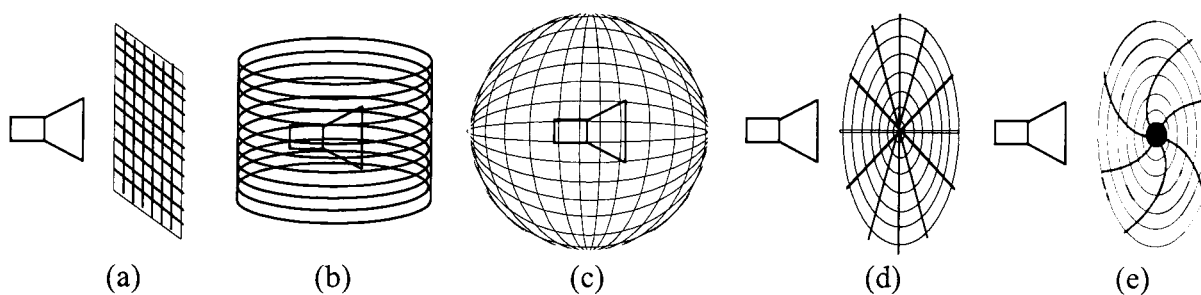


**Figure 2.5 The Five Scanning Surfaces Used For Antenna Near-Field Measurement**  
**(a) Planar (b) Cylindrical (c) Spherical (d) Plane-Polar and (e) Bi-Polar**

To reproduce the Far-Field from measurements made on a planar surface in the antenna Near-Field, the data collected must be representative of the whole field radiated by the antenna. This means that the measurement surface is required to encapsulate the majority of all radiated energy. Another important factor is that it is the total field information that has to be measured, meaning that both amplitude and

phase information is needed. As in any discrete system, for the collected data to correctly represent the antenna pattern it must meet a minimum sampling criteria, the Nyquist rate. For very large antenna this can mean that extremely large data sets are necessary resulting in longer data collection times.

Apart from the collection of large data sets, the other major drawback of this technique is that in order to measure the complex field at discrete sample points, a VNA is required to provide the phase component, which leads to a high cost measurement facility. To accurately measure the phase component at very high frequencies an anechoic measurement facility is necessary along with an automated positioning system; at THz frequencies it is not possible to measure the phase directly due to the availability of suitable equipment, rendering the direct application of this method impossible. A typical Planar Near-Field Range is shown in Figure 2.6, the probe is moved over a regular rectangular grid of points with samples of magnitude and phase collected at each. The sampling plane is usually located just outside of the reactive Near-Field to maximise the use of the available sampling plane size.

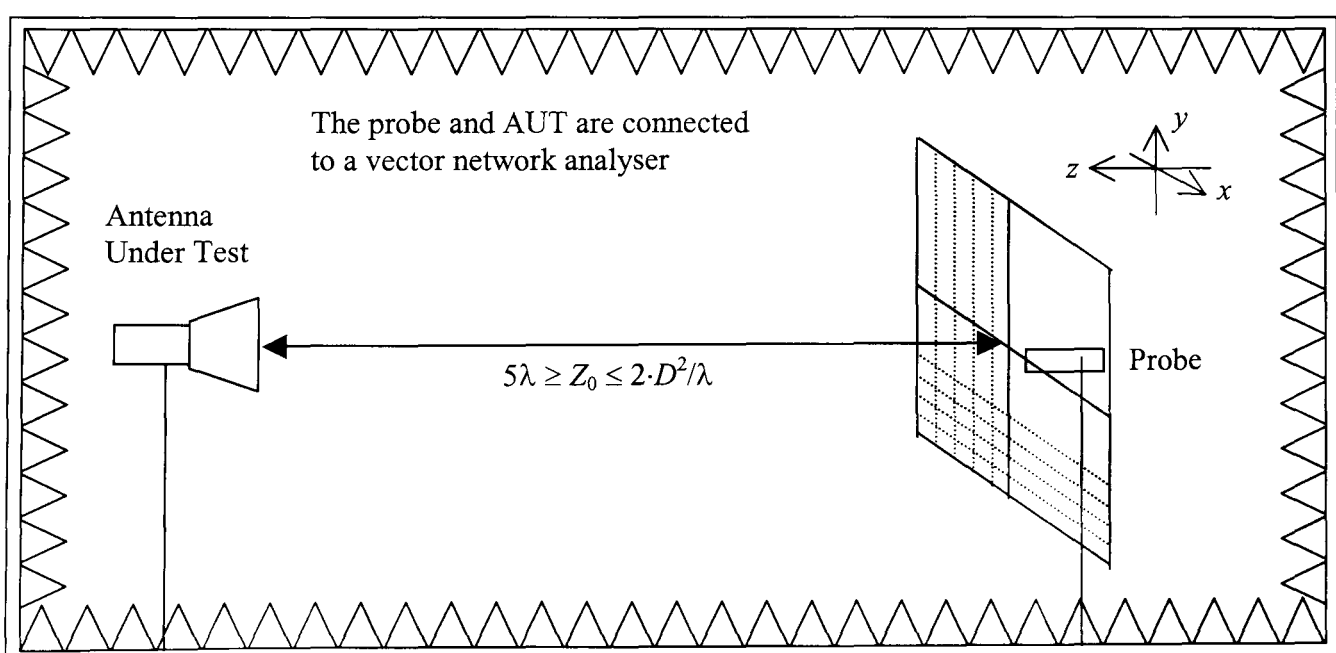


Figure 2.6 A Typical Planar Near-Field Test Range

A large portion of research work was carried out in the late 1980's on the Near-Field range. The work was mainly concerned with error prediction and analysis regarding probe positioning and accuracy of the computation techniques involved. These works although required at the time to attain the desired levels of accuracy have become somewhat surplus to requirements. This is down to the advent of the high-speed computers now available that provides the ability to perform high accuracy calculations at great speed and also the development of highly accurate positioning systems [23]. These works are therefore not dealt with in this thesis, however reference to a special issue of the IEEE Transactions on Antennas and Propagation devoted entirely to this field of work [24].

Over the past five to six years, much of the Near-Field range development work has been concerned with scanning instrumentation development and the reduction of data acquisition and scan times, especially in the measurement of very large antenna. A 2004 paper by Resnburg [25], details the use of a constant intensity contouring truncation, where rather than using the standard rectangular grid of points the data is truncated at a pre-selected level and the contour around the field pertaining to that level is used for the truncation. A 20% reduction in scanning time was achieved for while the same level of Far-Field pattern accuracy was obtained.

Another focal point of Near-Field range development has been the movement away from the direct measurement of phase to the cheaper scalar measurement. This is partially due to the cost of the measurement facility required in order to measure the phase and partially due to the movement of operating frequencies to millimetre wave

frequencies where direct phase measurement is not possible. These intensity only Near-Field measurement ranges are the topic of discussion in the next section.

The theoretical basis for the planar Near-Field to Far-Field transform is well founded, widely used and accepted. The details of the theory will be given in Chapter 3 and then demonstrated by simulation, in order to provide comparisons with simulation work developed later.

## **2.6 Intensity Only Near-Field Ranges**

The problems associated with the need to measure the phase in Near-Field, fuelled the search for ways both mathematical and physical to measure close to the antenna without requiring the phase of the field. Two methods were devised, namely holography and iterative phase retrieval; these methods will now be discussed.

### **2.6.1 Holographic Near-Field imaging**

As this topic represents the major part of this work, only a brief history of the development of holography will be provided here, leaving the in depth discussion and mathematical examination to later chapters.

Holography, was pioneered by D. Gabor in the late 1940's in the optical field [26]-[28], while attempting to improve the resolution of an electron microscope. Gabor realised that by recording the interference between, waves scattered from an object and a well-known source all of the information about both waves was retained in the recording. He also realised that if the well-known source could be recreated and used to re-illuminate the recorded interference then the object information could be fully

recovered. The main problem in his early work was that, in order to create a good quality hologram a truly coherent light source was required to provide both waves. At the time, the best approximation to this was obtained using a mercury arc lamp; this restricted Gabor to only working with transparencies to provide two-dimensional images. The images he managed to produce were of very poor optical quality; this was because the wanted image that was produced was obscured by a twin image generated inherently as part of the procedure.

It wasn't until the development of the Laser around 1960, a truly coherent light source, that two scientists E. Lieth and J. Upatineks [29]-[33], realised the potential of the hologram for imaging in three-dimensions from their work in side looking radar. Their solution for removing the twin image entailed physically offsetting the well-known wave from the wave scattered by the object. This became possible because of the laser, which meant that they were able to produce the first high quality three-dimensional holographic images (these were of a train and a bird). A subsequent explosion in holography work began and still continues today.

In the early 1970's the optical holographic principal was incorporated into the microwave field by Anderson [34] and especially Bennett et. al. [35], [36], who specifically looked at its use in the measurement of large microwave antenna radiation patterns; Huang [37] then implemented this work in the THz frequency range. It is not possible to simply apply the optical principals developed in previous years at microwave frequencies, because not all of the assumptions that can be made in the optical domain can be held in microwave domain due to the much larger wavelength. It is some of these issues that are the focus of this thesis.

## 2.6.2 Iterative phase retrieval

The technique of iterative phase retrieval was, like holography, developed for use in optics where direct measurement of phase is not possible, it has also found use in areas such as electron microscopy, X-Ray crystallography and astronomy [38]. The first phase retrieval algorithm is known as the Gercheberg and Saxton algorithm [39]. Unlike the holographic technique, the iterative method does not rely on the production of a coherent reference wave. Instead, the intensity distribution is recorded as per the normal Near-Field technique over one of the surfaces shown in Figure 2.5, however it is measured two or more times over identical planes set at different distances from the antenna. Knowing the distance between the planes the phase retrieval algorithms can be applied to the data to extrapolate the relative phases at each point. However this method relies on an initial estimate of the field distribution and attempts to solve for the phase by iterating back and forth between the measured planes and the initial guess to find a best-fit solution.

Many algorithms have been developed for phase retrieval; these have not been studied as part of this work though many texts exist e.g. [40], [41]. A typical arrangement for planar phase retrieval is shown in Figure 2.7. Some of the problems with this method are in aligning the measurement plane with the AUT, this is because any phase error incurred across the measurement plane will increase errors in the output of the algorithm. Also, in general at least two planes of data have to be collected to use a phase retrieval algorithm increasing the test duration, some algorithms have been developed around single plane scanning but are usually less accurate in their solutions Anderson et. al. [42], [43].

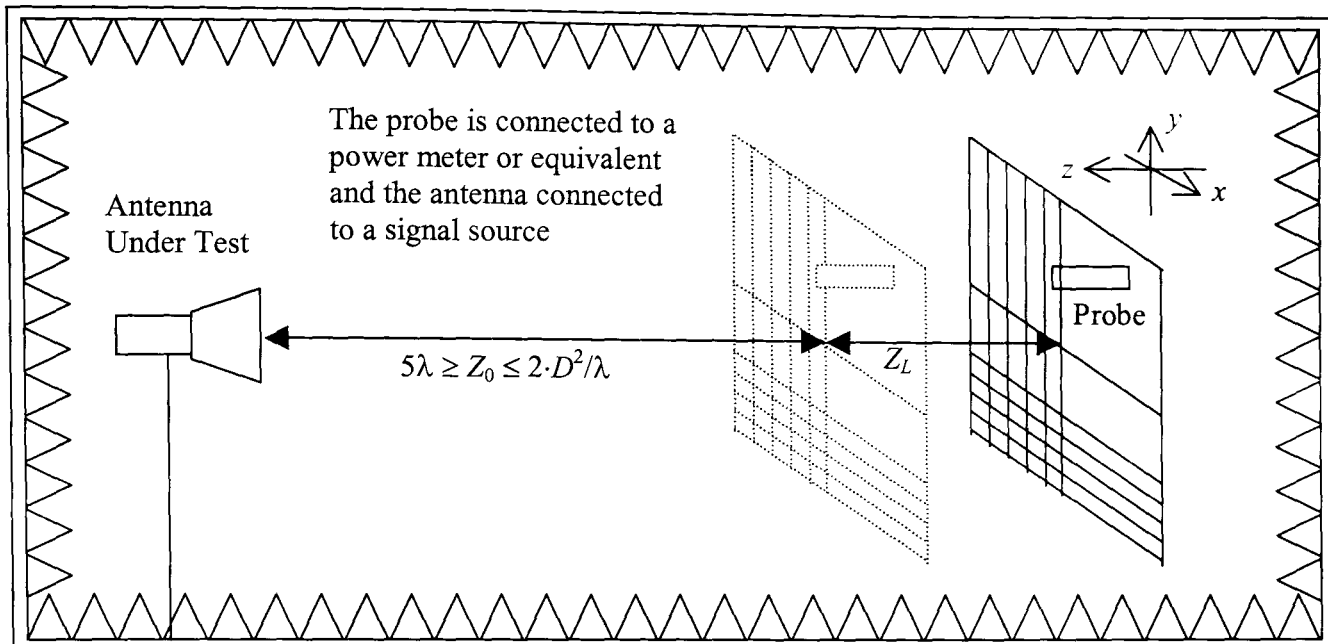


**Figure 2.7 Iterative Phase Retrieval Test Range**

An interesting third method of retrieving the phase from an intensity only Near-Field measurement has been suggested recently by Costanzo et. al. [44], in which two co-planar probes are used to simultaneously receive the Near-Field of the AUT using one of the standard Near-Field measurement surfaces. The phase of each sample point can be determined implicitly from the two measurements, which due to the co-planarity of the probes used are at quadrature to each other. This work has been carried further by El-Said and Attiya [45], who used two similar probes to simultaneously sample to Near-Field recording the squared power from each as well as the sum of the squared power of the received samples in phase and a specified amount out of phase. Knowing these four components and the phase shift between the two components the phase can be deduced.

## 2.7 Summary

This chapter has presented and explained the basic theory regarding antenna fields and outlined the property of the antenna that is going to be measured later in this thesis. An examination has been made of the methods that have been previously developed for the measurement of the antenna Far-Field radiation patterns.

This began with the traditional Far-Field range for which it was discussed that, with increasing frequencies and antenna sizes the distance that the probe needed to be located from the AUT can become unfeasibly large due to measurement contamination from noise and reflections from the surrounding environment. The need to measure at shorter distances was shown to have led to two forms of reduced distance range the compact range as discussed in Section 2.4 and then the Near-Field ranges in Section 2.5. The need to measuring phase on a Near-Field range and the equipment required to do so leads to a high cost or at THz frequencies simply is not achievable due to equipment limitations. Two further ranges were developed as discussed in section 2.6 which were variations of the Near-Field range the require only a scalar measurement. Of these two, the hologram based technique is seen to provide the most efficient means of measurement requiring only a single scan and not requiring an initial guess on which to form an approximate field distribution.

The literature review highlighted an inequality between the optical holographic technique on which this microwave antenna measurement process is based and its physical application at microwave frequencies. The initial work carried out by Bennet [35] and then furthered by Huang [37] both comment on the inability to produce the highly desirable plane wave as used in optics for the reference wave. In this thesis a

synthetic reference plane wave is developed to improve the formation of Off-Axis indirect microwave holograms, as will be explained in Chapter 4.

Prior to the development of the holographic system first the theoretical analysis behind the standard planar Near-Field technique will be presented and explained in Chapter 3. This is necessary as it is fundamental to the holographic system to be developed later.

# CHAPTER 3 NEAR-FIELD FAR-FIELD TRANSFORM THEORY AND MEASUREMENT

## 3.1 Introduction

Having examined the development of currently used measurement processes and highlighted the direction in which this research will move, it is now necessary to focus in detail on the theory and practices involved in Planar Near-Field measurements as this is the foundation on which, the holographic technique used later, is formed.

An introduction to the planar measurement theory is given in section 3.2 followed by a detailed analysis of the Plane Wave Spectrum (PWS) representation of electromagnetic waves and the determination of the Far-Field patterns from Near-Field planar measurements in section 3.3. The physical application and sampling criterion are stated and discussed in section 3.4 showing the relationship between the spatial and spectral domains. The applicability of the Fast Fourier Transform to the processing of the Near-Field data is shown in section 3.5. The ability of the PWS representation of the antenna field to provide information regarding the antenna aperture distribution through a back propagation process is discussed in section 3.6. The errors associated with planar Near-Field scanning are discussed in section 3.7. Finally a simulation of the Near-Field –Far-Field transform and aperture imaging process is provided in section 3.8

## **3.2 Introduction to Near-Field Measurement Theory**

The complex Near-Field measurement method can be described as being a direct holographic method, since total information about the antenna field is recorded. The field is recorded in both amplitude and phase, over the selected measurement surface. The planar surface is concentrated on here as it applies directly to the manner in which holograms will be formed at a later stage.

The planar Near-Field to Far-field transform process first requires that the energy radiated from the antenna be measured over a well-defined plane located in the antenna Near-Field. The measurement plane must be large enough and positioned so that it encapsulates the majority of the radiated energy. This means that the method is of use for directional antenna that radiate into only one hemisphere.

The transform from Near-Field to Far-Field is performed in two parts, firstly a two-dimensional complex field distribution is translated to a two-dimensional PWS and then, the PWS can be expanded into the third dimension allowing the radiation pattern to be found at any distance from the measurement plane. The PWS and its form will now be discussed.

## **3.3 The Plane Wave Spectrum & Near-Field Far-Field Evaluation**

The plane wave spectrum representation of electromagnetic fields was developed in the 1950's by Clemmow and has been widely used ever since. The plane wave is the most basic trial solution to Maxwell's equations and can be written as [14], [46]:

$$\mathbf{E}(\mathbf{k}) = \mathbf{A}(\mathbf{k}) \cdot e^{-j\mathbf{k}\cdot\mathbf{r}}, \quad (3.1)$$

where  $\mathbf{A}(\mathbf{k})$  is the vector amplitude,  $\mathbf{r}$  is the position vector to any point  $x, y, z$  and the vector  $\mathbf{k}$  denotes the direction of propagation, given as:

$$\mathbf{k} = k_x \hat{x} + k_y \hat{y} + k_z \hat{z}, \quad (3.2)$$

where  $k_x, k_y$  and  $k_z$  are the wave vector components.

The dot product  $\mathbf{k}\cdot\mathbf{k} = k_0^2$  is the square of the wavenumber ( $2\pi/\lambda$ ), and therefore, for any given wave only two components of  $\mathbf{k}$  may be independently specified.

It can be stated that any monochromatic but otherwise arbitrary wave, assuming that the region of free space around it contains no free charge, can be represented as a superposition of plane waves of the form (3.1), all of the same frequency and travelling in different directions, Paris and Leach [47]. The object of the plane wave expansion is to determine the amplitudes, phases and directions of propagation of the plane waves in the superposition. To put this into context, if the complex radiating field of an antenna is known over a two-dimensional aperture, then a modal expansion can be performed to provide the plane wave spectrum equivalent to that aperture field, which can in turn be transformed through the third dimension to any distance from the known plane. The modal expansion is of the form of a continuous FT, given as (3.3):

$$\mathbf{E}(x, y, z) = \frac{1}{2\pi} \int_{-\infty}^{\infty} \int_{-\infty}^{\infty} \mathbf{A}(k_x, k_y) \cdot e^{-j(k_x \cdot x + k_y \cdot y)} \cdot e^{-j k_z \cdot z} \cdot dk_x \cdot dk_y, \quad (3.3)$$

where both  $\mathbf{E}$  and  $\mathbf{A}$  are two-dimensional vectors with their third component defined implicitly.  $\mathbf{E}$  is the electric field component over a plane  $x, y$  and  $\mathbf{A}$  is the plane wave spectrum that represents that would give rise to the electric field.

The result of (3.3), is that if the tangential field is known over a plane in  $x, y$ , at a fixed distance  $z$  (generally chosen as 0 for simplification) then its inverse transform will yield the PWS as follows:

$$\mathbf{A}(k_x, k_y) = \frac{e^{-j k_z z_0}}{2\pi} \int_{-\infty}^{\infty} \int_{-\infty}^{\infty} \mathbf{E}(x, y, z = z_0) \cdot e^{j(k_x x + k_y y)} \cdot dx \cdot dy. \quad (3.4)$$

Evaluation of the integrals in (3.3) above is difficult, however if  $k_z z \gg 1$  i.e. in the Far-Field, (3.3) can then be represented via an asymptotic expansion using the method of steepest descent, which yields [2], [46]:

$$\mathbf{E}_{\text{FF}}(\theta, \phi, r) = \frac{j \cdot k_z \cdot e^{-j k_0 r}}{r} \cdot \mathbf{A}(k_x, k_y), \quad (3.5)$$

where  $\theta$  and  $\phi$  are the general spherical co-ordinates in a right-handed Cartesian system and  $r$  is the radial distance.

The wave vectors are related to the spherical co-ordinates by:

$$k_x = k_0 \cdot \sin(\theta) \cos(\phi), \quad (3.6)$$

$$k_y = k_0 \cdot \sin(\theta) \sin(\phi), \quad (3.7)$$

$$k_z = k_0 \cdot \cos(\theta). \quad (3.8)$$

Since the PWS consists of a set of plane waves all having the same frequency then the value  $k_z$  for a given  $x, y$  distribution is:

$$k_z = \begin{cases} (k_0^2 - k_x^2 + k_y^2)^{0.5} & \text{if } k_x^2 + k_y^2 \leq k_0^2 \\ -j(k_x^2 + k_y^2 - k_0^2)^{0.5} & \text{otherwise.} \end{cases} \quad (3.9)$$

The negative root is used here to ensure that the wave is bound at  $\infty$ . The only values of  $k_z$  which can be present in the Far-Field of the antenna pattern correspond to those

for which  $k_x^2 + k_y^2 \leq k_0^2$ , the maximum value of both  $k_x$  and  $k_y$  must therefore be  $k_0$ . All other values of  $k_z$  are interpreted as being generated by evanescent energy, which diminishes rapidly with increasing  $z$ . This presents a useful spatial filter for the Far-Field, truncating the spectrum at  $k_0$  in all dimensions, Wang [48].

Now that the derivation of the Near-Field to Far-Field transform has been dealt with, the discrete physical measurement of the antenna field must be considered in light of the continuous transforms detailed above.

### **3.4 Sampling in the Near-Field**

The transforms in (3.3) and (3.4) above are continuous and the integrations are over infinite planes, therefore they cannot be implemented directly. Instead the field will be sampled at discrete points over a specified surface area, this means that the double integrals become double summations, with finite limits, and the transforms are in the form of Discrete Fourier Transforms (DFT), suitable for processing the discrete data to be collected (Yaghjian [49]):

The spatial sampling of the field requires that a sampling criterion be defined to avoid aliasing. Since the spectrum is band-limited in its size then the general Nyquist sampling theorem can be used, which states that there must be at least two samples per cycle of the highest spectral component present. The sample spacing in  $x$  and  $y$  are related to the maximum spectral frequency as given in (3.10)-(3.15) (Joy and Paris [50])

$$\begin{aligned}\Delta x &= \frac{\pi}{k_{XMAX}}, \\ \Delta y &= \frac{\pi}{k_{YMAX}},\end{aligned}\tag{3.10}$$

where  $k_X$  and  $k_Y$  extend between  $\pm k_{XMAX}$  and  $\pm k_{YMAX}$ .

From the previous section we know that the Far-Field contains no component above  $k_0$ . In terms of planar Near-Field scanning this means that the spectrum is band limited at  $\pm k_0$  in both  $x$  and  $y$  axes, the maximum required sample spacing in  $x$  and  $y$  must then be:

$$\begin{aligned}\Delta x &= \frac{\pi}{k_0} = \frac{\lambda}{2}, \\ \Delta y &= \frac{\pi}{k_0} = \frac{\lambda}{2}.\end{aligned}\tag{3.11}$$

As the spatial and spectral samples are to provide a FT pair then, the relationship between the spectral spacing and the spatial domain can also be defined. As in (3.11) the spectral spacing is directly related to the width of the spatial domain given by:

$$\begin{aligned}\Delta k_x &= \frac{\pi}{X_{MAX}}, \\ \Delta k_y &= \frac{\pi}{Y_{MAX}},\end{aligned}\tag{3.12}$$

where  $X_{MAX}$  and  $Y_{MAX}$  are the spatial extents of the sampling plane.

If there are  $N_X$  and  $N_Y$  elements in  $x$  and  $y$  respectively, then the total number of points to be sampled is defined as  $N_X \times N_Y$  and:

$$\begin{aligned}
2 \cdot X_{MAX} &= N_X \cdot \Delta x, \\
2 \cdot k_{XMAX} &= N_X \cdot \Delta k_x, \\
2 \cdot Y_{MAX} &= N_Y \cdot \Delta y, \\
2 \cdot k_{YMAX} &= N_Y \cdot \Delta k_y.
\end{aligned}
\tag{3.13}$$

Each sample point in both domains can be defined over a range as:

$$\begin{aligned}
x_s &\in [-X_{MAX}, X_{MAX}], \\
k_{Xg} &\in [-k_{XMAX}, k_{XMAX}], \\
y_t &\in [-Y_{MAX}, Y_{MAX}], \\
k_{Yh} &\in [-k_{YMAX}, k_{YMAX}],
\end{aligned}
\tag{3.14}$$

where  $s$ ,  $g$ ,  $t$ , and  $h$  are given by:

$$\begin{aligned}
&\left. \begin{aligned} s &\in [0, N_X - 1], \\ t &\in [0, N_Y - 1], \end{aligned} \right\} \text{Spatial domain} \\
&\left. \begin{aligned} g &\in [0, N_X - 1], \\ h &\in [0, N_Y - 1]. \end{aligned} \right\} \text{Spectral domain}
\end{aligned}
\tag{3.15}$$

A diagrammatic representation of the sampling defined in equations (3.10) - (3.15) that would be carried out is given in Figure 3.1. It shows how the sample spacing and number of samples in each dimension are related to each other.

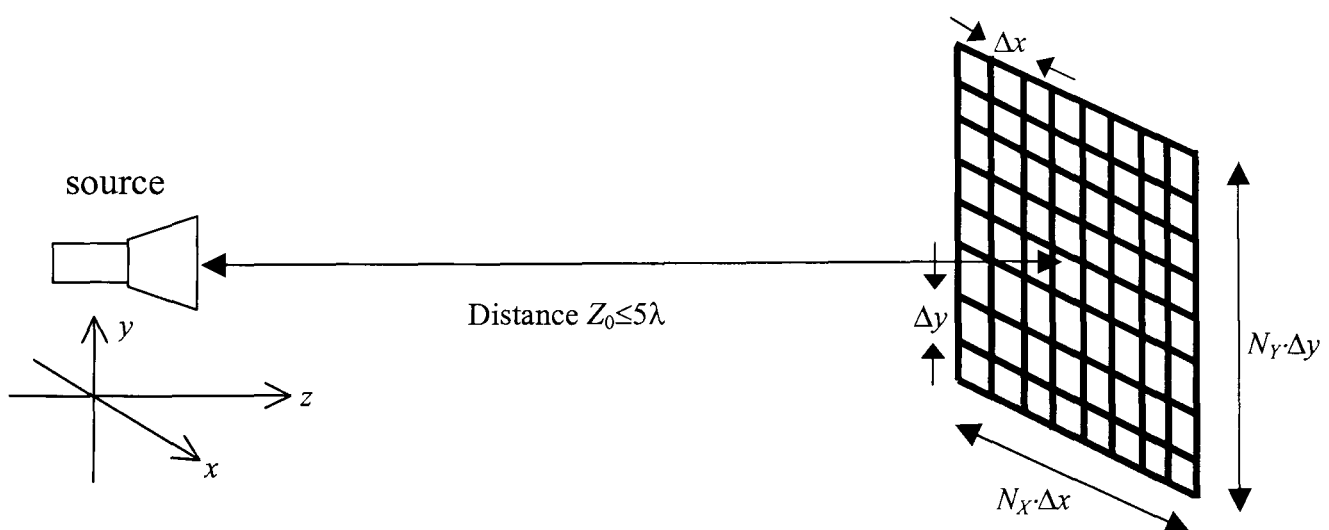


**Figure 3.1 Planar Near-Field Scanning Surface**

This sampling criterion and the spatial/spectral relationships defined, allow the DFT to be written as follows:

$$\mathbf{A}(k_{xg}, k_{yh}) = \frac{e^{-j \cdot k_z \cdot z_0}}{2\pi} \sum_{s=-N_x/2}^{N_x/2-1} \sum_{t=-N_y/2}^{N_y/2-1} \mathbf{E}(x_s, y_t, z = z_0) \cdot e^{j \cdot (k_{xg} \cdot x_s + k_{yh} \cdot y_t)}. \quad (3.16)$$

### 3.5 The Fast Fourier Transform

The above sampling relationships lead to a transform, which is suitable for processing using the Fast Fourier Transform (FFT) algorithm. This allows faster processing by exploitation of the redundancy inherent in the DFT. Consideration of the argument of the exponential of the DFT in (3.16), in any one dimension allows it to be simplified to (3.17). The redundancy in the DFT defined previously is now apparent, since the period is  $2\pi$  the second half of the exponential cycle must be the same as the first half, [51].

$$\begin{aligned} k_{xg} \cdot x_s &= g \cdot \Delta k_x \cdot s \cdot \Delta x, \\ \Rightarrow \frac{g \cdot \pi}{X_{\max}} \cdot s \cdot \Delta x &= \frac{g \cdot 2 \cdot \pi}{N_x \cdot \Delta x} \cdot s \cdot \Delta x, \\ &= \frac{2 \cdot \pi \cdot g \cdot s}{N_x}. \end{aligned} \quad (3.17)$$

Care should be taken in implementing this function as an FFT, since the origin of both the spatial and spectral domains are at their centre. Where the software used to perform the processing does not allow the origin of the vectors to be changed the output data requires some re-arranging. This involves a shift through  $\pi$  in the FFT output followed by a multiplication of each odd element by  $-1$ .

### 3.6 Aperture Imaging

It is often desirable to be able to image an antenna aperture, especially for large parabolic reflectors, where small deviations in the surface of the reflector can result in antenna focussing problems, or in phased arrays, to ensure the array elements are fed in the correct manner providing the desired beam pointing. The ability to do this offers the opportunity to evaluate the design and build of an antenna by making a comparison with its initial design and simulation. Where the Far-Field has been measured but the desired radiation pattern has not been achieved, then aperture imaging can provide evidence of disturbances in the aperture field, and enable areas of faulty manufacture or design to be located.

Aperture imaging is performed in this case using a back propagation process. Upon attaining the PWS of an antenna from its measured complex Near-Field distribution, as described previously, it is possible to then shift the PWS through a given distance by applying the required weighting to each of the plane wave's phases. This is achieved by assigning the exponential  $z$  component in (3.3) to  $-Z_0$ . Having back propagated the PWS to the aperture the inverse transform then yields the plane aperture magnitude and phase distributions as in (3.18), Rahmat-Samii et. al.[52].

$$\mathbf{E}(x_s, y_t, z = -z_0) = \frac{1}{2 \cdot \pi} \sum_{g=-N_x/2}^{N_x/2-1} \sum_{h=-N_y/2}^{N_y/2-1} \mathbf{A}(k_{Xg}, k_{Yh}) \cdot e^{-j \cdot (k_{Xg} \cdot x_s + k_{Yh} \cdot y_t)} \cdot e^{-j \cdot k_z \cdot -z_0} \quad (3.18)$$

The mathematical relationships that have been defined here will be utilised later in the formulation of holograms and to process both intensity only and complex Near-Field data.

Prior to implementation of the technique it is important to define and be aware of the sources of error inherent in planar Near-Field scanning systems and the limitations these errors introduce, these will now be discussed.

### **3.7 Physical Error Sources**

There are many sources of error, which cause degradation to the quality of the result obtained in the Planar Near-Field measurement technique, these can be attributed to physical properties including probe field errors, probe positioning errors and data truncation due to the limited size of the scanning surface, instrumentation errors and environmental errors. The effects of the physical errors can be minimised or corrected using either mathematical processes or with careful consideration of the equipment used and the sample space criteria adopted. Each of these error sources will be discussed with in turn.

#### **3.7.1 Probe field**

Probe field errors are caused as a result of the probe's non-isotropic nature. As the probe is moved over the plane it does not remain at a constant distance from the AUT, therefore the directional characteristics of the probe must have an effect on the proportion of the radiation being received. In Figure 3.2 it is shown that if the probe has directional characteristics then when it is on boresight with the AUT it is receiving more energy than it is as it moves away from boresight.

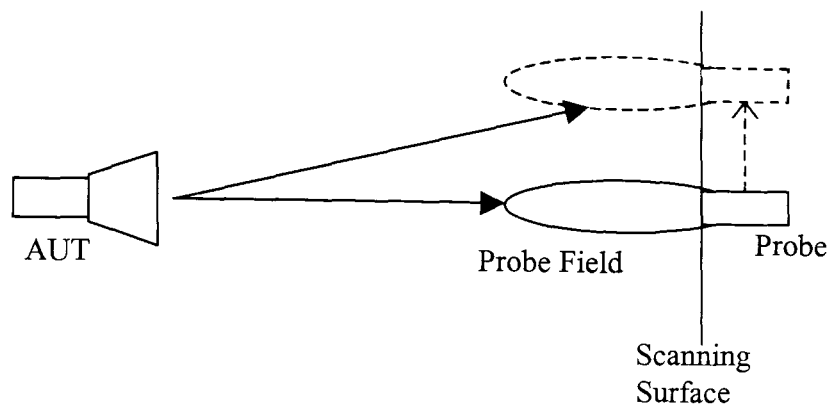


**Figure 3.2 Probe Field Effects On Planar Measurements**

This effect of the probes field can be compensated for mathematically provided prior knowledge of the probes field is possessed. As discussed in Chapter 2, Kerns first published a formulation for the correction of the probes field, later Paris, Leach and Joy [47], [53] showed that the true AUT field could be recovered from planar scanning with knowledge of the Far-Field magnitude response of the probe by consideration of the Lorentz reciprocity theorem. The measurements made in the Near-Field actually represent the convolution of the inverse of the probes field with the desired AUT field, given as:

$$\mathbf{E}(x_s, y_t, z = 0) = \frac{1}{2 \cdot \pi} \sum_{g=-N_x/2}^{N_x/2-1} \sum_{h=-N_y/2}^{N_y/2-1} \mathbf{A}_{\text{MNF}}(k_{Xg}, k_{Yh}) \cdot e^{-j \cdot (k_{Xg} \cdot x_s + k_{Yh} \cdot y_t)}, \quad (3.19)$$

where  $\mathbf{A}_{\text{MNF}}$  is the actual measured Near-Field values.

$$\mathbf{A}_{\text{AUT}}(k_X, k_Y) = \frac{\mathbf{A}_{\text{MNF}}(k_X, k_Y)}{\mathbf{A}_{\text{P}}(k_X', k_Y')}, \quad (3.20)$$

where  $\mathbf{A}_{\text{AUT}}$  is the PWS of the AUT and  $\mathbf{A}_{\text{P}}$  is the PWS of the probe.

Therefore if the probe field is known and the PWS has been calculated from the Near-Field measurements, the AUT's PWS can also be calculated. Provided the probe field does not contain any nulls, as this would mean that no signal has been received on which to perform compensation.

In general a probes field will be of the form shown in Figure 3.2. The effect of the field on the measured data is that the power level received by the probe at wider angles will be reduced as the inverse of the probe field. Therefore the sizes of the AUT's sidelobes are degraded and the nulls become less prominent.

Without due care and attention, probe compensation can introduce more error into the measurements than it removes, as the probe field must have previously been measured. Therefore the effect to which the compensation can be effective is dependant on the accuracy of the measured probe field.

### **3.7.2 Probe positioning errors**

Probe positioning errors play a big part in the accuracy of any measurement facility, especially in terms of the measurement of the phase of the AUT field. Where a positioning error occurs in the measurement plane (in this case  $x$  and  $y$  planes), the main effect is on the measurement of the AUT field phase rather than magnitude. At a frequency of 10 GHz an error of 1mm in positioning in the planes will result in a phase error of around  $12^\circ$ . This additional phase will result in a shift in the obtained Far-Field pattern. Ranges have been developed to achieve positioning accuracy up to  $25\mu\text{m}$  using laser tracking, Rose [54].

In some cases to increase the size of the scan plane ( $S_x, S_y$ ) the antenna is mounted on a movable platform in front of the scan plane and the scan is performed in several sections covering one part of the antenna at a time. The sections usually overlap to allow the scans to then be layered on top of each other and any ambiguity in overlapping measurement can be averaged out, McCormick and Da Silva [55]. In

other situations two measurements are taken over the same cross section one horizontally and one vertically and an average taken in an attempt to reduce the positioning error, Francis et. al. [56].

Probe positioning errors in the direction of propagation (in this case  $z$  direction), can cause more problems than those in the measurement plane. A shift in this case can create a larger discrepancy in the measurement of the magnitude of the AUT field, causing a greater affect on the sizes of the sidelobes obtained in the consequent Far-Field pattern, this was detailed by Corey and Joy [57] who suggested a compensation technique for a known  $z$  plane positioning error for all  $x$  and  $y$ .

### 3.7.3 Data set truncation

Clearly the data measured over the plane has to be able to represent the AUT's radiating field. To capture all of the radiation from the AUT on a plane then the AUT must radiate into a region not exceeding one hemisphere, as to measure the field at  $90^\circ$  to the antenna the plane would have to be infinitely large. This is not practical and therefore with a finite plane size some truncation of the measured field must be tolerated. This is particularly problematic for planar scanning surfaces in comparison to a spherical surface, for example where a full spherical scan results in no truncation.

The size of the planar scanning surface  $N_x \times N_y$  is chosen to meet the following criteria: It must be wide enough to contain the main part of the radiated energy, however data sets should be kept as small as possible to reduce the memory required for data storage and data processing. The size of the plane is also limited by the

anechoic environment available and by the accuracy of the positioning equipment. The larger the range the more scope there is for error in the positioning of the probe.

Truncation of the data results in two types of error, firstly as a direct result of not measuring all radiated energy, then the FFT of the truncated data set will not yield the true PWS of the AUT. The PWS will have lower sidelobe levels and the prominence of nulls will decrease the level of this discrepancy is dependant on the level of the truncation. The secondary error is caused by the FFT operation; the non-periodicity of the measured data will result in the perceived presence of a step function. To minimise this ringing effect the measurement plane needs to extend out to a point at which the AUT field is negligible in all directions.

The size of the data set is dependant on the width of the plane and the sample spacing used. As previously stated the maximum sample spacing is half wavelength in each dimension ( $x, y$ ) assuming that the maximum spectral component being  $\pm k_0$  in both planes. If a prior knowledge of the antennas pattern is known and that it is expected to be highly directive thus having a narrow angular spectrum, then the maximum spectral value in each plane could be  $< \pm k_0$ . As a result of this sample spacing can in effect be increased beyond half a wavelength. The maximum sample spacing for a beam-limited PWS becomes:

$$\Delta x_{BL} = \frac{\pi}{k_0 \cdot \sin(\theta_{XBL})},$$

$$\Delta y_{BL} = \frac{\pi}{k_0 \cdot \sin(\theta_{YBL})},$$
(3.21)

where  $\theta_{XBL}$  and  $\theta_{YBL}$  define the angle to which the Far-Field pattern is beam-limited in each dimension.

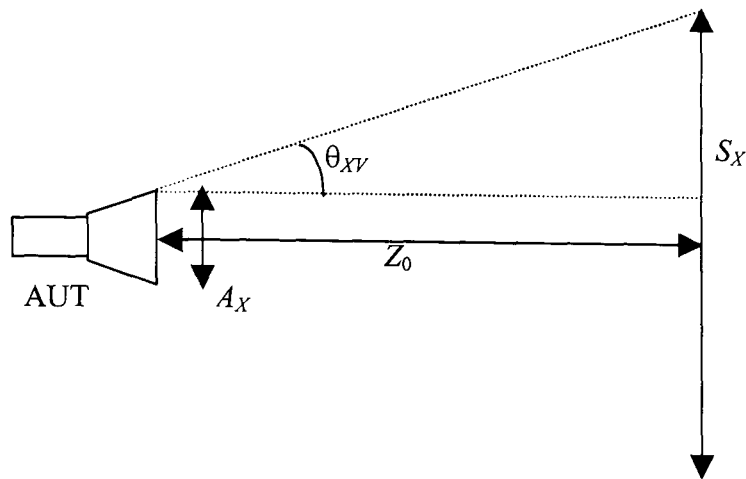


**Figure 3.3 Valid Angle Of The Far-Field Obtained By Planar Scanning**

The width of the sampling plane and the distance from the AUT at which it is positioned dictates the valid angular extent of the PWS obtained. The distance to the sampling plane  $Z_0$  must be chosen to be large enough to place it outside of the antenna reactive Near-Field region, for this work the minimum distance is defined as  $Z_{MIN} \geq 5\lambda$ . The valid angle can be surmised from consideration of the simple geometry of Figure 3.3 given in the  $x$ -axis, however the same geometry exists in the  $y$ -axis, which is also given below, [52]:

$$\theta_{xv} = \tan^{-1} \left( \frac{S_x - A_x}{2 \cdot Z_0} \right), \quad (3.22)$$

$$\theta_{yv} = \tan^{-1} \left( \frac{S_y - A_y}{2 \cdot Z_0} \right),$$

where  $S_x$  and  $S_y$  are the widths of the scanning plane and  $A_x$  and  $A_y$  are the widths of the antenna in the  $x$  and  $y$  axes respectively, and  $Z_0$  is the distance to the scanning plane.

### **3.7.4 Instrumentation and equipment error**

In any measurements system the instrumentation used to make the measurement is always a limiting factor. The dynamic range of the receiver and its inherent non-linearity reduce the accuracy of the measurement. However prior knowledge of the equipment can be used to significantly reduce the effects these errors can have.

In a planar measurement system a probe is mechanically moved to sampling locations in the AUT Near-Field, however to connect the probe received signal to the VNA cables must be used. The flex of the cables as they are moved across the scanning surface will introduce error in both magnitude and phase. The use of high quality microwave cables as in the practical work later in this thesis renders this error negligible. Where the amplitude and phase error is repeatable across the scan plane it can be measured and characterised to provide some compensation, Rose [54].

### **3.7.5 Environmental errors**

Three main environmental factors that need to be considered are temperature change, multiple reflections and background noise.

Temperature change becomes significant at high frequencies, especially for cables where small changes in temperature can result in a change in length. In materials such as Teflon used in coaxial cables, the change in temperature can also significantly affect the relative permittivity, consequently changing the material characteristic impedance. Thus resulting in an alteration of both magnitude and phase of signals propagating within the cable. The temperature variations are also likely to affect the

microwave source power level and receiver linearity. A well-controlled environment allows minimisation of this error [54].

Multiple reflections in the measurement system are greatly problematic causing standing waves to occur. The standing waves are caused by reflections within the equipment as well as reflections from the surrounding environment. Moving the probe in the  $z$  plane provides a means of detection of these standing wave patterns. As the probe is moved through half cycles, some periodic variations in amplitude may be observed and these may be attributed to the multiple reflections. Increasing the distance between the AUT and probe allows for little opportunity of standing waves to occur [54].

The affect of reflections from the room can be greatly reduced by the use of a carefully designed anechoic environment. Due to the major advances in the design of high frequency absorbers it is possible to neglect these in comparison to errors from other sources. The anechoic environment also results in a reduction in the background noise level.

In all of the experiments conducted throughout this work, microwave absorber has been used to cover the surrounding environment to reduce the effect of any reflections. With the exception of probe field correction, the quantification of the system errors described is very difficult due to the resources available for the construction of the measurement system, which will be shown later. To provide some quantification of the system accuracy, multiple sets of measurements will be taken where possible and the repeatability of the measurements will be considered.

### 3.8 Near-Field Far Field Simulation

A simulation has been developed using *Mathcad 2001i* (mathematical development tool), to demonstrate the Near-Field to Far-Field transform and the aperture imaging discussed in section 3.6. The program is based on a one dimensional aperture (located in the  $x$ -axis radiating in the  $z$  direction) of width  $32\lambda$  operating at a frequency of 10 GHz. It is useful to use such a large aperture due to the narrow beam Far-Field it generates. Applying (2.1) for the distance to the Far-Field ( $\approx 2D^2/\lambda$ ) it is found to be located at a distance of approximately 61.5 m. The aperture is defined as shown in Figure 3.4; it exhibits uniform magnitude and uniform phase over its length.

The Near-Field generated by this aperture can be deduced using Huygens's principal, which states that "Each point on a primary wavefront can be considered to be a new source of secondary spherical wave and that a secondary wavefront can be constructed as the envelope of these secondary spherical waves" [58]. This means that assuming there are no free sources outside of the aperture, the aperture distribution can be broken down into a discrete number of elements, which can then be summed through their relative distances to an arbitrary point in space to obtain the field value at that point. Using this concept a plane is generated, parallel to the aperture within its Near-Field segmented into a set of points at a sample spacing that satisfies the Nyquist sampling criteria i.e.  $\Delta x = \lambda/2$  ( $\approx 0.015$  m), by summing the discretised aperture distribution to each of those Near-Field points. The valid angle ( $\theta_{xv}$ ) from Figure 3.3 is considered in deciding sampling plane width. Zero buffering of the Near-Field distribution prior to using the FT allows adequate spectral spacing to be obtained.

To choose the valid angle and hence the Near-Field plane width, the location of the nulls in the antenna radiation pattern are considered. For a rectangular aperture on a ground plane with a uniform distribution the Far-Field radiation patterns characteristics are governed by (3.23) [2]:

$$\frac{\sin\left(\frac{k_0 \cdot A_X}{2} \cdot \sin(\theta)\right)}{\frac{k_0 \cdot A_X}{2} \cdot \sin(\theta)} \Rightarrow \frac{\sin(W)}{W}, \quad (3.23)$$

where  $k_0$  is the propagation constant and  $A_X$  is the width of the antenna.

The spectral width to be obtained is chosen to be the Second Null Beamwidth (SNBW). This is because beyond this point, using (3.23), the magnitude of the pattern relative to boresight is less than 20 dB down, which for the purposes of this work will be regarded as the significant portion of radiated energy. The location of the SNBW can be evaluated from (3.23) by consideration of the *sinc* function. For  $W = \pm n\pi$  (where  $n$  is an integer) the radiation pattern is zero; for the location of the second null  $n = 2$ .

$$\begin{aligned} W = \frac{k_0 \cdot A_X}{2} \cdot \sin(\theta_{Xn}) &= \pm n \cdot \pi \text{ for } n=2 \\ \Rightarrow \theta_{X2} &= \text{asin}\left(\frac{2 \cdot \lambda}{A_X}\right) \text{ and } \therefore \text{SNBW} = 2 \cdot \theta_{X2} \end{aligned} \quad (3.24)$$

Therefore for the  $32\lambda$  aperture, the  $\text{SNBW} \approx 7.17^\circ$  ( $\theta_{XV} = 3.5^\circ$ ) and at a distance of  $5\lambda$  from the aperture the Near-Field plane must be a minimum width of:

$$\begin{aligned} S_{XMIN} &= 32\lambda + 2(\tan(\theta_{XV}) \cdot 5\lambda) \text{ for } \theta_{XV} = \theta_{Xn=2} \\ &\approx 1\text{m}. \end{aligned} \quad (3.25)$$

This is the minimum width of the plane necessary to accurately predict a beamwidth of  $7.17^\circ$  at a distance of  $5\lambda$ . Since the consequent processing involves the FT, in order to take advantage of the FFT algorithm the data set will be fixed to a length of  $2^l$ . To find the value of  $l$  required to achieve the minimum Near-Field width in (3.25) of 1 m:

$$\begin{aligned}
 l &= \text{ceil} \left( \log_2 \left( \frac{S_{XMIN}}{\Delta x} \right) \right) \\
 &= \text{ceil}(6.05) = 7,
 \end{aligned} \tag{3.26}$$

where the ceil function rounds up to the next integer.

The Near-Field is therefore calculated over 128 samples, which equates to a length of 1.92 m. Additionally zero buffering is used to provide interpolation between data points in the FT output resulting in a smoothed spectrum. The zeros are placed evenly on either side of the data. The zero buffering used is twice the size of the data in order to maintain a power of 2 elements. This means that the plane appears to be 3.84 m wide with the origin at the centre. Zero buffering does not change the valid angle of the calculated pattern  $\theta_{XV}$  as this is solely dependent on the width of the data measured. In this case by meeting the  $2^l$  requirement of the FFT the valid angle has become  $\theta_{XV} \approx 72^\circ$ . The Near-Field calculated across the plane by application of Huygens principle is shown in Figure 3.4. It shows that at a distance  $Z_0 = 0.15$  m, the field has started to spread out, though it is concentrated over an area that extends only a short distance beyond the aperture width. At a distance of 0.01 m on either side of the aperture the field is already 20 dB down from the centre.

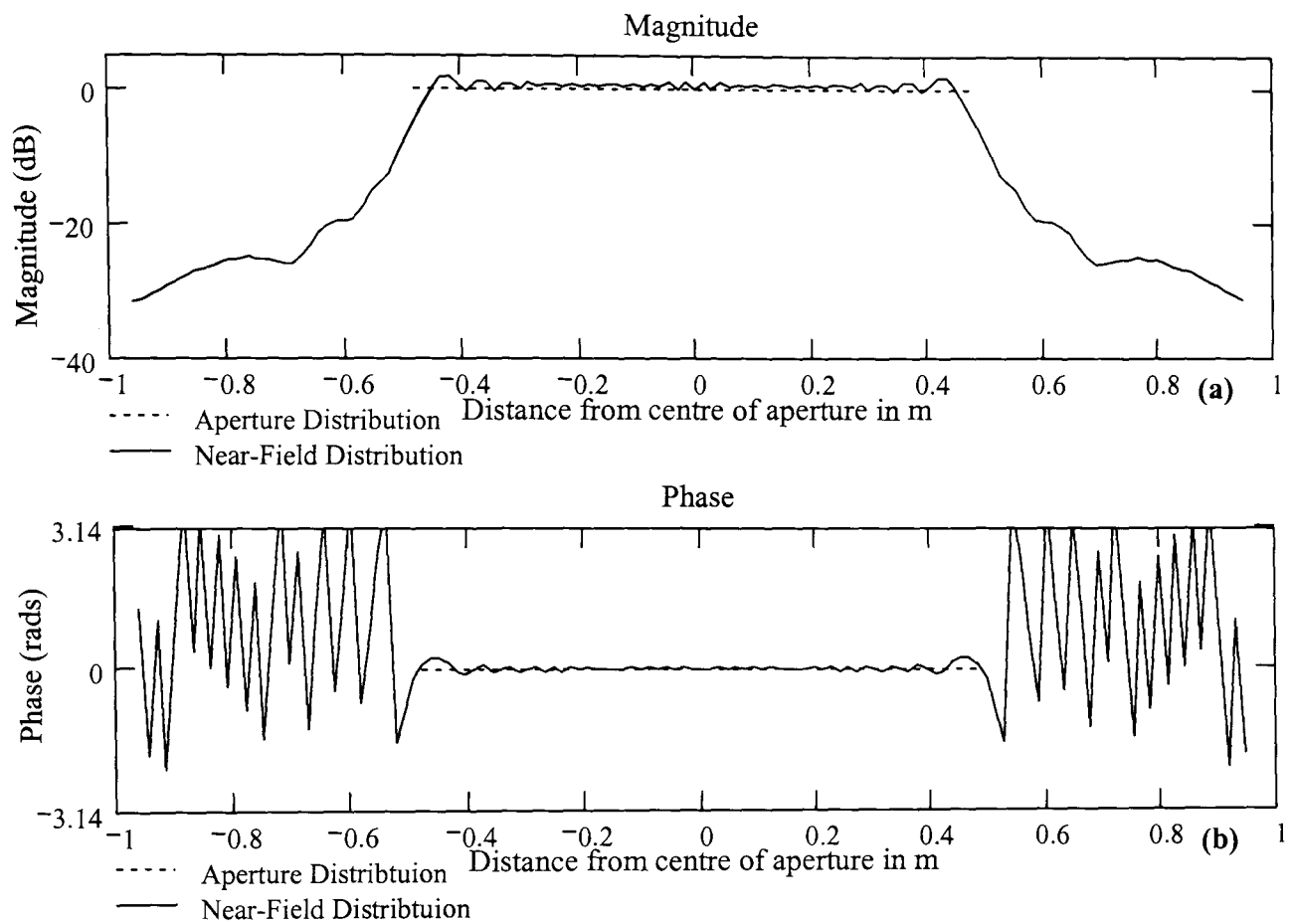


**Figure 3.4 (a) Magnitude And (b) Phase Of A  $32\lambda$  Uniform Aperture Distribution And Its Near-Field Calculated At  $Z_0 = 5\lambda$**

The FT is used to generate the PWS from the Near-Field shown in Figure 3.4 after it has been buffered by zeros to 1.92 m, the size found using (3.25) and (3.26). The PWS obtained is shown in Figure 3.5.

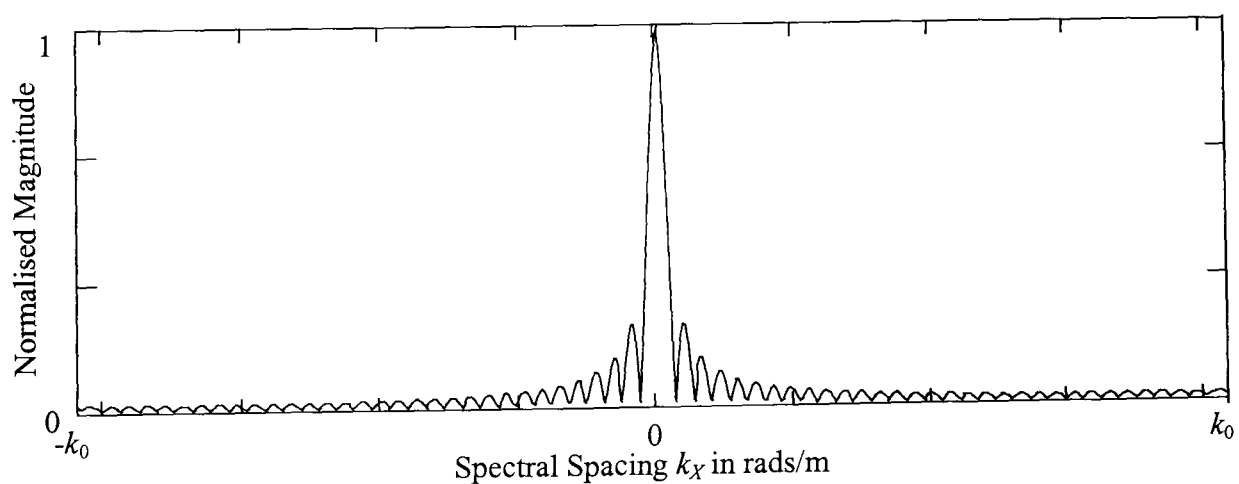


**Figure 3.5 Plane Wave Spectrum Magnitude Normalised to Maximum Magnitude**

Applying (3.5) to this PWS allows the Far-Field pattern to be obtained; this is shown in Figure 3.6. It can be seen that the SNBW predicted by (3.24) is the same in the figure.

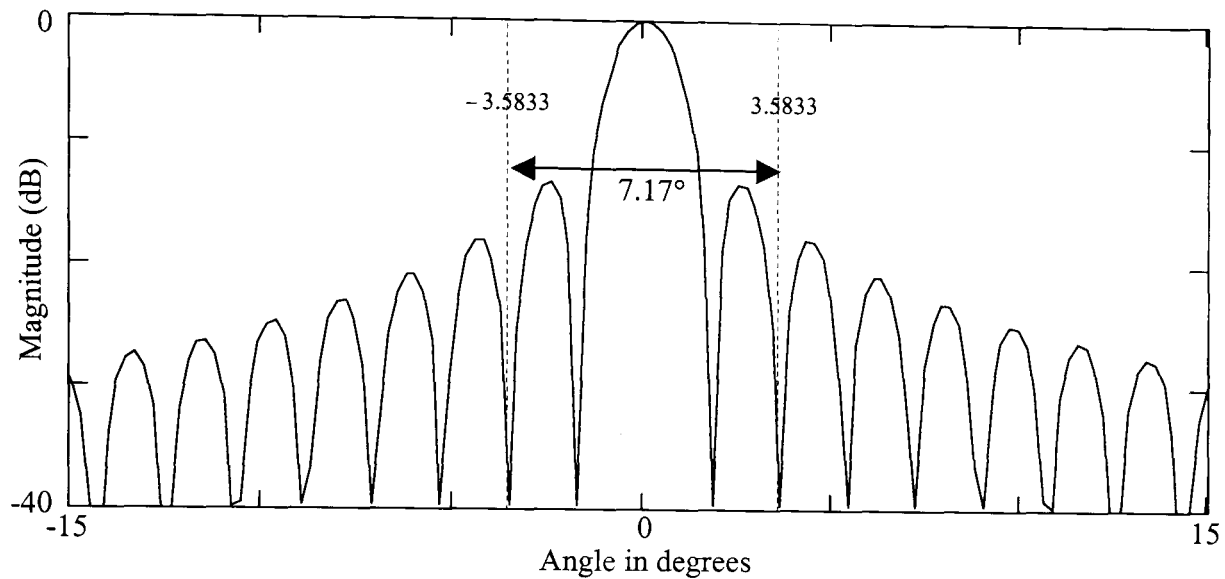


**Figure 3.6 Simulated Far-Field Radiation Pattern Calculated From A Truncated Near-Field Distribution Formed At  $5\lambda$  From A  $32\lambda$  Aperture With Uniform Illumination**

The other mechanism to be discussed is the imaging of the aperture field having obtained the PWS of the antenna, using (3.18). The reconstructed aperture distribution is shown in Figure 3.7 along with the original aperture distribution. The band limiting of the Near-Field causes the ripple observed on the reconstructed aperture magnitude and phase distributions. Observation of the calculated Near-Field in Figure 3.4 shows that a small amount of the radiated energy still exists beyond the planes extent, however the effect of these missing portions of radiation is negligible.

The case chosen represents the worst possible scenario, as the uniform illumination results in an infinitely wide spectrum, though the reconstructed aperture results obtained are clearly highly correlated to the original aperture distribution.

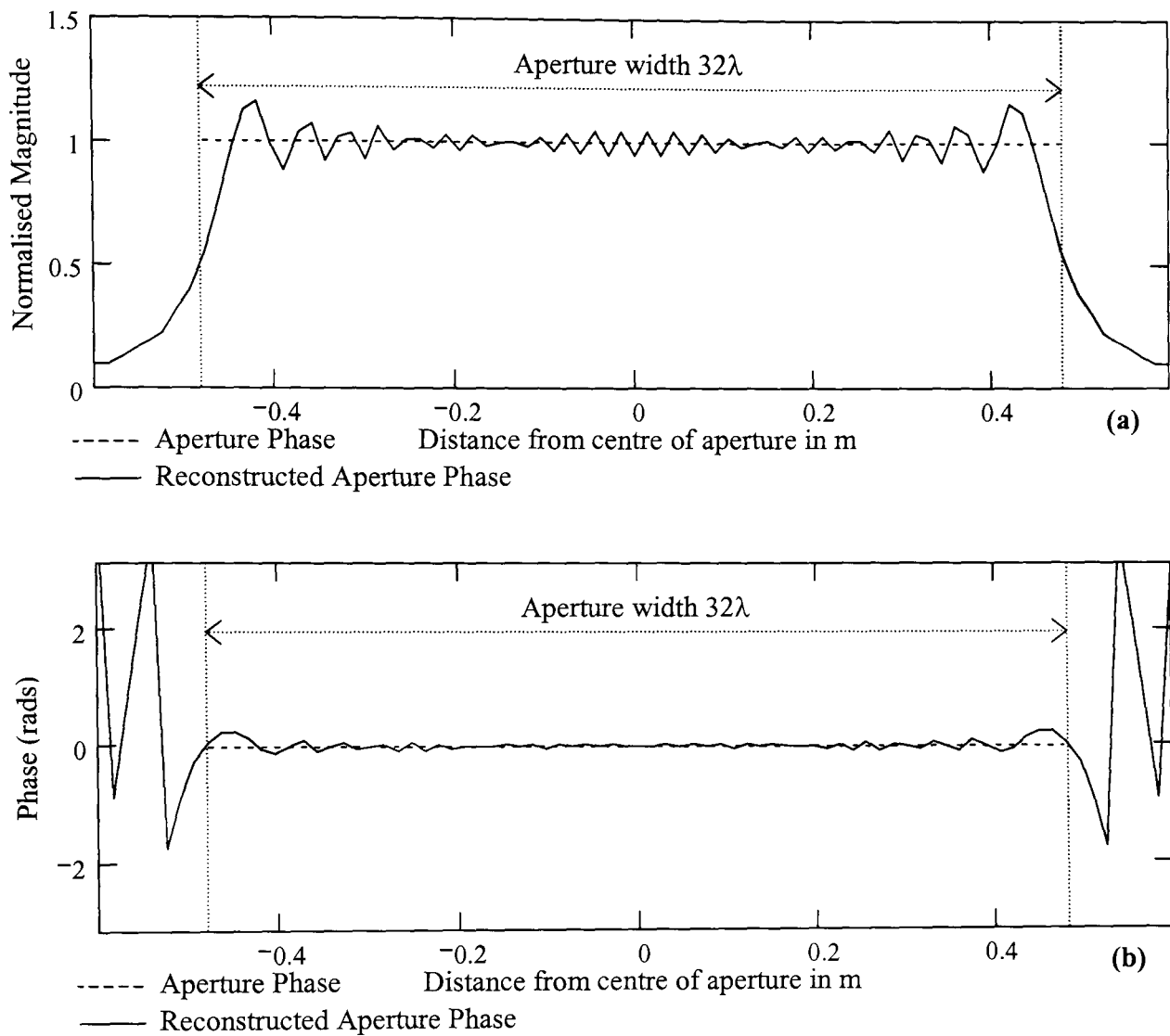


**Figure 3.7 Original And Reconstructed Aperture Distributions  
(a) Magnitude Normalised To Unity and (b) Phase Normalised To 0**

The phase of the reconstructed aperture field in Figure 3.7 varies rapidly outside of the aperture. The variation is caused as a result of the small magnitude values obtained outside of the aperture. These areas can be ignored as the reconstruction is only valid within the aperture.

### 3.9 Summary

In this chapter the Plane wave synthesis technique developed in the mid 1900's has been defined, explained and related to the process of antenna Near-Field measurements and the Near-Field to Far-Field transform. The sampling criterion has been defined and the necessity to meet the Nyquist sampling rate stated. These fundamental concepts need to be introduced in order to provide an understanding of the indirect holographic system to be developed in the rest of this work.

A simulation has been used to demonstrate the validity of the method and also to expose some of the limitations inherent in the methodology. The main one being the unavoidable band-limiting inherent in the planar technique due to the inability to measure the antenna field over an infinite size aperture, which results in some of the field being lost. The restricted angle over which an antenna radiation pattern can be predicted has been related to the sampling plane width and distance to the antenna. The simulation was based on an aperture of length  $32\lambda$ , Huygens principle was applied to the aperture to allow the formation of a Near-Field distribution and from this it was possible to calculate the Far-Field radiation pattern. It was then shown that the original aperture distribution could be reconstructed by a back propagation of the PWS.

The error sources that exist in planar Near-Field measurements have been identified and discussed, the need to measure phase has been identified as both problematic and expensive. It has been recognised that a full error analysis of the system that will be constructed is not practical due to the available equipment. Instead to provide some

quantifiable evaluation of the system reliability it is suggested that system repeatability will be observed.

Other useful papers regarding the planar Near-Field Far-Field technique can be found in the following references [3]-[62].

Having defined and demonstrated the planar Near-Field to Far-Field technique and identified the need to measure phase for Near-Field scanning is a major limitation in the system, the indirect holographic solution to recovering phase from intensity only measurements will now be discussed in the next chapter.

# CHAPTER 4 HOLOGRAPHY AND THE USE OF HOLOGRAMS

## 4.1 Introduction

Chapters 2 and 3 have provided the necessary background and understanding regarding antenna Far-Field radiation pattern measurement and outlined the underlying theory behind planar Near-Field measurement theory. Prior to being able to develop the holographic antenna measurement system to be created as a result of this research, it is first necessary to gain an appreciation of the holographic concept. This chapter offers an introduction to basic holography concepts at first in its more familiar optical format and finally in the microwave region where the interest of this research resides.

The structure of this chapter is as follows; firstly section 4.2 offers an explanation of what is meant in this thesis by holography and why it is being considered in this research. Section 4.3 then provides an examination of the development of the two optical holographic principles, namely In-Line and Off-Axis with the aim of showing what is required in the holographic system in order to achieve the desired result. The areas in which these optical principles have been applied at microwave frequencies are discussed in section 4.4. Finally, a discussion of the factors that contribute to the quality of a hologram is provided in section 4.5 emphasising on the microwave region.

The general holographic theory discussed throughout this Chapter can be found in '*Optical Holography*', P. Hariharan [63].

## 4.2 Optical Holography

A hologram can be broadly defined as a two-dimensional recording of a set of scattered waves that is capable of reconstructing the object that created the scatter, in three dimensions. The term holography simply means the recording of the total field, i.e. phase and amplitude information of a field is attained, this allows two categories of holography to be defined, direct holography and indirect holography.

In the direct method the two-dimensional image is recorded by physically measuring both the amplitude and phase of the beam scattered by an object. This is only possible at frequencies up to around 120 GHz with the use of vector network analysers, which makes this a very expensive technique for the collection of total field information; in the optical domain phase cannot be measured directly. At optical frequencies, recording is performed by media such as photographic film or measured at points by photoconductive components (photosensitive diodes for example); these are only capable of recording intensity distributions. This means that recorded data is void of any phase information, i.e. information regarding the relative distances of light paths from each point in the recorded scene to each point on the image is not retained. If an intensity only distribution of an objects radiated image is recorded or captured, then as a result of the loss of the relative phase information, a full three-dimensional reconstruction of the object is not possible [63].

Indirect holography is a method of incorporating total field information into intensity only recordings. Gabor, [27] was the first to realise that by mixing two coherent light beams together and recording the intensity of the resulting interference pattern over a surface, provided one of the sources is either known or can be reproduced, then the other beam used to generate the interference could be re-attained.

### **4.3 Indirect Holography**

As has been briefly described, the indirect holographic process requires that a known beam (reference) be mixed with a desired scattered wave (object) in order to attain the phase information in the object wave. The way in which the indirect hologram is recorded is one of the important factors in obtaining good quality reconstructed images. The two basic methods of generating holograms are In-Line and Off-Axis.

#### **4.3.1 The In-Line hologram**

The In-Line or Gabor hologram was pioneered by Gabor as the first holographic technique. Gabor demonstrated the principle by placing a transparency containing some small opaque details in a monochromatic beam of light and recording the intensity pattern produced by this on a photographic film. The transparency here was being utilised as an object and the monochromatic light source was providing both a reference wave transmitted through the transparency and a scattered wave due to the details printed on the transparency. The process Gabor used to record his In-Line hologram is shown below in Figure 4.1.

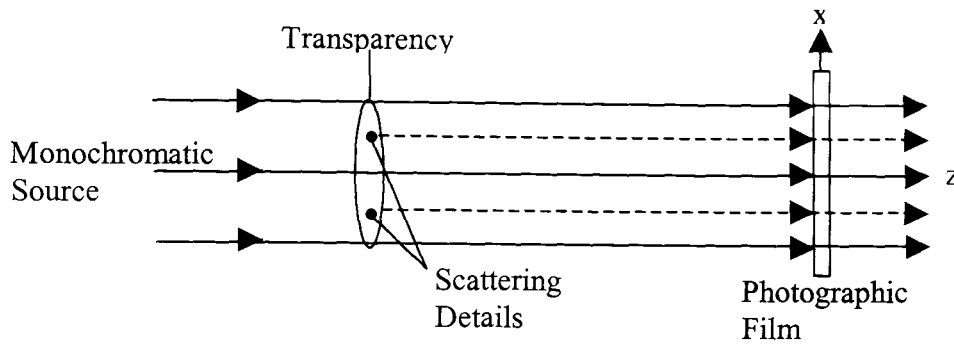


**Figure 4.1 In-Line/Gabor Hologram Generation**

The solid lines in the figure represent a uniform plane wave and the dashed lines represent the scattered waves generated by the details on the transparency. As the two waves illuminate the photographic film, it records the interference between the two of them and this recording is the hologram. Clearly the choice of object here is important, it must produce a scattered wave component but also allow enough of the reference wave to pass through it. In this case the transparency was able to perform this task with minimal disturbance to the reference beam.

This holographic process can be mathematically described by defining the variation of the reference beam  $E_R(x,y)$  and object beam  $E_O(x,y)$  in both magnitude and phase over the photographic film as (4.1) and (4.2). The intensity produced on a photographic film located in the  $x, y$  plane can then be found as the magnitude squared of the sum of the two waves; this is given in (4.3) as  $I_{IL}(x,y)$  [63]:

$$E_R(x, y) = R(x, y) \cdot e^{j\theta_R(x,y)}, \quad (4.1)$$

$$E_O(x, y) = |O(x, y)| \cdot e^{j\phi_O(x,y)}, \quad (4.2)$$

$$\begin{aligned}
I_{IL}(x, y) &= |E_R(x, y) + E_O(x, y)|^2 \\
&= |E_R(x, y)|^2 + |E_O(x, y)|^2 \\
&\quad + E_R(x, y) \cdot E_O^*(x, y) + E_R^*(x, y) \cdot E_O(x, y),
\end{aligned} \tag{4.3}$$

where  $R$  is the reference magnitude and  $\theta_R$  is the reference phase,  $O$  is the object magnitude and  $\phi_O$  the object phase all over the plane  $x, y$  and  $*$  denotes the complex conjugate of the component.

In this case the propagation of the plane wave  $E_R$  is perpendicular to the plane in which the photographic film is placed. Therefore it provides no variation in amplitude or phase across the surface of the film, i.e.  $R(x, y)$  is constant and  $\phi_O = 0$ . Therefore  $E_R(x, y)$  can simply be replaced by a constant (denoted  $R$ ) and the intensity given as, [26]:

$$I_{IL}(x, y) = R^2 + |E_O(x, y)|^2 + R \cdot E_O^*(x, y) + R \cdot E_O(x, y). \tag{4.4}$$

From (4.4), it is seen that there are four components contained within the recorded intensity distribution. The last component in (4.4) contains the magnitude and phase information of the scattered object wave multiplied by a constant value. The third term also contains the object information however it is in complex conjugate form.

In practice, the actual intensity pattern recorded by the photographic film would be subject to other light sources such as background light, exposure time and the physical properties of the film used. These sources should be minimised by controlling the recording environment; for the purposes of attaining an understanding of the principal they are ignored here, for the readers interest more information is available in [63].

Reconstruction of the object information from the intensity pattern takes place by illumination of the hologram recorded on the film by the reference source under the same conditions as in its recording. In doing this, two images are produced as well as the transmittance of the reference beam. A virtual object appears in its original position as when the hologram was recorded and a real object appears at the same distance from the film but in the transmitted reference beam. This is shown in Figure 4.2 and is expressed mathematically by [63]:

$$\begin{aligned}
 T_{IL}(x, y) &= R \cdot I_{IL} \\
 &= R \cdot \left( R^2 + |E_O(x, y)|^2 + R \cdot E_O^*(x, y) + R \cdot E_O(x, y) \right) \\
 &= R^3 + R \cdot |E_O(x, y)|^2 + R^2 \cdot E_O^*(x, y) + R^2 \cdot E_O(x, y).
 \end{aligned} \tag{4.5}$$

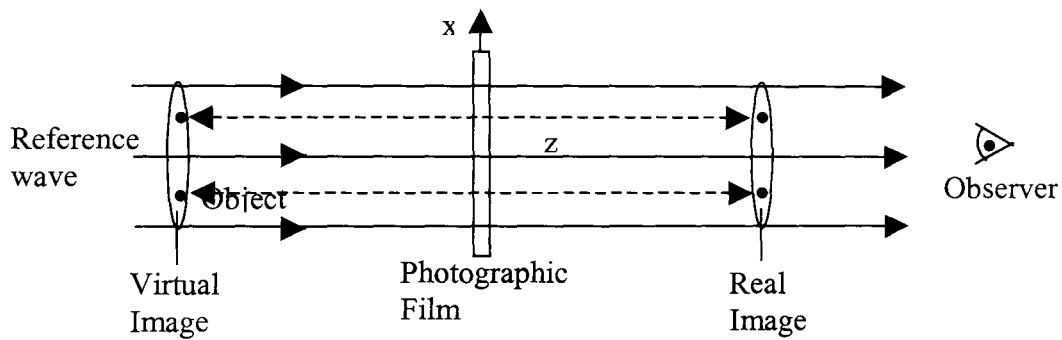


**Figure 4.2 Image Reconstruction From An In-Line/Gabor Hologram**

The first term in (4.5) corresponds to the reference wave, which is directly transmitted through the hologram, the second term is negligible in comparison to the first as it can be assumed that  $|E_R| \gg |E_O|$ . The third and fourth terms are the object wave and its complex conjugate both multiplied by the constant reference squared, and are also smaller than the transmitted reference.

In Figure 4.2 it is clear that from the viewing position both objects (real and virtual) will be observed on top of each other as well as a high level of background contamination due to the reference beam. Reasonable results could be observed for

certain types of object, for instance if a reversible object image is used (a symmetrical image), then the problem of seeing both real and virtual objects superimposed is not significant as they will provide some reinforcement. However the image that is not being directly focused upon will appear blurred. It should be noted that the hologram recorded on the photographic film should be a positive and not a negative, if a negative is generated as the hologram then the reconstructed object waves will produce a negative of the object.

From Figure 4.2 it is clear that it would be very difficult if not impossible to extract the object information, free from contamination by other components. Lieth and Upatnieks while working on side looking radar, read Gabor's paper and applied their radar technique to the generation of holograms to show that physical separation of the object terms in the intensity pattern could be attained. This is known as the Off-Axis hologram.

### **4.3.2 The Off-Axis hologram**

To separate the object image from the reference beam Lieth and Upatnieks considered introducing the reference beam to the hologram plane at an angle [29]. In their new formulation the reference beam still has a constant magnitude across the hologram surface, but its phase changes linearly as shown for the  $x$ -axis in Figure 4.3. One of the main advantages of recording in this manner over the In-Line technique is that the object need not be transparent, as the reference does not need to pass through it in order to illuminate the photographic film. This also means that the object does not create irregularities in the purity of the desired plane wave reference over the photographic film. The object must be illuminated with a coherent light source, which

became possible post the invention of the laser [64]. Another advantage is that the relative intensities of the object and reference waves can be controlled separately.

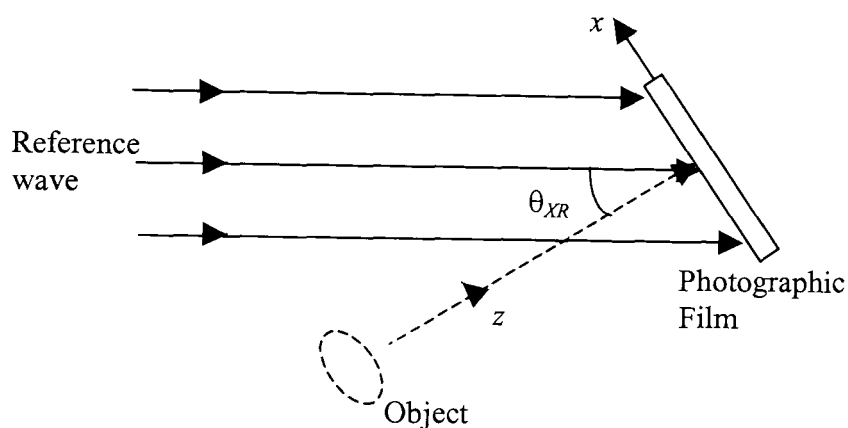


**Figure 4.3 Generating An Off-Axis Hologram**

Reconstruction of the object is performed in the same manner, as in the In-Line technique, placing the hologram back into the same reference beam used during recording. As with the In-line hologram there are four components generated by the re-illuminated hologram. However this time when the components are formed the two objects can be seen fully separated from the other components, providing certain constraints have been met in the recording, seen in Figure 4.4.

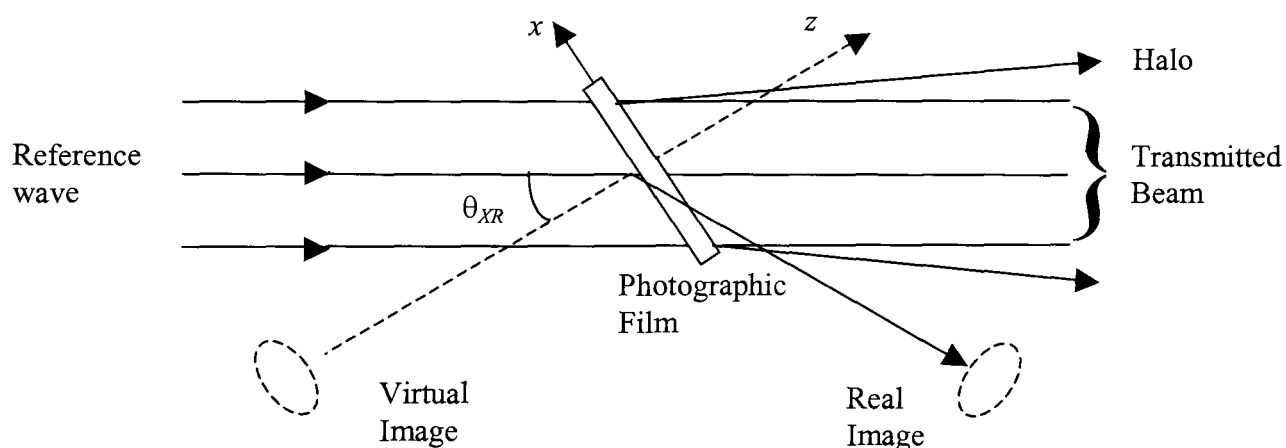


**Figure 4.4 Image Reconstruction From An Off-Axis Hologram**

Figure 4.4 shows that the reference beam is transmitted through the photographic film and is observed surrounded by a halo after exiting the hologram. The two object images are also re-formed, the object in its original position and the conjugate of the

object at the conjugate angle to it. Provided the angle  $\theta_{XR}$  is large enough and the distance from the object to the photographic film is large enough then the two object images can be seen free from interference of the reference beam and each other.

Following on from the diagrammatic explanation the mathematical analysis of the Off-Axis hologram provides further insight. Writing an expression for the interference formed by the Off-Axis reference wave and the scattered object wave gives  $I_{OA}(x,y)$ , where the reference  $E_R$  now has constant magnitude and a linear phase variation across the aperture related to the angle at which it is incident on the hologram plane [63].

$$\begin{aligned}
 I_{OA}(x,y) &= |E_R(x,y) + E_O(x,y)|^2 \\
 &= R^2 + |O(x,y)|^2 + R \cdot e^{j \cdot k_0 \cdot \sin(\theta_{XR}) \cdot \Delta x} \cdot |O(x,y)| \cdot e^{-j \cdot \phi_O(x,y)} \\
 &\quad + R \cdot e^{-j \cdot k_0 \cdot \sin(\theta_{XR}) \cdot \Delta x} \cdot |O(x,y)| \cdot e^{j \cdot \phi_O(x,y)},
 \end{aligned} \tag{4.6}$$

where  $\theta_{XR}$  is the angle at which the reference wave intercepts the hologram plane as shown in Figure 4.3.

As in the In-Line hologram the third and fourth terms in (4.6) contain the object total field information and its complex conjugate respectively. These terms are multiplied by the conjugate reference and the reference respectively. It is the linear phase variation of the reference across the hologram which gives rise to the separation of the reformed objects.

To reform the object, the recorded intensity pattern/hologram is illuminated (multiplied) by the reference beam represented as follows:

$$\begin{aligned}
 T_{OA}(x, y) &= I_{OA}(x, y) \cdot E_R(x, y) \\
 &= R^3 \cdot e^{j \cdot k_0 \cdot \sin(\theta_{XR}) \cdot \Delta x} + |O(x, y)|^2 \cdot R \cdot e^{j \cdot k_0 \cdot \sin(\theta_{XR}) \cdot \Delta x} \\
 &\quad + R^2 \cdot e^{2 \cdot j \cdot k_0 \cdot \sin(\theta_{XR}) \cdot \Delta x} \cdot |O(x, y)| \cdot e^{-j \cdot \phi_O(x, y)} + R^2 \cdot |O(x, y)| \cdot e^{j \cdot \phi_O(x, y)}.
 \end{aligned} \tag{4.7}$$

The first term in (4.7), relates to the reference wave being transmitted through the hologram at its angle of insertion and the second term is transmitted along with the reference and is related to the intensity of the object beam. It is the latter term which gives rise to the so called halo surrounding the reference upon its exit from the hologram. The third term is the conjugate image of the object produced at an angle twice the reference beam insertion angle. The final term is the original object beam produced in the same position as it began.

This improved hologram recording technique overcomes most of the disadvantages of the original In-Line hologram, allowing non-transparent objects to be imaged and recovering the object without the interference caused by the conjugate object image and transmitted reference beams inherent in the In-Line hologram.

The ability of this method to produce separation of the desired object terms is limited; consideration of the angular distribution of a hologram (Intensity pattern) shows this. The angular spectrum is found as in Chapter 3 by taking the FT of the intensity pattern. Treating each of the components in (4.7) individually [63]:

$$\begin{aligned}
T_{F1}(k_x, k_y) &= \mathfrak{F}\left\{R^3 \cdot e^{-j \cdot k_0 \cdot \sin(\theta_{XR}) \cdot \Delta x}\right\} \\
&= R^3 \cdot \delta(k_x + k_{XR}, k_y),
\end{aligned} \tag{4.8}$$

$$\begin{aligned}
T_{F2}(k_x, k_y) &= \mathfrak{F}\left\{|O(x, y)|^2 \cdot R \cdot e^{-j \cdot k_0 \cdot \sin(\theta_{XR}) \cdot \Delta x}\right\} \\
&= R \cdot \left[ o(k_x, k_y) \oplus o(k_x, k_y) * \delta(k_x + k_{XR}, k_y) \right],
\end{aligned} \tag{4.9}$$

$$\begin{aligned}
T_{F3}(k_x, k_y) &= \mathfrak{F}\left\{R^2 \cdot e^{-2 \cdot j \cdot k_0 \cdot \sin(\theta_{XR}) \cdot \Delta x} \cdot |O(x, y)| \cdot e^{-j \cdot \phi_O(x, y)}\right\} \\
&= R^2 \cdot o^*(k_x, k_y) \otimes \delta(k_x + 2k_{XR}, k_y),
\end{aligned} \tag{4.10}$$

$$\begin{aligned}
T_{F4}(k_x, k_y) &= \mathfrak{F}\left\{R^2 \cdot |O(x, y)| \cdot e^{j \cdot \phi_O(x, y)}\right\} \\
&= R^2 \cdot o(k_x, k_y),
\end{aligned} \tag{4.11}$$

where  $\oplus$  and  $\otimes$  denote the auto-correlation and convolution operations respectively and  $k_{XR}$  the angular spectrum value corresponding to the angle at which the reference is inserted.

These 4 transformed components are shown in Figure 4.5 plotted against  $k_x$ ,  $k_y$ , showing how separation is obtained.

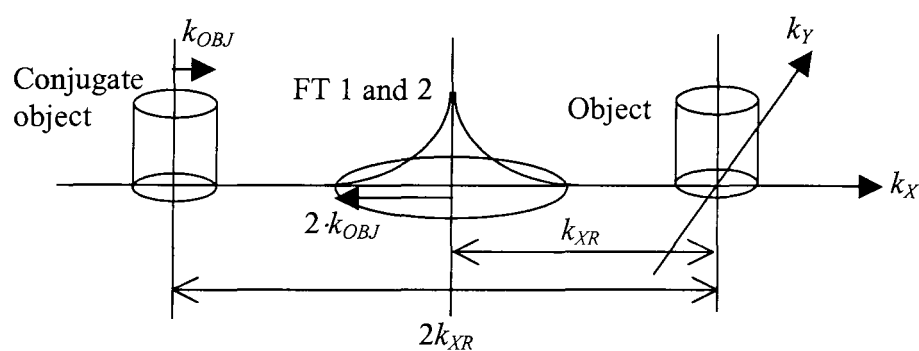


**Figure 4.5 Angular Frequency Spectrum Of An Off-Axis Hologram**

The central component shown in the spectrum above, represents the transforms in both (4.8) and (4.9). The width of this element is in most cases controlled by the angular extent of the object beam, as the auto-correlation in (4.9) will generate a spectral component that is approximately double the size of that produced by the

transforms in (4.10) and (4.11). This in comparison to the width of the delta function generated by the transform in (4.8) can be assumed to be much wider. This is because the delta function is infinitesimally narrow while the auto-correlation function produces a spreading effect. Consideration of this allows the minimum spectral value  $k_{XR}$  required to produce separation of the components to be estimated.

$$k_{XR} \geq 3 \cdot k_{OBJ}, \quad (4.12)$$

where  $k_{OBJ}$  is the highest spectral component of the object beam.

The position at which  $k_{XR}$  occurs in the spectrum is calculated as a function of the angle at which the reference beam intercepts the holographic plane:

$$k_{XR} = k_0 \cdot \sin(\theta_{XR}). \quad (4.13)$$

From Figure 4.3 it is apparent that the maximum angle at which the reference beam can intercept the holographic plane is  $90^\circ$ . As the angle increases beyond this, then the separation produced in the spectral plane becomes smaller as the real and conjugate images of the object swap ends of the spectrum and re-converge on the centre. The angle used to insert the reference should therefore be chosen to produce separation of the object terms.

Not only is it necessary to ensure that the angle of intercept of the reference meets the requirement of (4.12), but it is also essential that the distance from the hologram to the object is large enough to place the object outside of the reference beam. From this it is clear that the separation of the terms results from two dependant variables, angle of intercept and distance, for any defined one of these a minimum of the other can be found by considering the simple geometry in Figure 4.3 or Figure 4.4:

$$Z_{MIN} \Big|_{0 < \theta_{XR} < 180} = \frac{S_X + O_X}{2} \cdot \tan(90 - \theta_R), \quad (4.14)$$

$$\theta_{XRMIN} \Big|_{Z_0 > 0} = \tan^{-1} \left[ \frac{2 \cdot Z_0}{S_X + O_X} \right], \quad (4.15)$$

where  $Z_{MIN}$  is the minimum distance from the object to the hologram plane and  $\theta_{XRMIN}$  the minimum angle for the reference,  $O_X$  and  $S_X$  are the object and hologram plane widths respectively.  $\theta_{XR}$  can take any value from 0-360°.

As long as these conditions are met then it can be said that the components will be separated when the images are regenerated by the application of the reference wave to the hologram. The formulation has been made in terms for the  $x$ -axis, however the same expressions are valid in the  $y$ -axis

Having now discussed the fundamental practices of optical holography that are relevant to this body of work, the process will be discussed focussing on its adaptation into the microwave region.

#### 4.4 Microwave Holography

At microwave frequencies holography can be separated into two categories, Direct and Indirect; however, unlike the optical case where direct holography is not a valid solution to total field recording because it is not possible to measure the relative phase of the wavefront, at microwave frequencies it is possible though increasingly expensive and difficult as the frequency increases. The general arrangement for producing an indirect hologram at microwave frequencies is the same as in the optical case. However a microwave signal generator replaces the monochromatic light source

and recording is by means of, depending on the application, either probing the interference at discrete points or recording the interference on a microwave sensitive media. The three general areas in which microwave holograms and indirect holography have been applied are:

1. **Object imaging**, although there is a reduced resolution in comparison to optical imaging because of the longer wavelength in the microwave region, the ability of microwaves to penetrate materials allows them to be used to image concealed objects, unlike optical frequencies, which cannot penetrate opaque objects. Other higher frequency regions such X-rays, which can provide better resolution than microwaves, are ionising forms of radiation that for many applications are neither suitable nor desirable. The use of holograms to record the object images can significantly reduce the cost in the imaging process.
2. **Holographic Antennas**, holograms are generated which when illuminated by the reference wave produce as the object field a synthetic aperture antenna characteristic.
3. **Total Field Recovery**, the numerical recovery of the total fields scattered by objects such as antennas, where measurement of phase is required but not possible or convenient it can be achieved by the formation of holograms.

It is the last of these that is of interest in this work, since it is the total field recovery of an antennas Near-Field that is required, in order to find the Far-Field radiation pattern. The process will be discussed in detail in relation to the recording of antenna fields, in Chapter 5. First, it is constructive to take a brief look at the other two areas in order to provide an insight into the general field of microwave holograms.

#### **4.4.1 Object imaging**

Dooley [65] first published results of object imaging using microwave holograms in 1965, where he created an In-Line microwave hologram by illuminating an object in a similar fashion to that shown in Figure 4.1. The recording was made as a set of probed samples and then the object image was synthetically reconstructed by optically scaling the recorded image. The results he obtained were of very poor quality due to limitations of the equipment which was used. Aoki [66] also presented results using the In-Line method, however the recording was done using optical media and the image reproduction was carried out by illuminating the hologram with an optical beam resulting in a scaling effect, again the results were poor. Iizuka [67], extended the principal of recording images of objects onto photosensitive media to the mapping of electric fields of antenna using a technique similar to that of the Off-Axis hologram described above illuminating the media from two sources. More recently microwave holograms and indirect holographic techniques have gained much interest for their use in the imaging of concealed objects. Smith and Leach et. al. [68], [69] have utilised the novel technique described in the following chapters to produce images of metal and plastic objects hidden beneath various materials from microwave holograms recorded via a sampling method.

#### **4.4.2 Holographic antennas**

The holographic antenna was pioneered by Checcacci [70] in the holographic boom of the late 1960's, the idea behind this work was that the need for a physically large antenna could be replaced, by generating a hologram which when illuminated by a reference beam (as per object reconstruction Figure 4.4), produces as its object component the desired antenna characteristic, effectively synthesising the desired

antenna. Sazonov [71], discusses the design of the holographic antenna. One of the main problems faced is in getting enough power into the synthesised antenna as most of the illuminating reference wave is transmitted straight through the hologram, these efficiency problems have been detailed by Thingvold et. al. [72].

#### **4.4.3 Total field recovery**

Having very briefly defined the other two areas of microwave holography, the focus returns to total field recovery. A direct holographic method that is well documented and has been applied for many years is the Near-Field testing of antenna, as described in Chapter 3. This is because the relative magnitude and phase of the wavefront is recorded over a two-dimensional plane and this recording is capable of producing a three-dimensional image. As highlighted this is not the most desirable solution to total field recording mainly due to the expense of the two-channel receiver (VNA) required to measure the phase.

In this work, the recording of indirect holograms both In-Line and Off-Axis is realised by the collection of discrete sets of field samples. The two-dimensional surfaces used for the formation of holograms are shown in Figure 2.5, provided a suitable reference wave can be generated; here the planar surface is the focus.

Recovery of the object field total information is achieved by the processing of the intensity only data sets collected. The processing involved is relatively straightforward and will be discussed in depth in the next chapter, however it is suffice to say here that the spectral distribution of the collected intensity data in (4.8)-(4.11) and as seen in Figure 4.5, contains a component separated from the rest of the

spectrum that represents the spectral distribution of the object field. This can be used to obtain the total field information at the hologram plane as a result of the wave scattered by the object. The transformation between the spatial and spectral distributions is achieved via the FT and Inverse Fourier Transform (IFT) of the data.

The recording of the intensity over the planar hologram surface is subject to the same sampling constraints as discussed in Chapter 3, as a result of this the spectral width is governed by the sample spacing due to the relationship between the two dimensions in the FT. With reference to (4.13) and recalling that there a maximum angle at which the reference wave can be inserted ( $90^\circ$ ), means that there is a maximum angle at which the object components can be displaced from the centre of the spectrum, and from (4.13) this must be dependent on the insertion angle and the sample spacing. This implies that as the sample spacing increases (making the spectral width smaller) or as the reference angle decreases then the separation also decreases. This will be discussed in more detail in Chapter 7 where the method will be used to measure antenna radiation patterns.

Measurement apparatus that could be used to generate both In-line and Off-axis microwave holograms are shown in Figures 4.6 and 4.7. The interference could be physically recorded onto a suitable medium using microwave sensitive material, placed over the measurement surface, as with the photographic plate in Figure 4.1 or Figure 4.3, or it could be collected as a set of probed samples as shown here.

Figure 4.6 is the microwave equivalent of the optical system described by Figure 4.1. The object in this case is not transparent to the microwaves and therefore the

reference wave and object wave have to be formed separately and then combined. The signal from the microwave source is divided into two coherent parts, one used to illuminate the object to produce the scattered wave and the other is used to provide a constant reference level. The scattered wave is then sampled over a plane as in Figure 3.1 with the same sampling criterion. At each sample point the power received by the probe is fed to one co-planar arm of a Hybrid-Tee and the reference signal is fed to the other co-planar arm. Taking the signal from the summation port of the Tee and using a square law detector to measure the intensity provides the desired  $I_{IL}(x,y)$  in (4.3), since the reference wave at every sample point is constant.

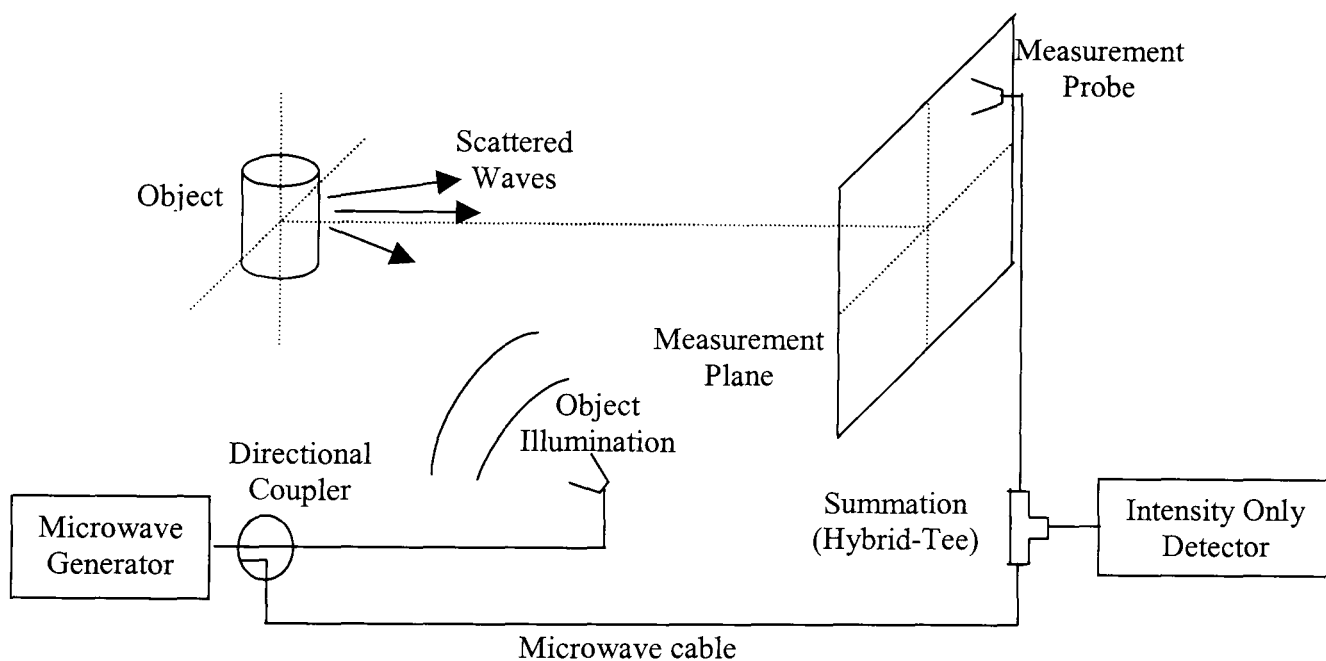


**Figure 4.6 Arrangement For Microwave In-Line Hologram Recording**

Figure 4.7 is the microwave equivalent of the optical system described by Figure 4.3. It is seen that as in Figure 4.6 the object is still illuminated in the same manner and that the recording takes place over the same sampling plane. However the reference signal that was previously carried by a microwave cable to the receiver end is now radiated. To provide the reference with a uniform magnitude and linear phase shift across the measurement surface as defined in (4.6), it is now radiated from a second source located at an angle to the measurement plane. The wave radiated by the

reference source is assumed to be plane and provide a linear phase gradient over the measurement plane. In reality, no microwave radiating structure is capable of producing a plane wavefront and therefore the reference that is actually generated is not uniform with a linear phase gradient. This is a limitation of the system that will be discussed further in section 4.5. It is the freespace interference created by the intersection of the scattered wave and the reference wave at each sample point that is received by the probe and then fed to a square law detector to provide the interference intensity.

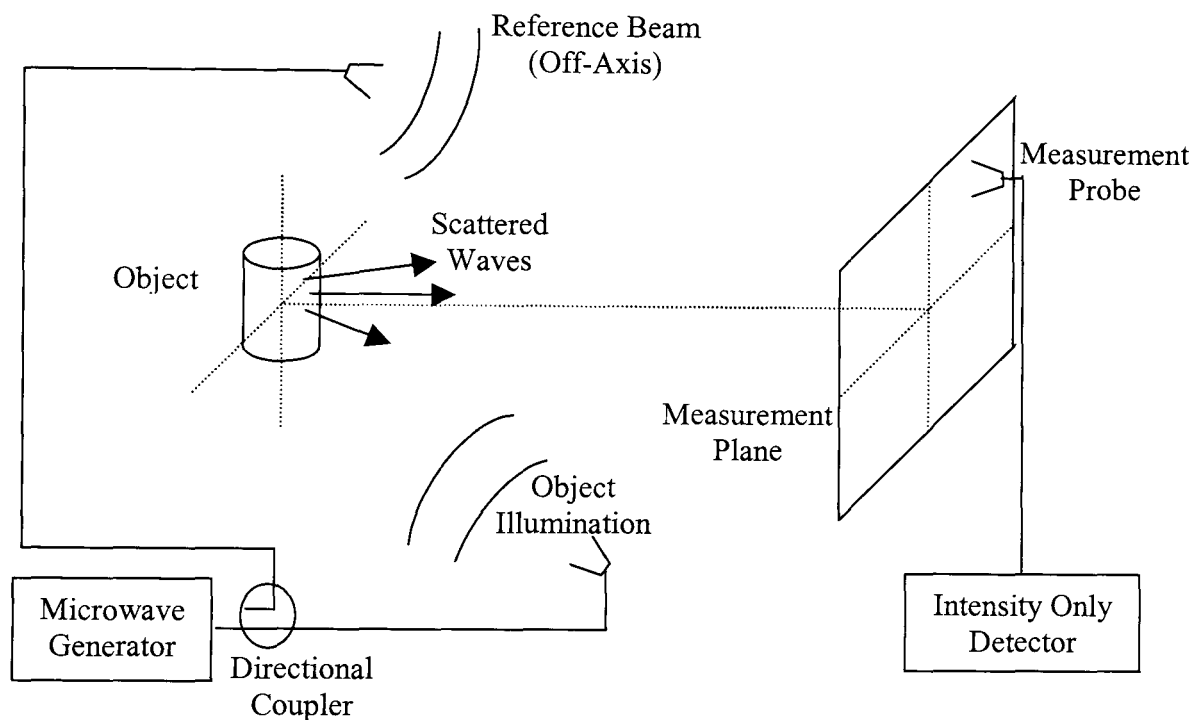


**Figure 4.7 Arrangement For Microwave Off-Axis Hologram Recording**

The main difference between these two sets of apparatus is the inclusion of the radiated Off-Axis reference source. The Off-Axis system therefore requires more space than the In-Line system and control of the reference insertion angle requires careful positioning of the reference wave antenna. The use of this radiated reference wave is not only physically problematic but it also raises some issues regarding error sources in the production of microwave holograms, as will be discussed in the next section.

An overview of the initial applications and techniques in microwave holography can be found in a paper published by Tricoles and Farhat [73] in 1977. These are still valid today.

## **4.5 Improving The Quality Of The Recorded Hologram**

Although the same basic principals are used to produce holograms at microwave frequencies as at optical frequencies, there are several issues that arise in creating adequate conditions for the reference beam and the scattered beam at the hologram plane. Firstly, regarding the reference beam, at optical frequencies it is possible to assume plane wave conditions over a relatively short distance due to the optical wavelength (in 1 m of the order of  $10^6$  wavelengths), however at microwave frequencies it is not possible to create a plane wave front due to the much longer wavelengths involved (in 1 m of the order of 10-100 wavelengths). The spectral extents of the components in the spectrum are generally much wider at microwave frequencies than in the optical case. As such, methods of decreasing interference between the spectral terms in Figure 4.5 need to be considered as the processing described relies on the ability to filter the object component from the spectrum void of interference from other spectral terms.

### **4.5.1 The non-planar reference beam**

The best approximation to a planar reference wave that can be achieved using a single transmitter, such as an open-ended waveguide or small horn for the reference, has a broad spherical wavefront. This cannot be assumed to have a negligible magnitude variation over the hologram surface especially in the Off-Axis configuration. The phase front can be assumed to be plane in the Far-Field of the reference antenna, but

the desired linear phase gradient is difficult to produce across the hologram surface. The non uniform nature of the reference applied to (4.6), would mean that the desired object term is no longer seen in the spectrum multiplied by a constant, rather the reference now has a shaped characteristic across the measurement plane and as such the spectral output will appear as the convolution of the object wave and the reference.

One novel option for producing the desired plane wave would be to use the compact range topology of Figure 2.4 to provide the reference, locating the hologram plane in the test zone. The planarity of the quiet zone would then be subject to the same errors as the compact range and the size of the hologram would be limited by the ability to construct the reflector.

A single source is commonly used and the wavefront is assumed to be close to that of the desired plane wave. A major part of this thesis is the development of a novel way in which the Off-Axis wave can be synthesised allowing the original optical assumptions to be valid; this is presented in Chapter 6.

#### **4.5.2 The relative magnitude of image terms**

Consideration of how to reduce the interference between the spectral terms by exploiting the properties of the reference signal and the object signal is useful. Observation of the spectral terms shows that the width of the centre component in Figure 4.5 is only determined by the auto-correlation of the object beam. However by studying (4.8)-(4.11) it is seen that the magnitude of the components produced by the product of the reference and real and imaginary object terms are proportional to the

magnitude of the reference. In contrast the magnitude of the auto-correlation of the object beam is void of any association with the reference. This means that it is possible to increase the amplitude of the object images by increasing the magnitude of the reference beam in relation to the auto-correlation term. In doing so the affect of the auto-correlation term on the object in the spectrum as an interfering source, is reduced as the object becomes greater in magnitude. An example of this is shown in the graph of Figure 4.8 where two spectrums have been simulated the first has equal reference and object amplitude and the second has a reference magnitude two times that of the maximum object magnitude.

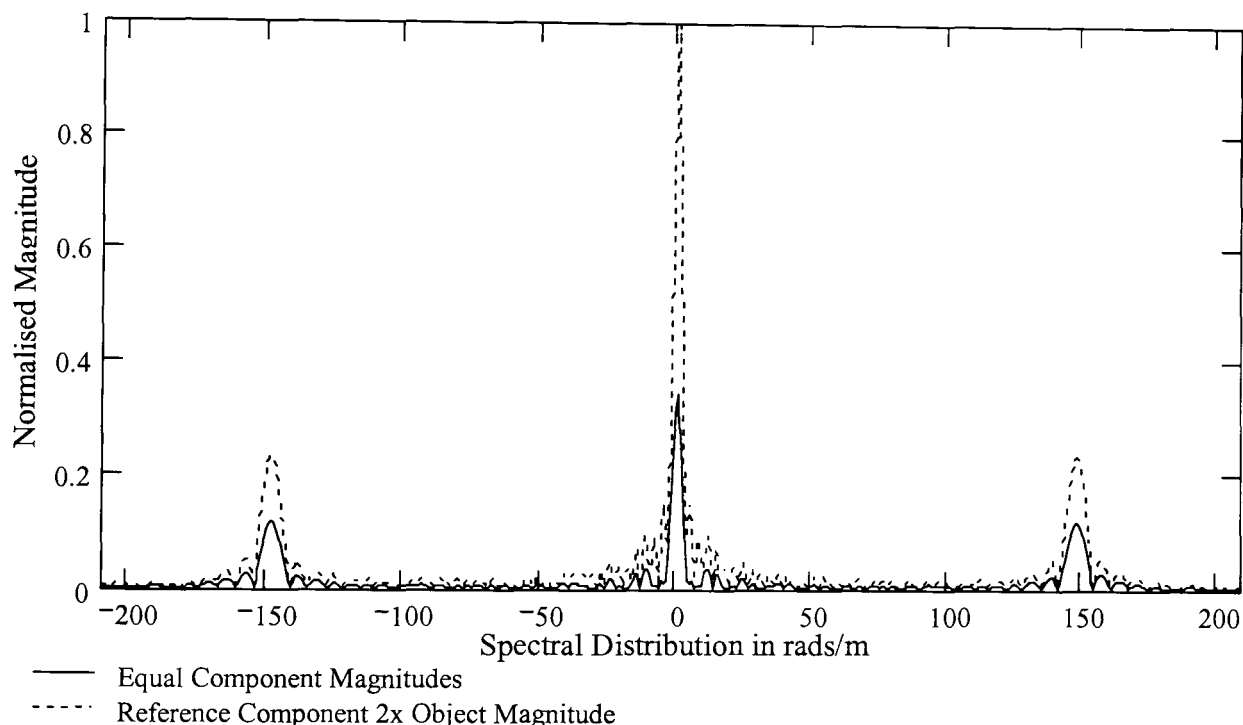


**Figure 4.8 Comparison Of Off-Axis Hologram Spectrums With Varying Magnitudes Of Reference Beam Relative To The Object Beam Normalised To The Maximum Magnitude**

There is a limit to which the continued increase in the magnitude of the reference can aid in this matter. Increasing the reference magnitude too much in comparison to the object will decrease the fidelity of the reproduced object image. This is because the amount by which the reference is modulated by the object in the interference pattern becomes smaller. Bennett, [35] discusses that the degradation of the object image as a result of an increase in reference field strength is related to the number of digitisation

levels used to measure the intensity. Clearly, for a system with fixed quantisation levels, if the depth of modulation decreases then less quantisation intervals will be used to define the object portion of the distribution.

Maximum efficiency occurs when the maximum reference signal level is equal to the maximum object signal level. Therefore the penalty for an increased reference signal level is degradation in the fidelity of object recording.

### **4.5.3 Mathematical removal of the auto-correlation terms**

If the amplitude distributions of both the reference beam and the object beam are known over the hologram plane then it is possible to mathematically remove them from the measured intensity samples before the FT operation. The drawback of this is that two extra scans over the hologram plane have to be made in order to obtain the two required amplitude distributions. If the reference beam could be assumed plane over the surface then this could be reduced to one further scan, Huang [37]. Multiple scanning for this purpose requires highly accurate repositioning of the probe to each sample location, otherwise an increase in error may result

## **4.6 Summary**

An introduction to the optical technique of phase front recording using holography has been provided in this chapter. The two main techniques for the formation of holograms have been presented, starting with the early pioneering efforts of Gabor and then onto the more recognisable format of the Off-Axis hologram developed by Lieth and Upatnieks. The mathematical relationships formed within the two techniques have been discussed and spectral requirements have been highlighted. It

has also been shown that the reference wave magnitude can be used to control the clarity of the desired object information, stating that the best dynamic range and modulation depth is generated when the reference magnitude is the same as the maximum object magnitude.

A review of the application of the holographic principle at microwave frequencies has been made. One of the main problems encountered in these applications was the inability to produce a plane wave Off-Axis reference at microwave frequencies. This is one of the issues, regarding the measurement of antenna total field information that will be dealt with in the remainder of this thesis.

The conditions necessary to ensure that the desired image term can be acquired, separated from the other components produced in the hologram spectrum, have been stated. The limitations to which this is possible have been identified such as the maximum angle to which the Off-Axis reference wave can be inserted. This is the second area that will be addressed in terms of antenna total field measurement in the remainder of this thesis.

The current application of indirect holography to the measurement of microwave antenna radiation patterns by collection of intensity only data in the antenna Near-Field is presented in Chapter 5 together with a simulation of the mathematical processing involved.

# CHAPTER 5 INDIRECT HOLOGRAPHIC MICROWAVE ANTENNA RADIATION PATTERN MEASUREMENT

## 5.1 Introduction

In Chapter 4 the optical holographic process was presented. It was shown how the total field information in an optical wavefront could be retained in a scalar recording and how the information could be recovered from that recording. The adaptation of this process was then discussed for use in the microwave domain. The ability to translate the optical holography process into the microwave domain means that the phase information contained in a microwave wavefront could be recorded without the use of a VNA. This chapter considers the application of the optical holographic process specifically to the measurement of microwave antenna using the theory previously developed.

The chapter begins with a discussion of the previous work that has taken place in the application of the process to microwave antennas. It highlights one of the main limitations regarding the use of the implementation of the technique at microwave frequencies is the production of a suitable reference wave.

In sections 5.3 and 5.4 the In-Line and Off-Axis holographic processes are presented with reference to microwave antenna measurement. The equations given in Chapter 4 for both types of hologram are first reformulated to represent their application to antenna measurement. It is seen that there the optical reformation process of re-

illumination of the hologram by the reference source is not required. Instead the desired AUT information can be obtained directly from the intensity pattern recording. The ability of each of the hologram techniques to yield the desired information is also discussed. In section 5.5 the capacity of total field recovery to detect faults in an aperture is simulated by using implementation of an Off-Axis hologram. The limitations of the technique in the microwave domain, particularly in terms of spectral restrictions are discussed in section 5.6 and finally, the sources of error that occur in implementing the holographic technique are discussed in section 5.7

## **5.2 Microwave Antenna Radiation Pattern Measurement Using Indirect Holography**

The term microwave antenna holography has in recent years become synonymous with the back propagation of antenna radiation patterns to find the antenna aperture fields for the purposes of fault diagnosis, Rahmat-Samii [52], Rachblatt [74]. This work is solely concerned with the generation of microwave indirect holographic intensity patterns/holograms for the purposes of obtaining antenna radiation fields; including the imaging of antenna apertures.

The idea of using this indirect holographic principle to reconstruct the complex Near-Field of a microwave antenna and hence find its Far-Field pattern did not arrive until 1973 when Bennett et. al. [1] published work on an 'Investigation of the Characteristics of a Large Reflector Antenna Using Microwave Holography'. This paper shows how the process can be used to image the aperture of a reflector antenna by measuring amplitude only on a spherical surface in the Near-Field of the antenna.

Prior to this the technique had been applied to acoustic antenna by Napier and Bates [75].

The method employed by Bennett uses a single transmitting antenna to provide a near plane wave to the reflector under test as well as providing a portion of the transmitted signal to a small probe antenna offset from the reflector and static, acting as a reference. The desired linear phase shift of the reference is generated using a phase shifter. The intensity is obtained using a hybrid junction to sum the two signals and a simple diode detector to provide a squared output. The system used is shown in Figure 5.1 below:

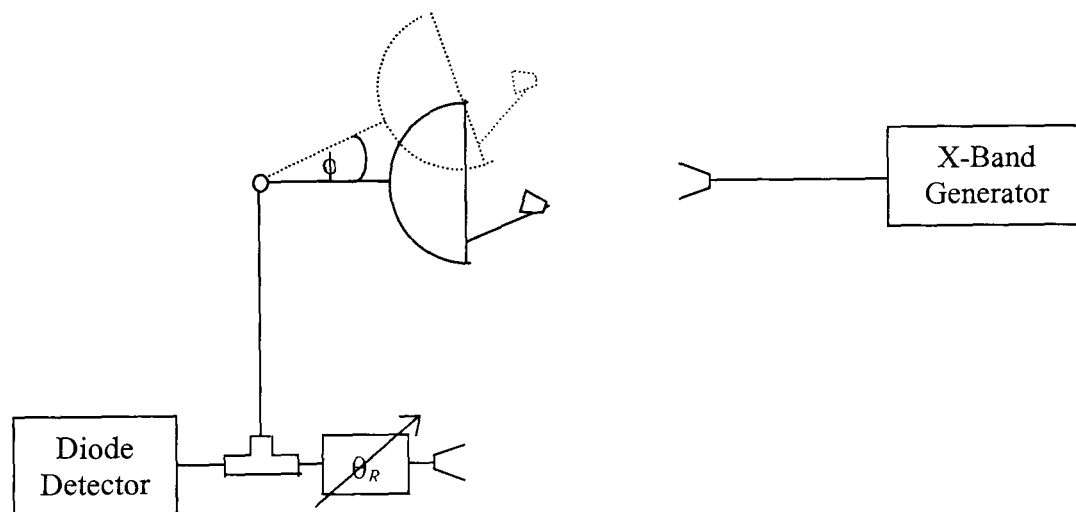


**Figure 5.1 Equipment Employed By Bennett For Off-Axis Hologram Formation For Microwave Antenna, Intensity Only, Near-Field Testing [1]**

The intensity pattern was measured by rotating the reflector in its elevation axis through  $\pm 6^\circ$  and through  $\pm 9^\circ$  in the azimuth axis, for each step in the azimuth plane the phase shifter was incremented.

The recorded intensity pattern is used, to reconstruct the AUT Near-Field image. Consideration of the components of the intensity pattern shows that providing the reference phase shift is linear and its magnitude is uniform the Near-Field component

can be acquired without the multiplication of the reference as in the re-illumination process discussed in Chapter 4. This will be seen in more detail later.

The results obtained by Bennett were favourably comparable to both standard Far-Field measurements and traditional Near-Field techniques (direct holography). This showed the ability of this technique to provide similar results to other traditional methods without measuring phase over a reduced distance. However, the technique was used with only large antenna exhibiting high gains due to the restricted spectral width that originates from the discretely sampled field.

Huang and Bennett [76], [77] extended the scope of the method into the Terahertz region, where in the past it was impossible to accurately measure the phase of the antenna field making direct holographic Near-Field measurements impossible. This indirect holographic method differs from that described above as the Off-Axis reference was generated physically by offsetting a horn antenna in the traditional sense of Figure 4.7.

More recently Smith and Leach [78], [79], [80], have proposed a novel system in which there is no radiated reference in a bid to ensure the planarity of the reference wave and to make the adaptation of the system into current planar Near-Field systems more simple. This is dealt with in detail in Chapter 6.

The two indirect holographic methods, In-Line and Off-Axis are now discussed with reference to attaining antenna patterns from intensity only measurements collected over a plane.

### 5.3 Antenna Measurement Using In-Line Holograms

In this section, the adaptation of the In-Line hologram for the measurement of antenna radiation patterns will be discussed. It is useful to start with the In-Line hologram as it helps to highlight some of the requirements that need to be met in obtaining total field information using holograms.

#### 5.3.1 In-Line hologram recording for antenna Near-Field measurement

An arrangement for the measurement of an antenna radiation pattern using the In-Line hologram method over a planar surface is shown in Figure 5.2

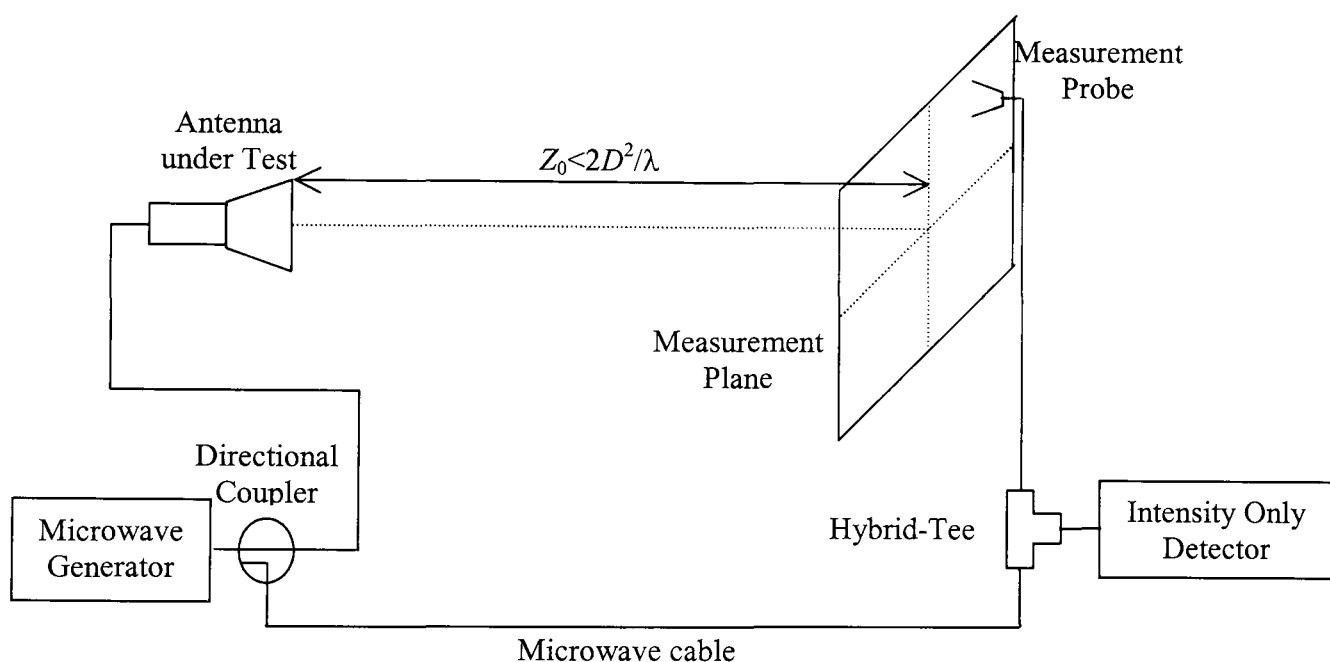


Figure 5.2 Near-Field In-Line Holographic Antenna Measurement System

In this arrangement it can be seen that the microwave source is split into two parts, one is fed to the AUT and the other direct to one of the co-planar junctions of a Hybrid-Tee. The AUT field replaces the field scattered by the object under illumination in Figure 4.6. The probe is moved over the hologram surface (measurement plane) on a predetermined grid. At each grid point the signal received by the probe antenna is fed to the other co-planar junction of the Tee and the intensity

is measured at the output of the summation port using a diode detector or similar square law device. The grid over which the probe is moved must be defined to meet the Nyquist sampling criteria and is subject to the same spatial and spectral relationships as defined for planar sampling in Chapter 3.

To obtain the Near-Field data the spectrum of the intensity pattern is attained and as seen in Chapter 4, if the 4 components contained in the intensity pattern can be separated then the Near-Field spectral information can be acquired by filtering. For the In-Line hologram this can only be achieved providing two pre-requisites have been met. Firstly, the removal of the two auto-correlation functions generated as a result of the magnitude distributions of the reference and the Near-Field. Secondly, where the antenna pattern is perfectly symmetrical since the virtual and conjugate image terms will appear on top of each other in the spectrum.

### **5.3.2 In-Line hologram simulation for antenna Near-Field measurement**

Simulations have been developed to show the In-Line hologram process when applied to a one-dimensional antenna aperture. The simulation is based upon a reformulation of equations (4.3) - (4.5), to incorporate the AUT Near-Field and to account for the lack of the re-illumination of the hologram by the reference. The aperture is  $32\lambda$  in size at a frequency of 10 GHz and has been simulated for a uniform distribution as in Chapter 3; The Near-Field distribution located a distance of  $5\lambda$  from the aperture can be seen in Figure 3.4. The reference wave is defined as uniform with a magnitude equal to the largest magnitude in the calculated Near-Field distribution and has no phase variation across the measurement plane. The intensity pattern is calculated by substituting the AUT Near-Field into (4.4) resulting in:

$$INF_{IL}(x, y) = R^2 + |E(x, y, z_0)|^2 + R \cdot E(x, y, z_0)^* + R \cdot E(x, y, z_0). \quad (5.1)$$

Figure 5.3 shows the intensity pattern obtained using (5.1), when the reference is set to have equal magnitude and inverse phase to that of the central/maximum Near-Field component.

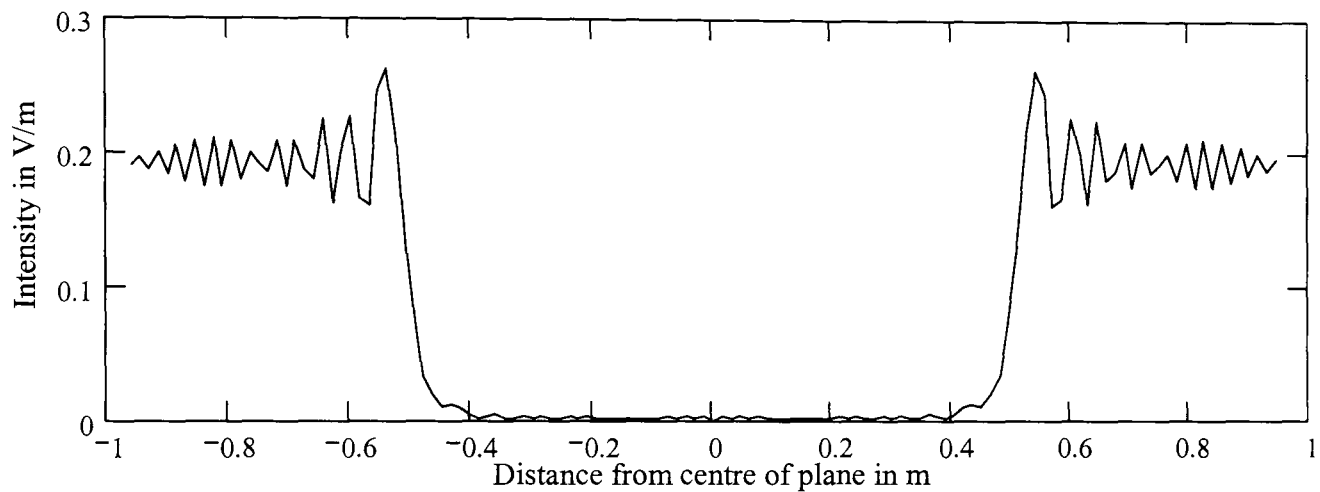


**Figure 5.3 In-Line Hologram/Intensity Pattern Formed By The Near-Field Of A  $32\lambda$  Aperture With Uniform Distribution And Reference Exhibiting Uniform Magnitude And Phase**

The equal magnitude and opposite phase of the object and reference components cancel out in the centre producing an intensity level of zero. This is advantageous as it increases the dynamic range of the measurements over the centre of the antenna distribution where generally it is slow varying.

The FT of this In-Line intensity pattern will generate the following four spectral components from consideration of (5.1):

$$\begin{aligned}
IL1(k_x, k_y) &= \mathfrak{F}\{R^2\} \\
&= R^2 \cdot \delta(k_x, k_y),
\end{aligned}
\tag{5.2}$$

$$\begin{aligned}
IL2(k_x, k_y) &= \mathfrak{F}\{|E(x, y)|^2\} \\
&= A(k_x, k_y) \oplus A(k_x, k_y),
\end{aligned}
\tag{5.3}$$

$$\begin{aligned}
IL3(k_x, k_y) &= \mathfrak{F}\{R^2 \cdot E(x, y)\} \\
&= R^2 \cdot A^*(k_x, k_y) \otimes \delta(k_x, k_y),
\end{aligned}
\tag{5.4}$$

$$\begin{aligned}
IL4(k_x, k_y) &= \mathfrak{F}\{R^2 \cdot E(x, y)\} \\
&= R^2 \cdot A(k_x, k_y) \otimes \delta(k_x, k_y).
\end{aligned}
\tag{5.5}$$

The normalised magnitude spectrums of these components are shown in Figure 5.4, for *IL3* and *IL4* ((5.4) and (5.5)) only one of the components has been plotted. This is because they are complex conjugates of each other and so in terms of magnitude are the same for the symmetrical pattern simulated.

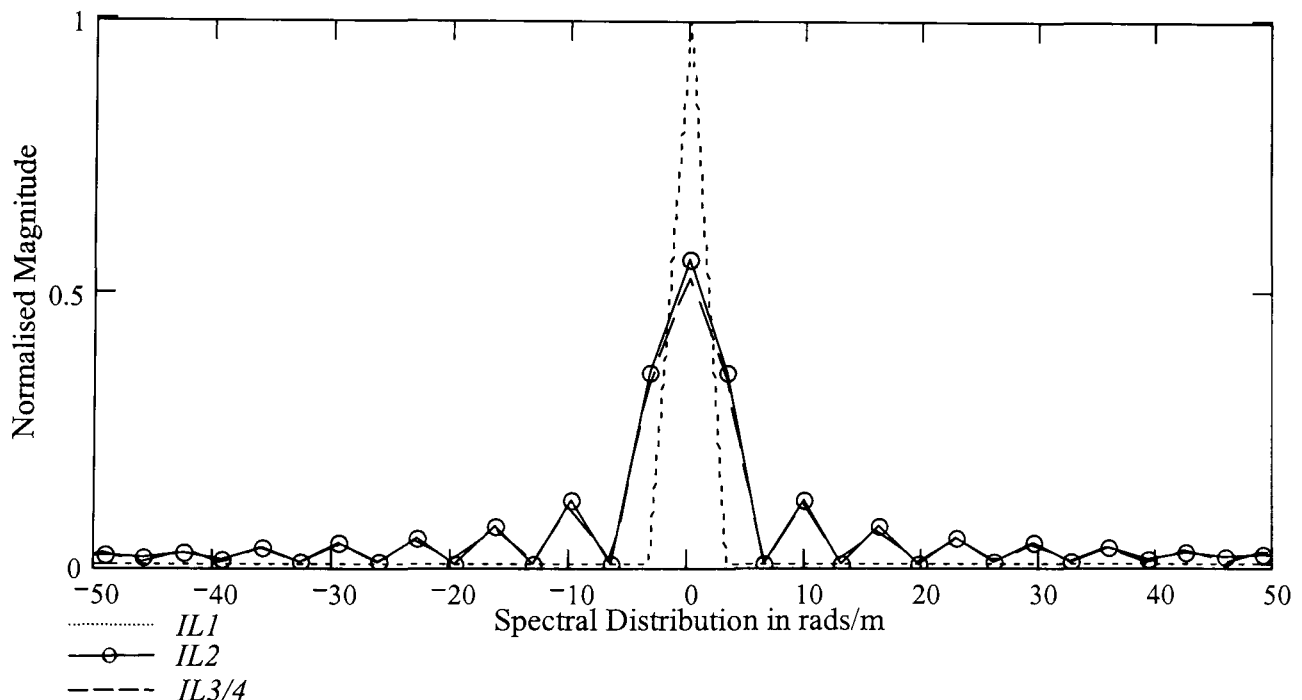


**Figure 5.4 Spectral Plots Of The Intensity Components Of An In-Line Hologram (5.2), (5.3) and (5.4)/(5.5) Normalised To The Maximum Magnitude**

Clarification that the spectrum generated by the FT of this intensity pattern will not yield the antenna Near-Field data free from interference is shown in Figure 5.5. The

spectral terms are all centralised and overlapping. It is not possible to remove the required information from the spectrum.

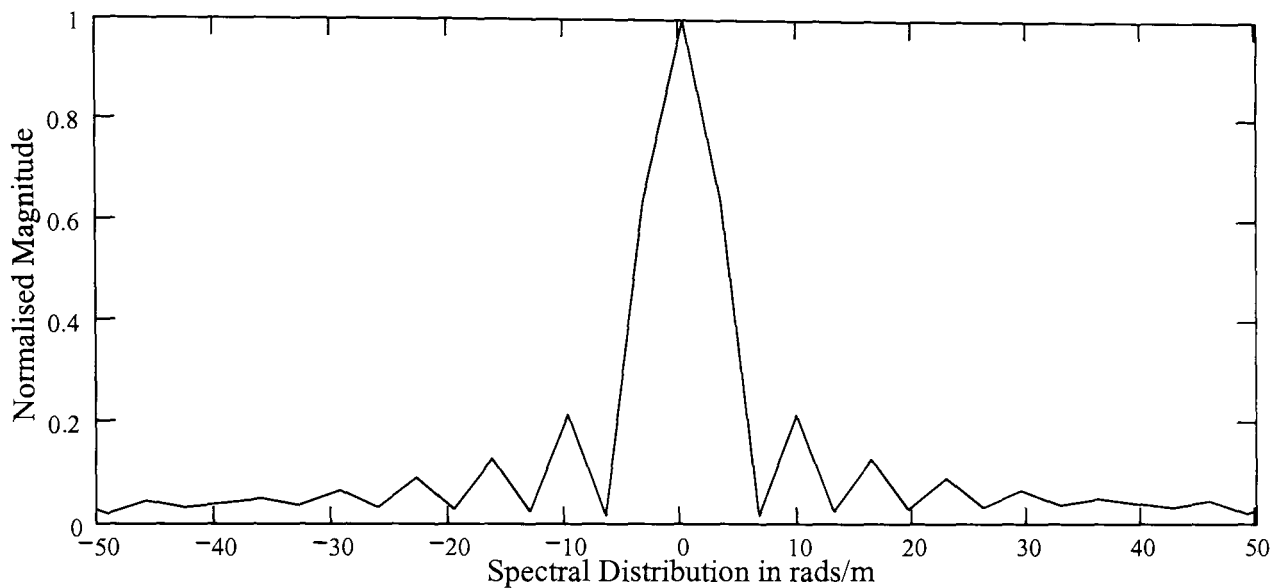


**Figure 5.5 Spectrum Of An In-Line Hologram Normalised To The Maximum Magnitude**

The predominant term in the centre is the delta function resulting from the uniform reference beam. The spectrum is obtained by the direct FT of the intensity pattern without pre-processing such as zero buffering. The antenna Near-Field cannot be recovered from this recording. However, if the auto-correlation terms can be removed and the AUT spectrum can be assumed symmetrical in magnitude and phase then the relative magnitude of the resulting spectrum is the same as the AUT PWS and therefore the Far-Field can be calculated by application of (3.5).

#### **5.4 Antenna Measurement Using Off-Axis Holograms**

Having shown the inability of the In-Line hologram recording method to yield the total field information of the antenna, the exploitation of the Off-Axis technique is now reviewed.

### 5.4.1 Off-Axis hologram recording for antenna Near-Field measurement

An Off-Axis recording system is shown in Figure 5.6. A small horn antenna placed at an angle to the measurement plane replaces the microwave cable used to feed the reference signal to the Hybrid-Tee in the In-Line system, as in Figure 5.2. This horn provides a reference wave, which due to its physical offset from the measurement plane means that it has a phase shift across the plane. The phase shift provided by the reference antenna across the measurement plane is assumed to be linear and its magnitude is assumed uniform, though as discussed in section 4.5.1 at microwave frequencies this is not possible due to the spherical nature of the radiation from any radiating aperture. The reference horn antenna must be located such that it does not block or scatter any of the field radiating from the AUT into the measurement plane. The interference between the waves occurs in free space and is sampled directly by the probe with the intensity measured at the output of a square law detector as in the In-Line case.

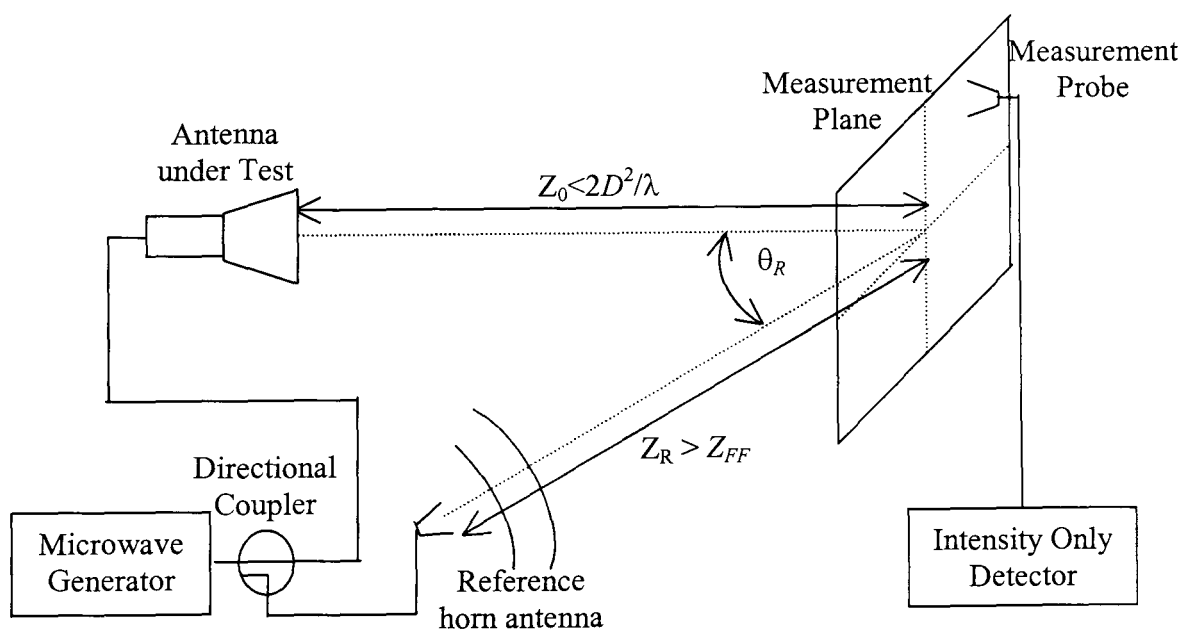


**Figure 5.6 Basic Near-Field Off-Axis Indirect Holographic Antenna Measurement System**

The expression for the intensity pattern produced as a result of this interference, is found by substituting the AUT Near-Field into (4.6) and realising the discretised

reference wave as having a linear phase gradient as a function of the angle  $\theta_{XR}$  and the sample spacing  $\Delta x$  and uniform magnitude:

$$\begin{aligned} INF_{OA}(x, y) = & R^2 + |E(x, y)|^2 + R \cdot e^{j \cdot k_0 \cdot \sin(\theta_{XR}) \cdot \Delta x} \cdot E(x, y)^* \\ & + R \cdot e^{-j \cdot k_0 \cdot \sin(\theta_{XR}) \cdot \Delta x} \cdot E(x, y). \end{aligned} \quad (5.6)$$

Following the same route as in the In-Line case, the equations presented in (4.6)-(4.11) are reformulated to include the AUT Near-Field and account for the lack of the re-illumination of the hologram by the reference. It is known that the FT of the intensity spectrum will contain a component equivalent to the angular spectrum of the complex field distribution of the object across the hologram plane i.e. in this case the AUT PWS. Considering the individual transforms of the four terms in (5.6):

$$\begin{aligned} OA1(kx, ky) = & \mathfrak{T}\{R^2\} \\ = & R^2 \cdot \delta(kx, ky), \end{aligned} \quad (5.7)$$

$$\begin{aligned} OA2(kx, ky) = & \mathfrak{T}\{|E(x, y)|^2\} \\ = & A(k_x, k_y) \oplus A(k_x, k_y), \end{aligned} \quad (5.8)$$

$$\begin{aligned} OA3(k_x, k_y) = & \mathfrak{T}\{R^2 \cdot e^{j \cdot \theta_{XR}(x, y)} \cdot E(x, y)^*\} \\ = & R^2 \cdot A^*(k_x, k_y) \otimes \delta(k_x + k_{XR}, k_y), \end{aligned} \quad (5.9)$$

$$\begin{aligned} OA4(k_x, k_y) = & \mathfrak{T}\{R^2 \cdot e^{-j \cdot \theta_{XR}(x, y)} \cdot E(x, y)\} \\ = & R^2 \cdot A(k_x, k_y) \otimes \delta(k_x - k_{XR}, k_y). \end{aligned} \quad (5.10)$$

In comparison to the spectral components formed in (4.8)-(4.11) where the hologram has been re-illuminated by the reference signal, here they are found to be, as in the In-Line case, smaller in amplitude by a factor  $R$ , the magnitude of the (reference wave). It is also notable that the location of each component within the spectrum has changed in comparison to their relative locations in Figure 4.5. The spectrum is now centred at

the mid point of the auto-correlation terms not the wanted image term, as shown in Figure 5.7. This is because the added phase component has not been removed by the multiplication (re-illumination) of the reference wave.

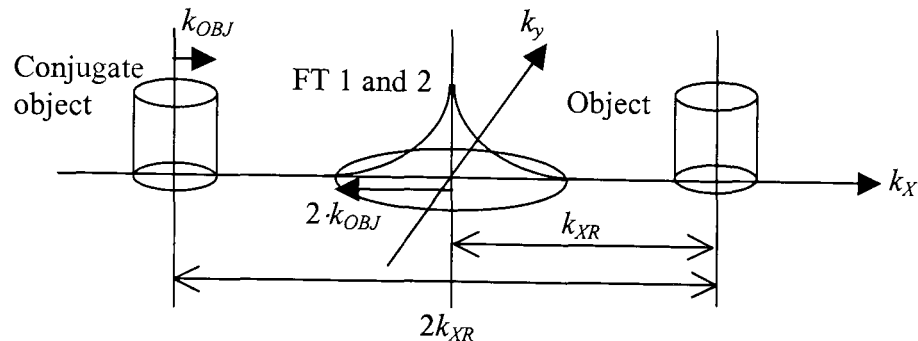


**Figure 5.7 Typical Spectrum Of An Off-Axis Hologram**

#### **5.4.2 Off-Axis hologram simulation for antenna Near-Field measurement**

A simulation of the Off-Axis system has been developed using the same parameters as previously defined for the In-Line simulation and the Near-Field to Far-Field transform applied in Chapter 3. The aperture and Near-Field distributions are those of Figure 3.4 and the reference field exhibits a linear phase shift across the intensity plane. The intensity pattern produced when the reference wave is introduced at  $45^\circ$  ( $\theta_{XR}$ ) is shown in Figure 5.8. The  $45^\circ$  offset angle corresponds to an increment of approximately  $127^\circ$  per half wavelength sample. The initial condition of the reference wave is set so that at the central point it has the same magnitude and opposite phase to that of the antenna Near-Field distribution, this is to force the measured intensity to become zero and maximise the intensity dynamic range.

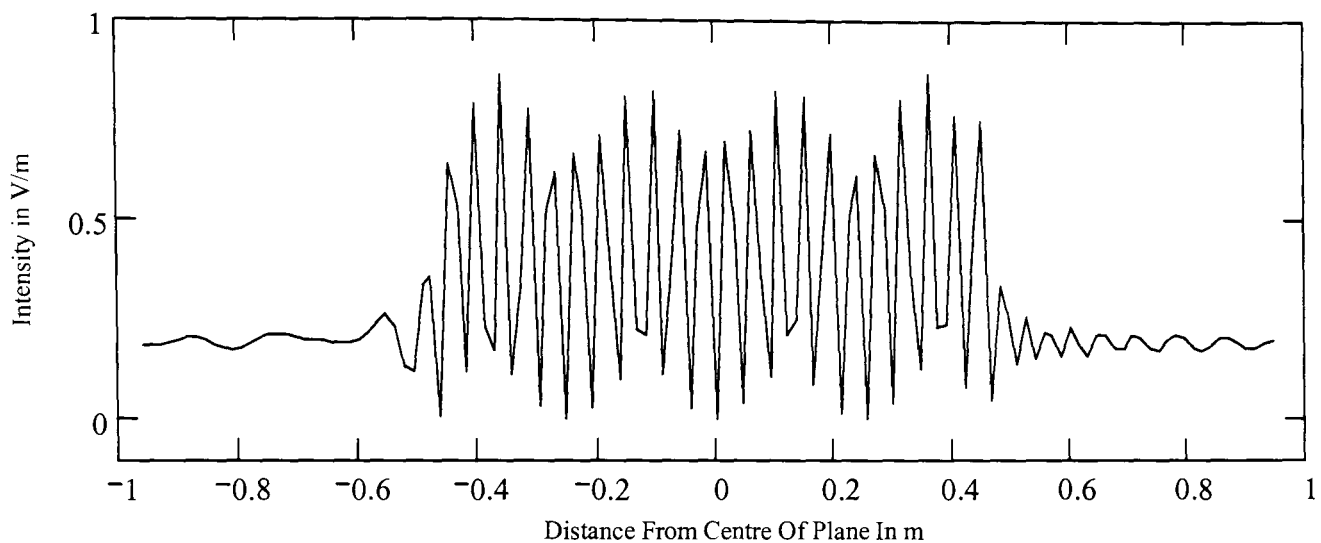


**Figure 5.8 Off-Axis Hologram/Intensity Pattern Formed By The Near-Field Of A  $32\lambda$  Aperture With Uniform Distribution And A Reference Exhibiting Uniform Magnitude At An Angle Of  $45^\circ$**

The intensity varies more rapidly in comparison to the In-Line intensity pattern due to the slow varying phase of the Near-Field summed with the rapidly varying phase of the reference component.

The four individual spectral components of (5.7)-(5.10) are plotted in Figure 5.9, where the effect of the phase shift on the spectrums is clear. The two Near-Field image components are shifted along the spectrum to the positions of  $\pm k_{XR}$ , (for a positive phase increment the conjugate image to  $+k_{XR}$  and the real image to  $-k_{XR}$ ), the correlation components remain at the centre of the spectrum.

The spectrum resulting from the simulated Off-Axis intensity pattern is shown in Figure 5.10; the terms are seen to be separated from each other, allowing the AUT PWS to be obtained directly. The method of obtaining the Far-Field or Near-Field distributions is dealt with in the next section.

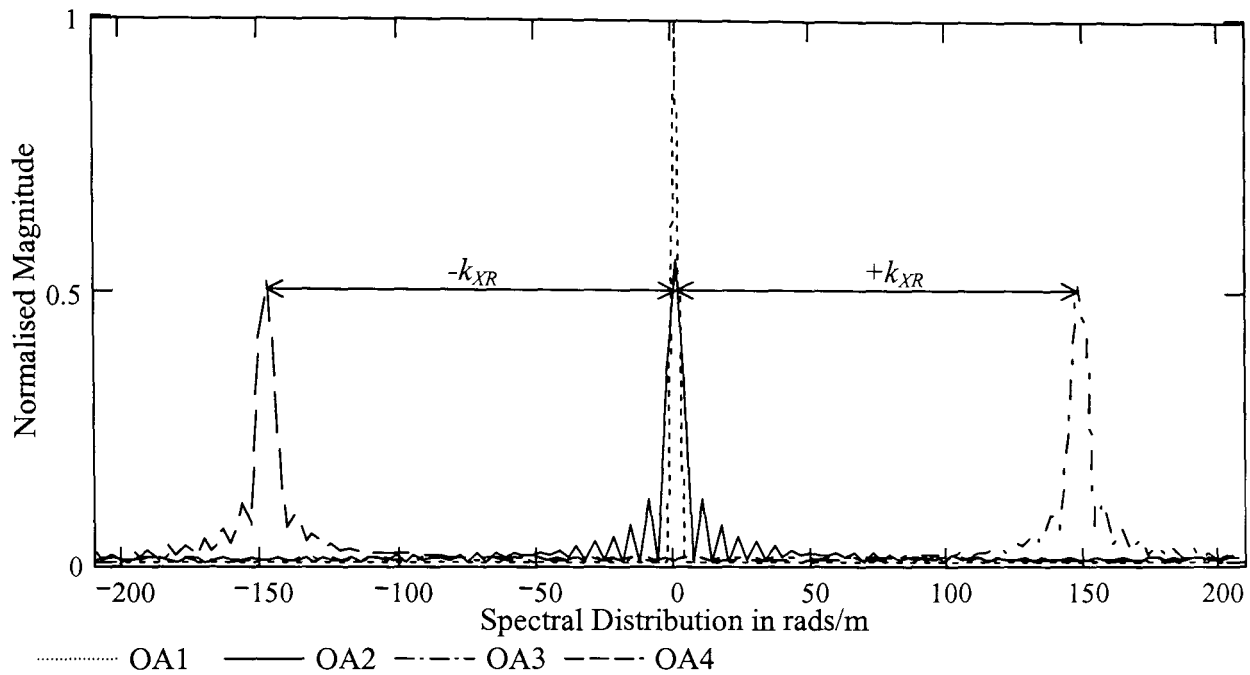


**Figure 5.9 Spectral Plots Of The Intensity Components Of An Off-Axis Hologram (5.7) - (5.10) Normalised To The Maximum Magnitude**

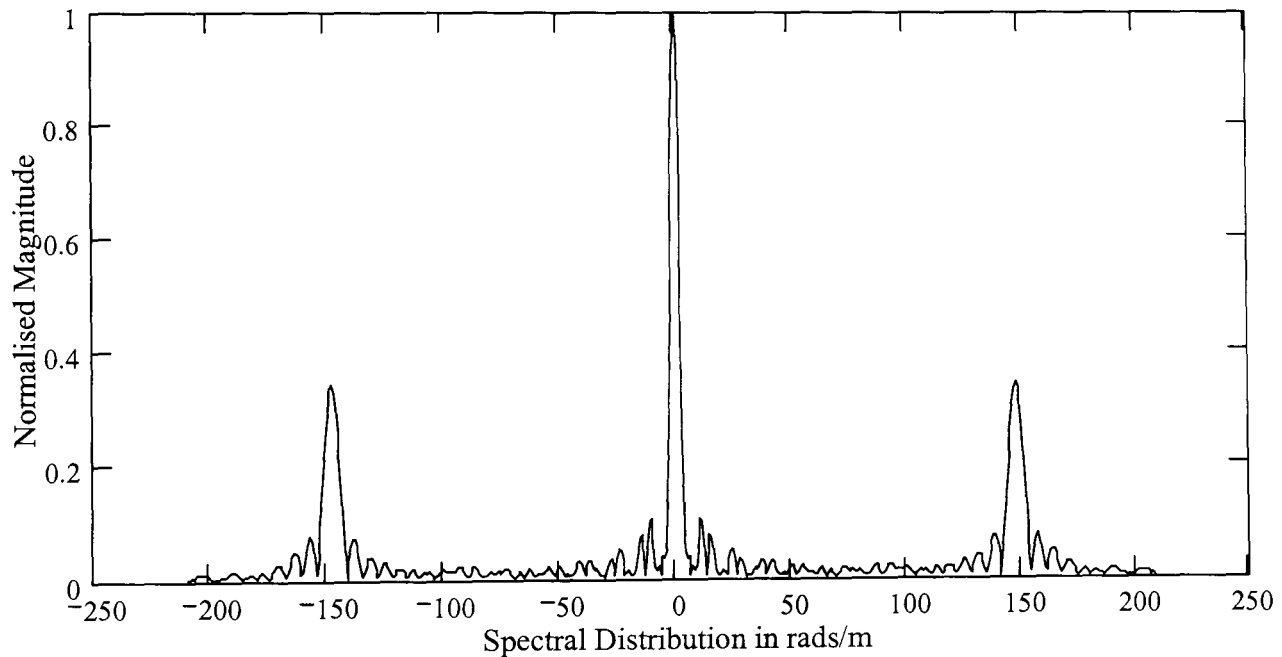


**Figure 5.10 Spectrum Of An Off-Axis Hologram Normalised To The Maximum Magnitude**

In the work by Huang [37], both techniques described above were implemented at frequencies into the THz range. As well as the planar technique, Huang also used the cylindrical scanning process. Though this work was still based around electrically large antenna with high gains.

### 5.4.3 Acquiring the Far-Field radiation pattern from the Off-Axis hologram

The AUT PWS is generated directly in the intensity pattern spectrum as the shifted real Near-Field image component. To find the antenna Far-Field radiation pattern the AUT PWS is extracted directly from the spectrum of the recorded intensity pattern and processed in the normal way, by application of (3.5). As part of filtering the PWS from the spectrum it must be re-centred about zero manually.

To provide interpolation in the transform, the intensity data is zero buffered. Prior to the zero buffering the Direct Current (DC) component of the intensity pattern is removed by subtracting the average intensity from each data point. This is necessary since the intensity pattern does not converge towards zero but towards the magnitude of the reference wave at its spatial extents. This can be seen from both the In-Line and Off-Axis intensity patterns. If the DC level is not removed then after zero buffering the intensity pattern will appear on top of a pulse, which in the transform will appear as a correlation of the pulse with the intensity pattern, resulting in a large ripple throughout the spectrum due to the *sinc* component of the pulse.

The real and conjugate AUT PWS's have been extracted from the spectrum produced by the simulation of the Off-Axis hologram. The Far-Field radiation pattern has been calculated for the real Near-Field image, this is shown in Figure 5.11 compared with the pattern obtained from the direct holographic method discussed in Chapter 3. The two patterns Far-Field patterns show the same main features i.e. Half Power Beamwidth (HPBW), null beamwidths and side lobe locations and amplitudes.

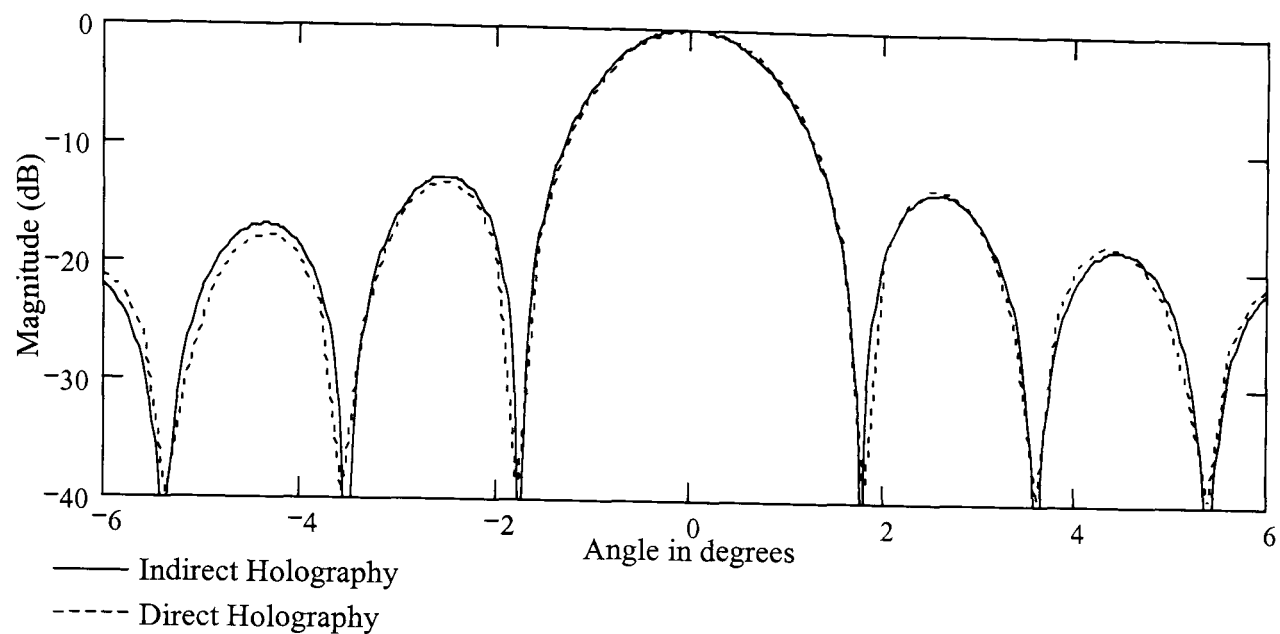


**Figure 5.11 Simulated Far-Field Radiation Patterns For A  $32\lambda$  Uniformly Illuminated Aperture Using Direct and Indirect holographic Techniques**

#### **5.4.4 Acquiring planar Near-Field distribution and the antenna aperture distribution from the Off-Axis hologram**

In the case where the complex Near-Field of the antenna is desired then further processing is required. As discussed in Chapter 3, the AUT complex Near-Field and the AUT PWS are a FT pair. Therefore having filtered the PWS out of the spectrum of the Off-Axis hologram, its IFT will yield the AUT complex Near-Field distribution over the measurement plane. A comparison of the Near-Field used to produce the hologram and the regeneration of the Near-Field from the IFT of the indirectly obtained PWS is shown in Figure 5.12. The width of the filtered spectral component is much smaller than the width of the whole spectrum and as such its direct IFT would result in a change in the sampling relationship between the two domains, specifically an increase in sample spacing in the reconstructed Near-Field plane would be observed. In order to maintain the sampling relationships, the filtered spectral component is zero buffered to the same size as the original buffered intensity data prior to its transform.

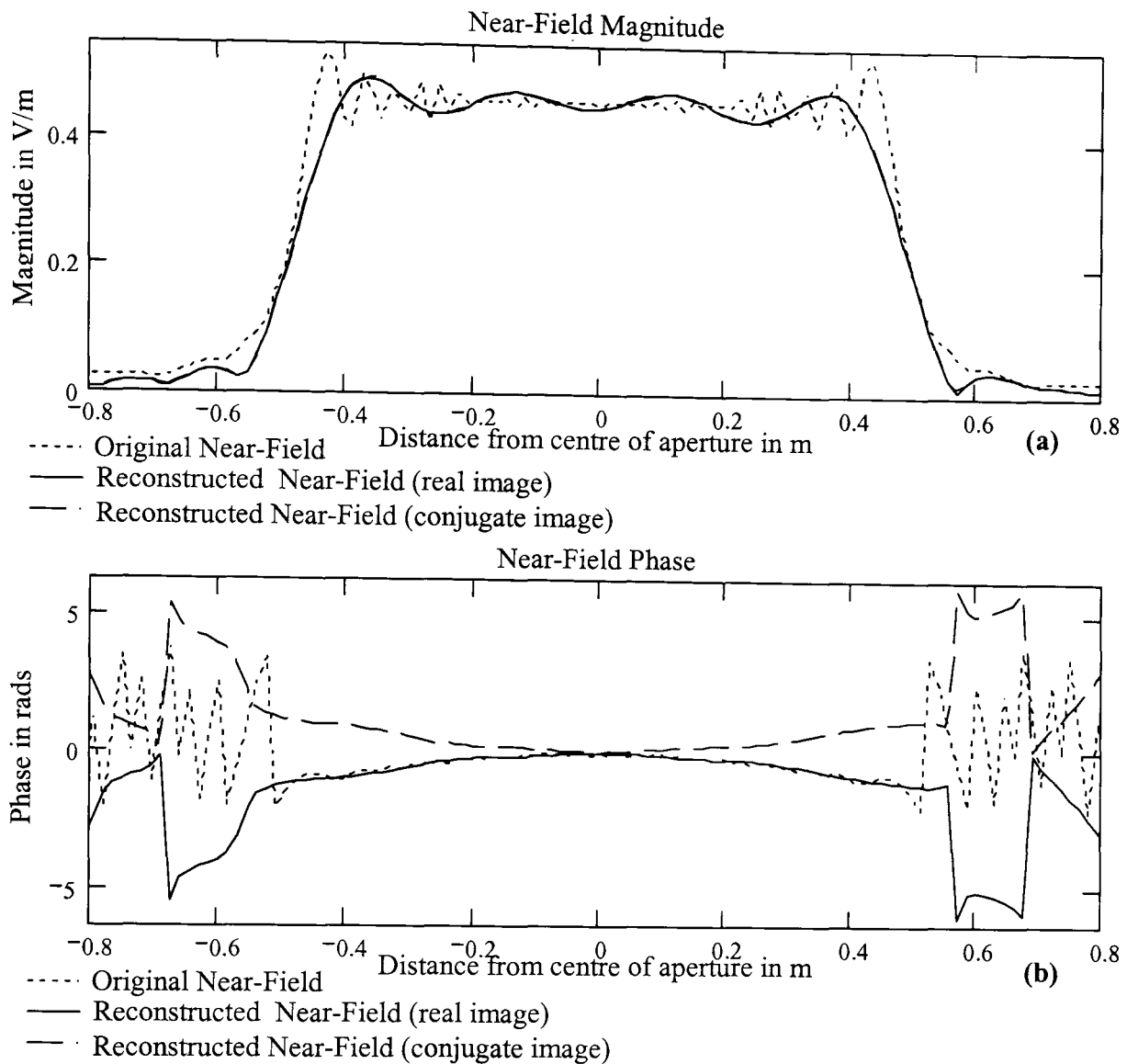


**Figure 5.12 Comparison Of A Simulated Complex Near-Field For A  $32\lambda$  Uniformly Illuminated Aperture And The Complex Near-Field Reconstruction From Intensity Only Samples And Application Of Indirect Holographic Theory (a) Magnitude And (b) Phase**

A high level of agreement is achieved between the reconstructed Near-Field (real image) and the original Near-Field, especially over the central region where the significant portion of the radiated energy exists. The inability of the reconstructed Near-Field to follow the rapid variations originally present is due to the band-limiting inherent in filtering. The difference in phase outside of the region containing the significant part of the signal, between approx.  $\pm 0.5$  m, is also a result of band limiting. The asymmetry in phase is due to the interference of the spectral components towards the edge of the filter. The conjugate PWS image has also been included in Figure 5.12

to show the inverted phase obtained by processing the conjugate Near-Field spectral image.

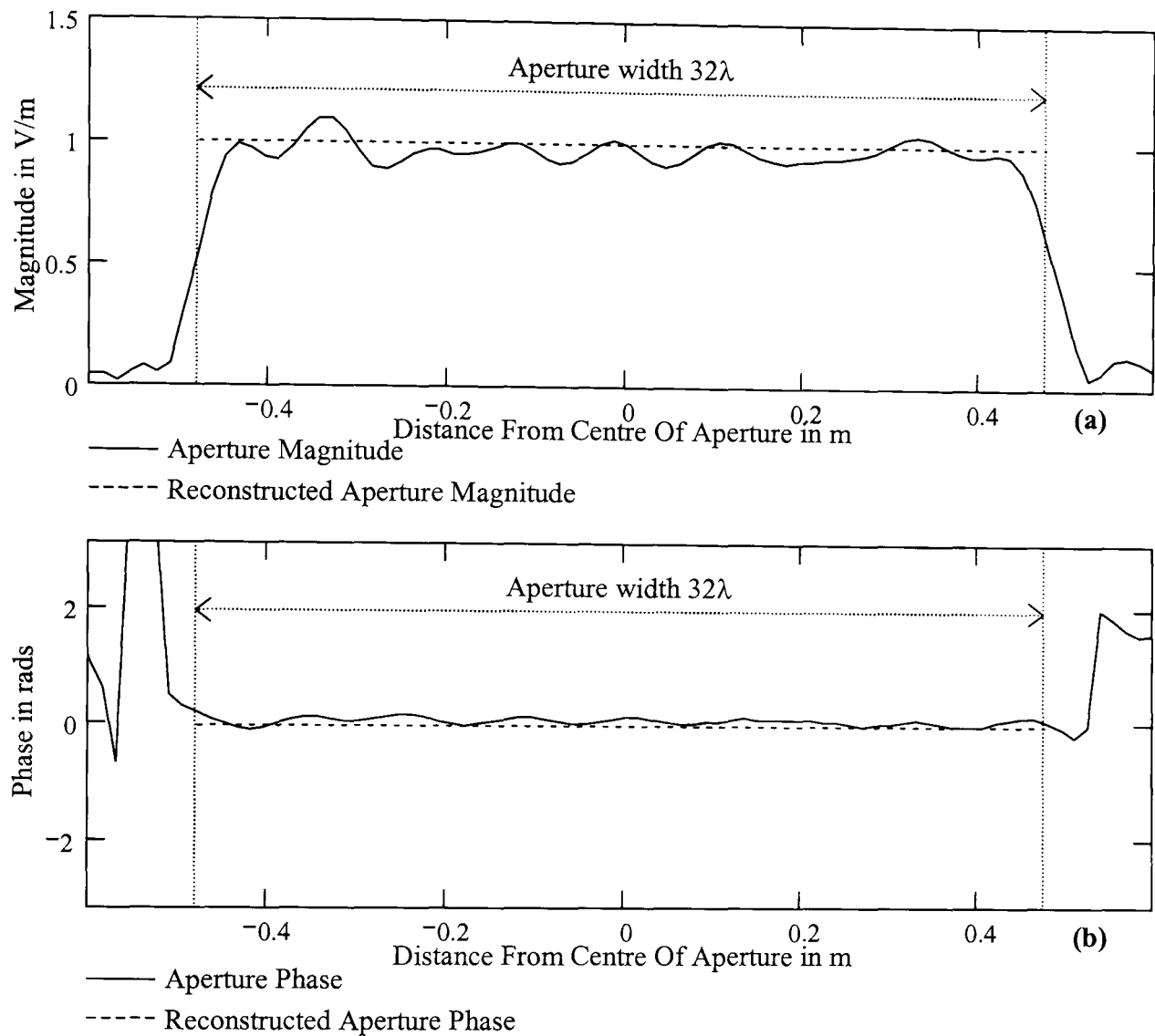


**Figure 5.13 Comparison Of Initial Aperture Distribution and Reconstructed Aperture Distribution Through Simulation Of The Indirect Holographic Technique (a) Magnitude And (b) Phase**

Once the PWS has been extracted, it can be transformed through any distance along the  $z$  co-ordinate using (3.18). To reiterate, the PWS is multiplied by the phase term  $kz \cdot z_0$  where  $z_0$  is the vector distance from the sampling plane to the aperture, this is negative since the propagation is in the  $-z$  co-ordinate. The result of this back propagation is shown in Figure 5.13, once again the beam-limiting that occurs in filtering the PWS from the spectrum has given rise to ripple in both the magnitude and phase. Once again asymmetry is observed especially in the phase as a result of the interference between components in the spectrum. Even with the ripple the

reconstructed aperture field shows a high degree of similarity to the original aperture distribution.

## 5.5 Locating Faults In The Aperture Field

Where the Far-Field pattern has been obtained and is not as designed or expected, it may be attributed to the manufacture of the antenna. These manufacturing errors may be visible by observing the field at the antenna aperture. A simulation has been generated to illustrate this; a  $32\lambda$  aperture with cosine illumination containing a nulled region of  $\lambda/10$  in width is created to represent a bad element in the aperture at a frequency of 10 GHz. The effects on the Far-Field radiation pattern obtained using the same process detailed above is shown in Figure 5.14 together with the Far-Field that would have been obtained if the null was not present. From the figure, the Far-Field generated by the aperture with the null is asymmetrical and clearly deformed in comparison to the Far-Field generated in the absence of the null.

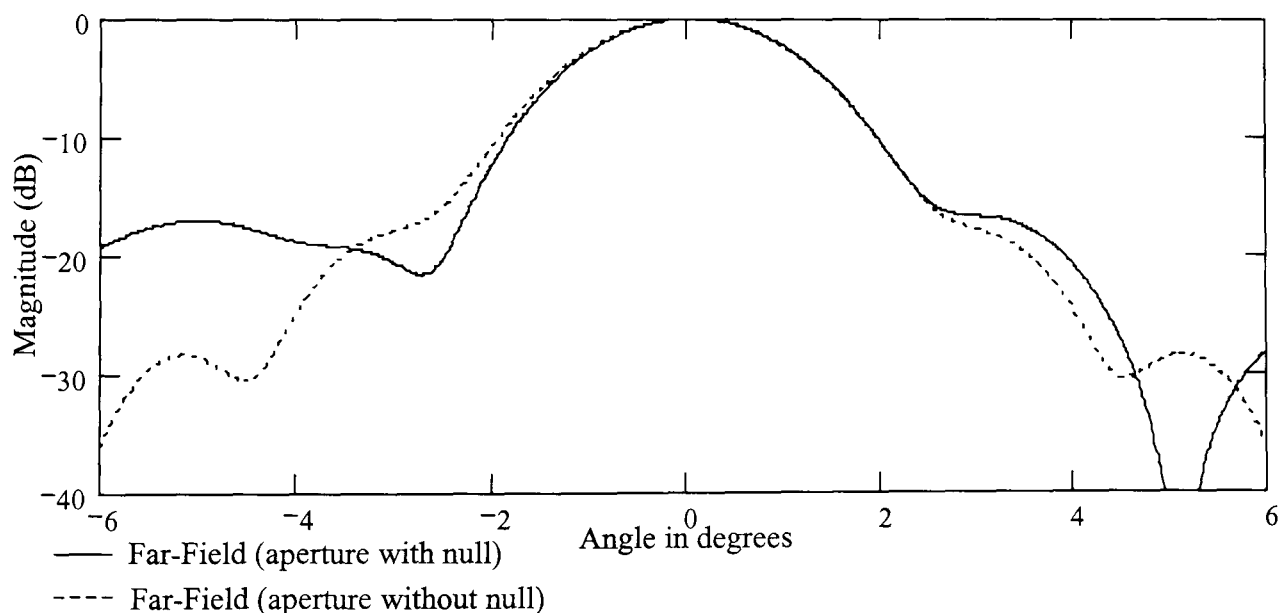


**Figure 5.14 Comparison Of Far-Fields Obtained Through Simulation Of The Indirect Holographic Method For A  $32\lambda$  Cosine Distribution With And Without A Nulled Region**

The two PWS's obtained have been used to reconstruct the aperture fields from which they were generated, see Figure 5.15. In defining the original aperture fields a discrete spacing of  $\lambda/30$  (i.e. 1 mm) to provide high definition. The Near-Field distributions are formed at a spacing of  $\lambda/2$  (0.015 m) the result of this is that the aperture reconstruction can only be resolved to the same sample spacing as the Near-Field and therefore some definition is lost in the sampling process. Interpolation by further zero buffering only allows for smoothing of the reconstructions it does not provide extra information.

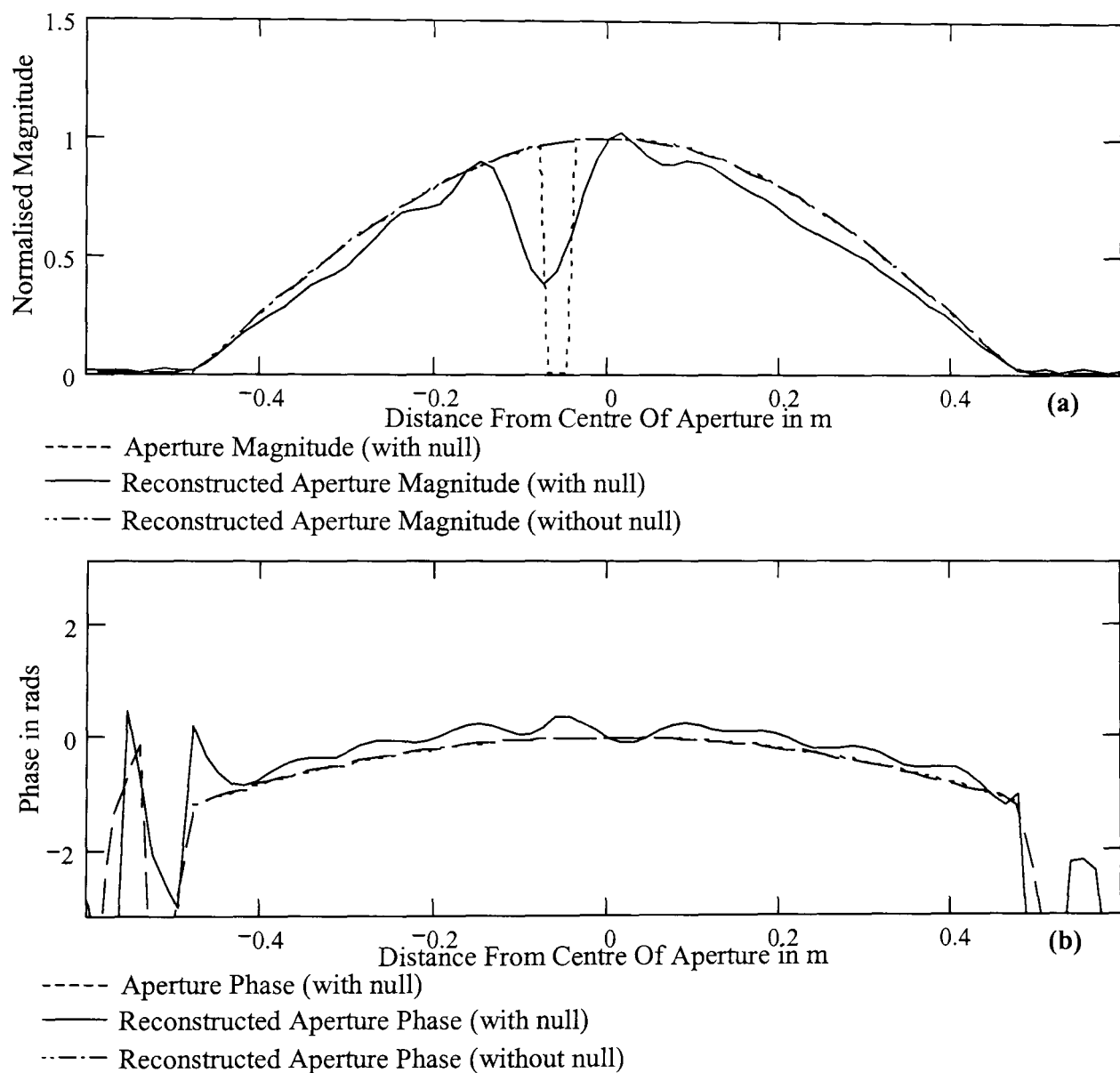


**Figure 5.15 Comparison Of Reconstructed Aperture Distributions For An Initial Aperture With And Without A Nulled Region Through Simulation Of The Indirect Holographic Technique (a) Magnitude Centrally Normalised To Unity And (b) Phase Centrally Normalised To 0**

Comparing the aperture field with a null and its reconstruction there is a clear correlation between the two, though again band-limiting has prevented the reconstructed aperture field from following the original aperture field with the square edges around the null. Also, as discussed the reconstruction has a greater sample spacing than that originally defined. Smith, Leach and Sambell [78] obtained similar results for the imaging of a null located in a uniform aperture distribution showing that the null was clearly visible in the reconstruction of the aperture field from intensity only Near-Field sampling.

It is noteworthy that it has been possible to reconstruct the aperture without the null in both the magnitude and phase void of any visible interference or distortion from filtering. This is because in comparison to the uniform aperture distribution used previously the spectrum of the cosine distribution is much narrower.

## **5.6 Sampling and Processing Intensity Data**

The effect of sample spacing, measurement aperture size and reference beam angle on the intensity pattern spectral distribution and how these characteristics may be chosen to provide maximum separation of the Off-Axis hologram spectral components is now discussed.

The planar measurement system is primarily used to measure directive antenna radiating into one hemisphere, as the plane will measure only forward radiation. The radiation pattern of the antenna is therefore band-limited at  $\pm 90^\circ$ , or  $\pm k_0$  in the angular spectrum. Anything appearing outside of this spectral limit is classified as evanescent radiation which decays rapidly with distance from the antenna and does not appear in

the Far-Field radiation pattern. Limiting the spectral width to  $\pm k_0$  allows the minimum required sample spacing to be defined as  $\lambda/2$ , (3.11), and observing the Nyquist rate means that no extra information is gained by sampling at less than this. The sampling requirements in forming an intensity pattern over a planar surface are the same as those outlined in Chapter 3 for the complex Near-Field measurements.

With  $\lambda/2$  sampling then the spectral width of the FT is implicitly defined by (3.10). This means that the spectral width into which the four components of the hologram spectrum must be incorporated including adequate separation between them is also defined,  $\pm k_0$ . From Figure 5.7 assuming that the spectral width of the auto-correlation term of the AUT pattern is dominant and approximated as double the spectral width of the AUT pattern, it can be seen that for separation of the terms, then the maximum angular width of the AUT must fit into the total spectrum eight times, therefore:

$$k_{XAUTMAX} = \frac{2 \cdot k_{XMAX}}{8} = \frac{k_0}{4} = \frac{\pi}{2 \cdot \lambda}, \quad (5.11)$$

$$\therefore k_{YAUTMAX} = \frac{\pi}{2 \cdot \lambda}.$$

This also requires that the Off-Axis reference wave angle be such that the centre of the AUT PWS image is located at a distance of  $3k_{XMAX}/4$ . If  $k_0$  is equivalent to  $90^\circ$  then the AUT spectral width can be up to  $45^\circ$  wide ( $45^\circ$  non-negligible beamwidth).

## 5.7 Sources of Error

The sources of error in planar Near-Field scanning were discussed in detail in Chapter 3, all of which are applicable to the any planar scanning system. There were some further error sources detailed in Chapter 4 regarding the production of a suitable Off-Axis reference beam at microwave frequencies in the recording of Off-Axis holograms. The novel technique, which will be presented over the following three chapters, is focused on dealing with some of these problems. The problems to be addressed are defined below.

The quality of the image contained in an Off-Axis hologram lies to a large part in the ability to produce an Off-Axis reference beam that is uniform in amplitude with a linear phase shift over a given plane. At the present time a microwave-radiating element cannot be used or adapted to produce this desired reference wave. Placing the reference antenna at a large distance from the measurement plane and hence using only a narrow part of the beam over the plane provides the best solution. However the distance at which this can be located from the hologram plane is restricted by the space available in the test environment.

The radiated reference signal is subject to any noise in the environment and if it is not carefully placed or the environment does not permit it to be placed at a suitable distance then cross coupling between the AUT and the reference horn may occur.

The restricted bandwidth available in the spectral distribution of the intensity pattern limits the types of antenna that can be tested in this manner, currently it is used for

only high gain antennas to prevent any problems of overlap between the three component areas.

## **5.8 Summary**

In this Chapter the two methods of generating holograms for the measurement of microwave antenna radiation patterns have been discussed. The ability of the Off-Axis hologram to provide total field recovery from intensity only measurements offers a significant advantage over standard direct Near-Field measurement techniques. This has been discussed and demonstrated using simulations.

The simulations showed that for large apertures, the Off-Axis hologram could be used to attain the total information of the antenna field from intensity only measurements and the degree to which this is possible is related to the band-limiting of the antenna spectrum as a result of the spectral filtering of the hologram and the measurement plane width.

Chapter 6 focuses on the generation of the Off-Axis reference wave, by synthesis. The implementation of a raster scanning method will also be looked at with a view to improving the manner in which data collection takes place.

# **CHAPTER 6 NOVEL OFF-AXIS HOLOGRAM APPROACH FOR INDIRECT NEAR-FIELD ANTENNA MEASUREMENT**

## **6.1 Introduction**

The principles of holography were discussed in Chapter 4 in its more familiar optical environment. This was then further developed into the microwave region with details of how the technique has been implemented for antenna measurement in Chapter 5. The plane wave generation for use as the reference was also highlighted in Chapter 5 and it is the development of the manner in which the reference wave is introduced to the hologram that forms the rest of this thesis. This chapter focuses on a novel technique for the production of holographic intensity patterns by synthesising a plane wave for use as a reference.

The outline of the novel synthetic reference holographic system is given in section 6.2 detailing the component structure and the methodology used for data collection. The advantages that can be attained through the application of this new system in comparison to the holographic systems discussed in Chapter 5. The initial system is constructed for one-dimensional measurement in section 6.3 and a process is developed to provide verification of the system. Sections 6.4 and 6.5 deal with the measurement, processing and comparison of the holographic data with the other methods as will be defined. The limitations of this initial one-dimensional system and an assessment of the errors involved are discussed in sections 6.6 and 6.7.

## **6.2 Synthetic Reference Off-Axis Hologram Generation**

An innovative way of generating the plane wave reference beam desired in forming Off-Axis holograms has been proposed by Smith and Leach [78], [79], [80] for the measurement of microwave antenna radiation patterns, which will now be discussed.

### **6.2.1 Proposed Off-Axis hologram antenna measurement system - overview**

Figure 6.1 shows the novel implementation of the Off-Axis hologram proposed for the indirect holographic measurement of antenna radiation patterns using a planar surface located in the Near-Field of the antenna. Comparing the physical arrangement to those of the methods previously described, shown in Figures 5.2 and 5.6, it is most apparent that there is no radiated reference beam. The system has two-branches, one radiated (from the AUT) and the other bounded in suitable microwave components, such as waveguide and microwave cable with the interference between the two occurring at a square law detector connected to the summation port of a Hybrid-Tee.

A continuous wave from a signal generator is connected to a multi-hole waveguide directional coupler. This allows the input signal to be divided into two, coherent waves, with the primary arm feeding the AUT and the coupled arm used to provide a reference signal.

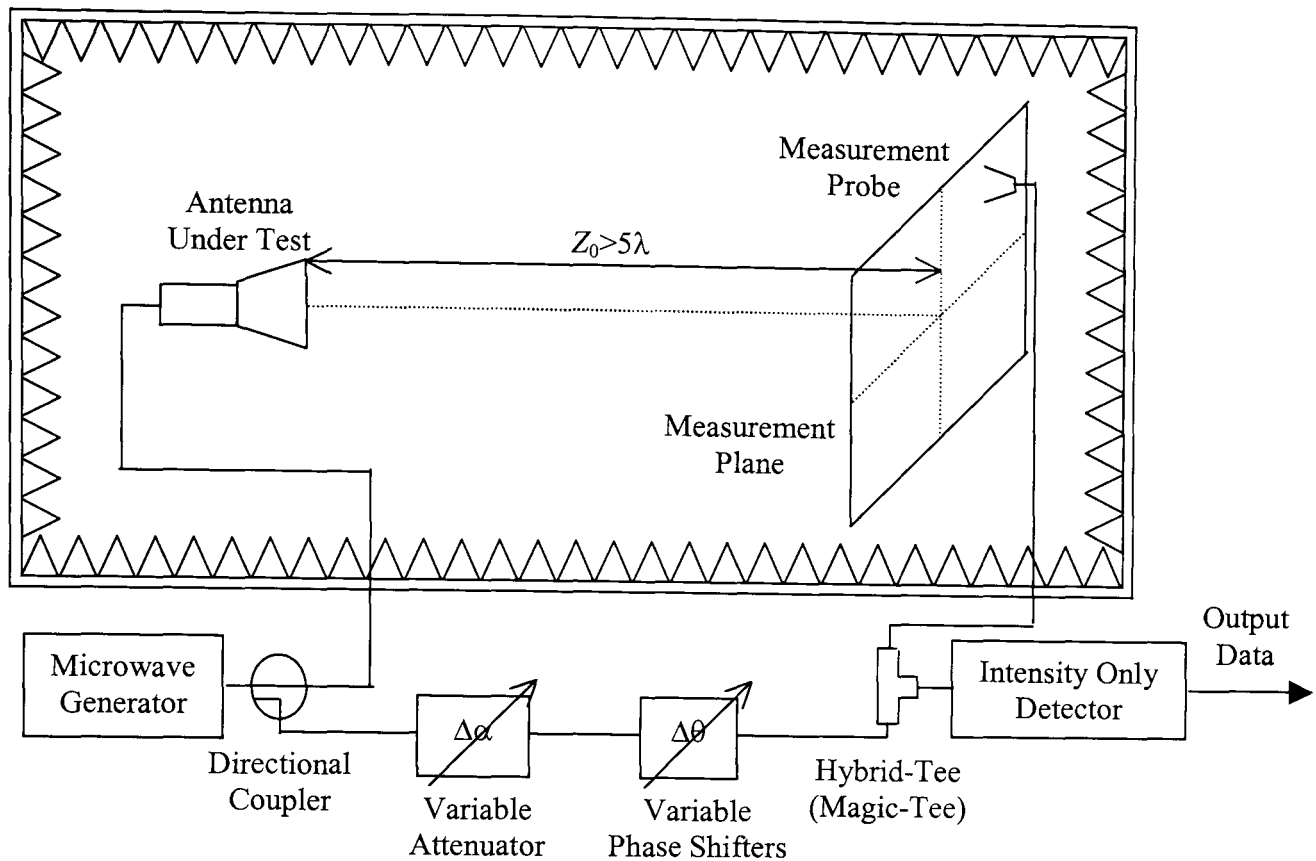


**Figure 6.1 Proposed New System For Indirect Holographic Imaging Of Microwave Antenna Radiation Patterns**

The level of power division in the coupler is chosen such that, at the point of interference the maximum AUT signal magnitude and the reference magnitude are approximately equal maximising the dynamic range of the recorded intensity pattern (as discussed in Chapter 5). In this implementation there will generally be less power required in the reference, as it is not radiated. The directional coupler used here is a 20 dB coupler, i.e. the power in the coupled arm (reference), is 20 dB less than the power in the primary arm output (AUT), though different size couplers maybe used depending on the relative gain of the AUT. A variable attenuator is used to adjust the reference magnitude to satisfy the power equality for different antenna.

Two variable phase shifters are used in the reference signal path, one is used to synthesise the linear phase gradient of the reference wave by adjusting the phase of the reference signal path by the desired amount at each sample location. This phase shifter should be capable of a total phase change of  $\geq 360^\circ$ , whilst producing no

variation in attenuation, ideally it should be computer controlled. The second phase shifter is used in tandem with the attenuator to ensure equal reference and AUT Near-Field components.

If the phase shifter used to synthesise the linear phase gradient is able to do so without producing any variation in attenuation, then the reference signal applied to the Hybrid-Tee will exhibit plane wave qualities. Furthermore, the phase gradient and magnitude of the reference can be closely controlled providing good initial calibration is performed and implemented within the control system.

The AUT should be mounted parallel to the measurement plane and located central and square to the centre of the measurement plane. The separation distance between the AUT and the measurement plane is determined by the frequency of operation and size of the AUT as discussed previously. To ensure being beyond the evanescent region (Reactive Near-Field), a minimum of  $5\lambda$  is used here.

The field probe should be moved accurately over a rectangular grid of points, using a Personal Computer (PC) controlled planar positioning system. The grid over which the probe is moved must be flexible in order to meet the sampling requirements at the frequency of operation and the width of the plane must be large enough to capture the majority of the radiated energy as described in Chapters 3 and 5. The probe field at each sample location is fed to the Hybrid-Tee. The output from the Tee is taken at its summation port, the difference port is terminated in a matched load and a square law detector (e.g. a power meter) is used to record the intensity at each sample point.

## 6.2.2 Measurement methodology

The methodology used to perform a scan using the proposed system is as much a novel aspect of the system as the synthesised reference wave. Due to the manner in which the reference wave is applied the process of data collection can be adapted to allow only a limited number of changes in phase, reducing the likelihood of error in the phase change.

The initial condition of the system is first set-up; this involves adjustment of the reference beam to the desired power level. It is assumed that the AUT and measurement plane have been aligned so that the boresight of the antenna points at the centre of the measurement plane and that the measurement plane is square to the principal planes of the antenna; it is also assumed that the maximum field from the AUT occurs at boresight where there is no priori knowledge of the field. Where there is a priori knowledge of the field, the location of the maximum is used when setting the initial condition. With the probe receiving the maximum field signal, the manual phase shifter is then used to reduce the received intensity to as small as possible through maximising the destructive interference between the reference and the received Near-Field. Once the minimum has been located using the phase shifter, the variable attenuator used in the same manner; this process is performed iteratively adjusting the phase shifter and then the attenuator until the received intensity is at its minimum (the noise floor). On achieving this, the two signals can be assumed to be equal in magnitude but opposite in phase.

The data collection process used requires that the phase increment of the reference wave between two consecutive samples be chosen so that its value repeats within one

or two full cycles, e.g.  $90^\circ$  or  $120^\circ$ , which have 4 and 3 phases in one cycle respectively. This means that the phase shifter used to generate the reference phase gradient needs a limited number of phase settings (e.g. 0, 120, 240), furthermore by setting one of these phase values, all locations in the sampling plane that require the same reference phase shift can be collected at the same time. This reduces the amount of time spent changing the phase shifter between samples and hence the total scan time. It also reduces any error in the repeatability of the phase shifter response. With a shift of  $120^\circ$ , three separate scans are performed; one for each phase shift meaning that in each scan every third sample point in the direction of the phase gradient is measured. Note that this phase shift is denoted by  $\theta_{XI}$  and is related to the angle  $\theta_{XR}$  and the sample spacing  $\Delta x$  by:

$$\theta_{XI} = k_0 \cdot \Delta x \cdot \sin(\theta_{XR}). \quad (6.1)$$

### 6.2.3 Advantages of proposed technique

The advantages over current systems in opting to utilise this technique of synthesising the Off-Axis reference wave can be divided into three areas, direct total reference control, system power requirements and range size. Firstly, the use of waveguide phase shifters and an attenuator in this novel way allows total control the reference wave in both magnitude and phase at all points in the scan; subject to calibration. This is in comparison to either a physically Off-Set transmitted reference wave, where the uniform amplitude and linear phase gradient desired over the sampling plane cannot be generated or easily controlled. Or a system like that of Figure 5.1 where a static reference horn and phase shifters are used to generate the uniform magnitude and linear phase gradient, this could be subject to interference or cross coupling between

the AUT and reference horn. It is also more difficult to control the relative magnitude of the reference signal in this set-up.

Secondly, operation at lower power levels is possible as the reference beam does not have to be radiated and therefore unlike the Bennett system, where a portion of the energy has to be incident on the reference horn, here the radiated energy is only concerned with the AUT.

Finally, a smaller anechoic environment is necessary as there is no need to allow space to mount the reference horn and ensure it is operating in its Far-Field. Only the AUT and the probe with its positioner need to be placed in the anechoic environment, and therefore it needs to be no bigger than a standard complex Near-Field measurement chamber would have to be for any given antenna. This means that the system could be easily integrated into current planar Near-Field measurement systems.

### **6.3 Verification Of Proposed Off-Axis Reference Synthesis**

To verify that the proposed system is able to produce indirect holographic Off-Axis intensity patterns that can in turn be processed using the theory set out and simulated in Chapter 5 to provide antenna radiation patterns, an initial one-dimensional scanning system has been assembled.

### 6.3.1 Design of a one-dimensional measurement system

The scanning system is shown in the photographs in Figure 6.2. The one-dimensional positioner allows the open-ended waveguide probe to be moved horizontally over a width of 0.4 m. An isolator has been included at the input to the directional coupler to prevent any unwanted signals being reflected back to the source, the reference arm of the directional coupler consists of three waveguide phase shifters and one waveguide attenuator, these are connected in series directly to one of the Hybrid-Tee's H-Plane co-linear arms. Three phase shifters are required as each can produce only  $180^\circ$  of phase shift therefore two are needed to implement the linear phase gradient rather than the one used in the proposed system of Figure 6.1. An open-ended waveguide probe is mounted on the positioning system as the measurement probe; this is connected to the opposite collinear arm of the Hybrid-Tee via microwave cable. The summation output port of the Tee is connected to a spectrum analyser, which is used to measure power, whilst the subtraction port is terminated in a matched load. All of the waveguide components operate within X-Band ( $\approx 8-12.5$  GHz).

The alignment of the antenna and scan plane is performed using rulers and spirit levels. Initially no computer control is used, positioning of the probe is achieved by hand turning a rotating ball screw with the distance measured against a ruler in mm. The linear phase gradient is applied by manually adjusting the waveguide phase shifters to pre-determined points, calibrated using a VNA. The addition of a microwave counter has been made in order to monitor the stability of the signal generator output.

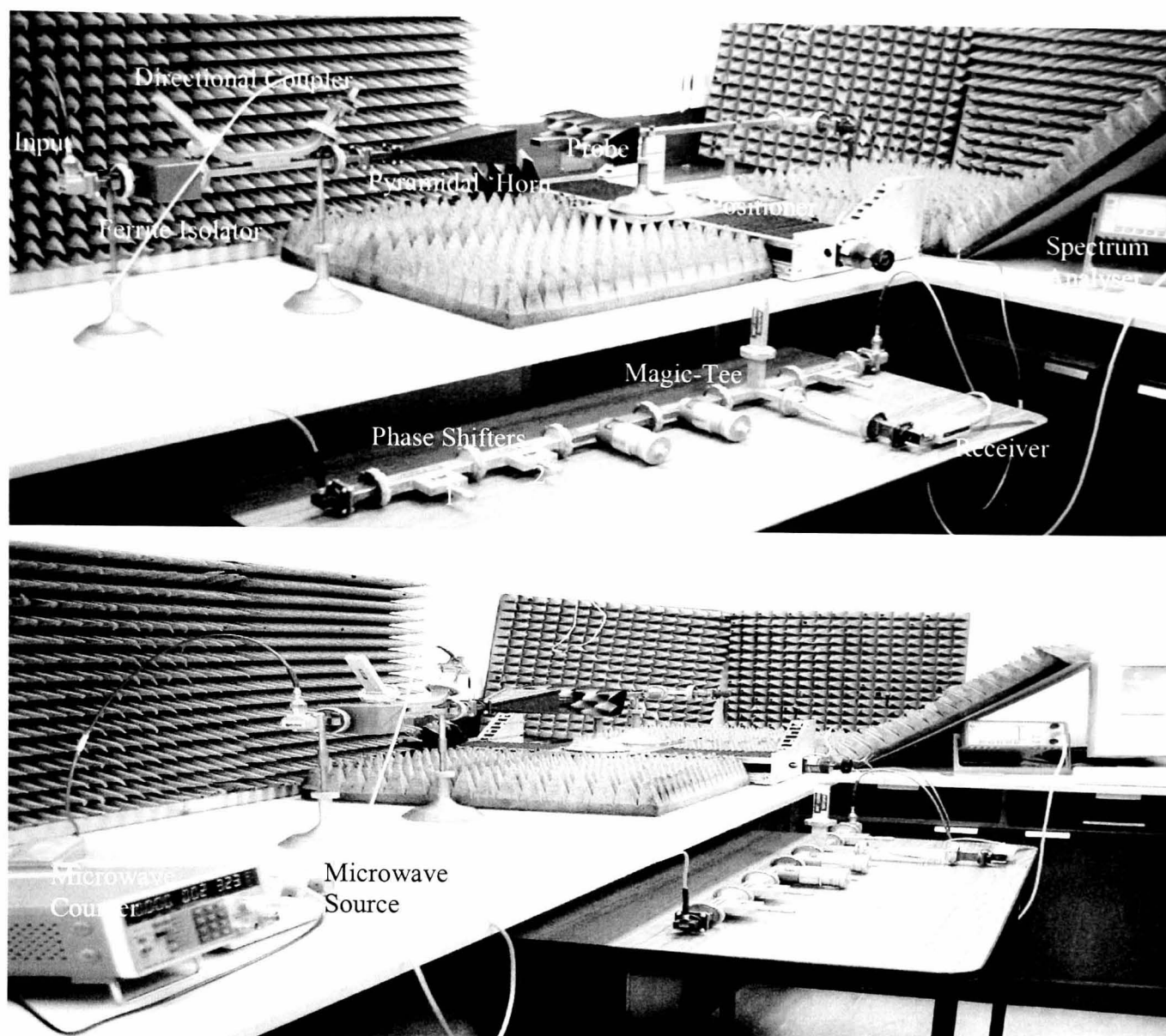


**Figure 6.2 Photographs Of One-Dimensional Indirect Holographic Measurement System**

### **6.3.2 Selection of test antenna**

A suitable antenna that falls within the limitations of the available system must be chosen to perform a test of the proposed system. Three main criteria need to be considered in the choice of antenna, these are the width of the antenna PWS, the antenna physical size and the frequency of operation.

All available waveguide components are X-Band (8.5–12.7 GHz) therefore the antenna used must operate within this band. The physical size of the antenna should be less than the maximum width of the sampling plane (0.4 m) to maximise the valid angle of the predicted PWS. The angle should be at least large enough to ensure that

the desired portion of the AUT PWS is attained at the measurement distance used ( $5\lambda$ )

Three antennas are available that meet these two criteria and are detailed in Table 6.1, the PWS width to be obtained for each antenna can be evaluated from the properties listed. The values for the parabolic dish are taken from data supplied by the manufacturer (Andrews Corp. [81]). No data is available for the pyramidal horns; the features have initially been estimated using standard aperture distributions [2].

Antenna	Flann Microwave Pyramidal Horn Model 16240		Flann Microwave Pyramidal Horn Model 17240		Andrews Corporation Parabolic Dish Model VHLP1-130-211	
	E-Plane	H-Plane	E-Plane	H-Plane	E-Plane	H-Plane
Aperture Size (m)	0.079	0.109	0.067	0.094	0.35	
Frequency Band	X-Band 8.2-12.5 GHz		X/Ku-Band 9.84-15 GHz		X/Ku-Band 12.7-13.25 GHz	
Frequency of operation	10 GHz		10 GHz		12.7 GHz	
$\approx$ FNBW (degrees)	73	66	90	78	11	10
First Side lobe Max (to main) (dB)	-13.26	-23	-13.26	-23	-19	-15
$\approx$ SNBW in degrees	87°	99°	64°	106°	22	20
Second Side lobe Max (to main) (dB)	-17.8	-38.5	-17.8	-38.5	-25	-23
Max Valid Beamwidth $2 \cdot \theta_{VALID}$	92°	88°	96°	91°	24°	24°

**Table 6.1 Antenna Properties**

For all three antennas the SNBW is taken as the desired beamwidth, to ensure that the majority of the radiated energy is contained within the given valid angle. It is assumed that the energy outside of this beamwidth is of negligible size in consideration of spectral spacing requirements with reference to the off-axis hologram technique.

Using standard sample spacing ( $\lambda/2$ ) the angular spectrum was shown in Chapter 3 to extend between  $\pm k_0$ . By defining the phase shift per sample to be used, then the reference offset angle  $\theta_{XR}$  and its associated spectral value  $k_{XR}$  can be found and hence the location of the centre of the AUT PWS in the hologram spectrum is known allowing the maximum spectral width that can be separated can be approximated. To limit the number of reference phases required and therefore simplify the calibration task, the phase shift per sample is chosen as  $120^\circ$  (i.e. only three phase shifts are necessary as they repeat at every third sample point).  $\theta_{XR}$  and  $k_{XR}$  are found using (6.1) and (4.13).

$$\begin{aligned}\theta_{XI} &= k_0 \cdot \Delta x \cdot \sin(\theta_{XR}), \\ \theta_{XR} &= \sin\left(\frac{120}{\pi}\right) = 41.8^\circ, \text{ or} \\ k_{XR} &= k_0 \sin(\theta_{XR}) = k_0 \cdot 0.667 \text{ rads/m},\end{aligned}\tag{6.2}$$

where  $\theta_{XI} = 120^\circ$  and  $\Delta x \approx \lambda/2 = 0.01$  m at 12.7 GHz.

Now that the offset angle  $\theta_{XR}$  is known, in order for the terms to be separated in the hologram spectrum, then the maximum non-negligible  $k$  value from the AUT ( $k_{XAUTMAX}$ ) must fit within the value  $k_{XR}$  three times accounting for the approximate double spectral width of the auto-correlation term.

$$k_{XAUTMAX} = \begin{cases} \frac{k_{XR}}{3} & \text{if } \frac{k_{XR}}{3} < k_{XMAX} - k_{XR} \\ k_{XMAX} - k_{XR} & \text{otherwise} \end{cases}.\tag{6.3}$$

In general the reference beam angle will be chosen such that the first condition of (6.3) is always true, the second condition is included to avoid problems of wrap around in the spectral domain. At 12.7 GHz  $k_{XAUTMAX}$  becomes:

$$\begin{aligned}
k_{XAUTMAX} &= \frac{0.667 \cdot k_0}{3} \text{ where } k_0 \approx 261.8 \\
&= 58.2 \text{ rads/m or } \theta_{XAUTMAX} \approx 12.8^\circ.
\end{aligned}
\tag{6.4}$$

To satisfy separation of the terms in the spectrum, the desired SNBW of the AUT must be less than  $2\theta_{XAUTMAX}$ . Having considered the three criteria for antenna selection set out initially, operating frequency, antenna size and PWS size, all three antennas were found to meet the first two criteria, but from Table 6.1 only the parabolic dish antenna is seen to meet the final criteria.

The format of the system verification must now be defined to ensure a fair evaluation of this proposed can be made.

### 6.3.3 Verification methodology and measurement parameters

There are limitations on the application of a one-dimensional scan to construct antenna Far-Field radiation patterns. Benjamin and Griffiths [82] discussed the issue of plane separability; for a rectangular aperture exhibiting a symmetrical field both planes can be separated in the FT and so a one-dimensional measurement across each of the principal planes is able to predict the polar response in that plane. For a non-rectangular aperture (e.g. parabolic dish) the planes are not separable and as such a one-dimensional measurement is not sufficient as is described below.

Consider a uniform distribution over a rectangular aperture as shown in Figure 6.3, by discretising the field into a regular grid of points, and then summing each of the points vertically to the centre. The distribution gained along that centre line represents an equivalent current source for the aperture, propagating into the same plane. In this

case the distribution over a one-dimensional cut through either of the principal planes is the same as the summation of the two-dimensions into an equivalent current source along that plane.

Now considering a circular aperture also with a uniform distribution (Figure 6.3), it is clear in following the same process that the equivalent line source is not equal to the field that would be measured over one-dimension. As seen, the field at the edge of an equivalent source for the circular aperture must be smaller than the field at the centre.

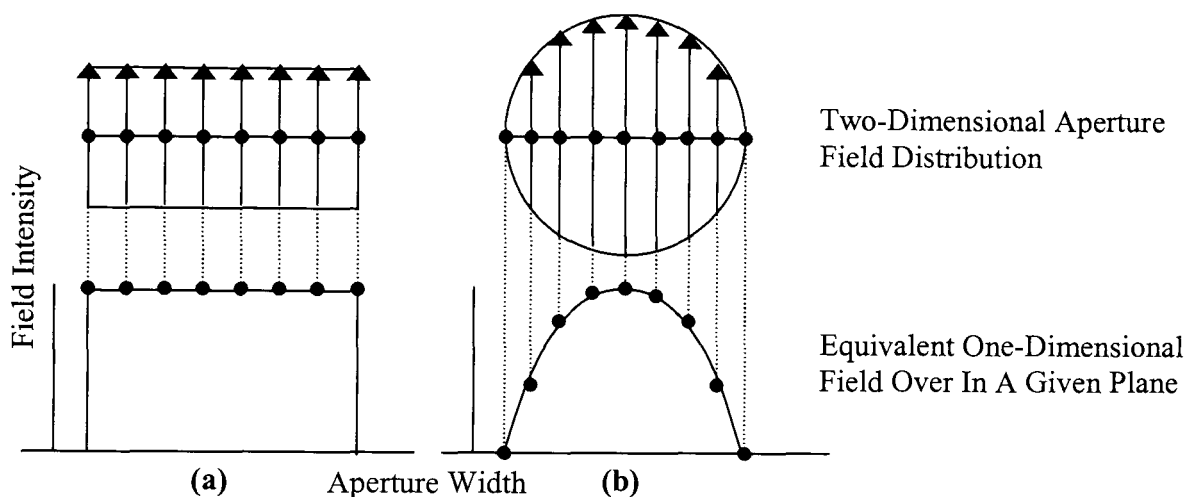


**Figure 6.3 Equivalent One-Dimensional Current Source For  
(a) A Rectangular Aperture Distribution and (b) A circular Aperture**

The result of this is that in this initial system the one-dimensional scan of the parabolic dish is not able to provide its PWS or Far-Field pattern, therefore verification of the system cannot be achieved by comparing the PWS that will be obtained with the true antenna PWS, a different form of verification is required.

A more logical comparison of the results obtained can be made if the direct holographic technique (measurement of the complex field) of Chapter 3 is applied. By measuring the total field over the same one-dimensional plane, and performing the equivalent processing technique (i.e. FT), then the two PWS's that will be attained are directly comparable, as they are formed from samples of the same field points and are

subject to the same measurement restrictions. Direct measurement of the complex Near-Field data provides the opportunity to compare not only the PWS obtained using each method, but also complex field reconstructed from the novel approach.

A summary of the measurement parameters is given in Table 6.2:

<b>Parameter</b>	<b>Specification</b>
<b>Antenna</b>	Andrews Corp. Parabolic Dish VHLP1-130-211
<b>Frequency Wavelength</b>	12.7 GHz $\approx 0.0236$ m
<b>Antenna Diameter</b>	$D = 0.35$ m
<b>Distance to AUT Far-Field</b>	$\approx 7.5$ m
<b>Waveguide Probe</b>	WR90
<b>Distance to sampling plane</b>	$Z_0 = 0.12$ m
<b>Width of sampling plane</b>	$S_X = 0.4$ m $\pm X_{MAX} = 0.2$ m
<b>Sample spacing</b>	$\Delta x = 0.01$ m $\Delta x_{MAX} \approx 0.0118$ m
<b>Number of samples in plane</b>	$N_X = (X_{MAX}/\Delta x) + 1 = 41$
<b>Spectral width</b>	$\pm k_{XMAX} = \pi/\Delta x = 100\pi$ rads/m
<b>Sample spacing in k-space</b>	$\Delta k_x = 2\pi / N_X \Delta x \approx 2.5\pi$ rads/m
<b>Valid angle <math>\theta_{XV}</math> Valid Beamwidth <math>\theta_{XBW} = 2 \cdot \theta_{XV}</math></b>	$\theta_V = \text{atan}(X_{MAX} - D/2 \cdot Z_0) \approx 12^\circ$ $\theta_{XBW} \approx 24^\circ$
<b>Reference phase shift per sample</b>	$\theta_{XI} = 2\pi/3$ rads or $120^\circ$
<b>Reference beam angle</b>	$\theta_{XR} \approx 0.73$ rads or $41.81^\circ$

**Table 6.2 Measurement Parameters For Initial One-Dimensional Scanning System Verification**

The system is first assembled to perform a measurement using the Off-Axis hologram approach as described and then reconnected so that the input to the antenna is derived from one channel of a VNA and the output from the probe is connected directly to the second channel of the VNA. The VNA is calibrated and set to work in Continuous Wave (CW) mode with the magnitude and phase recorded by hand. This reconnection does not require the antenna or the scanning plane to be moved retaining continuity in the sampling plane in relation to the antenna.

## **6.4 One-Dimensional Measurements**

The parabolic dish is mounted so that its H-Plane is parallel to the scan plane (in the  $x$ -axis) and its E-Plane orthogonal to it (in the  $y$ -axis). From the antenna properties listed in Table 6.1 it is seen that the beam is narrower in the H-Plane, offering marginally better conditions than the E-Plane for separation in the hologram spectrum. The results obtained using the novel indirect holographic method will be presented first followed by those for the direct holographic method. Both are applied using the relevant information from Table 6.2.

### **6.4.1 Indirect holography – intensity only measurement**

Prior to implementation of the Off-Axis technique, the two manual phase shifters used to synthesise the linear phase gradient of the reference must be calibrated. The phase shifters are connected to a VNA and then adjusted to find three positions that are spaced at  $120^\circ$  intervals and that exhibit the same attenuation. It is important that the change in attenuation across the phase shifters is negligible between the three phases, to preserve the uniform magnitude of the reference signal. A table of the three phase

shifter micrometer settings used and their associated phases and attenuations are shown below in Table 6.3.

Phase Shifter		Required Phase Angle (degrees)	Actual Phase Angle (degrees)	Attenuation (dB)
A	B			
0	1.59	0°	-0.8°	-1.35
8	1.46	120°	119°	-1.36
0	4.43	-120°	-121°	-1.4

**Table 6.3 Phase Shifter Settings at 12.7 GHz**

The variation from the desired 120° steps in is within  $\pm 0.2^\circ$  and the variation in attenuation is  $\approx \pm 0.025$  dB. Calibration was performed multiple times ensuring repeatability.

The initial conditions are set using the third phase shifter and attenuator in the reference, so that the recorded intensity value at the centre of the scan plane, i.e. antenna boresight, is a minimum, this is estimated as the recorded power level when no input is connected to the power meter,  $\approx -55$  dB. This is done with the phase gradient setting at the value it will take at that position during the scan. In this case it is the third phase, shown as  $-120^\circ$  in Table 6.3.

The scan is performed starting at  $-X_{MAX}$  with the phase shifters in position 1 ( $0^\circ$ ), the probe is moved through distances of  $3\Delta x$  until reaching its maximum point within the scan plane. The probe is then repositioned to start at  $-X_{MAX} + \Delta x$  and the phase shifters changed to position 2 ( $120^\circ$ ), it is then moved in steps of  $3\Delta x$  again. Finally, the probe is moved to  $-X_{MAX} + 2\Delta x$  the phase shifters set to position 3 ( $-120^\circ$ ) and is moved once again in steps of  $3\Delta x$ . At the end of this final traverse all of the intensity data has been

collected. The phase is being manipulated to provide  $+120^\circ$  per sample in the  $+x$  direction, corresponding to a plane wave intercepting the measurement plane at an angle of  $\approx 41.8^\circ$ .

Four sets of intensity data have been collected to show system repeatability and offer reassurance in the validity of the results this will be discussed further in section 6.5.

Only two of the data sets are shown in Figure 6.4 to avoid over cluttering of the graph.

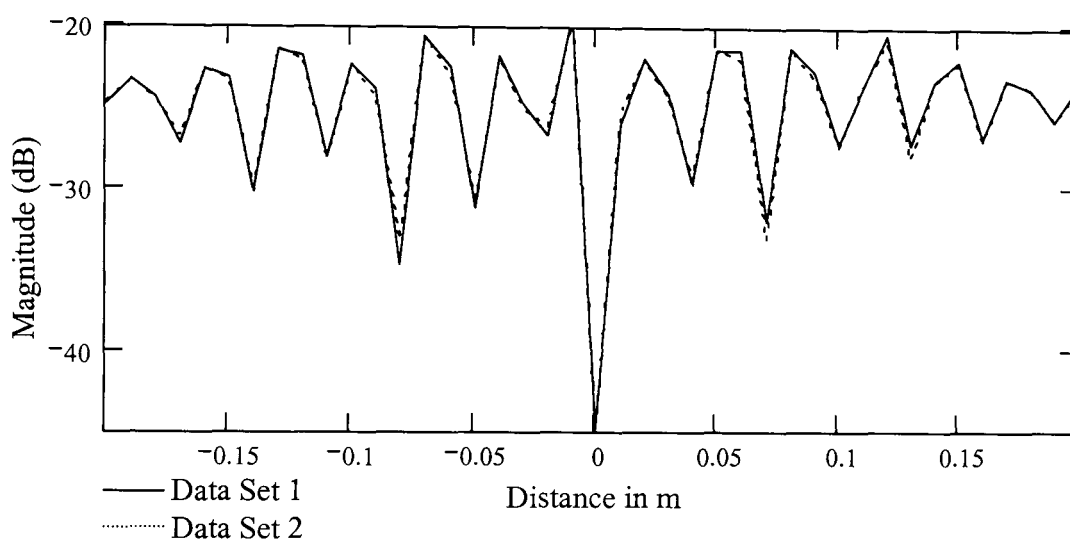


**Figure 6.4 Intensity Patterns Measured For Andrews Parabolic Dish With  $\Delta x = \lambda/2$  and  $\theta_{xT} = 120^\circ$**

The depth of the interference is seen to reduce towards the edges of the scanning plane. Ideally, the variation in the level of the interference would become negligible with the intensity level converging towards a constant at the edges of the scan. This would signify that only the reference remains present with the AUT beam being wholly contained within the scanning plane. Here there is still some variation indicating that the scanning plane does not intersect the whole AUT beam.

The intensity data collected is processed in the same manner as that described in Chapter 5. First the data is converted from dB to V/m, the average is removed prior to

zero buffering followed by the FT. The spectrum obtained from one of the measured intensity data sets from Figure 6.4 is shown in Figure 6.5

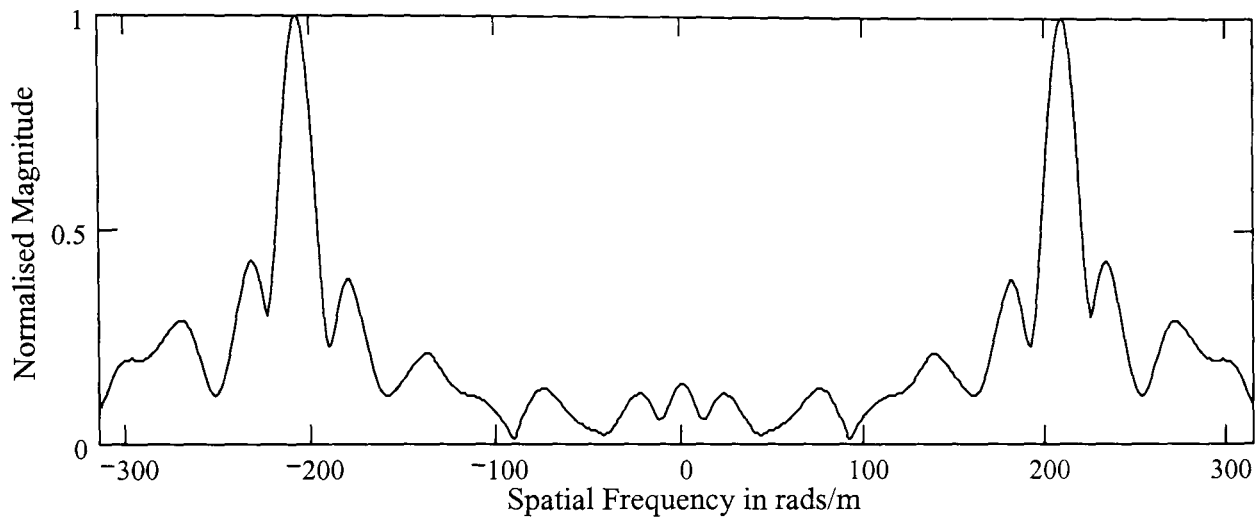


**Figure 6.5 Spectrum Of Measured Intensity Pattern In Figure 6.4 Normalised to Maximum Magnitude**

In the spectrum, two images are visible off-set from the centre as in Figure 5.7, while the two central auto-correlation terms have been suppressed by the removal of the DC/average.

For the reference angle used the location of each of the image terms can be found  $\pm k_{XR}$ . The desired component, in this case at  $-k_{XR}$  due to the positive phase increment per sample is then filtered from the spectrum. The width of the spatial filter used to remove the wanted object component is set by the valid beamwidth of the measurement system  $\theta_{XBW}$ . The filtered lower component from the spectrum is shown below in Figure 6.6 having been re-centred at  $0^\circ$ .

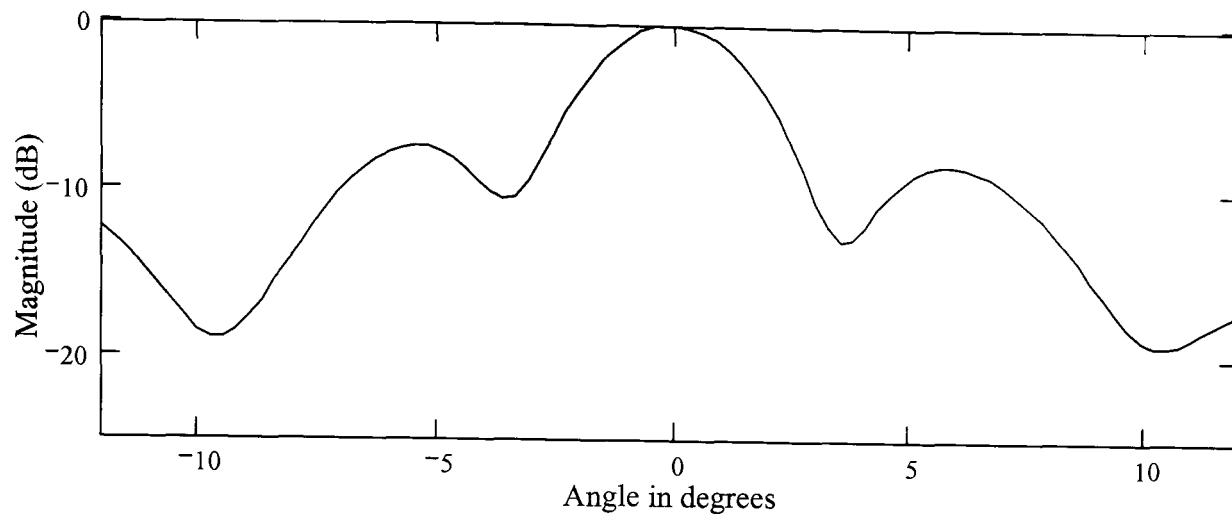


**Figure 6.6 PWS Filtered From Spectrum The Spectrum In Figure 6.5**

As previously discussed there is little value in comparing this H-Plane pattern to the Far-Field radiation pattern measured by Andrews Corp. on their Far-Field test range. It will however be compared to direct holographic data collected over the same plane.

#### **6.4.2 Direct holography – complex Near-Field measurement**

To collect measurements of magnitude and phase it is necessary to use a VNA. With the antenna connected to port one and the probe connected to port two, the analyser is set to continuous wave mode to measure the amplitude and phase of the transmit signal against the received signal.

Measurements of magnitude and phase have been collected at each point over the same scanning plane as used for the indirect method at the same sample locations. The positioning is carried out by hand and measurements are read directly from the front panel of the analyser. The network analyser is fully calibrated for 12.7 GHz.

Four sets of data have been measured to assure repeatability, one of which is shown plotted Figure 6.7. The measured magnitude of the field across the plane is largely

symmetrical, falling to  $\approx -20$  dB at the edges of the plane. The phase also exhibits good symmetry about the centre of the scan plane, with a range of  $\approx 110^\circ$ .

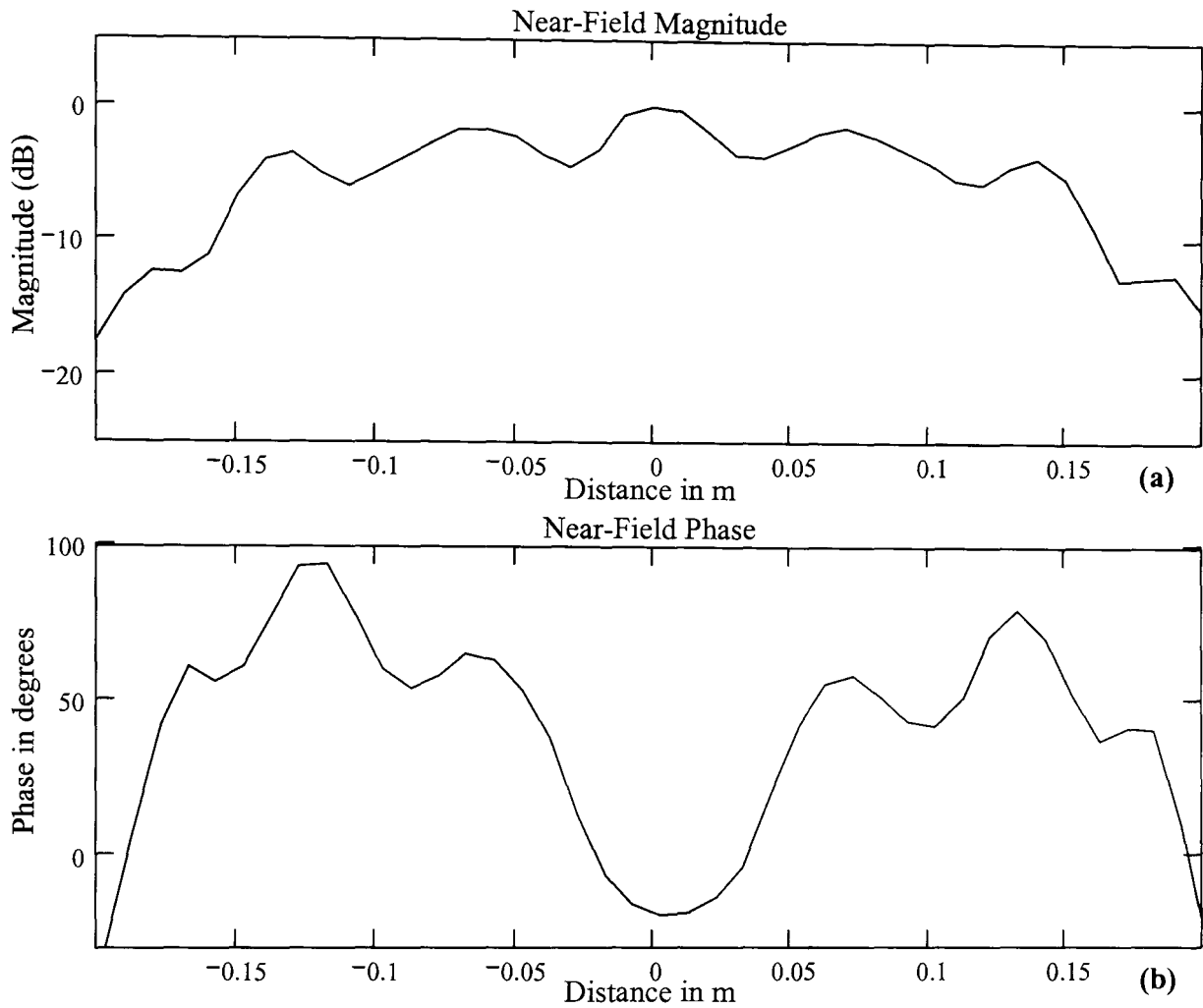


**Figure 6.7 Measured Complex Near-Field Data (a) Magnitude And (b) Phase**

The data has been processed following the Near-Field Far-Field theory set out in Chapter 3. Firstly the data is converted from dB to V/m and zero buffering is performed to provide interpolation. The same amount of zero buffering is used here as in the indirect technique, as this improves the comparability between the two sets of results, as their respective spectrums will have the same resolution. The data is then FT as per (3.16); the result of this processing is shown below in Figure 6.8, with the valid beamwidth highlighted.

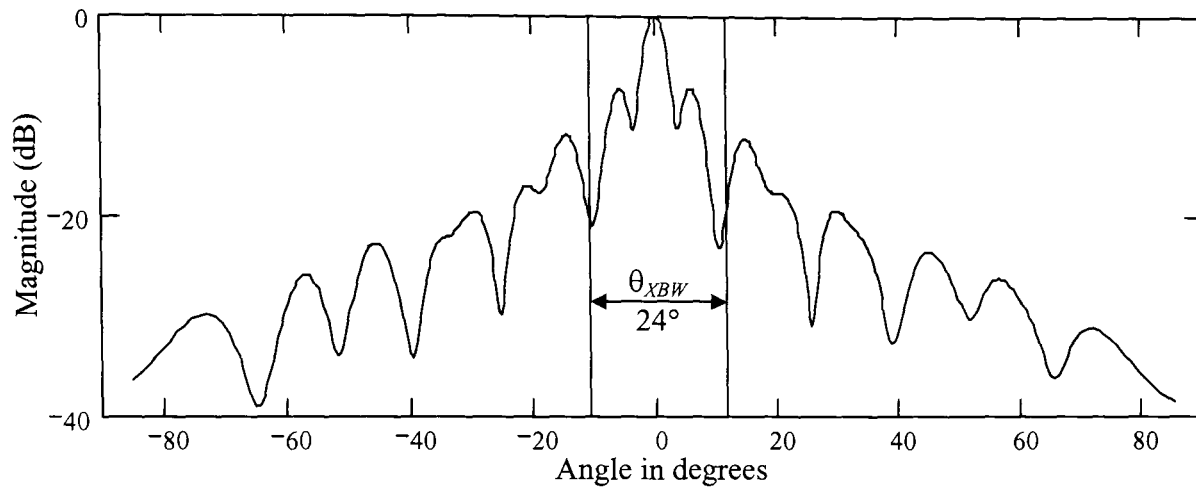


**Figure 6.8 Near-Field Far-Field Transform Of Direct Holographic Measurements**

The two scanning methods will now be compared to provide verification of the ability of the indirect holographic technique to be used to obtain equivalent information to that of the Near-Field direct holographic technique

### **6.4.3 One-dimensional scan results - discussions and comparisons**

The discussions made in this section are divided into two parts; first the PWS produced by each measurement technique will be compared and then the measured complex Near-Field will be compared in both phase and magnitude with that obtained indirectly.

The PWS's obtained using the two measurement techniques are compared in Figure 6.9, to verify that the proposed indirect holographic system can successfully provide the same level of information as standard techniques.

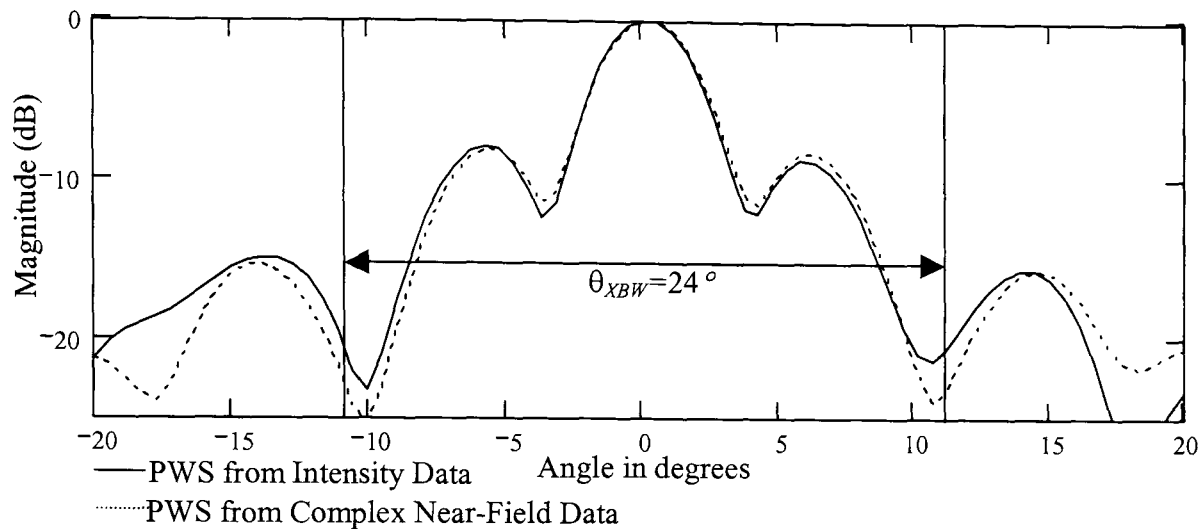


**Figure 6.9 Comparison Of One-Dimensional Directly and Indirectly Obtained PWS's**

The general trend and shape of the PWS's produced by the two different methods offer a high degree of agreement, to within  $\pm 0.5$  dB over the majority of the valid beamwidth with the largest variation coming in the second null where the signal is already  $-20$  dB down. They exhibit the same HPBW and First Null Beamwidth (FNBW) and SNBW. The differences in the two patterns are small over the valid angle with the deviation becoming greater beyond the valid angle. This can be attributed to the overlapping of terms in the intensity spectrum. The pattern outside of the valid angle is not representative of the true AUT PWS and should therefore be ignored.

Figure 6.9 has shown the validity of the proposed Off-Axis hologram technique to produce both valid intensity patterns, but also provide PWS information comparable to standard methods. A comparison of the Near-Field magnitude and phase data measured directly using the VNA and reconstructed from intensity only data will now be made.

As described and simulated in Chapters 3 and 5, by taking the IFT of the AUT PWS the complex Near-Field of the AUT is obtained. A comparison between the original Near-Field data and the Near-Field obtained via the IFT of the PWS obtained via the indirect method is shown in Figure 6.10.

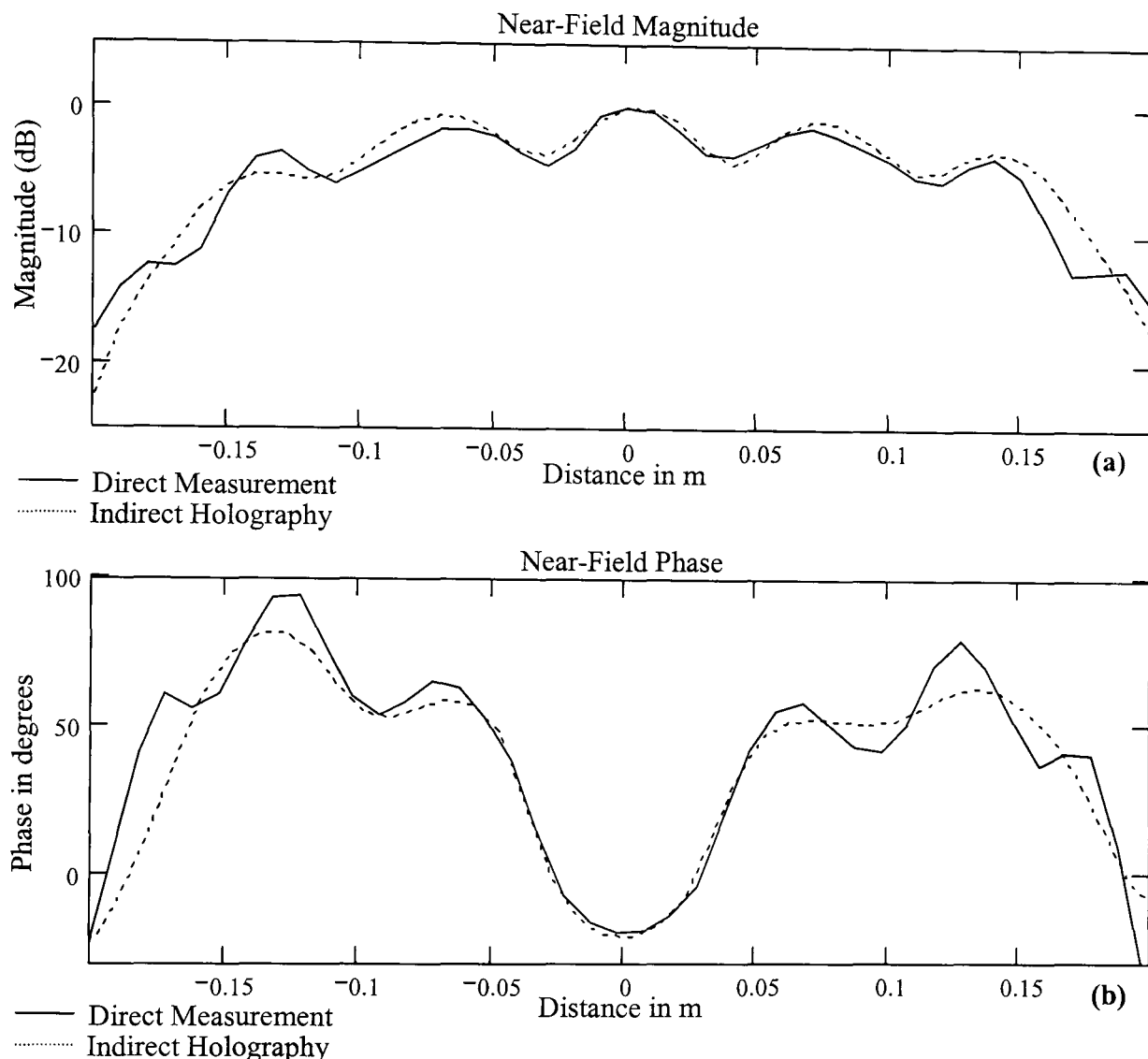


**Figure 6.10 Comparison Of Measured Near-Field And Near-Field Calculated Via The Indirect Holographic Method (a) Magnitude And (b) Phase**

The two Near-Fields, apart from their general shape and trend, are significantly numerically different, of the order of  $\pm 3$  dB and  $\pm 20^\circ$  in magnitude and phase respectively. Further consideration leads to the conclusion that the beam-limiting of the PWS spectrum in the indirect holographic method limits the ability of the complex field to be reconstructed. As the beam-limiting is defined by the width of the scanning plane, antenna and distance to the scanning plane, it is not possible to increase the

valid angle any further in this instance. Therefore to provide a more logical comparison, the PWS obtained from the direct holographic method is beam-limited at  $\pm\theta_{XV}$  and the IFT applied. This reconstructed Near-Field has the same spectral information as the one reconstructed from the indirect measurement.

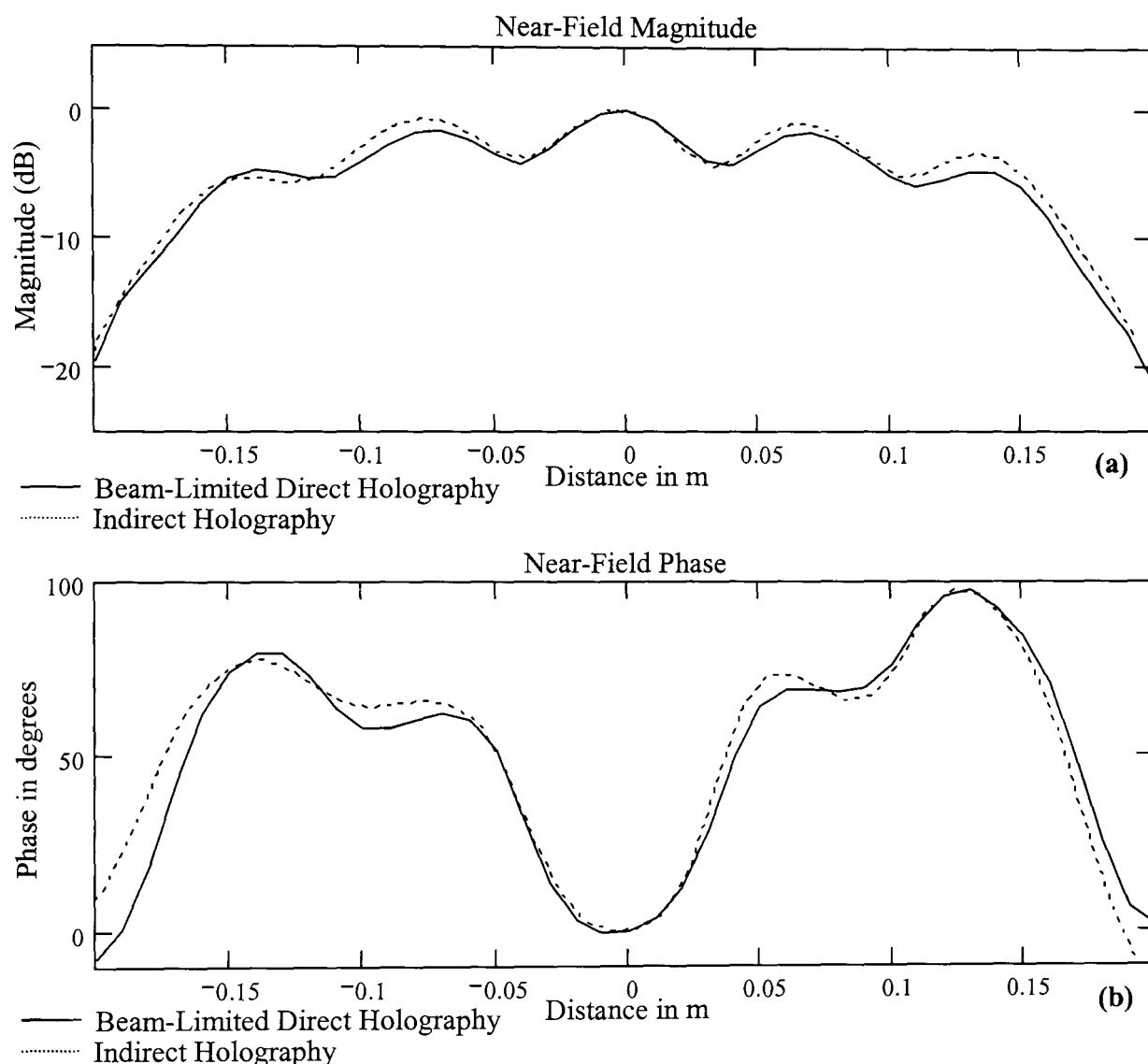


**Figure 6.11 Comparison Of Beam-Limited Spectral Near-Field And Near-Field Calculated Via The Indirect Holographic Method (a) Magnitude And (b) Phase**

The inverse transforms of the two beam-limited spectrums are shown in Figure 6.11. It can be seen from this graph that the two fields show a far greater similarity in both phase and magnitude than previously. The magnitude is within a range of  $\pm 1$  dB, and a phase variation of no greater than  $\pm 8^\circ$ .

It has been shown that the novel indirect holographic system proposed here is able to produce an antenna PWS comparable to that obtainable through traditional Near-Field techniques. It has also been shown that when both sets of data are subject to the same conditions, comparable predictions of the complex Near-Field to those measured can be achieved. Smith and Leach have published several papers detailing similar results for the same one-dimensional measurement system [69], [79], [80].

## **6.5 System Error Sources**

The error sources associated with planar scanning were discussed in Chapter 3. In this system a major part of the error is expected to come from the hand positioning of the probe, it is envisaged that the positioning is repeatable within  $\pm 0.5$  mm. Also the hand adjustment of the waveguide phase shifters, which there is no way of monitoring, have to be assumed repeatable from the calibration of the system as previously defined in Table 6.3. Other variable errors that cannot be accounted for include the stability of the cables used, environmental noise and stability of the microwave generator used in the intensity only measurements

Where possible, microwave absorber has been used to cover the surrounding environment to reduce the environmental noise error and the signal generator was monitored using microwave counter over the period of the measurement, this was seen to vary within 0.5% of 12.7 GHz. The cable error due to cable flex as the probe is moved is assumed negligible by using high grade microwave cable and preventing the cable becoming taught or pinched.

The data has been collected by manually reading values from device front panels, the level of accuracy to which the data can be recorded is dependent on the power of the signal being measured. Both the spectrum analyser used in the intensity only measurements and the VNA used for the complex field measurements provide a magnitude resolution of 0.01 dB, and the VNA a phase resolution of 0.01°.

The constant updating of these displays means that the resolution to which they can be read is less than the maximum resolution and is dependant on the received signal level. Over the main region of radiated energy, down to around -15 dB from the maximum, the resolution is around 0.1 dB for both the VNA and the spectrum analyser and 0.5° for the phase on the VNA. At magnitudes of lower than this the resolution can reduce to as much as 1 dB and 1°. Though this initially seems poor resolution it should be noted that the maximum power received by the VNA during the measurement is around -25 dB, therefore -15 dB below this means that the received power is approaching the noise floor. Taking these values as the normal data resolution, a quantitative evaluation of the system performance can be made by looking at the repeatability of the measurements.

For the intensity only measurements, the resolution is not such a problem, because the intensity level does not decrease to such a small value as the probe is moved to areas of low AUT Near-Field power. Instead the intensity level is converging towards the reference power level and so the resolution to which the spectrum analyser can be read remains at 0.1 dB for the whole intensity scan.

To quantify the repeatability of the measurement, the average of the maximum variance at each data point over the four data sets is calculated. This figure provides a good estimate of the range of the total error to which the results are subjected.

$$\begin{aligned}
 Var &= \frac{1}{N_x} \cdot \sum_{x=0}^{N_x-1} |\max(D1_x, D2_x, D3_x, D4_x) - \min(D1_x, D2_x, D3_x, D4_x)| \\
 Var_I &= 0.24 \text{ dBm (Intensity Only Variation)} \\
 Var_{NFM} &= 0.36 \text{ dBm, } Var_{NFP} = 0.28^\circ \text{ (Magnitude and Phase Variation)}
 \end{aligned} \tag{6.5}$$

where  $D1$ - $D4$  represent the four measured data series.

It is seen that the average variance for the intensity only measurement from the spectrum analyser is greater than the normal measurement resolution. From the VNA the average variance in magnitude and phase measurements are less than the minimum measurement resolution.

Despite the variance being greater than the measurement resolution, it is small in comparison to the dynamic range of the measurements. For the intensity only measurements the dynamic range is  $\approx 25$  dB and for the complex Near-Field measurements it is  $\approx 20$  dB and  $\approx 110^\circ$ . This equates to around 1% of the dynamic range for intensity only measurements and 1.8% and 0.25% for the complex field measurement. This can be regarded as only a small variance in consideration of the manual means in which the measurements were collected, which is as pointed out subject to human error such as probe positioning.

The probe used is an open-ended waveguide operating in its Far-Field region. This is a standard piece of equipment used to perform antenna measurements in the Near-Field [2]. Ideally, the probe should have an isotropic radiation characteristic, whereas

the open-ended waveguide has a uni-hemispherical directive characteristic though, it is broad beam in that hemisphere. The principal E and H planes for the probe Far-Field are shown below in Figure 6.12. These Far-Field planes were measured directly in an anechoic chamber.

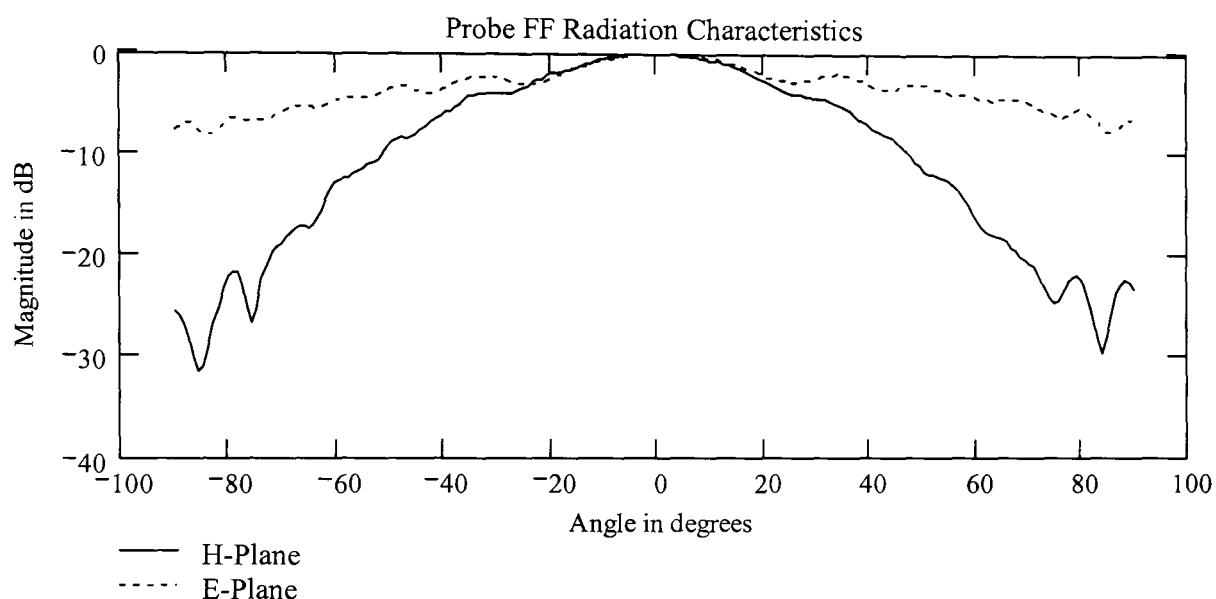


**Figure 6.12 Far-Field Radiation Pattern Of Open Ended Waveguide Probe**

The patterns show that the beam of the probe is almost flat over a range of  $\pm 10^\circ$  dropping by only  $\approx -0.3$  dB in both planes. Beyond  $\pm 10^\circ$  the probe characteristic drops more rapidly to  $-3$  dB and  $-2$  dB in the H and E-Planes by  $\pm 20^\circ$ .

No probe compensation has been performed in this instance as the PWS's compared are subject to the same measurement constraints. As such, the compensation applied to each of the measurement sets would be the same and therefore not change the outcome of the comparison.

## 6.6 System Limitations

Having obtained highly comparable results to the direct holographic technique it is useful to define the limitations of the current system and discuss where improvements can be made. Firstly, the mathematical and spectral restrictions will be defined and secondly, the physical restrictions of the available system are discussed.

### 6.6.1 Mathematical and spectral restrictions

Using the Off-Axis hologram method proposed it has been shown that the PWS of a suitably narrow beamwidth antenna can be acquired. For the given system and sampling scheme, the maximum beamwidth obtainable using this technique is  $\approx 25^\circ$  (6.4). It has also been shown that complex field samples can be reconstructed, though the extent to which this is possible is dependent on the spectral information available.

Two areas of interest exist, firstly, obtaining better separation of the Off-Axis hologram spectral components to allow less directive antenna to be measured. Secondly, a larger scanning aperture is required to increase the valid angle since even where adequate separation is obtained, the spectrum cannot be held valid outside of the valid angle and so this restricts the spectral cut-off point. For the purposes of this work it is deemed sufficient to be able to extend the application of the system for use with less directive antenna, since equipment is not currently available to further extend the scan width. It is noteworthy that for aperture antenna that in general the directivity reduces as the aperture size decreases and therefore, in looking at less directive antenna the valid angle will increase.

The application of the system to less directive antenna will be dealt with in Chapter 8 where a combination of the unique ability afforded by using a synthetically generated reference wave in tandem with the sample spacing is shown to produce the desired result.

### **6.6.2 Physical restrictions**

The limit of one-dimensional scanning with regards to the types of aperture to which it is applicable has already been discussed in 6.2.3. To show the accuracy of the current system against conventional Far-Field range measurements, it is necessary to extend the initial system to cover a two-dimensional scanning aperture.

Two-dimensional scanning not only allows a wider range of antenna to be considered it also allows the application of two dimensional reference phase shifting. The separability of the two dimensions in the FT means that the angular displacement of the reference can be exploited in both dimensions. Where previously phase increments were made per sample in one-dimension, in two dimensions the reference phase increment can be made per sample in both directions. The result is three reference phase combinations; for an aperture located in the  $x$ - $y$  plane these three combinations are shown in Figure 6.13.

The preference in phase shift direction can be chosen easily when using phase shifters to implement the phase gradient. No further calibration of the phase shifters is required for this, unless a smaller shift is desired in one dimension than the other.

To realistically function in two-dimensions system automation is required. If an equivalent two-dimensional scan to that performed above was to be realised then a

total of 1681 (41x41) measurements need to be made multiple times. Also the automation of the data collection comes with an increased measurement resolution. Two-dimensional scanning is developed in Chapter 7.

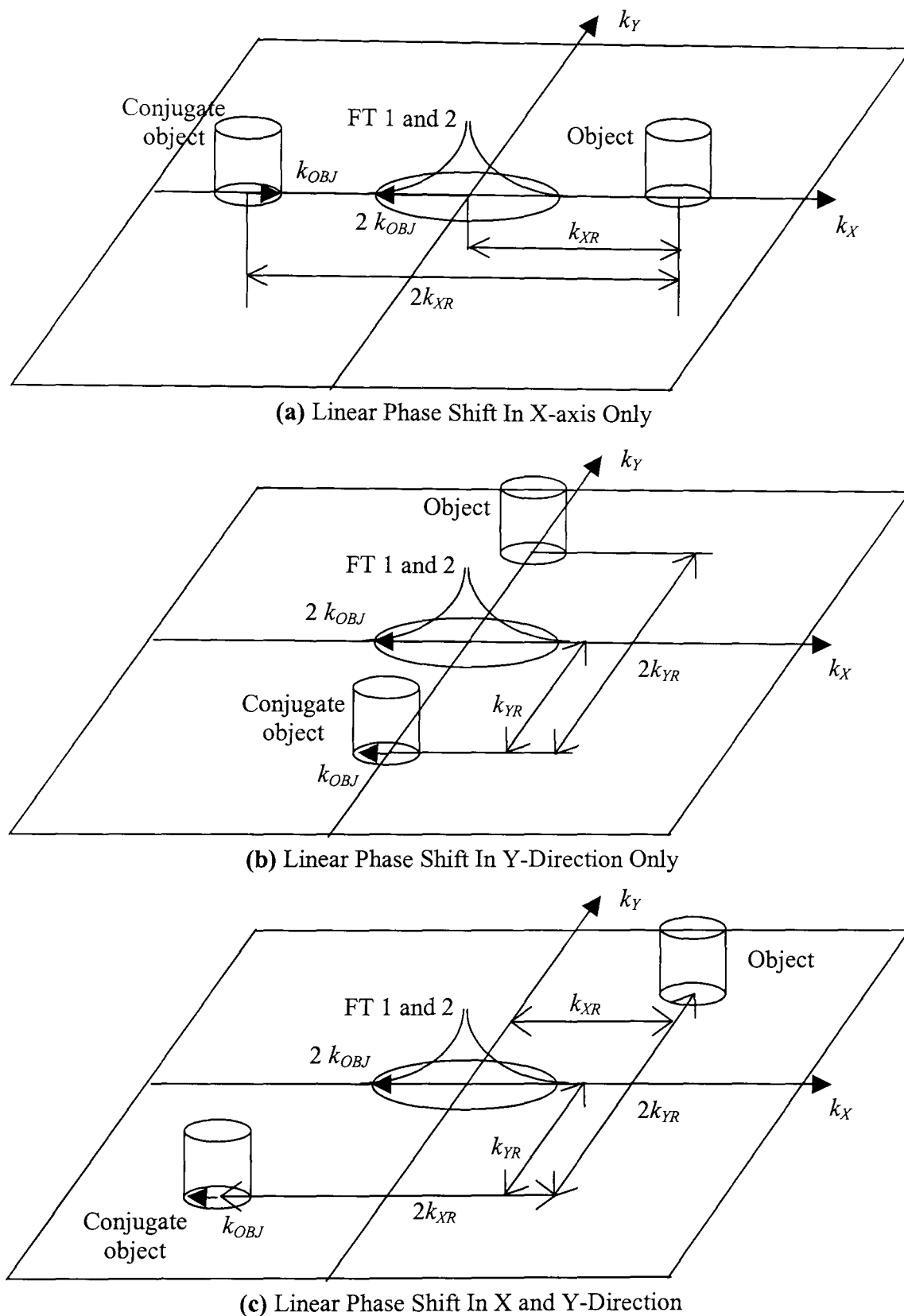


**Figure 6.13 Three Combinations Of Reference Wave Phase Shift For Two-Dimensional Indirect Holographic Scanning (a) Phase Shift In X Only (b) Phase Shift In Y Only And (c) Phase Shift In X and Y**

One further consideration with relation to the system is that the phase shifters must be recalibrated for each measurement frequency. This calibration is only required to be performed once and therefore should not affect the system cost. Also fixed frequency discrete phase shifters are cheap to manufacture as true time delays in the form of wire lengths.

## 6.7 Summary

A novel system for the synthesis of an Off-Axis reference in the generation of a hologram utilised for the indirect measurement of antenna Near-Field phase and amplitude has been proposed. The system has then been practically verified by comparison with a standard measurement technique (Direct Holography) for a one-dimensional scanning aperture. The implementation of this novel system offers several advantages over the traditional indirect holographic systems, by means of a more controllable reference signal and a reduction in the size of the anechoic environment required.

An evaluation of the PWS's produced by the two techniques showed a positive relationship out to the second null beamwidth, where the patterns were within  $\pm 1$  dB and exhibited the same null beamwidths and sidelobe locations. The effect of beam-limiting the PWS on the reconstruction of the complex Near-Field has been demonstrated. Though in this case the over-riding factor in beam-limiting is the valid angle.

The main sources of error have been identified, and their effects have been discussed by looking at the measurement repeatability with respect to the resolution of the

recorded data and the dynamic range of the data sets. The variance in the data was seen to be very small in terms of the dynamic range though greater than the data resolution. It is deemed that the small change with respect to the dynamic range is reasonable in consideration of the manual nature of the equipment used.

The limitations of the initial system have also been identified; two of these limitations will be addressed during the remainder of this thesis, firstly the scanning aperture shall be extended to operate in two-dimensions and secondly the directive restrictions that currently limit the types of antenna that can be tested in this manner as discussed will be considered.

# CHAPTER 7 TWO-DIMENSIONAL INDIRECT HOLOGRAPHIC SCANNING SYSTEM

## 7.1 Introduction

Chapter 6 presented a novel idea for generating holographic intensity patterns in the process of obtaining antenna radiation patterns. This was then verified by comparison with standard Near-Field antenna measurements as described in Chapter 3. In this chapter, the initial one-dimensional system is developed into a two-dimensional system.

The chapter begins with a description of how the plane reference wave can be generated in a two-dimensional system and how each of the three possible phase shifts described in Figure 6.13. A two-dimensional simulation of the holographic process is provided in section 7.3. In section 7.4 the measurement parameters are defined for the indirect hologram and the measurements are presented along with the complex Near-Field measurements and the manufacturers Far-Field measurements. These other measurement techniques are used to verify the results obtained using the novel method in section 7.5. It is important to be able to compare the novel technique with these standard techniques as the main point behind this research is to provide a cheaper alternative to currently used techniques, but that is able to produce comparable results.

## 7.2 Synthesising A Two-Dimensional Off-Axis Reference

The measurement of the field over a two-dimensional aperture is necessary, as one-dimensional measurement can only be used to validate the singular Far-Field planes of antenna with symmetric fields on rectangular apertures. The methodology to be employed in performing a scan will now be discussed followed by a two dimensional simulation.

In Chapter 6 it was shown that the angle of the Off-Axis reference beam could be varied in either one or both dimensions at the same time during the recording of the intensity pattern, allowing three different modes of separation in the intensity pattern spectrum to be achieved. In this case, where phase shifters are being employed to introduce the linear phase gradient, the size and direction of the phase shift is simple to control. The implementation of these different modes of phase shift can be achieved using the same phase shifters as in the one-dimensional system. Figure 7.1 shows how the phase shifters can be used to implement the three different separation modes.

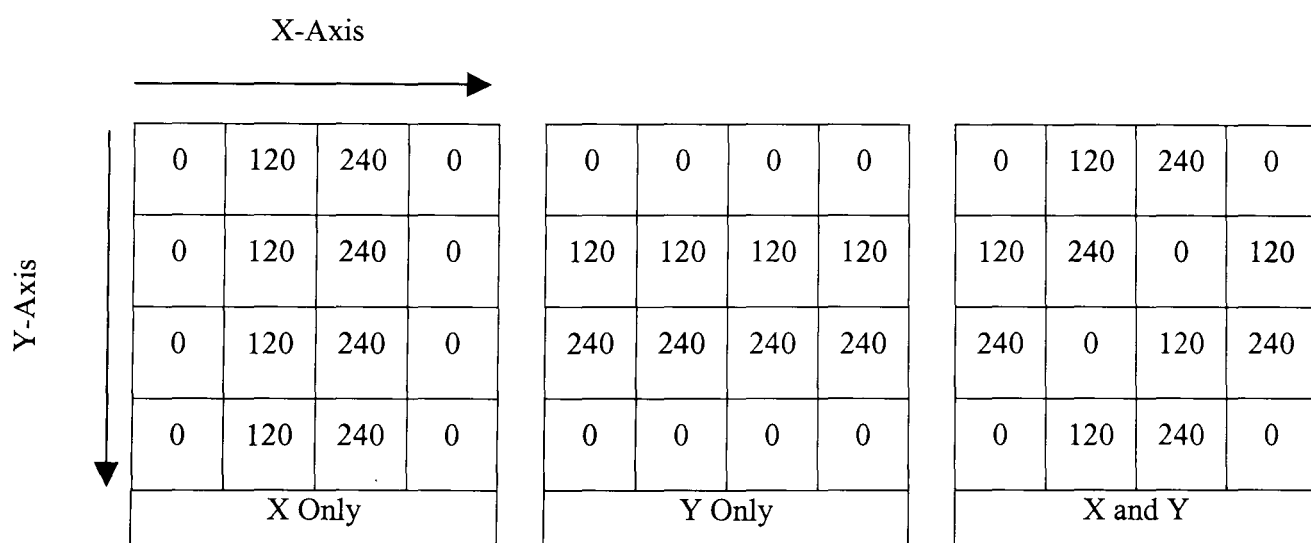


Figure 7.1 Implementation Of The Three Possible Phase Gradients using  $120^\circ$

Huang [37] used a radiated Off-Axis beam to implement a two-dimensional phase gradient at THz frequencies. At these frequencies radiating elements can produce near plane wave conditions over relatively short distances, due to the shorter wavelength in comparison to GHz. As discussed for one-dimension, using a radiating element to generate the desired Off-Axis plane reference wave over the measurement plane is difficult if not impossible. This problem is compounded further for two-dimensional measurement.

This novel system offers a simple solution for the control of the reference beam magnitude and phase allowing any plane wave to be produced and requires only a calibration of the phase sifters. A two-dimensional simulation of the process will now be used to verify its validity in two dimensions.

### 7.3 Two-Dimensional Off-Axis Hologram Simulation

Two-dimensional simulations have been generated using the theory developed in Chapters 4 and 5; due to its relative simplicity, a rectangular aperture is used; the size is chosen to be  $32\lambda \times 32\lambda$  at 10 GHz. The distribution is defined as uniform in the E-Plane and cosine in the H-Plane ( $TE_{10}$  mode) with a resolution of 0.001 m, using (7.1) and is shown in Figure 7.2, [2]

$$Ea(xa, ya) = E \cos\left(\pi \cdot \frac{xa}{Xa}\right), \quad (7.1)$$

where  $E$  is the maximum field magnitude (equal to 1), and  $Xa$  is the aperture length.

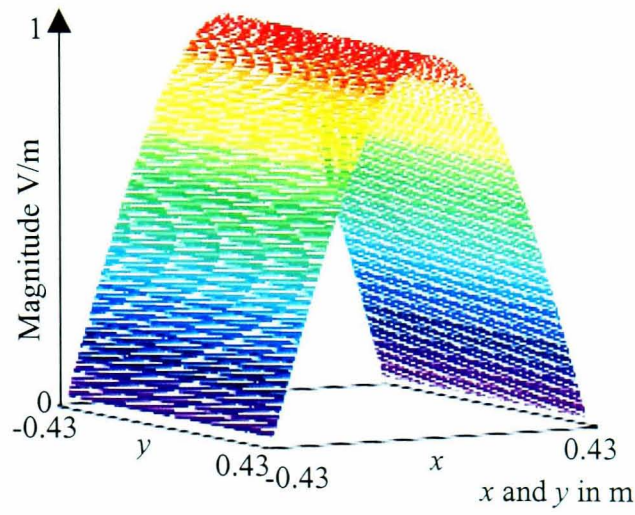


**Figure 7.2 Two-Dimensional Aperture Distribution Mode  $TE_{10}$**

The Near-Field plane generated by this radiating aperture distribution is calculated by performing the vector summation of each element on the aperture transposed through its distance to a point located on a regular rectangular grid located at a given distance (Huygens principal). The two-dimensional expression utilised is given in (7.2), [58].

$$E(x_{s_s}, y_{s_t}) = \sum_{a=0}^{N_{XA}} \sum_{b=0}^{N_{YA}} \left( \frac{Ea(xa_a, ya_b)}{\sqrt{Z_0^2 + (xs_s - xa_a)^2 + (ys_t - ya_b)^2}} e^{-j \cdot k_0 \cdot \sqrt{Z_0^2 + (xs_s - xa_a)^2 + (ys_t - ya_b)^2}} \right) \quad (7.2)$$

where  $Ea(xa_a, ya_b)$  is the field distribution of the antenna aperture,  $xa$  and  $ya$  are the aperture lengths in  $x$  and  $y$  centred at zero,  $N_{XA}$  and  $N_{YA}$  the number of samples in the aperture.

The Near-Field plane is set at a distance of  $5\lambda$  ( $\approx 0.15$  m) and the sampling plane length is chosen as approximately 2 m providing a valid angle of  $\gg 7^\circ$ , which was shown in Chapter 3 to contain the SNBW for this size aperture. The sample spacing defined over the Near-Field plane is  $\lambda/2$  ( $\approx 0.015$  m). The two-dimensional Near-Field magnitude obtained by applying the aperture distribution of Figure 7.2 to (7.2) is shown below in Figure 7.3.

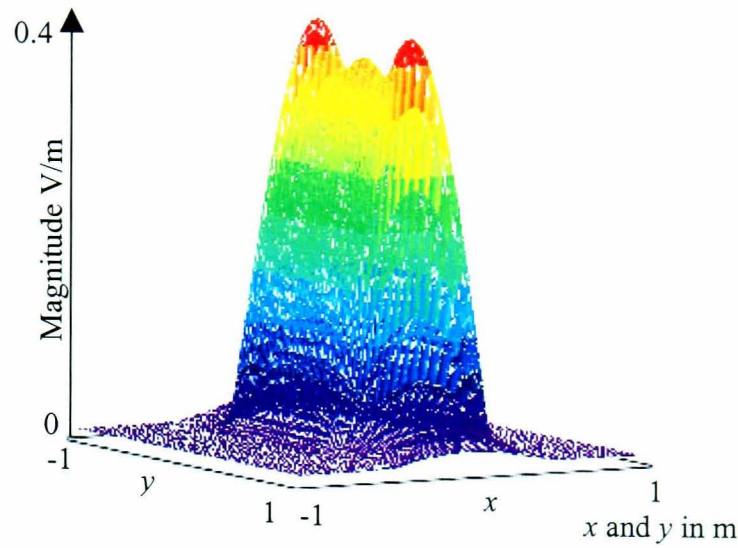


**Figure 7.3 Two-Dimensional Near-Field Distribution At  $Z_0=5\lambda$  For A  $32\lambda \times 32\lambda$  Rectangular Aperture With Mode  $TE_{10}$**

The reference wave required to form the intensity must be defined over the same Near-Field plane, [63]:

$$ER_{x_s, y_s} = R \cdot e^{j \cdot k_0 \cdot \left( \left( \Delta x \cdot \left( x_s - \frac{SX}{2} \right) \cdot \sin(\theta_{XR}) \right) + \left( \Delta y \cdot \left( y_s - \frac{SY}{2} \right) \cdot \sin(\theta_{YR}) \right) \right)}, \quad (7.3)$$

where  $\theta_{XR}$  and  $\theta_{YR}$  are the effective reference beam angles in each of the  $x$  and  $y$  axes and  $R$  is the magnitude set equal to the central Near-Field value.

By assigning one or both  $\theta_{XR}$  and  $\theta_{YR} = 41.81^\circ$ , equivalent to phase increments of  $120^\circ$  when the sample spacing is  $\lambda/2$  in  $x$ - $y$  ( $\theta_{XI}$  and  $\theta_{YI}$ ), the three patterns of Figure 7.1 can be generated. For the purpose of this simulation a phase shift in the  $x$ -axis only will be fully demonstrated, however all three possible intensity spectrums will be shown for clarification of the phase shift effect. The two-dimensional intensity pattern generated using (5.6) between (7.2) and (7.3) is shown in Figure 7.4 along with two one-dimensional cuts through the principal  $x$  and  $y$  planes.

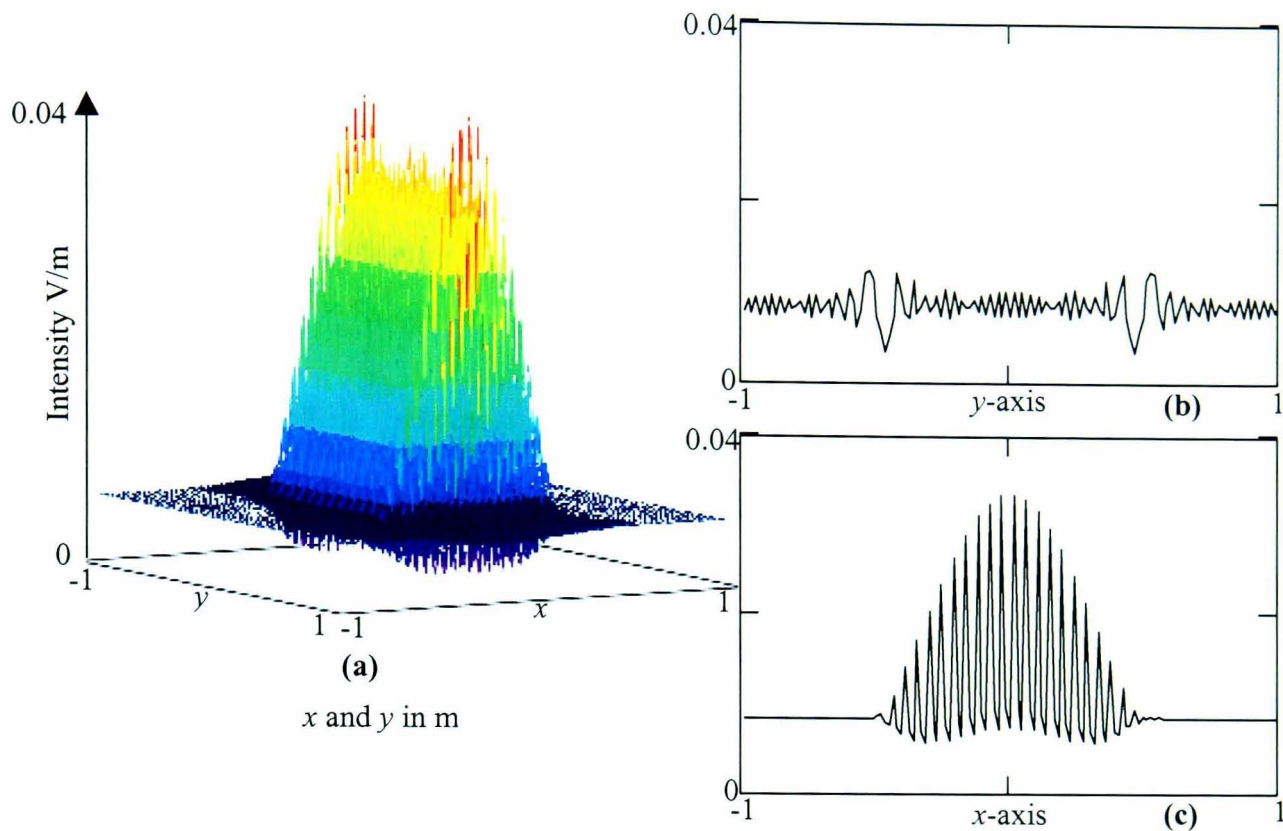


**Figure 7.4 Simulated Intensity Pattern Between The Near-Field Of Figure 7.3 And A Reference Wave With  $120^\circ$  Phase Gradient In The  $x$ -axis (a) Two-Dimensional plot, (b) Cut Through Centre Of The  $y$ -axis And (c) Cut Through Centre Of The  $x$ -axis**

Figure 7.4 shows a greater variation of intensity in the  $x$ -axis due to the  $120^\circ$  phase change per sample of the reference. Towards the edges of the pattern it is seen that in the  $x$ -axis the intensity has reduced to a constant level (i.e. the reference magnitude), and in the  $y$ -axis the intensity is still converging towards the reference magnitude.

Prior to the FT, the DC component is subtracted from each intensity value and the pattern is zero buffered in both directions to provide interpolation. The Intensity pattern spectrum is shown in Figure 7.5

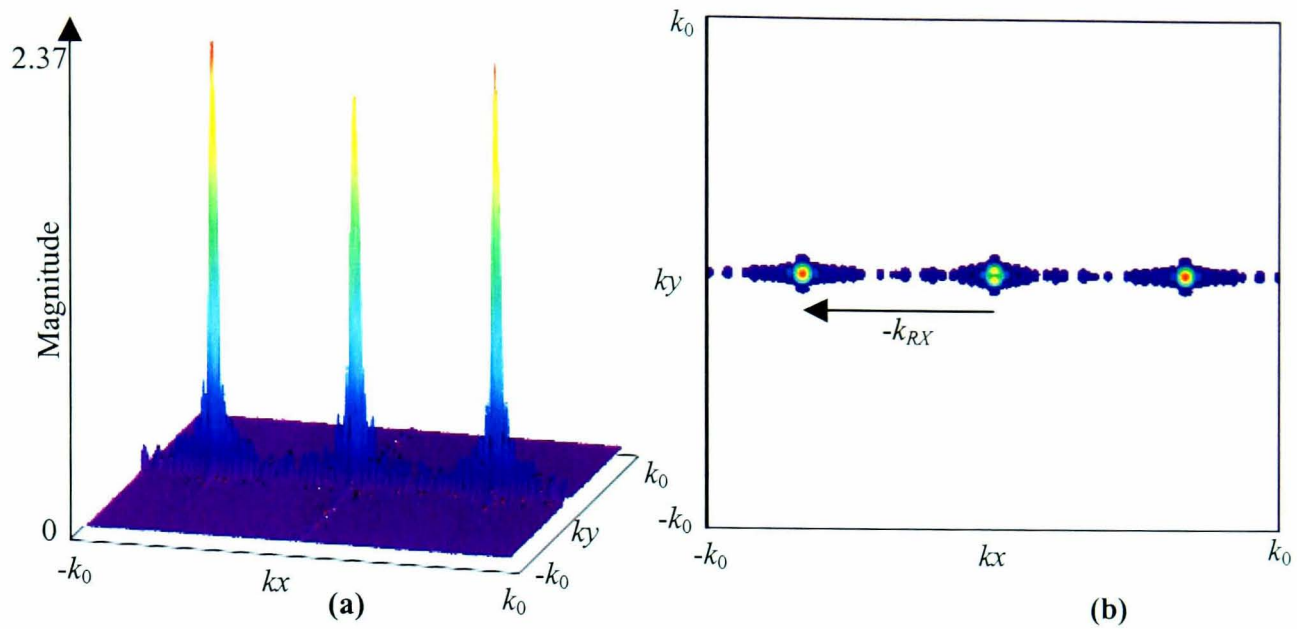


**Figure 7.5 Two-Dimensional Intensity Pattern Spectral Distribution With Phase Shift In  $x$ -axis Only (a) Surface Plot And (b) Contour Plot**

As expected the components in the spectrum are separated in the  $k_x$  plane by the value  $k_{XR}$  due to the phase shift being implemented in the  $x$ -axis only. The two spectrums obtained by applying the phase shift in the  $y$ -axis only and then in the  $x$  and  $y$  axes are shown in Figure 7.6. They exhibit the same component shifts as described in 6.6.2.

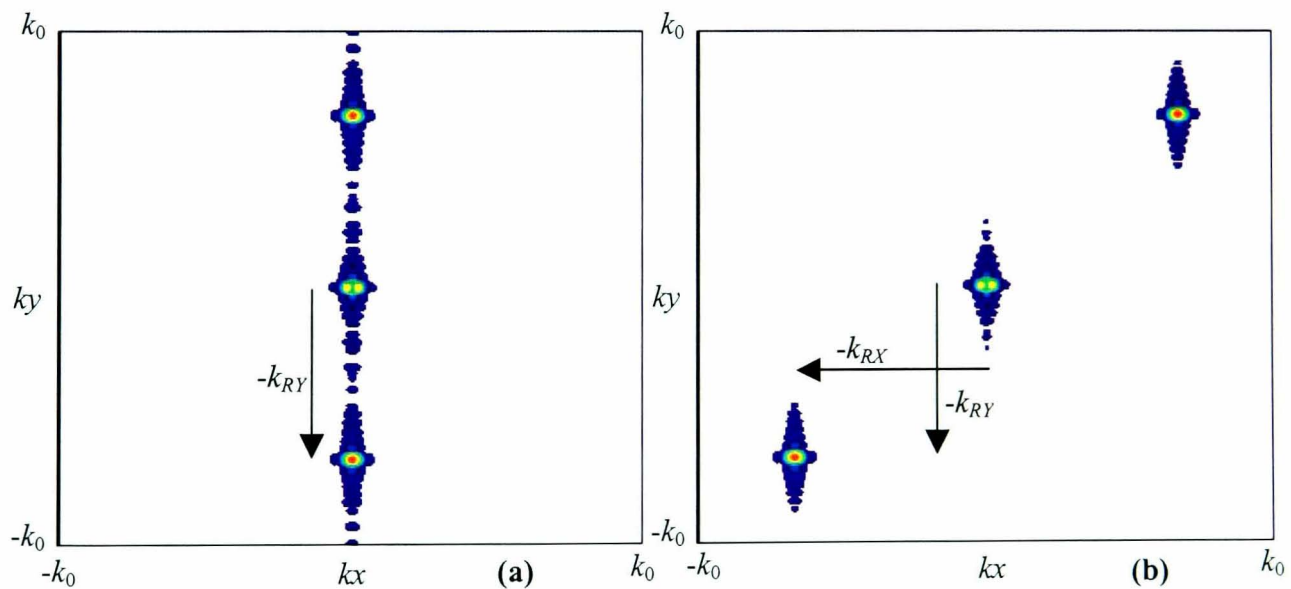


**Figure 7.6 Two Dimensional Intensity Pattern Spectral Distributions With (a)  $y$  Only And (b)  $x$  And  $y$  Phase Shifts**

As the phase increment used is positive, then the AUT PWS is located at  $-k_{XR}$ , this is filtered out from the intensity pattern spectrum with the limit of the filter window set

to encompass  $20^\circ$  in the H-Plane (direction of reference phase shift) and  $30^\circ$  in the E-Plane, the Far-Field is found using (3.5) as shown in Figure 7.7.

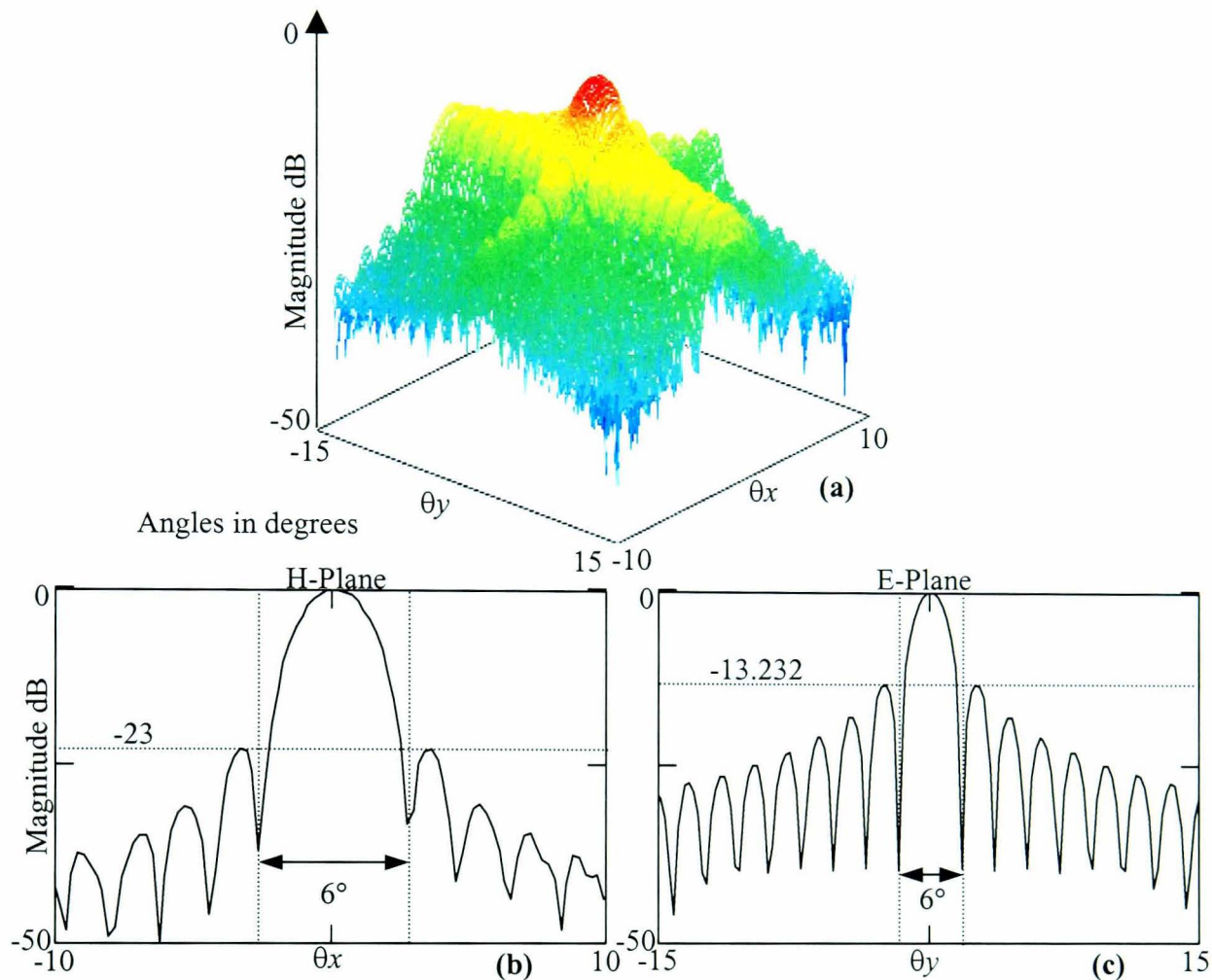


**Figure 7.7 Far-Field For A  $32\lambda \times 32\lambda$  Aperture With  $TE_{10}$  Mode Distribution Simulated Using Indirect Holography (a) Two-Dimensional Plot, (b) Principal H-Plane Cut And (c) Principal E-Plane Cut**

These Far-Field distributions can be compared with theoretical values obtained by application of standard theory for a rectangular aperture based on a  $TE_{10}$  mode distribution on a ground plane. The null beamwidth's and lobe sizes of the Far-Field produced by the rectangular aperture and predicted by theory are shown in Table 7.1. The comparison provides verification of the technique used to obtain the Far-Field pattern, the variation in beamwidth being down to hundredths of a degree and side lobe level down to 0.2 dB.

	Theoretical Rectangular Aperture On A Ground Plane		Simulated Indirect Holography	
	E-Plane	H-Plane	E-Plane	H-Plane
FNBW (degrees)	3.582	5.373	3.582	5.373
First Side lobe Max (to main) (dB)	-13.26	-23	-13.313	-22.593
SNBW (degrees)	7.167	8.962	7.167	8.962
Second Side lobe Max (to main) (dB)	-17.83	-30.671	-17.961	-30.877

**Table 7.1 Comparison Of Theoretical And Simulated Beam Properties For A  $32\lambda \times 32\lambda$  Aperture With  $TE_{10}$  Distribution**

It has been shown through simulation that the Far-Field radiation pattern of a radiating rectangular aperture can be obtained using the process in two-dimensions. The process will now be applied in practice; the parabolic dish antenna used in Chapter 5 must be used as the test subject as the same spectral restrictions apply and therefore it is the only antenna available that can provide a separable PWS in the intensity spectrum.

## 7.4 Two-Dimensional Measurements

In the Far-Field three measurement techniques will be used to provide comparisons: direct Far-Field measurements, complex Near-Field measurements (direct holography) and the novel indirect holographic technique being proposed in this thesis. The complex fields can only be compared for the direct and indirect holographic data being collected.

The direct Far-Field measurements of the two principal planes have been obtained from the antenna manufacturer (Andrews Corp.). The direct/indirect holographic

measurements have been carried out as in Chapter 6, however due to the large data sets required when measuring in two dimensions, an automated two-dimensional indirect holographic measurement system has been constructed with a scan range of 0.4x0.4 m. Stepper motors are used to achieve probe movement and are controlled via a computer; the computer is also connected to a power meter via an *IEEE-488* (General Purpose Interface Bus (GPIB) data link, which allows the intensity at each measurement point to be recorded automatically. Manual control of the phase shifters is required with the settings as per Table 6.3. The data collection methodology remains the same as in the one-dimensional system, whereby all intensities formed using the same reference phase shift are collected consecutively. A photograph of the two-dimensional positioning system is shown in Figure 7.8.

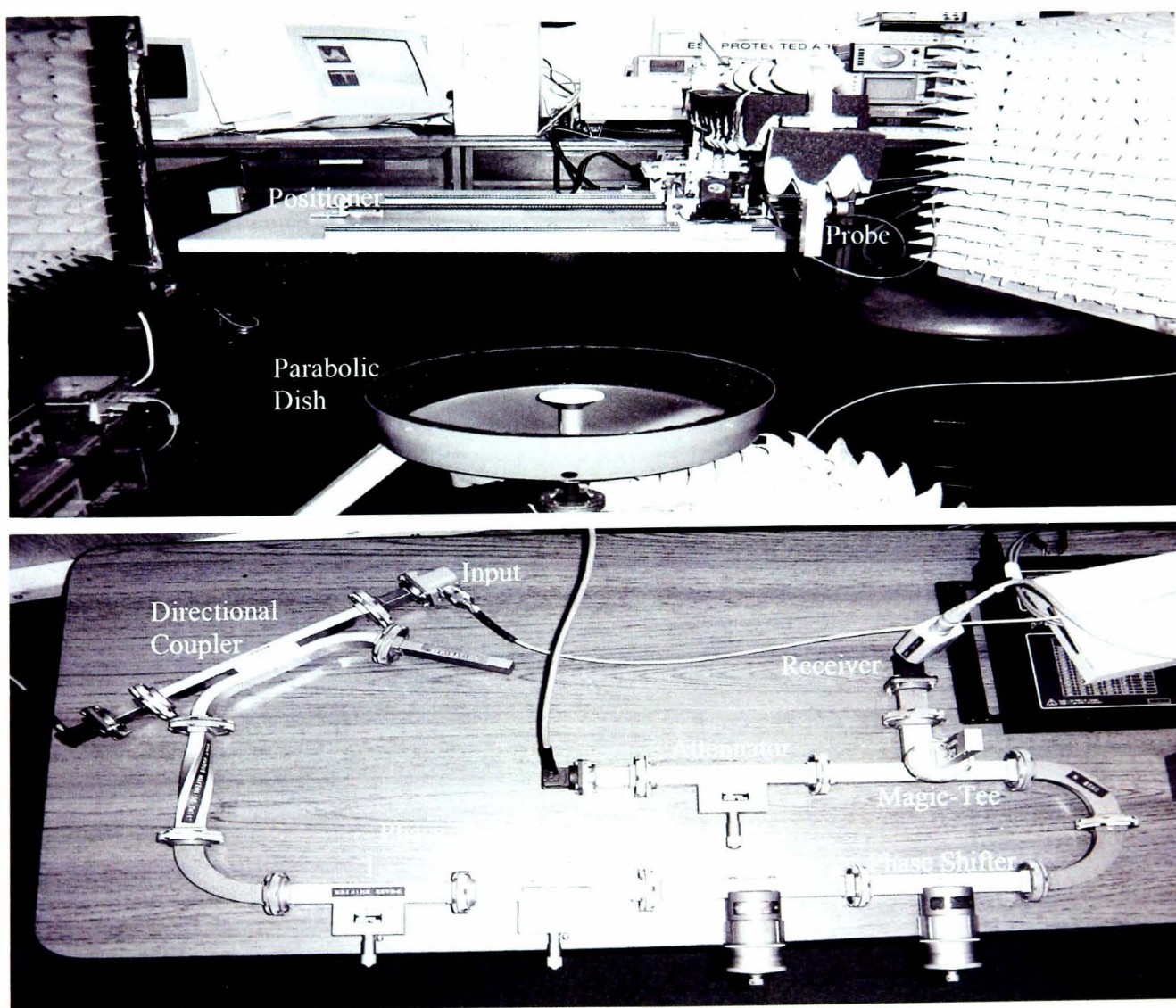
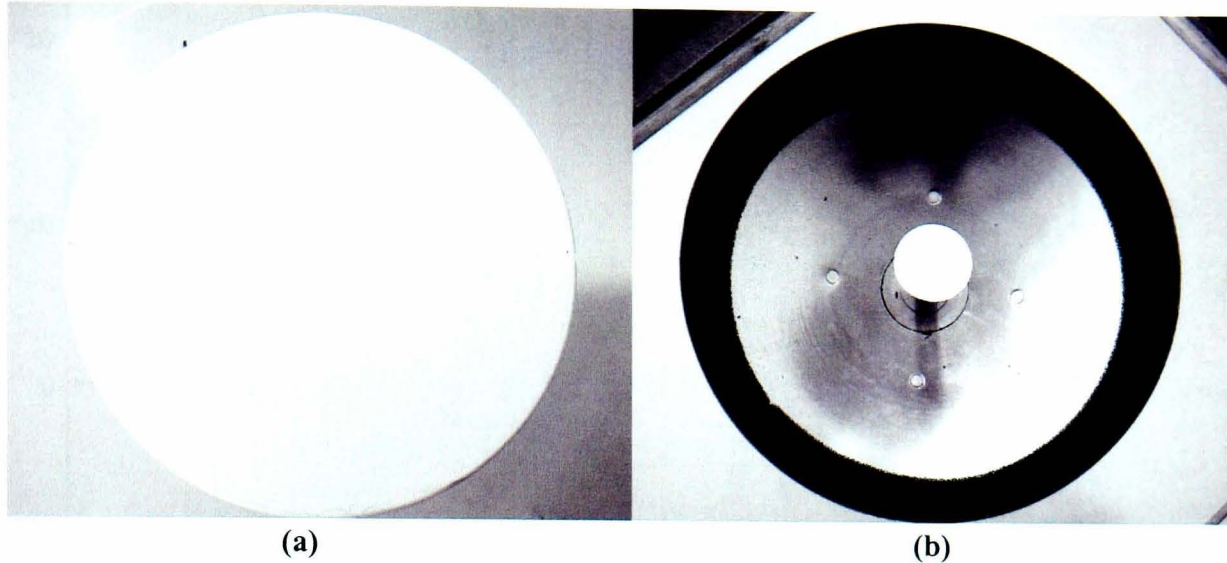


Figure 7.8 Photograph Of Two-Dimensional Positioning System

A photograph of the parabolic dish aperture with and without the radome cover is provided in Figure 7.9, to show the splash plate feed in the centre of the dish.



**Figure 7.9 Photographs Of Parabolic Dish Aperture (a) With And (b) Without Its Radome Cover**

The results of all three measurement techniques will first be presented followed by a comparison of the relevant fields obtained in each one.

#### **7.4.1 Direct Far-Field measurements**

Direct Far-Field measurements have been obtained from the antenna manufacturers Far-Field test range. The two principal planes of the parabolic dish are shown in Figure 7.10, for an operating frequency of 12.7 GHz. The figure shows that the antenna Far-Field pattern is symmetrical about boresight. The values for the main antenna properties such as FNBW and SNBW are provided in Table 6.1. The E-Plane is seen to roll off more rapidly with less prominent nulls than in the H-Plane signifying that the field across the aperture tapers more and has a greater phase shift in the E-Plane.

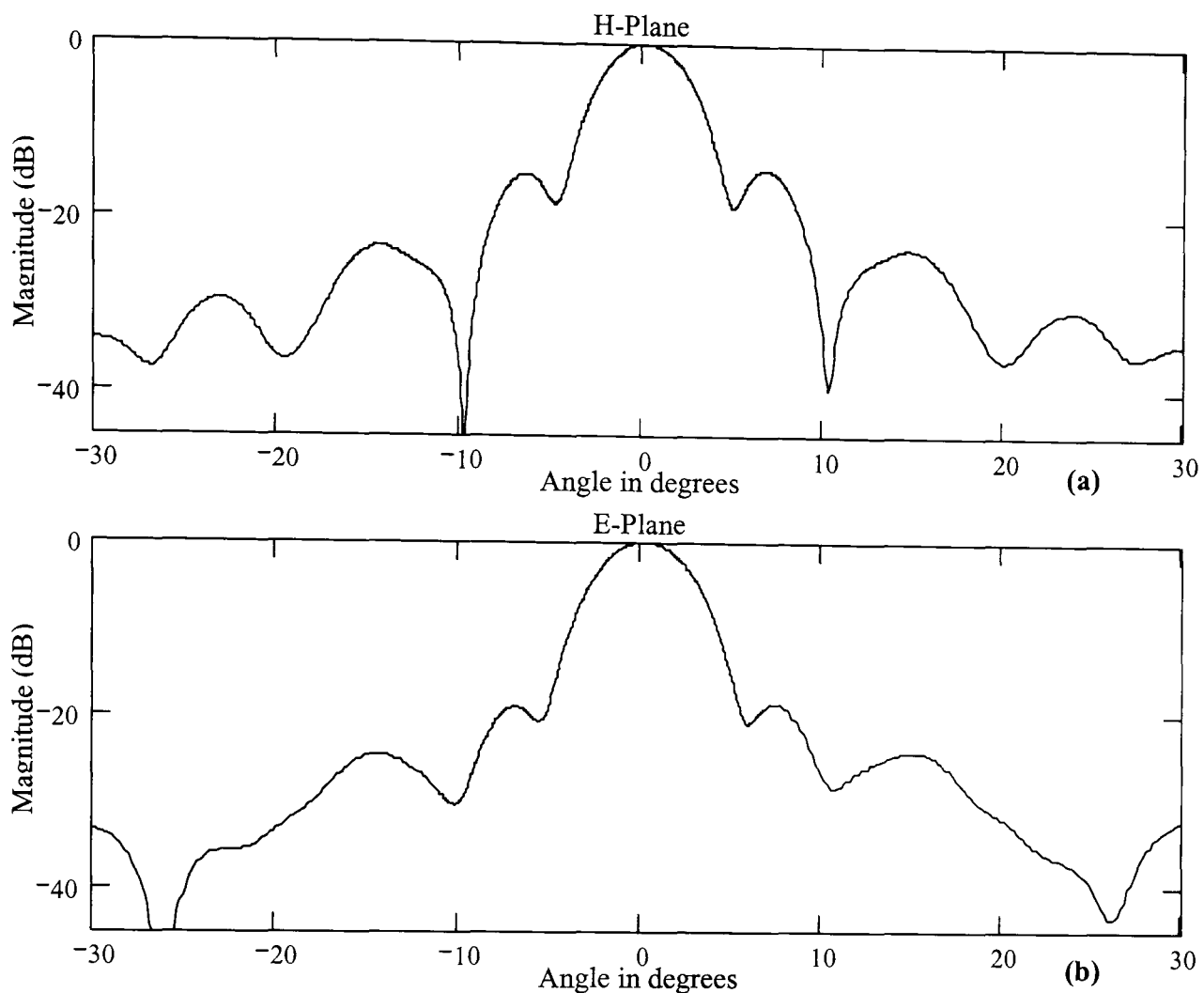


**Figure 7.10 Far-Field Measurement Of The Parabolic Dish (a) The Principal H-Plane And (b) The Principal E-Plane At 12.7 GHz By Andrews Corp.**

#### 7.4.2 Indirect holography – two-dimensions

The parameters used to perform this measurement are the same as in the one-dimensional case, given in Table 6.2, the parameters for the  $y$ -axis replicate those in the  $x$ -dimension. The same methodology is applied to data collection as mentioned previously. The raster scan motion is set to follow the direction of the reference phase shift (in this case the  $x$ -axis) stepping across the direction without a phase shift (in this case the  $y$ -axis) at either end of the scan. This means that the probe, for the most part, moves through a distance of three times the step size ( $3\Delta x$ ) for each sample in the traverse, but in single steps ( $\Delta y$ ) at the end of each traverse.

Using the parameters of Table 6.2, the amount of data required to be collected in a two-dimensional scan at a sample spacing of 0.01 m is 1681 measurements, where 0.01 m is approximately half wavelength sampling (at 12.7 GHz). This is the same minimum number that would be required for any planar Near-Field sampling technique. Three sets of intensity data have been collected consecutively to ensure repeatability as discussed later.

A two-dimensional intensity pattern shown in Figure 7.11 was recorded as a result of the application of the parameters previously stated. The system initial conditions were set-up as in Chapter 6, with the reference wave set equal to the central Near-Field magnitude and out of phase, creating a null. The Antenna is orientated so that the E-Plane lies in the  $x$ -axis and the H-Plane lies in the  $y$ -axis.

The outline of the circular aperture is depicted in the interference pattern as of a set of lines with alternating high and low intensities in the  $x$ -axis. The pattern is formed as sets of lines as the reference component is changing phase linearly across the antenna Near-Field whose phase changes slowly in comparison. The one-dimensional plots show that the interference does not converge to a constant level at the edges of the scanning window signifying a portion of the energy radiated by the AUT exists outside of this region.

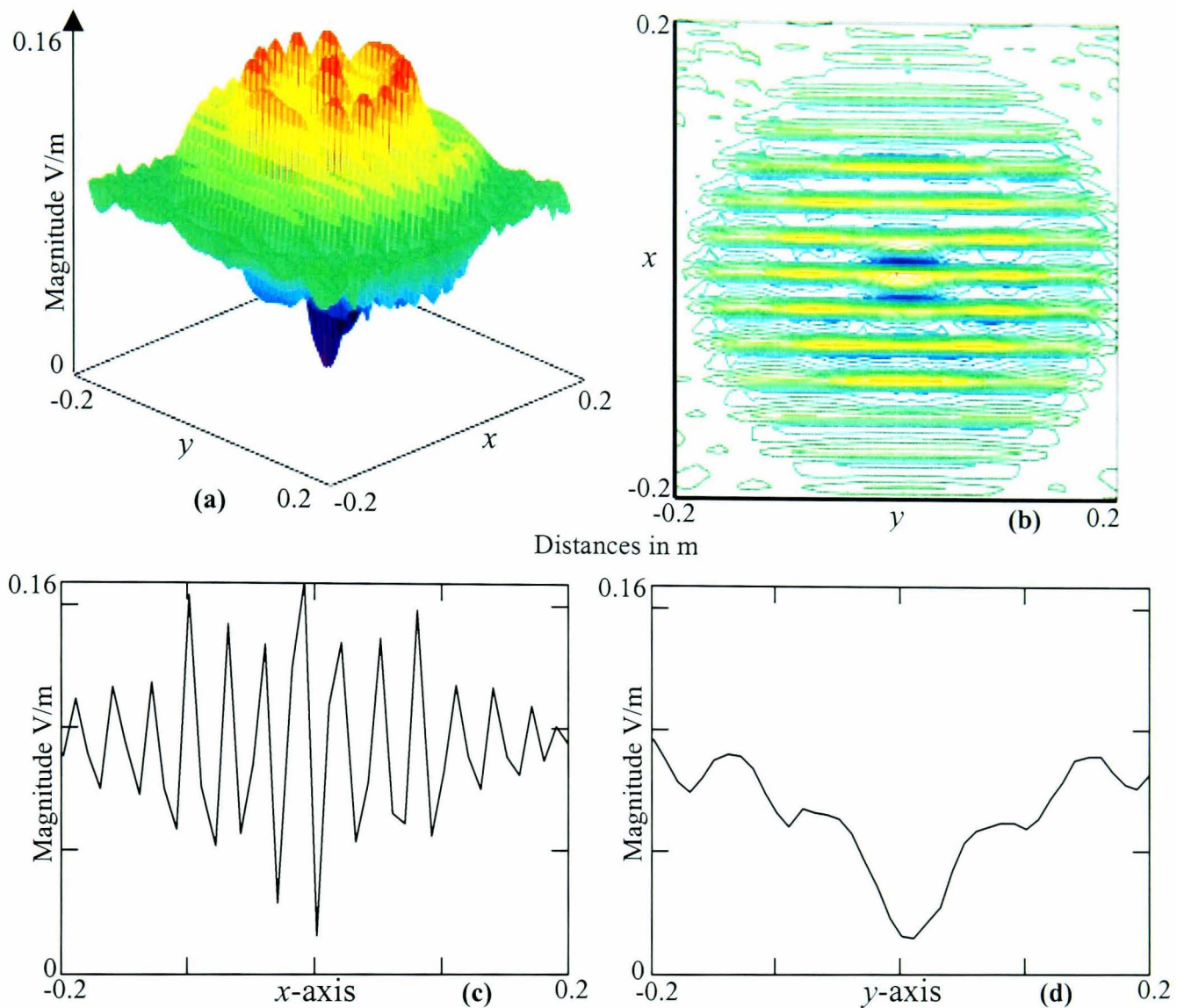


**Figure 7.11 Measured Two-Dimensional Intensity Pattern For Parabolic Dish With  $\Delta x=\lambda/2$ ,  $\Delta y=\lambda/2$  and  $\theta_{xI}=120^\circ$  (a) Surface Plot Of Measured Data, (b) Contour Plot Of Measured Data, (c) Cut Through Centre Of The x-Axis And (d) Cut Through Centre Of The y-axis**

The measured intensity data is processed in the same way as defined in the two-dimensional simulation. After converting from dB to V/m the average intensity over the data set is subtracted from each data point and then the pattern is zero buffered in both dimensions ( $x, y$ ) prior to the FT to provide interpolation in the spectral domain. The resultant intensity spectrum is shown in Figure 7.12.

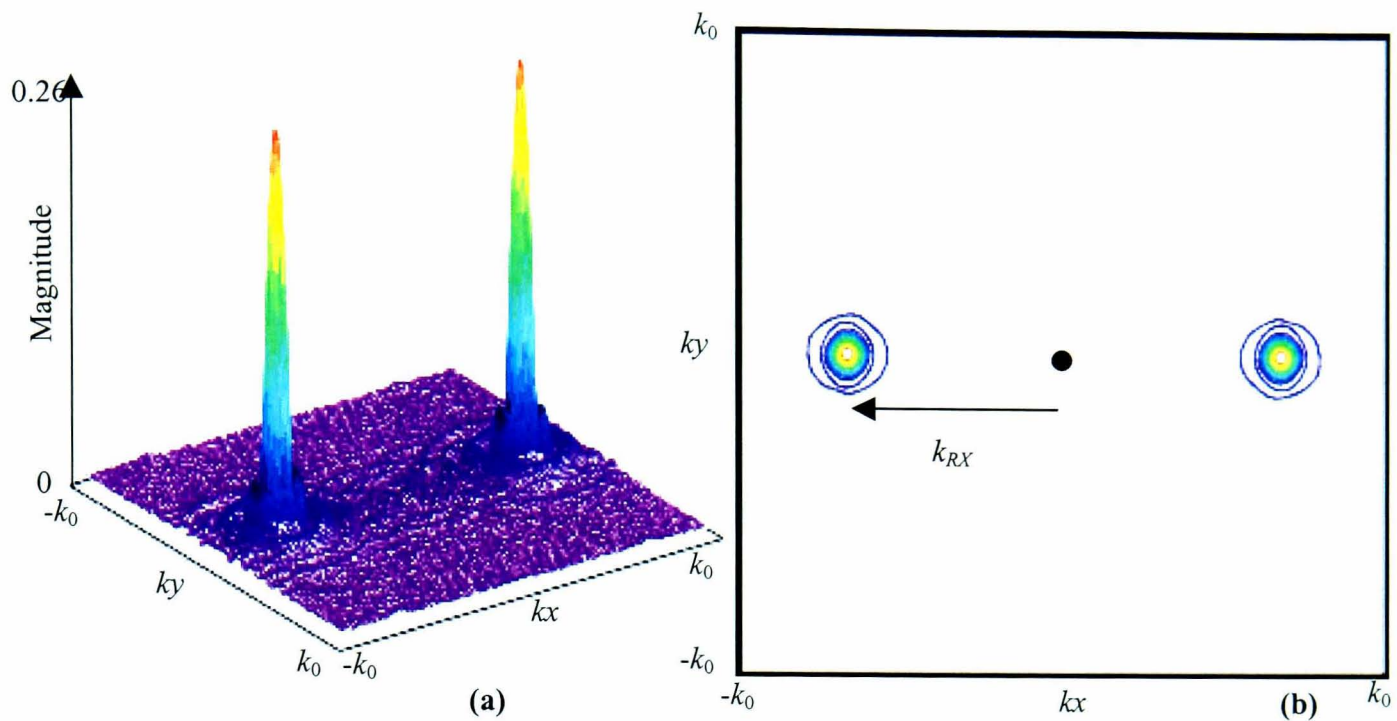


**Figure 7.12 Measured Two-Dimensional Intensity Pattern Spectral Distribution  
(a) Surface Plot And (b) Contour Plot**

Of the three regions known to exist in the spectrum, the two object components offset at  $\pm k_{XR}$  can be clearly seen while the third central component made up of the two auto-correlation terms is less distinct. This is due to the suppression of the DC component via subtraction of the average intensity from each data point. The central point in the contour plot has been highlighted.

The positive phase increment shifts the real AUT PWS to the negative side of the spectrum. The limits of the spatial filter used to extract the component are set at the valid angle of the AUT PWS with its centre located at  $-k_{XR}$ . The Far-Field is found by application of (3.5), this is shown in Figure 7.13 as both a two-dimensional surface plot and two cuts through the principal E and H planes.

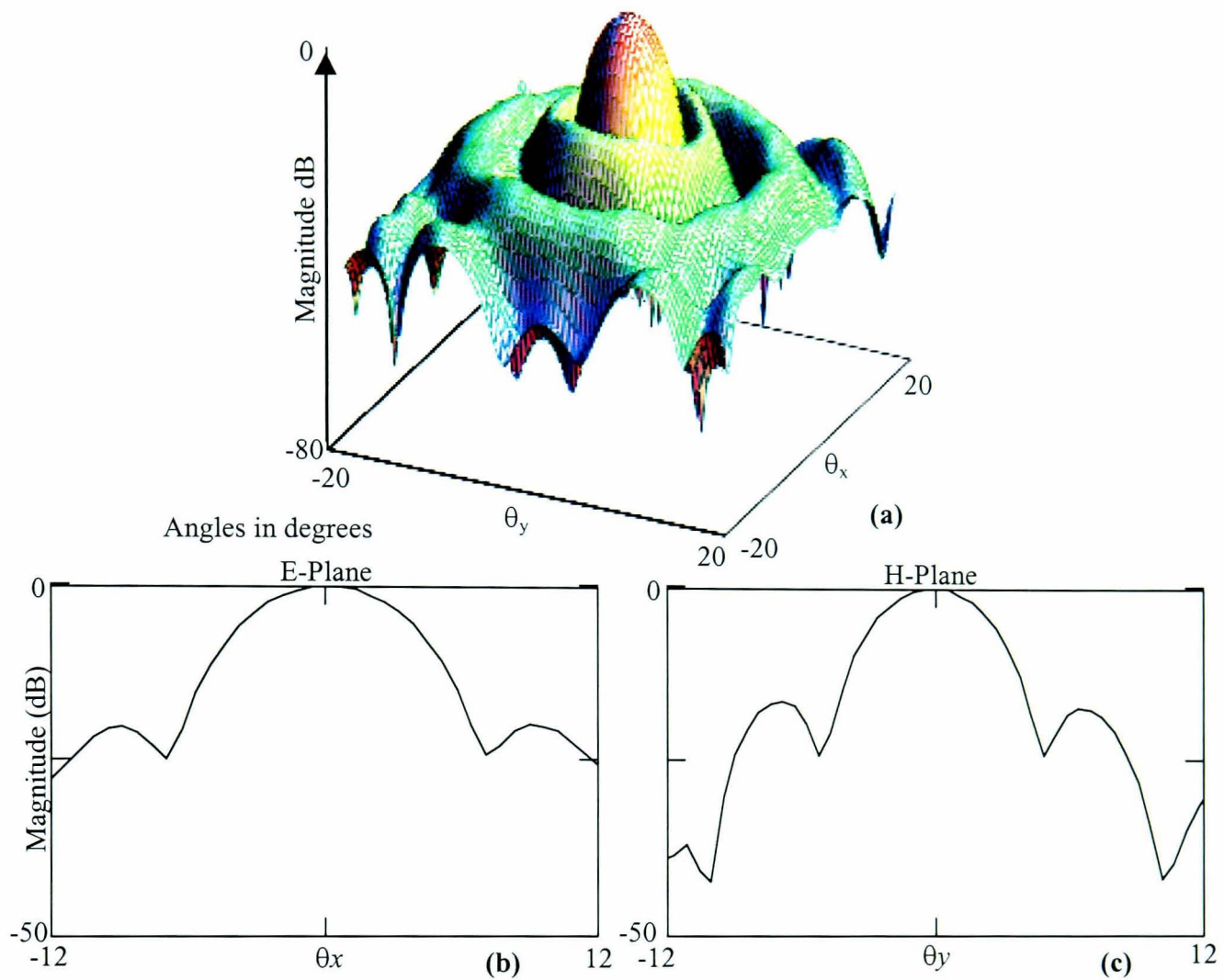


**Figure 7.13 Far-Field Radiation Pattern From Intensity Only Measurements**  
**(a) Two-Dimensional Surface Plot, (b) Principal E-Plane Cut And (c) Principal H-Plane Cut**

To obtain the complex Near-Field over the sampling plane the IFT is performed on the AUT PWS filtered from the intensity spectrum. Prior to the back propagation of the AUT PWS is zero buffered to be the same width as the original intensity spectrum, in order to achieve consistency in the image size and resolution between the spatial and spectral dimensions. The Near-Field obtained here will be compared with directly measured magnitude and phase and then as in the one-dimensional case the beam-limited form of the measured complex Near-Field, which is expected to provide a closer comparison.

The indirectly obtained magnitude and phase is shown in Figure 7.14. The magnitude of the Near Field drops to around  $-30$  dB from the maximum at the edges of the

scanning plane and the phase variation over the plane can be considered as nominal over the area directly above the AUT ( $\approx 10^\circ$ ), though outside of this the phase begins to vary rapidly. It is notable that the field in the  $x$ -axis is more uniform than the  $y$ -axis agreeing with the observation made earlier regarding the side lobe level and null prominence of the measured Far-Field principal planes.

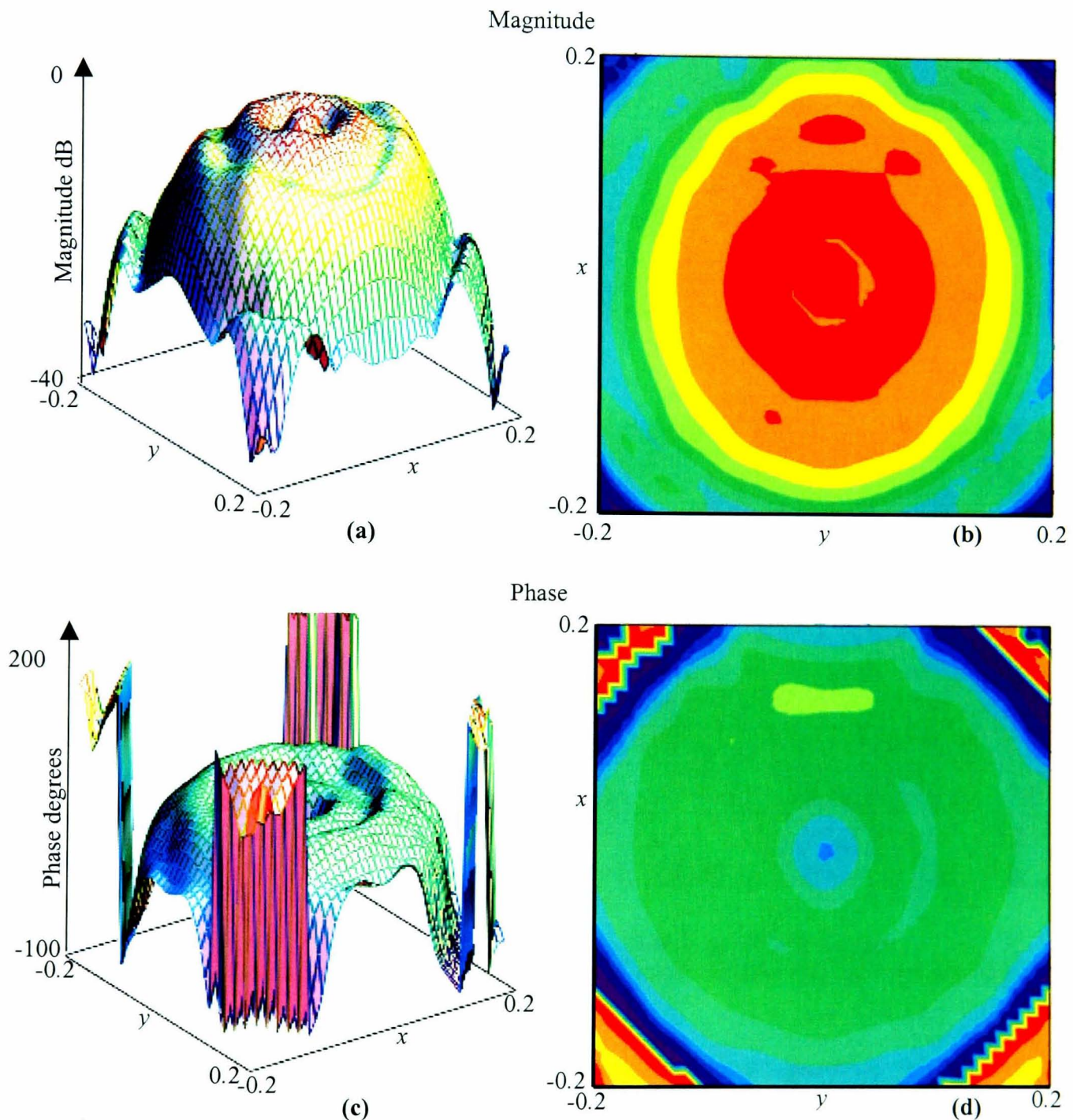


**Figure 7.14 Indirectly Measured Near-Field Magnitude (a) Surface Plot, (b) Contour Plot And Near-Field Phase (c) Surface Plot, (d) Contour Plot**

The field across the aperture of the antenna has also been evaluated by applying (3.18) to the AUT PWS extracted from the intensity spectrum. Again the AUT PWS is zero

buffered to the original width of the intensity spectrum prior to the transform to maintain resolution. The result of aperture imaging is shown below in Figure 7.15.

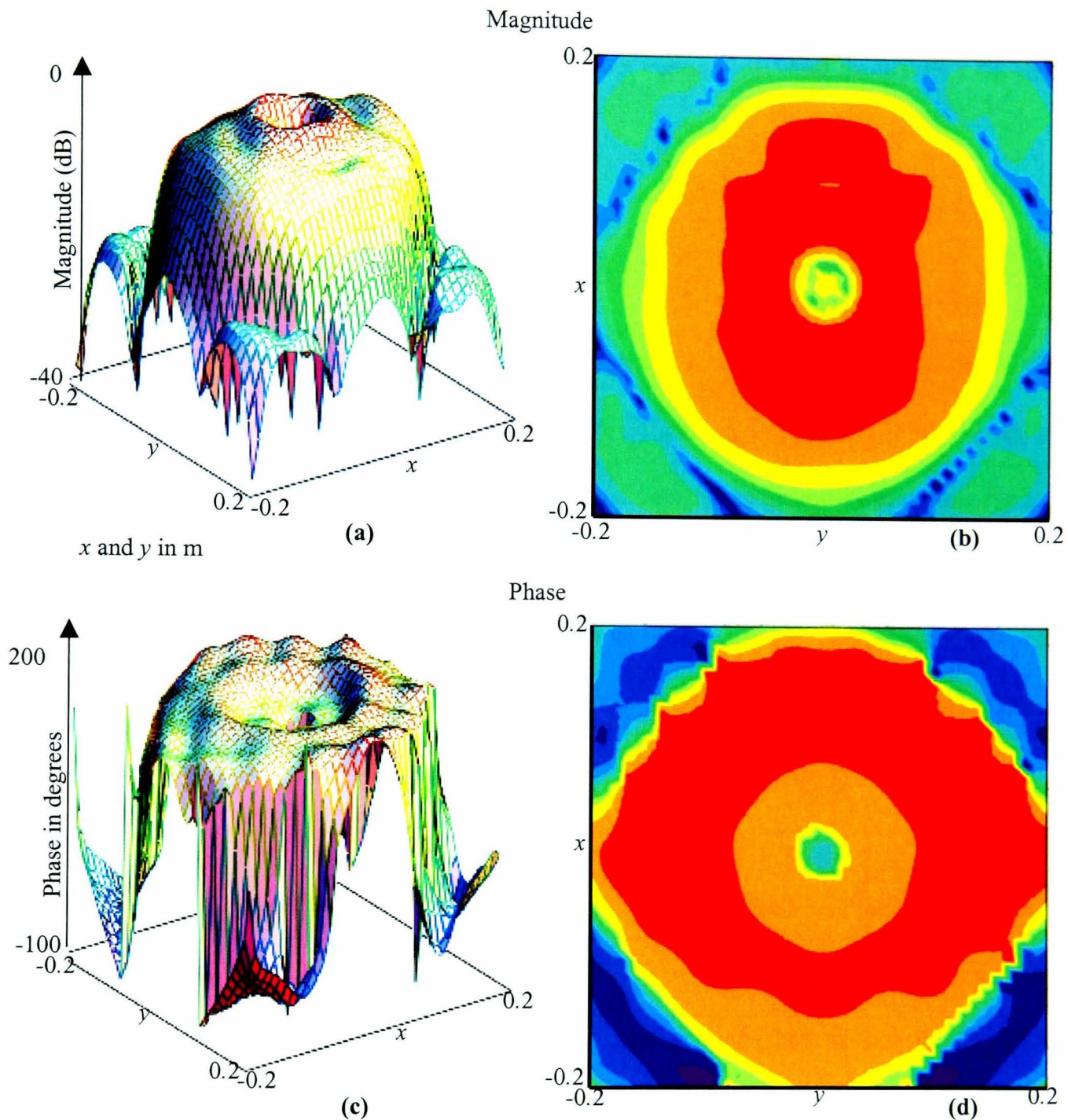


**Figure 7.15 Aperture Distribution From Indirectly Measurements**  
**Magnitude (a) Surface Plot (b) Contour Plot And Phase (c) Surface Plot (d) Contour Plot**

The field predicted across the aperture reiterates the points regarding the calculated complex Near-Field plane. The field is more tapered in the  $y$ -axis (E-Plane), which leads to the wider beamwidth and smaller sidelobes and nulls. The splash plate field located at the centre of the parabolic dish (as seen in the photograph in Figure 7.9) is clearly visible causing a blockage in the field, which leads to a fall in the magnitude

and a difference in phase distribution. It is an interesting result showing that the location of the splash plate can be seen, even through the radome covering the antenna. This result was presented by Smith and Leach et. al. in [68], a paper regarding hidden object detection. More results have also been presented for this measurement system in [83].

### **7.4.3 Direct holography – two-dimensions**

To perform complex Near-Field measurements port 1 of the VNA is connected to the AUT and port 2 to the probe. The VNA is fully calibrated for 12.7 GHz operating in CW mode. No data link is available for the VNA and as such the measurements are recorded by hand by reading the front panel, for this reason the data is collected only once. The same two-dimensional scanning system is used to move the probe over an identical scanning aperture using the same sample spacing. The magnitude and phase of the measured Near-Field are shown in Figure 7.16.

The magnitude plots show that the energy drops to  $-20$  dB from the maximum within the scanning aperture this signifies that a large portion of the radiated energy lies within the scanning aperture. The measurements appear symmetrical about each of the principal planes in both phase and magnitude. As predicted previously the magnitude is shown to taper more in the  $y$ -axis than in the  $x$ -axis.

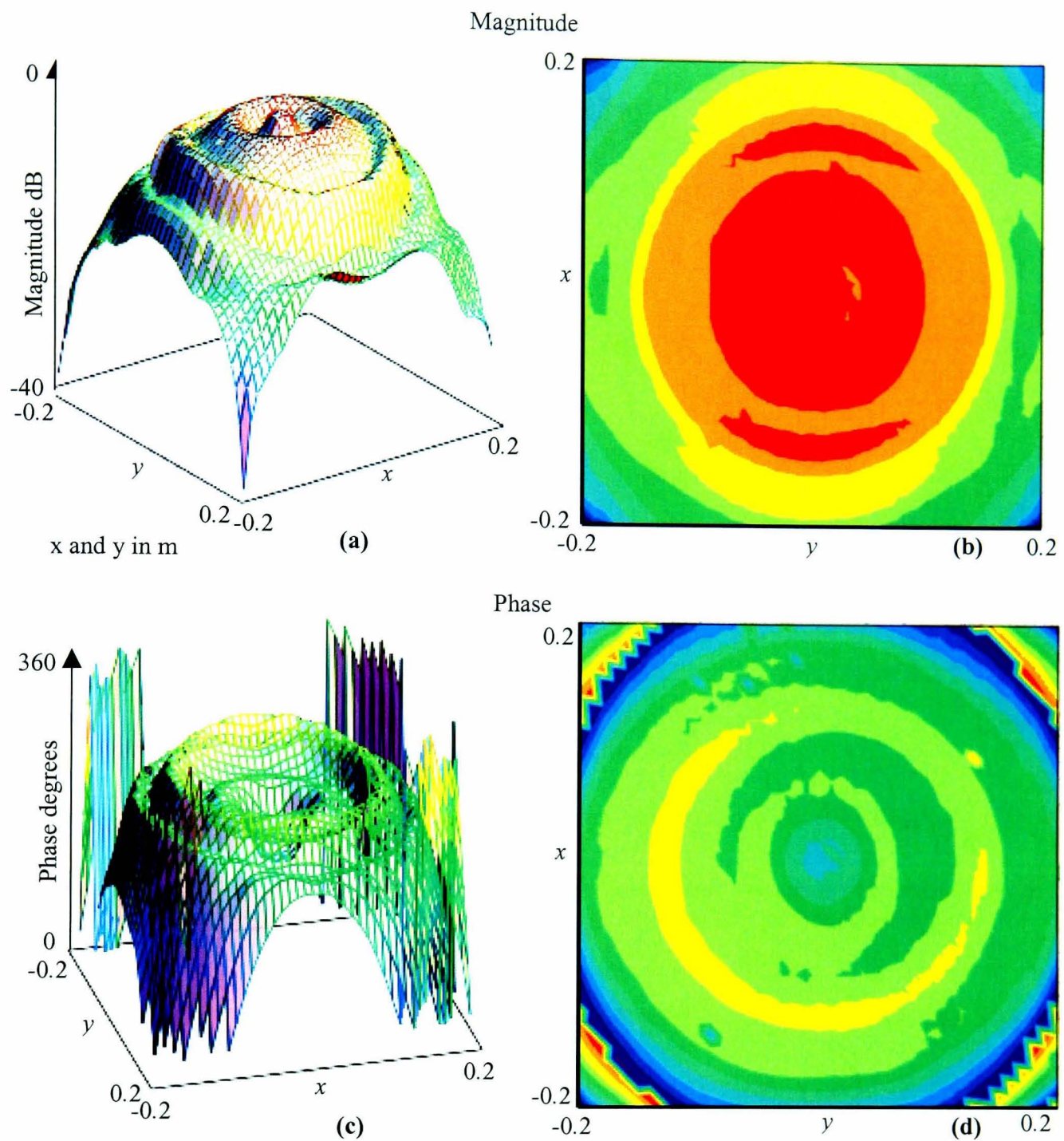


**Figure 7.16 Measured Near-Field Magnitude (a) Surface Plot (b) Contour Plot And Phase (c) Surface Plot (d) Contour Plot**

Using the Near-Field to Far-Field transform (3.16) and (3.5), this complex data is able to yield the antenna Far-Field radiation pattern. Prior to the transform the data has been zero buffered to the same width as the intensity data was in the indirect holographic method.

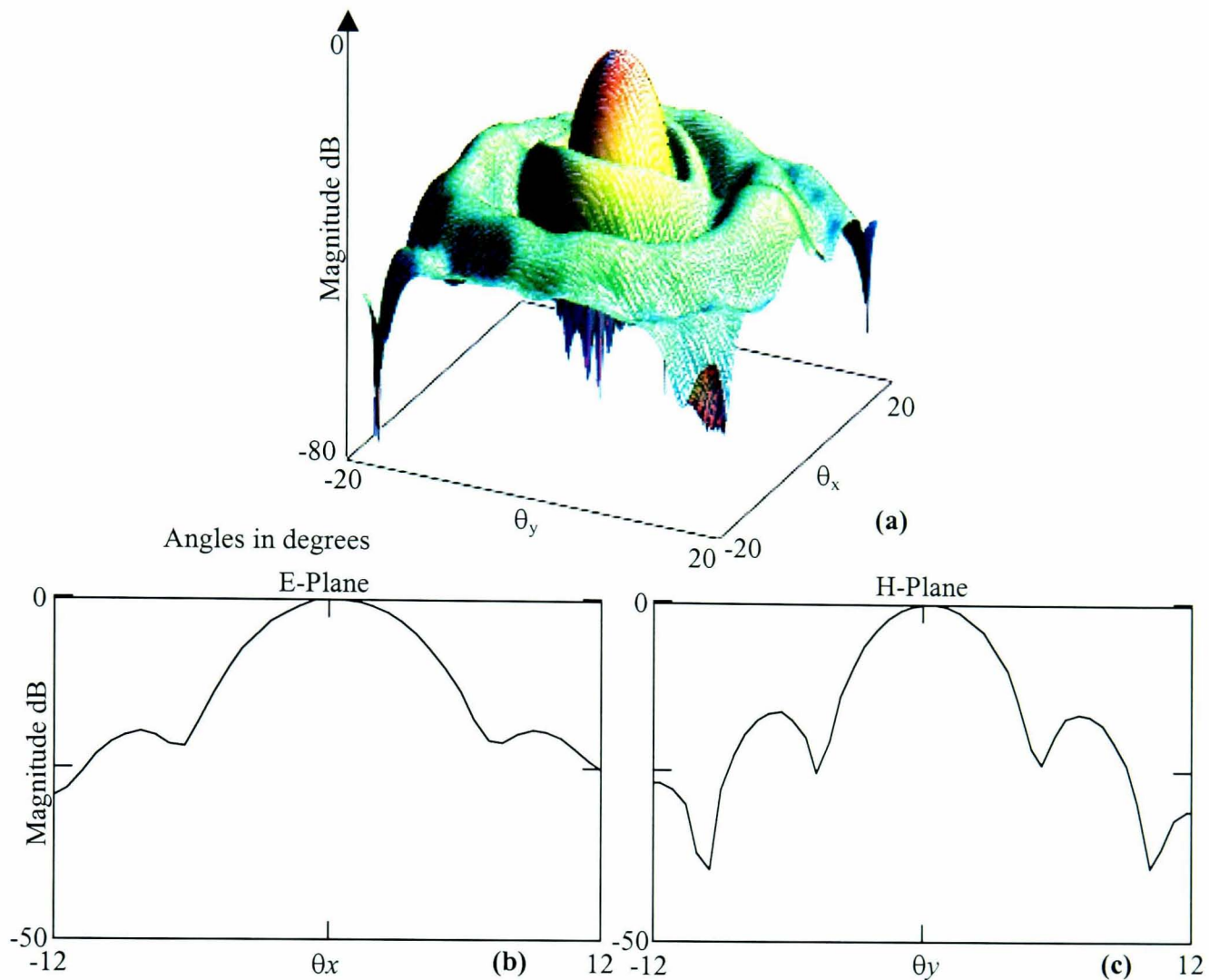


**Figure 7.17 Far-Field Radiation Pattern From Two-Dimensional Complex Field Measurement**  
**(a) Two-Dimensional Surface Plot, (b) Principal E-Plane Cut And (c) Principal H-Plane Cut**

The Far-Field produced is symmetrical about boresight in the two principal planes shown. The patterns highlight again that the H-Plane aperture field is more uniform than the E-Plane aperture field, as its sidelobes are larger and nulls are deeper, also the FNBW, SNBW and HPBW are narrower in the E-Plane than in the H-Plane. The valid angle here is the same as that for the indirect holographic method.

To make a further comparison between the measured complex Near-Field and the one predicted by the indirect holographic method, it is useful to reconstruct the complex Near-Field from the direct measurement method after beam-limiting the PWS by the same amount as in the indirect holographic method and then performing the IFT. The aperture distribution is also reconstructed from the complex Near-Field measurements

by back propagation of the beam limited PWS prior to the IFT. The result of this is shown in Figure 7.18.

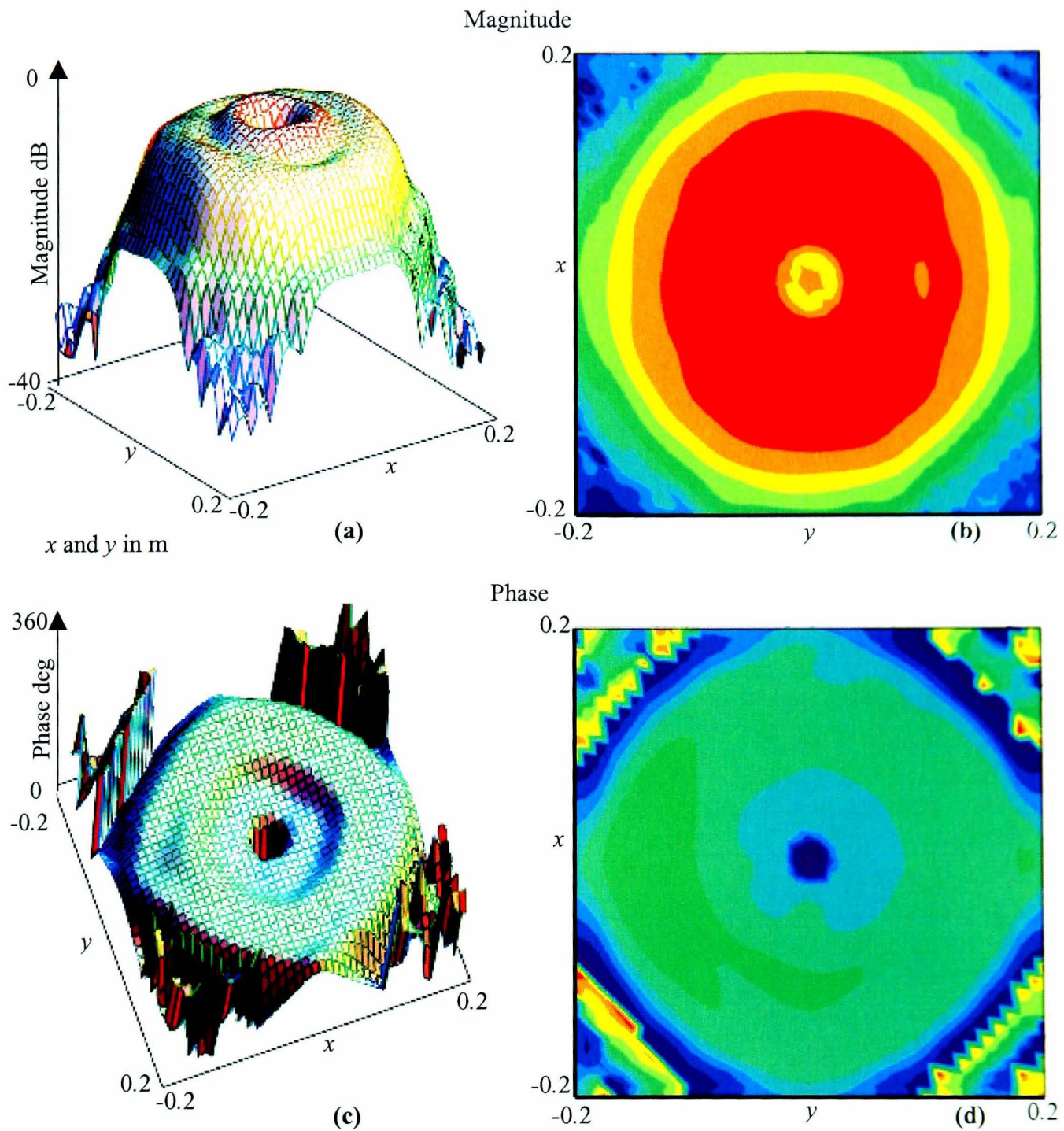


**Figure 7.18 Aperture Distribution From Two-dimensional Complex Near-Field Measurements**  
**Magnitude (a) Surface Plot (b) Contour Plot And Phase (c) Surface Plot (d) Contour Plot**

The magnitude of the aperture distribution, once again shows the blockage in the field produced by the splash plate feed at the centre of the dish. With the exception of the blockage in the centre the magnitude across the aperture as expected tapers more in the  $y$ -axis than in the  $x$ -axis.

Comparisons between the relevant information obtained from the different measurement techniques will now be made to verify the novel technique being proposed and evaluate its performance.

## **7.5 Result Comparisons and Discussions**

The comparison between methods is divided into two parts, firstly a comparison of the Far-Field characteristics using all three methods and secondly a comparison of the complex fields obtained via the direct and indirect holographic techniques, at both the Near-Field sampling plane and at the aperture plane.

### **7.5.1 Far-Field comparison**

The principal E and H planes of the AUT obtained from the three measurement techniques as presented above are shown in Figure 7.19. For the purposes of evaluation the directly measured Far-Field patterns obtained from the antenna manufacturer, measured on their industry standard outdoor test range, are taken to be the true Far-Field patterns against which the direct and indirect holographic methods implemented here will be compared.

All three techniques show a high degree of agreement in both the E and H Planes. Firstly considering the E-Plane pattern, over a beamwidth of  $10^\circ$ , which contains the main lobe, the variation between all three techniques is less than 0.1 dB, the FNBW occurs at  $\approx \pm 5.5^\circ$  within a variation of  $0.2^\circ$  over the three techniques and the location of the first sidelobe occurs at  $\approx \pm 7.25^\circ$  within a variation of  $0.5^\circ$ . The two holographic methods are seen to deviate from the directly measured Far-Field as the pattern

approaches the first null, they have deeper nulls than measured in the Far-Field. The maximum variation between the three techniques over the valid beamwidth is  $\approx \pm 1$  dB. The magnitude difference between the two holographic methods over the valid beamwidth is smaller  $\approx \pm 0.5$  dB.

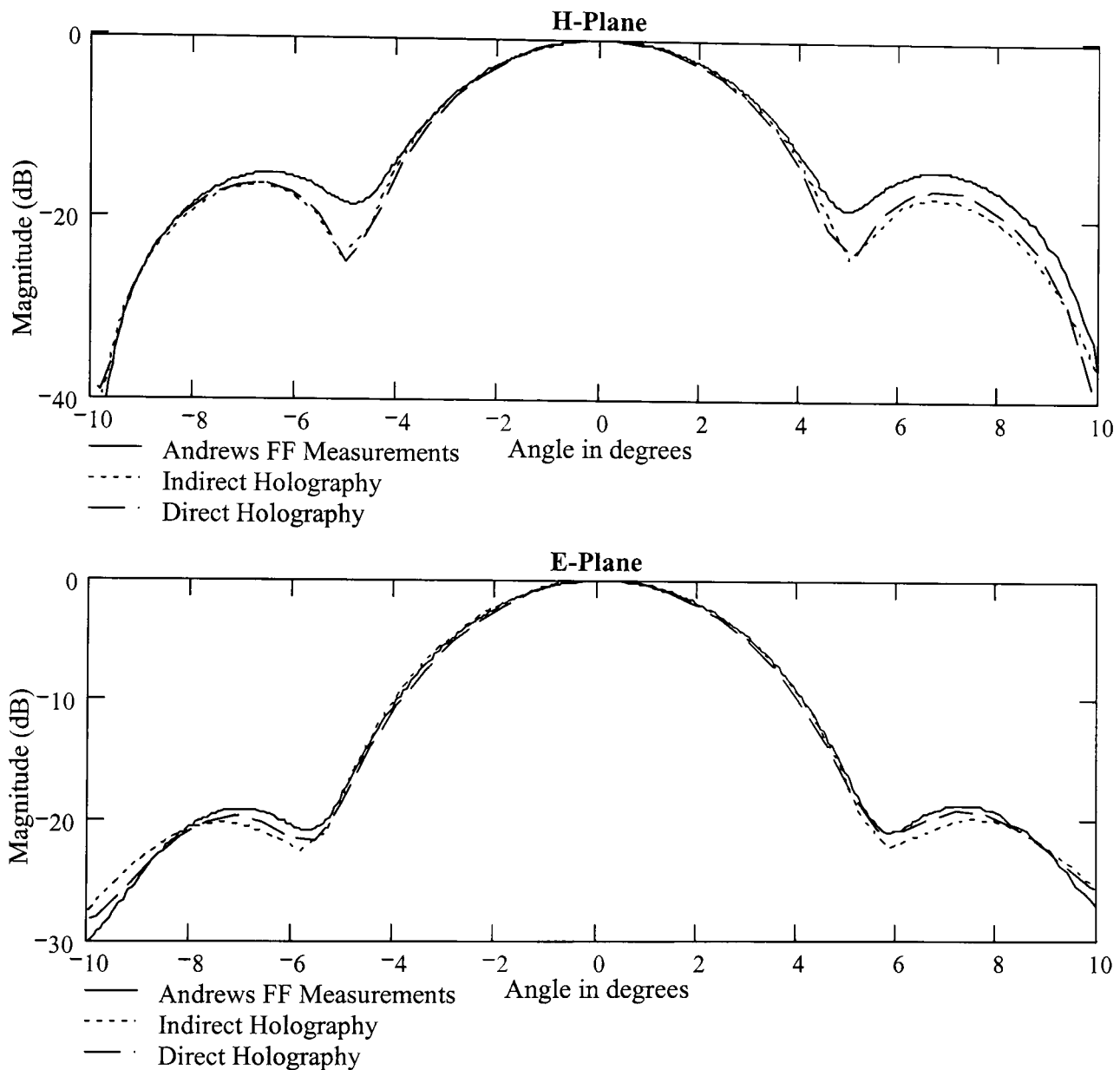


**Figure 7.19 Comparison Of Parabolic Dish Far-Fields From Indirect/Direct Holography And Direct Far-Field Measurement**

Now considering the variation between the H-Plane results from the three techniques, over a beamwidth of  $\approx 10^\circ$ , which encompasses the main lobe, the variation does not exceed 0.5 dB. The location of the FNBW is  $\approx \pm 4.75^\circ$  and the location of the first sidelobe maximum is at  $\approx \pm 6.5^\circ$ . The two holographic methods follow each other very

closely over the valid angle within a variation of  $\pm 0.2$  dB and  $\pm 0.3^\circ$ . The difference between the two holographic techniques and the direct Far-Field measurement is greater than seen in the E-Plane. The difference in first null depth is of the order of 3 dB and the difference in first sidelobe level is 1 dB. The reasons for this difference is now addressed below.

No probe compensation has been applied to these results, however over these small angles ( $\pm 12^\circ$ ) the effect of probe compensation can be considered negligible in view of the measured probe Far-Field shown in Figure 6.12. The probe field variation is of the order of 0.3 dB over this beamwidth.

The difference between the two holographic techniques and the directly measured Far-Field can be attributed, to the failure of the limited scanning aperture to intersect the whole of the radiated field. The differences between the holographic methods and the direct Far-Field measurement reflect this kind occurrence. The higher angular information has been lost and the effect this is for the side lobe levels to decrease and the nulls to become deeper. As should be expected in that case, the loss of this information in the H-Plane where the illumination is more rectangular has a bigger effect, than the loss of information in the more tapered E-Plane.

Both holographic techniques have been able to produce consistent Far-Field pattern results in close agreement to each other and the manufacturers Far-Field measurements. It is especially encouraging that using the same measurement system the Far-Field of an antenna has been predicted from intensity only measurements to

the same degree of accuracy as the standard complex Near-Field measurement technique over the valid angle, without the need for an expensive VNA.

### **7.5.2 Complex Near-Field comparisons and discussions**

For the purposes of complex Near-Field, only the two holographic techniques can be considered. The variation between them is used to determine the ability of the complex field to be recovered using the novel technique proposed in this thesis.

Two comparisons of the complex Near-Field will be made, firstly, a comparison of the directly measured complex Near-Field and the complex Near-Field obtained via the indirect holographic method. Secondly a comparison will be made between the complex Near-Field obtained via the indirect holographic method and the directly measured complex Near-Field after it has been subjected to the same beam-limiting as the indirect Near-Field. The PWS produced from the direct complex field measurement is beam-limited at the same angle that the PWS from the indirect method is filtered from the intensity spectrum. This provides a more comparable result in that the two Near-Fields contain the same amount of angular information. It also shows that the ability of the complex Near-Field to be reconstructed from the intensity only data is governed by the capacity of the scanning plane width to intersect the radiated field. The Near-Fields will be compared by examining two one-dimensional cuts through the centre of both the  $x$  and  $y$  planes in both phase and magnitude.

The plots of Near-Field magnitude from each technique follow the same general trend in both axes, though they are not comparable in size, differences of up to  $\pm 3$  dB exist

in some places. The phase obtained from each technique again follows the same general trend though there is a significant numerical variation of the order of  $25^\circ$  in places. These differences are due to the observations made in Chapter 6, filtering the PWS from the intensity spectrum at the valid angle means its frequency information is limited and therefore the reconstructed field is subject to that limitation.

Since it is the spectral filtering that results in the loss of information regarding the AUT field, then there must be a trade off between how much of the spectrum can be filtered and how much information can be lost. It is also necessary to recall that there is only a finite area of the spectrum into which the AUT PWS must fit, outside of which it becomes unacceptably interfered with by the other components in the spectrum. Quantification of this trade-off is not useful here as it is a purely subjective quantity dependant on the type of antenna being tested and its radiation pattern.

A comparison between the complex Near-Field obtained from the indirect holographic technique as seen in Figure 7.20 and the complex Near-Field measurements after their spectrum has been filtered to the same width is shown in Figure 7.21. From this comparison it is clear as it was in section 6.3.3, that the differences in the waveforms is in fact due to the restricted AUT PWS spectral width available for filtering in the intensity spectrum

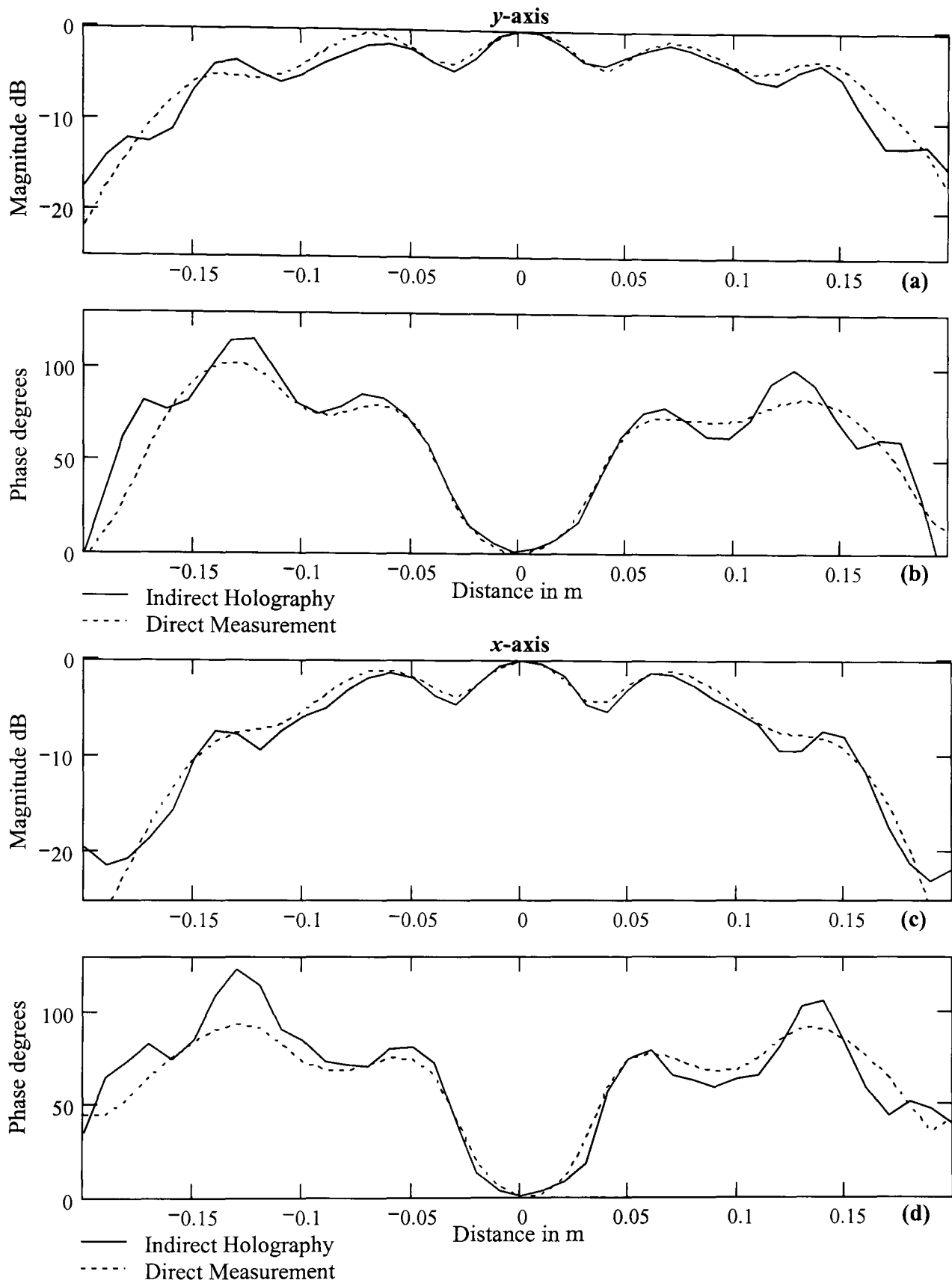


**Figure 7.20 Comparison Of Parabolic Dish Complex Near-Field Obtained From Indirect Holography And From Direct Complex Near-Field Measurements (a) Magnitude Across Centre Of The  $y$ -axis (b) Phase Across Centre Of The  $y$ -axis (c) Magnitude Across Centre Of The  $x$ -axis (d) Phase Across Centre Of The  $x$ -axis**

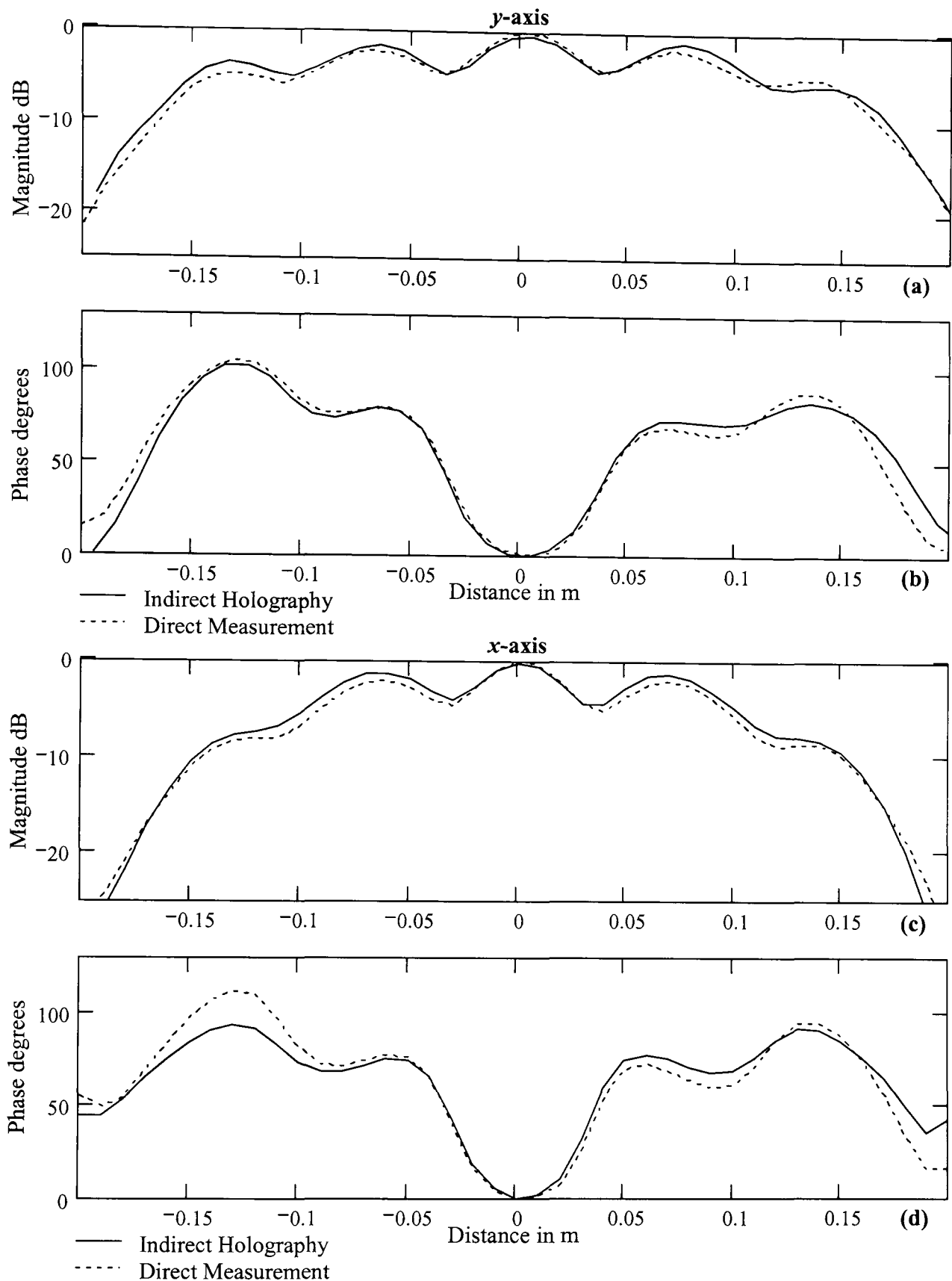


**Figure 7.21 Comparison Of Parabolic Dish Complex Near-Field Obtained From Indirect Holography And From Beam-Limited (Spectrally Filtered) Direct Complex Near-Field Measurements (a) Magnitude Across Centre Of The  $y$ -axis (b) Phase Across Centre Of The  $y$ -axis (c) Magnitude Across Centre Of The  $x$ -axis (d) Phase Across Centre Of The  $x$ -axis**

In agreement with those comparisons made in Chapter 6, the beam limited complex Near-Field shows a much closer agreement to that predicted by the indirect

holographic method than the directly measured field data. The variation in magnitude and phase does not exceed  $\pm 1$  dB and  $\pm 10^\circ$  in the  $x$ -axis, and  $\pm 1$  dB and  $\pm 5^\circ$  in the  $y$ -axis over the area directly above the antenna aperture  $\pm 0.175$  m.

### 7.5.3 Complex aperture field comparison and discussion

Figure 7.22 shows the complex field distributions across the centre of the aperture in both directions, obtained by the back propagation of the two beam-limited PWS's using (3.18). Both sets of plots clearly demonstrate the field blockage caused by the splash plate feed at the same location in the aperture plane. The splash plate is circular and 0.06 m in diameter, from the graph this can be seen to be the same size as the area of field blockage. The two methods show good correlation in shape for both the magnitude and phase. It is possible to demonstrate that the level of field blockage caused by the splash plate decreases by using different values of  $Z_0$  in (3.18) and observing the size of the dip in the complex field magnitude.

The complex aperture fields produced by the two techniques in Figure 7.22, both follow the same trend over the antenna aperture. Although there are differences in the absolute values of magnitude and phase, the fields are plotted are normalised. Therefore the variation in absolute value changes depending on which point is chosen for normalisation, in this case the centre point. Even in consideration of this, the magnitude and phase in the  $y$ -axis show a maximum variation of around 2 dB and  $25^\circ$  and in the  $x$ -axis 2 dB and  $15^\circ$ . If the purpose of attaining the aperture field is merely to locate faults on the antenna surface it is more the general trend of the field that is observed and not the absolute values. So, although the variation may seem large, the general trends of the plots are seen to be very close.

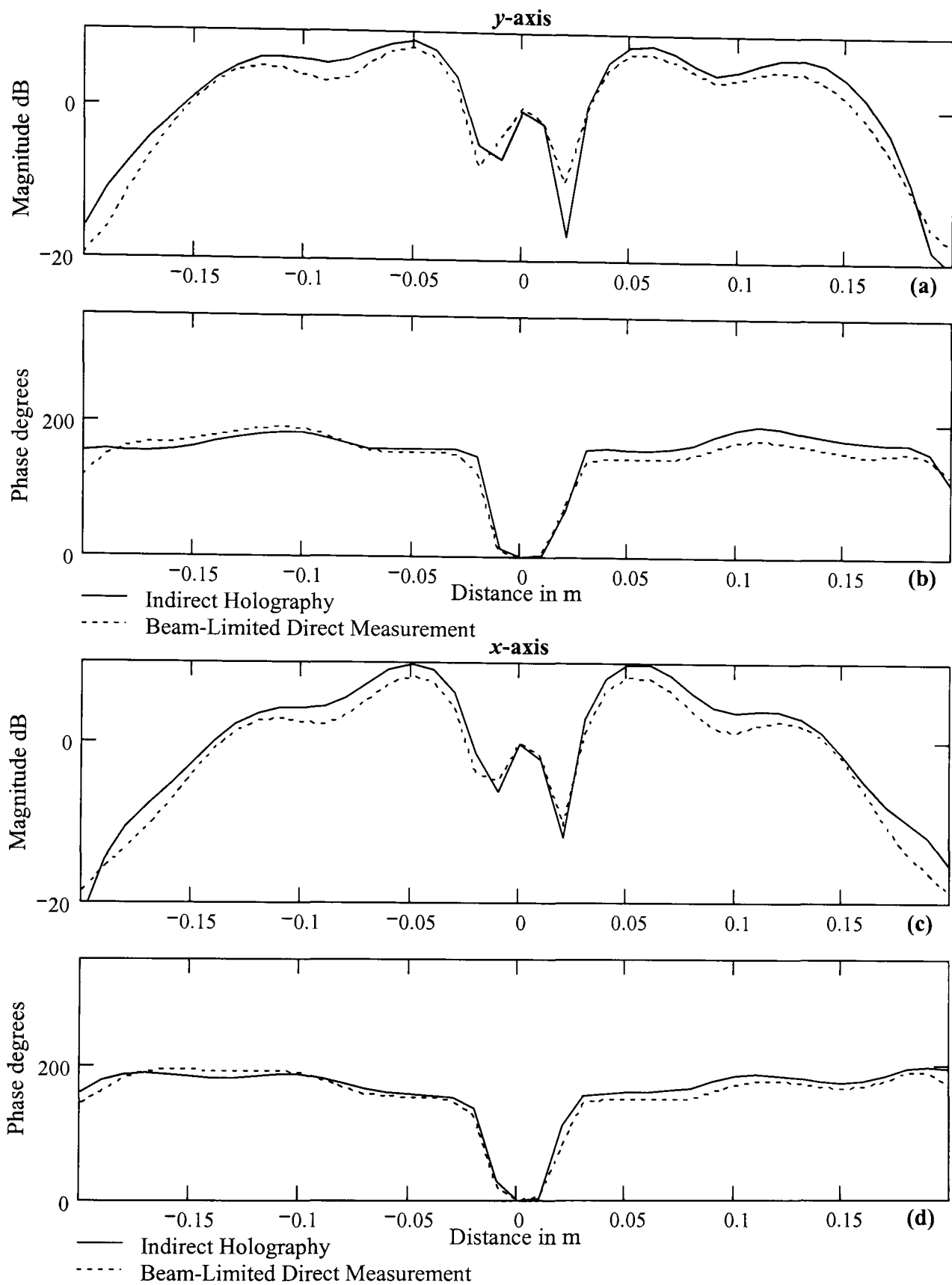


**Figure 7.22 Comparison Of Parabolic Dish Complex Aperture Field Obtained From Indirect Holography And From Beam-Limited (Spectrally Filtered) Direct Complex Near-Field Measurements (a) Magnitude Across Centre Of The y-axis (b) Phase Across Centre Of The y-axis (c) Magnitude Across Centre Of The x-axis (d) Phase Across Centre Of The x-axis**

The validation of the novel system has been performed successfully by comparison of the two-dimensional measurements obtained from the novel indirect holographic

technique with results obtained using the standard technique of direct complex Near-Field measurements and direct Far-Field measurement. The novel technique was able to yield the same Far-Field radiation pattern as standard complex Near-Field measurements to within 0.5 dB. The novel technique can be used to achieve complex Near-Field values to within 1 dB and  $10^\circ$ , when the system limitations are taken into account. It has also been shown that the general trend of the complex field over the aperture can be reproduced using the novel technique

Some Limitations of the system have been highlighted during this section, including the restricted size of the scanning aperture and the effect this has, not only on the PWS but also the complex Near-Field that can be reconstructed from intensity only measurement. It is necessary to consider the error sources in this two-dimensional system to provide some further justification for the differences observed between the two techniques.

## **7.6 System Error Sources**

The error sources discussed in Chapter 3 regarding planar measurements are applicable here. The automated positioning system is estimated to be able to repeat its movement over a given grid to within 0.1 mm. The arm on which the probe is mounted has little support and as such is subjected to small vibration each time the system moves from one sample point to the next. The PC takes two samples at each location and provides the average to reduce any effect of the vibration.

From the photograph of the system it can be seen that effort has been made to minimise reflections from surrounding surfaces by using microwave absorber. Cable

movement effects are assumed to be negligible through the use of high quality microwave cable. Environmental effects such as temperature could not be controlled over the length of time taken to perform a full set of measurements. For this antenna a full scan takes around 4 hours for the novel holographic system, and for a complex Near-Field measurement where recording was by hand a minimum of 6 hours was required. Temperature variation within this time frame could be as much as 6-7 °C, this could effect equipment such as cables, changing their impedance characteristics and hence altering measurements, as described in Chapter 3.

As in Chapter 6, the measure of the systems robustness is in terms of the variance between multiple sets of measurements. Three sets of intensity data have been collected to provide a means of measuring the repeatability of the novel indirect holographic system. The decision to take three sets was based primarily on the time it takes to collect one set of data, for the 41x41 matrix of points used here a full scan takes approximately 3 hours. The variance is calculated by a two-dimensional adaptation of (6.5):

$$Var = \frac{1}{N_x \cdot N_y} \cdot \sum_{y=0}^{N_y-1} \sum_{x=0}^{N_x-1} \left| \max(D1_{x,y}, D2_{x,y}, D3_{x,y}) - \min(D1_{x,y}, D2_{x,y}, D3_{x,y}) \right|. \quad (7.4)$$

$$Var_I = 0.119 \text{ dBm}$$

A smaller variance between data sets is obtained in comparison to the manual one-dimensional system used in Chapter 6 ( $Var_I = 0.24 \text{ dB}$ ). This should be expected since the computer control of the positioning system provides a better accuracy than hand positioning. The resolution of the automated system has increased from the previous non-automated system, with the data being recorded to 0.01 dB for every sample point. In comparison to the dynamic range of the measurements,  $\approx 24 \text{ dB}$ , the small

variance between the three data sets is negligible providing a high degree of confidence in the system.

The complex Near-Field data has been collected only once over the two-dimensional scanning aperture because the data must be recorded by hand with one scan taking upwards of 6 hours. The measurement was carried out over a continuous period, to ensure no disturbance to the equipment occurred and to maintain equipment stability. Although no evaluation of the repeatability of the system can be made from the single scan from the small variation in intensity only measurements the accuracy of the positioning system can be affirmed. The data is recorded from the VNA by hand, with a minimum resolution of 1 dB and 1° as in the previous case. It is reasonable to assume therefore that the variance does not exceed that calculated in Chapter 6 (0.36 dB and 0.28°), as the positioning system will have improved positioning accuracy.

## **7.7 Summary**

This chapter has focused on the development of the one-dimensional system utilised in Chapter 6 into a two-dimensional system. This development was necessary in order to show that the system could, first of all be used to produce a two-dimensional holographic intensity pattern and second that from this intensity pattern the antenna Near and Far-Fields could be obtained. Without a two-dimensional measurement system, the method would be limited to the rectangularly symmetric apertures described in section 6.2.3.

The ability to generate two-dimensional holographic intensity patterns in this system is governed by the production of the plane reference wave over the two-dimensional measurement surface. Section 7.2 detailed how this could be achieved using this system and discussed that the linear phase shift could be straightforwardly implemented in any one of three configurations.

A simulation based on a suitable rectangular aperture exhibiting a standard illumination was developed in section 7.3, showing how the indirect holographic technique can be utilised to obtain the Far-Field radiation pattern and complex fields of the antenna. The simulation also showed the effect that the three different modes of phase shift have on the intensity pattern spectrum. The results of obtained from the simulation were compared to fields obtained using standard techniques and were found to provide a very high degree of agreement.

Two-dimensional measurements of the same parabolic dish used in Chapter 6 have been carried out using both the traditional complex Near-Field measurement technique and the novel holographic system using parameters defined in section 7.4. The two dimensional measurement allows the Far-Field patterns generated to be compared directly with the direct Far-Field measurements supplied by the manufacturer. The results obtained through the processing of the measurements from the two reduced range techniques were found to be highly comparable. The Far-Fields to within 0.5 dB over the valid angle of the range used. In comparison to the direct Far-Field there was a discrepancy in sidelobe level and null depth, however this has been related to limitations of the available scanning system, especially the restricted width of the scanning plane. The comparisons of the complex Near-Fields obtained

from both techniques were also shown to be in good agreement when the spectral limitations of the novel holographic technique are taken in to account.

Despite the basic nature of the available system the variance in the measurements over four consecutive sets of data is 0.119 dBm while the dynamic range of the measurements is of the order of 20 dB. Some of the error sources that the system is subject to are detailed in section 7.6.

The remaining work in this thesis considers the extension of this indirect holographic technique for use with medium gain antenna (i.e. lower directivity). The ability to improve the separation of spectral components is the key to achieving this.

# CHAPTER 8 THE NOVEL INDIRECT HOLOGRAPHIC RANGE – ‘SLOW WAVE’ INTERFERENCE

## 8.1 Introduction

The holographic system which this thesis set out to develop utilising a synthetic reference wave has been discussed, developed and then validated over the course of the last three chapters. The system has been shown to produce Far-Field radiation patterns to the same standard as the traditional complex Near-Field measurements could produce under the same conditions. This signifies that the novel technique developed can be used to replace the expensive VNA required for complex field measurements with a scalar detector.

The types of antenna to which the technique can be applied have so far been limited to those which exhibit field patterns restricted to a small area of the intensity spectrum. The parameter, which has controlled this, is the angle  $\theta_{XR}$  or  $\theta_{YR}$  at which the reference wave has been introduced, i.e. the phase shift induced in the spectrum. This was discussed in detail in Chapter 6 when choosing the antenna to be used for system validation. In comparison to the direct holographic Near-Field measurement technique, where the limitations placed on the AUT are defined by the ability of the sampling plane to intersect its radiating field, the indirect technique is limited by both the plane size and the separability of the components generated in the intensity spectrum.

This chapter now details a sampling methodology for use with the novel holographic system, which means that the types of antenna that can be measured using the holographic technique are no longer limited by the ability to produce separation. Therefore antenna choice is limited only by the size of the scanning aperture available.

The sampling methodology is presented in section 8.2, which shows how the careful selection of sample spacing  $\Delta x$  and  $\Delta y$  and phase increment per sample  $\theta_{xI}$  and  $\theta_{yI}$  can be used to create any level of separation desired. A validation procedure for the novel sampling methodology is then developed in section 8.3. The validation is carried out first by simulation in section 8.4 and by physical measurement in section 8.5 using standard measurement techniques to provide comparisons. In both cases the inability of the standard sampling methodology is shown to be inadequate at providing separation of the terms in the intensity spectrum. Finally a discussion of the limitations of the currently available system is then provided in section 8.6.

## **8.2 Over Sampling to Increase Spectral Width**

The limitation of the intensity spectrum to provide separable components is controlled by two parameters. Firstly, the angle at which the wanted object component is located in the hologram spectrum and secondly, the spectral width of the object wave (or AUT in this case).

In general, the off-axis hologram is generated by radiating the reference wave at an angle to the hologram plane, as in Figure 4.3, the location of the wanted object in the intensity spectrum is proportional to the offset angle only. Consideration of the simple

geometry reveals that the physical offset is limited to  $\pm 90^\circ$  and that beyond this point the separation effect in the intensity spectrum decreases. This effect has been simulated for a one-dimensional  $32\lambda$  uniformly illuminated aperture at 10 GHz. The spectral distribution of the intensity pattern obtained by applying (5.6) to the Near-Field as given in Figure 3.4 and a reference of uniform magnitude and offset angle  $\theta_{XR} = 90^\circ$ , at a sample spacing of  $\lambda/2$ , is shown in Figure 8.1.

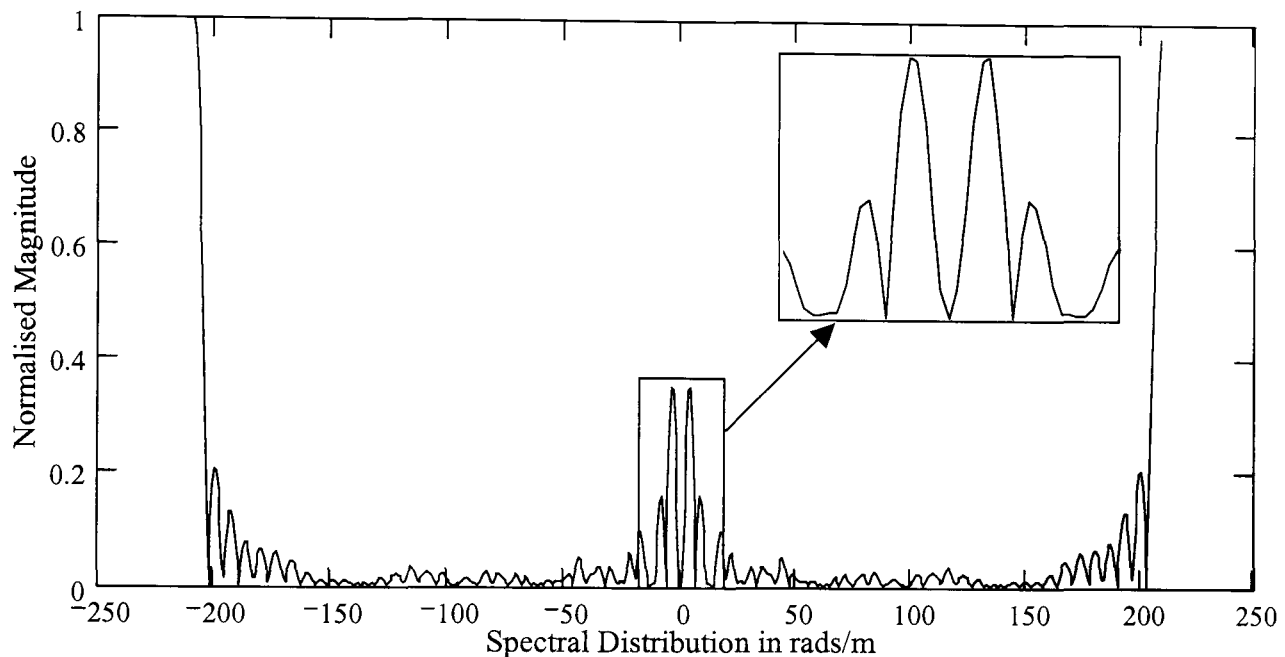


**Figure 8.1 Spectral Distribution Of An Intensity Pattern Generated By The Near-Field Of A Uniformly Illuminated  $32\lambda$  Aperture And Plane Reference Beam At  $90^\circ$  With  $\lambda/2$  Sample Spacing Normalised To The Maximum Magnitude**

From Figure 8.1, the two object components are seen located at  $\pm k_{XMAX}$ , (i.e. the same point in the spectrum) and cannot be separated. This demonstrates that the offset angle ( $\theta_{XR}$ ) at which to place the reference antenna must be chosen carefully to ensure that the best location in the spectrum is chosen for the relocation of the object components. The central section has been blown up to show that the D.C. component has been suppressed by the removal of the average intensity prior to the Fourier Transform.

Reducing the sample spacing increases the spectral width (by the relationship  $k_{XMAX} = \pi/\Delta x$ ). If the samples in the same simulation above are now set at  $\lambda/4$  apart, then the spectral width is increased to double its original size (i.e.  $\pm 2k_0$ ). With the reference wave offset angle remaining at the maximum of  $90^\circ$  then the location of the object and conjugate object will remain at the same location in the spectrum and the increased spectral width allows the components to be separated. This is shown in Figure 8.2, where the sample spacing of the previous simulation has been reduced to  $\lambda/4$ .

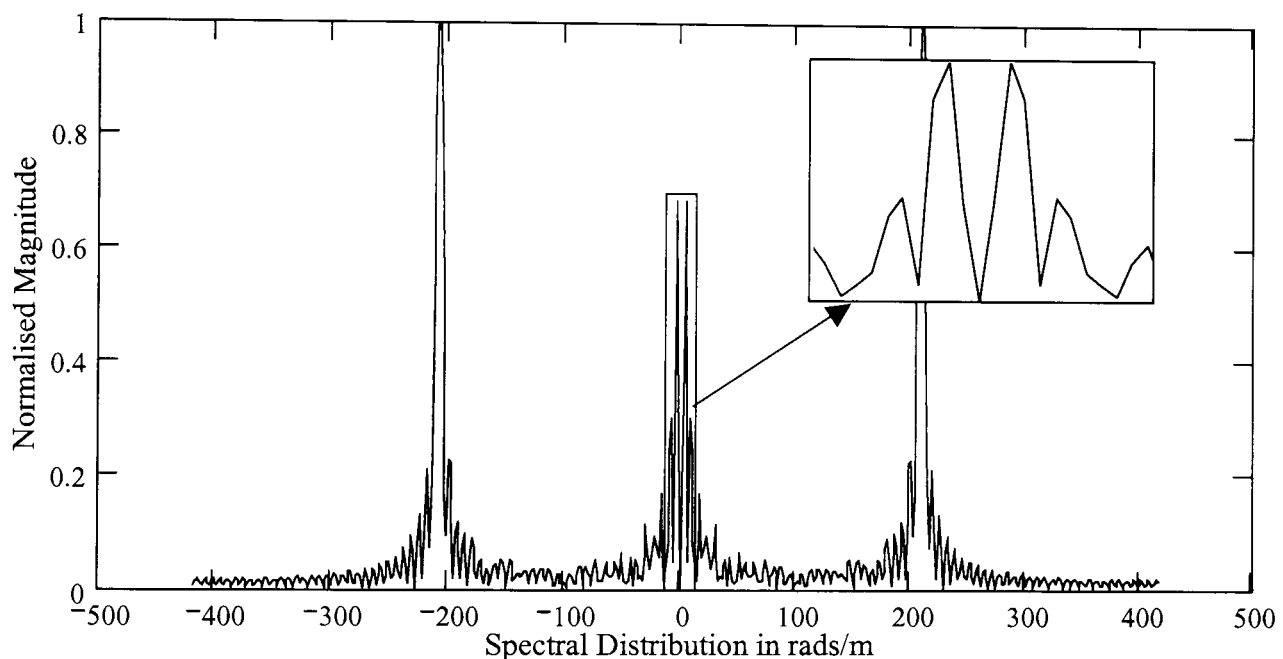


**Figure 8.2 Spectral Distribution Of An Intensity Pattern Generated By The Near-Field Of A Uniformly Illuminated  $32\lambda$  Aperture And Plane Reference Beam At  $90^\circ$  With  $\lambda/4$  Sample Spacing Normalised To The Maximum Magnitude**

It is seen above that now the real and conjugate terms are separated both from the central auto-correlation terms and each other enabling their individual extraction from the spectrum. This has been achieved at the sacrifice of doubling the amount of data to be collected and hence the amount of time taken to collect it. Here the components are seen spaced at the maximum achievable distance when using a radiated reference wave. Decreasing the sample spacing further will increase the spectral width, however the locations of the object components cannot be moved any further from the centre

and so a decrease in sample spacing here would simply serve to increase the amount of data to be collected without gain. The suppression of the D.C. component is also highlighted as in Figure 8.1.

A different situation exists in this case due to the novel manner in which the reference is introduced. Here it is not the offset angle that is chosen in order to generate separation in the intensity spectrum; rather it is the phase gradient across the hologram plane that is under direct control. There is no physical limit to the phase shift introduced per sample because phase shifters could theoretically be incremented through any amount up to  $180^\circ$  per sample. Redefining  $k_{XR}$  in (6.2) as a function of the increment angle gives:

$$k_{XR} = k_0 \cdot \sin(\theta_{XR}), \text{ where } \theta_{XR} = a \sin\left(\frac{\theta_{XI}}{k_0 \cdot \Delta x}\right) \quad (8.1)$$

$$= \frac{\theta_{XI}}{\Delta x}.$$

Now it is seen that the location of the object components in the spectrum is related to the phase insertion angle per sample  $\theta_{XI}$  and the sample spacing  $\Delta x$ . The sample spacing is usually constrained by the measurement systems capabilities or by the desire to keep the number of samples to be collected to a minimum. It is not considered a control parameter for the object offset angle, however it is seen here that as the sample spacing decreases if the phase increment remains constant then the offset angle will increase.

The value of  $k_{XMAX}$  is given by  $\pi/\Delta x$ , the maximum displacement of the object components from the centre of the spectrum is therefore obtained when the phase increment per sample is  $\theta_{IX} = 180^\circ$  (from (8.1)), resulting in the two object

components being located at the same point (i.e.  $\pm k_{XMAX}$ ) as was seen in Figure 8.1. This leads to the conclusion that, the object component displacement can now be greater than  $90^\circ$  ( $k_0$ ). A synthetic reference wave that produces an offset angle in the intensity spectrum  $>90^\circ$  (i.e.  $>k_0$ ) is termed a 'slow wave', as the phase delay produced between samples is greater than physically possible by radiating the reference wave. The larger displacement allows more of the spectrum to be utilised and hence provides more opportunity for the separation of the intensity spectral components, this means it is possible to apply the technique to the measurement of lower gain antennas. Smith and Leach detailed these findings in [84], [85], [86] by means of simulation.

For any planar measurement system the theoretical maximum possible prediction angle for an antenna PWS is  $\pm 90^\circ$ , which could only be achieved if the sampling plane was infinitely wide. As shown in Chapter 3, the valid angle for prediction of an AUT's PWS from planar measurements is based on the size of the AUT, the width of the measurement plane and the distance between them, (3.22). Provided that the measurement plane width and the distance it is set from the AUT have been chosen carefully so that the bulk of the radiated energy lies inside the valid angle. Beyond this angle the magnitude of the spectral distribution should reduce to a pre-determined negligible value, defined by the signal to noise capabilities of the system. If this is the case, then the components in the spectrum can be thought of as not interfering with each other outside of the valid angle. Hence the sample spacing and increment angle can be chosen such that there is no gap between the spectral components. This means that the required spectral width into which they can fit can be restricted as shown in Figure 8.3.

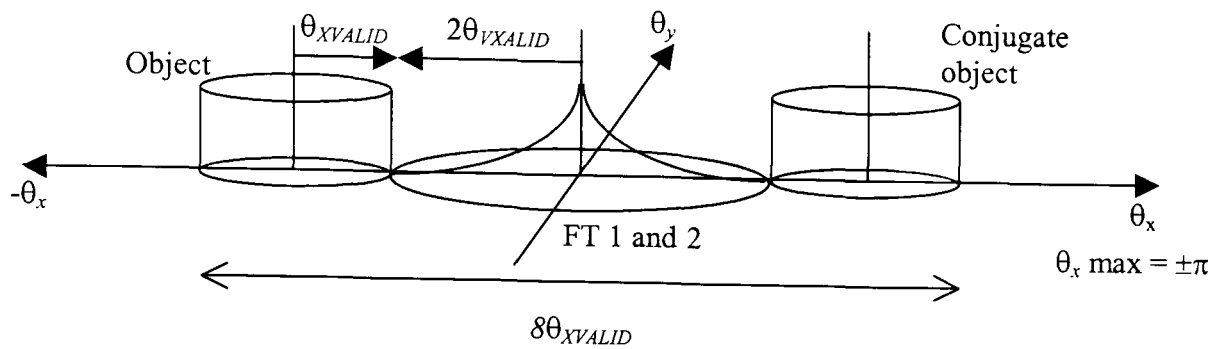


**Figure 8.3 Off-Axis Intensity Pattern Spectral Distribution For Minimal Sample Spacing**

It follows that, as each half of the spectrum contains two times the object spectral width (assuming that the object auto correlation does not exceed twice the object spectral width), then the valid angle from (3.22) can be used to define the sampling requirements of the measurement as:

$$\begin{aligned}
 k_{XV} &= k_0 \cdot \sin(\theta_{XV}) \text{ then,} \\
 k_{XMAX} &= 4 \cdot k_{XV}.
 \end{aligned}
 \tag{8.2}$$

Following on from this the sample spacing requirements defined in (3.10) can be re-written in terms of this minimum spectral requirement:

$$\Delta x \leq \frac{\pi}{k_{XMAX}} \leq \frac{\pi}{4 \cdot k_0 \cdot \sin(\theta_{XV})}.
 \tag{8.3}$$

This should be restricted to a minimum of the Nyquist rate in order to ensure that the information collected is representative of the information contained within the field.

The minimum width of the spectrum into which a pre-determined PWS will fit has been now derived, and the maximum size sample spacing to coincide with this width has been found. To use this criterion it is necessary to space the objects within the spectrum by careful choice of a reference angle ( $\theta_{XR}$ ). As the required spectral width has been designated by considering each component to be a multiple of the valid

angle, the centre of AUT PWS's (real and imaginary) need to be located at a point  $\pm 3/4$  of the way along the spectrum. This results in the following angles for  $\theta_{XR}$  and  $\theta_{XI}$ :

$$\theta_{XR} = a \sin\left(\frac{3 \cdot k_{XMAX}}{4 \cdot k_0}\right). \quad (8.4)$$

$$\begin{aligned} \theta_{XI} &= k \cdot \Delta x \cdot \sin(\theta_{XR}) \\ &= \Delta x \cdot \frac{3 \cdot k_{XMAX}}{4} = \frac{3 \cdot \pi}{4} \approx 135^\circ. \end{aligned} \quad (8.5)$$

This would not have been possible in previous systems utilising a radiated Off-Axis reference where the maximum  $\theta_{XR}$  would have been  $90^\circ$ .

An example in which a  $135^\circ$  phase increment per sample has been simulated is shown in Figure 8.4 using the same aperture distribution as previous with  $\lambda/4$  sample spacing. In comparison to the previous graphs in Figure 8.1 and Figure 8.2, it is seen that the centre of the two object components has been located further from the centre of the spectrum than was previously possible.

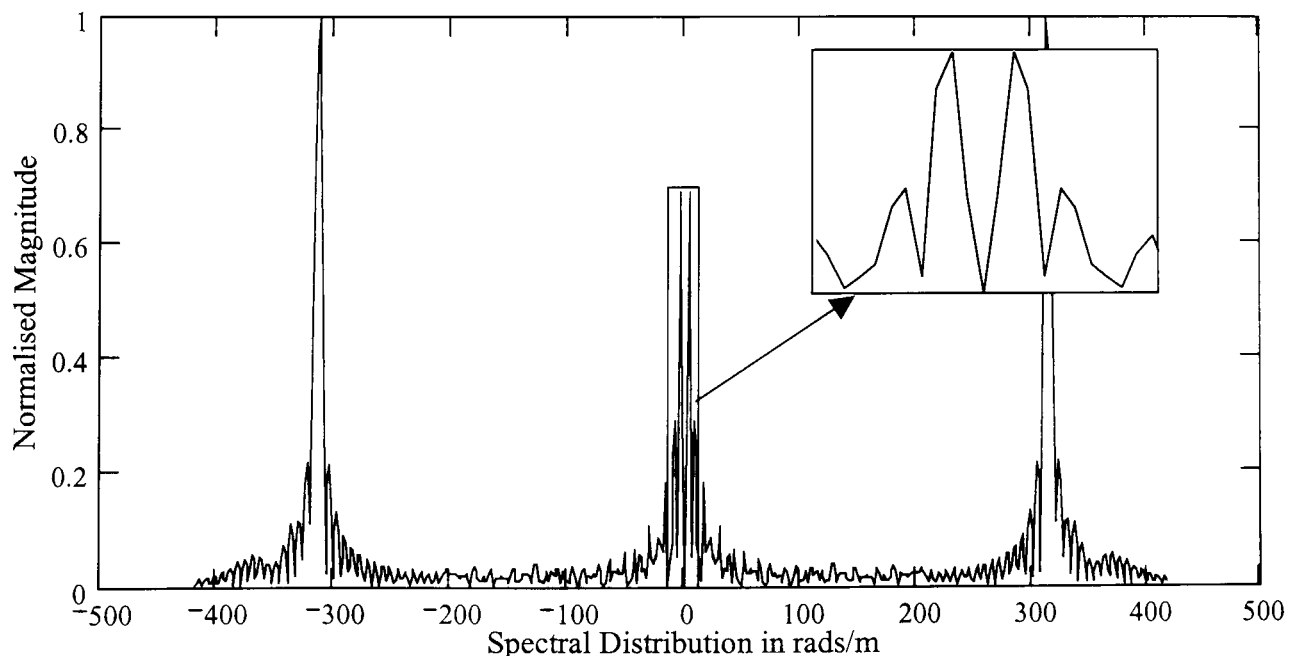


**Figure 8.4 Angular Spectrum For  $\lambda/4$  Sampled Data With Reference Beam Increment at  $135^\circ$  Normalised To Maximum Magnitude**

If it was possible to collect the data over an infinitely large plane, the valid angle would become  $90^\circ$ , then from (8.3) the minimum required sample spacing to be able to extract the object component out to the valid angle would be  $\lambda/8$ . This is achieved at the expense of collecting four times as many data points as the minimum required by the sampling theorem (Nyquist rate).

It has now been shown that due to the manner in which the reference wave is introduced, the limit to which the reference wave offset angle can be achieved is increased beyond the previous maximum of  $90^\circ$ . It has also been shown that the phase gradient at which the separation of the components is maximised is  $135^\circ$  or  $3/4k_{XMAX}$ .

The suggestion of this is that any antenna radiating into only one hemisphere can be measured using this technique with the separation being gained by manipulation of the sample spacing. The limitation on this is then the ability to make the sampling plane large enough and is not determined by the ability to separate the spectral components in the intensity pattern.

An experiment will be designed to show that the increased use of the spectrum will allow less directive, medium gain antenna to be measured using this technique. The verification will be performed using a mathematical simulation of the process and then by physical measurement.

### 8.3 Experimental Design and Parameter Definition

It was shown above by simulation that a greater separation of components in the intensity pattern spectrum is achievable by decreasing sample spacing but maintaining the phase increment per sample, in effect increasing the apparent Off-Axis angle of the reference wave. To verify this effect is valid for the measurement of antenna fields, an experiment based on an antenna with a suitably wide beamwidth, which using the standard technique (as in Chapters 6 and 7) would not be separable in the intensity spectrum, will be used. Once a suitable experimental procedure has been defined verification will be performed first by simulation and secondly by physical measurement. In both the simulation and the practical measurement standard sample spacing ( $\lambda/2$ ) and reduced sample spacing will be used, both with the same increment angle  $\theta_{XI}$ .

#### 8.3.1 Antenna properties and Far-Field measurement

A *WR90* Pyramidal horn has been chosen as the test subject. The medium gain horn manufactured by Flann Microwave (model 16240) has an aperture 0.109x0.079 m and operates at X-Band. The parameters estimated for this antenna have been given in Table 6.1. At 10 GHz; the distance to the Far-Field is given by:

$$\frac{2 \cdot D^2}{\lambda} \text{ where } D = \sqrt{.109^2 + .079^2} \text{ and } \lambda = 0.03 \text{ m} \quad (8.6)$$
$$\frac{2 \times (0.109^2 + 0.079^2)}{0.03} \approx 1.2 \text{ m.}$$

The magnitude distribution across the aperture of the pyramidal horn fed in its dominant  $TE_{10}$  mode is cosine in the H-Plane and uniform in the E-Plane. Due to the

relative lengths of the wave paths from the feed to the aperture, a quadratic phase variation across the aperture is also present.

The pyramidal horn antenna has been measured in the anechoic microwave facility within Northumbria University. As in Figure 2.3, the pyramidal horn is used as a source and a  $WR90$  waveguide probe receiver. The power received by the probe was recorded as the horn is rotated in  $0.9^\circ$  increments. This process is automated and has been carried out for both principal planes at 10 GHz. The patterns measured can be seen in Figure 8.5, the system has a lower detection limit of  $-40$  dB.

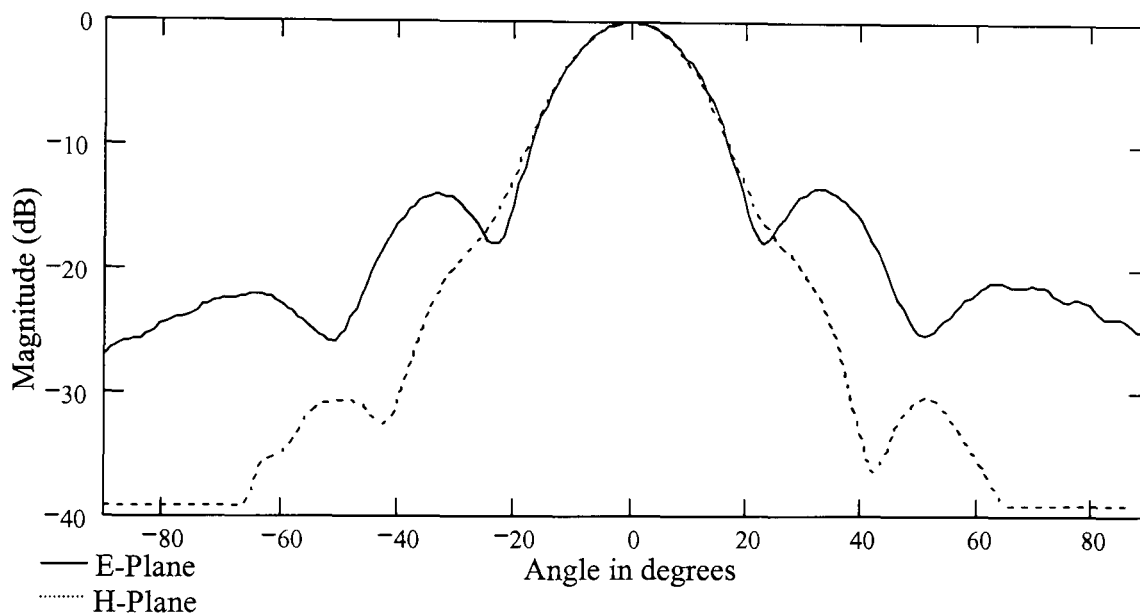


**Figure 8.5 Direct Far-Field Measurement Of Pyramidal Horn At 10 GHz**

As expected, the E-plane pattern has a wider characteristic than the H-plane due to its approximate uniform illumination and smaller dimension, in terms of the spectral width, it can be seen that both the H and E-planes are below  $-20$  dB beyond the SNBW. The SNBW for this antenna was estimated using an approximation for a rectangular aperture on a ground plane with  $TE_{10}$  mode distribution in Table 6.1, these measured patterns provide a SNBW within  $2^\circ$  of this approximation. These measured Far-Field patterns will be used for comparison of the other measurement techniques.

### 8.3.2 Measurement parameters

For the purposes of performing the measurement and to allow parameter definition to take place, it is useful to first decide on the orientation of the antenna in the coordinate system and then the type of phase gradient to be applied from the three possibilities.

The antenna has been located so that the H-Plane is in the  $x$ -axis and the E-Plane is in the  $y$ -axis. The same measurement plane used in Chapter 7 (i.e. 0.4x0.4 m) is located at the minimum allowable distance to the antenna to maximise the valid angle and ensure it is outside of the reactive Near-Field region. The standard value of  $5\lambda$  is used, locating the plane at a distance of 0.15 m. The valid angle in each plane can therefore be defined using (3.22), for  $S_X = S_Y = 0.4$  m,  $A_X = 0.109$  m,  $A_Y = 0.079$  m and  $Z_0 = 0.15$  m:

$$\begin{aligned}\theta_{xv} &= \tan^{-1}\left(\frac{0.4 - 0.109}{2 \times 0.15}\right) = 44.13^\circ \text{ in the H-Plane,} \\ \theta_{yv} &= \tan^{-1}\left(\frac{0.4 - 0.079}{2 \times 0.15}\right) = 46.94^\circ \text{ in the E-Plane.}\end{aligned}\tag{8.7}$$

In the H-Plane this valid angle will allow the pattern up to the SNBW to be predicted, encompassing all radiated energy down to  $-30$  dB. In the E-Plane the valid angle falls short of the SNBW encompassing the radiated energy down to around  $-22$  dB. Based on this information the phase shift is to be implemented in the  $x$ -axis only, coinciding with the H-Plane of the antenna, because the H-Plane pattern rolls-off faster and so less interference will occur between the components in the intensity spectrum. Consideration of the spectral width allows the minimum required sample spacing to obtain separation in the intensity spectrum to be found. This needs only be considered in the direction of the phase shift,  $x$ -axis, in the  $y$ -axis the sample spacing is restricted

only by the Nyquist rate. The valid spectral width of the horn in the two principal planes is:

$$\begin{aligned}
 k_{AUTMAX} &= k_0 \cdot \sin(\theta_{XV/YV}) \\
 &= 0.69 \cdot k_0 \text{ in the H-Plane,} \\
 &= 0.73 \cdot k_0 \text{ in the E-Plane.}
 \end{aligned}
 \tag{8.8}$$

The maximum sample spacing required in the  $x$ -axis to achieve separation in the intensity spectral distribution is given by (8.3):

$$\Delta x_{MAX} = \frac{\pi}{4 \times 0.69 \times k_0} = 5.43 \text{ mm, where } k_0 = 209.44 \text{ rads/m.}
 \tag{8.9}$$

The standard sample spacing of  $\lambda/2$  ( $\approx 0.015$  m) clearly does not meet this criteria. In this case a reduced sample spacing of  $\lambda/6$  (0.005 m at 10 GHz) will be employed; this equates to a spectral width of  $\pm 2.5k_0$ . The reason for this choice is the convenient sample spacing it provides i.e. an integer number of millimetres, whilst not over increasing the size of the data set or the time to perform a scan.

The reference phase shift per sample to be used is  $120^\circ$ , though it has been highlighted earlier that the best separation will occur when  $\theta_{XI} = 135^\circ$ , this would require eight phases on the manual phase shifters with no attenuation variation, to achieve a repeatable revolution with uniform magnitude. Using  $120^\circ$  will locate the AUT PWS and its conjugate at:

$$k_{XR} = \frac{\theta_{XI}}{\Delta x} = \frac{2 \cdot \pi}{3 \cdot 0.005} = 418.9 \text{ rads/m.}
 \tag{8.10}$$

Table 8.1 provides a summary of the measurement parameters that have been defined above and their spatial/spectral relationships.

Parameter	Specification
<b>Antenna and Dimensions</b>	Flann 16240 Pyramidal Horn H-Plane – 0.109 m, E-Plane – 0.079 m Length – 0.24 m
<b>Frequency &amp; Wavelength</b>	10 GHz, $\lambda \approx 0.03$ m
<b>Distance to AUT Far-Field</b>	$\approx 1.2$ m
<b>Waveguide Probe</b>	WR90
<b>Distance to sampling plane</b>	$Z_0 = 0.15$ m
<b>Maximum sampling plane</b>	$S_X = 0.4$ m, $S_Y = 0.4$ m
<b>Sample spacing 1</b>	$\Delta x_1 = 0.015$ m, $\Delta y_1 = 0.015$ m ( $\lambda/2$ )
<b>Number of samples in plane 1</b>	$N_{X1} = (X/\Delta x_1) + 1 = 27$ $N_{Y1} = (Y/\Delta y_1) + 1 = 27$
<b>Width of sampling plane 1</b>	$\pm X_{MAX1} = 0.195$ m, $\pm Y_{MAX1} = 0.195$ m
<b>Spectral width 1</b>	$\pm k_{XMAX1} = \pi/\Delta x_1 = 66.7\pi$ rads/m $\pm k_{YMAX1} = \pi/\Delta y_1 = 66.7\pi$ rads/m
<b>Valid angle <math>\theta_V1</math> Valid Beamwidth <math>\theta_{BW1}</math></b>	$\theta_{XV1} \approx 43^\circ$ $\theta_{XBW1} \approx 86^\circ$ $\theta_{YV1} \approx 46^\circ$ $\theta_{YBW1} \approx 92^\circ$
<b>Sample spacing 2</b>	$\Delta x_2 = 0.005$ m, $\Delta y_2 = 0.01$ m
<b>Number of samples in plane 2</b>	$N_{X2} = (X/\Delta x_2) + 1 = 134$ $N_{Y2} = (Y/\Delta y_2) + 1 = 41$
<b>Width of sampling plane 2</b>	$\pm X_{MAX2} = 0.198$ m, $\pm Y_{MAX2} = 0.2$ m
<b>Spectral width 2</b>	$\pm k_{XMAX2} = \pi/\Delta x = 333.3\pi$ rads/m $\pm k_{YMAX2} = \pi/\Delta y = 100\pi$ rads/m
<b>Valid angle <math>\theta_V2</math> Valid Beamwidth <math>\theta_{BW}</math></b>	$\theta_{XV2} \approx 44^\circ$ $\theta_{XBW2} \approx 88^\circ$ $\theta_{YV2} \approx 47^\circ$ $\theta_{YBW2} \approx 94^\circ$
<b>Reference phase shift per sample</b>	$\theta_{XI} = 2\pi/3$ rads ( $120^\circ$ ) $\theta_{YI} = 0$
<b>Apparent reference beam angle</b>	$\theta_{XR1} \approx 0.73$ rads or $41.81^\circ$ $\theta_{XR2} \approx 3.38$ rads or $193.68^\circ$

Table 8.1 Measurement Parameters Used For Pyramidal Horn

## 8.4 Simulation Of Reduced Sample Spacing For Pyramidal Horn

The simulation is formed using the parameters defined Table 8.1 and is structured in the following way. To generate the Off-Axis hologram first the Near-Field of the pyramidal horn must be found and a suitable reference wave defined then the intensity between the two can be formed by application of (5.6).

To form the antenna Near-Field firstly the antenna aperture must be defined. For a pyramidal horn the aperture can be considered to exhibit a  $TE_{10}$  mode illumination i.e. cosine in the H-plane, uniform in the E-plane and a spherical phase cap due to the horn flare in both planes, the resolution of the aperture is  $\lambda/30$  (1 mm) [2]. Using Huygens principal, as per (7.2), the complex field is calculated for each of the two sampling criteria over the sampling plane. The reference field is defined in the same form as that of (7.3), uniform in magnitude (equal to the central Near-Field component) with  $\theta_{XI} = 120^\circ$  and  $\theta_{YI} = 0^\circ$  for both sampling criteria over the same sampling planes. The approximated aperture illumination and the calculated Near-Field distributions for each sampling criteria, are shown in Figure 8.6 and Figure 8.7.

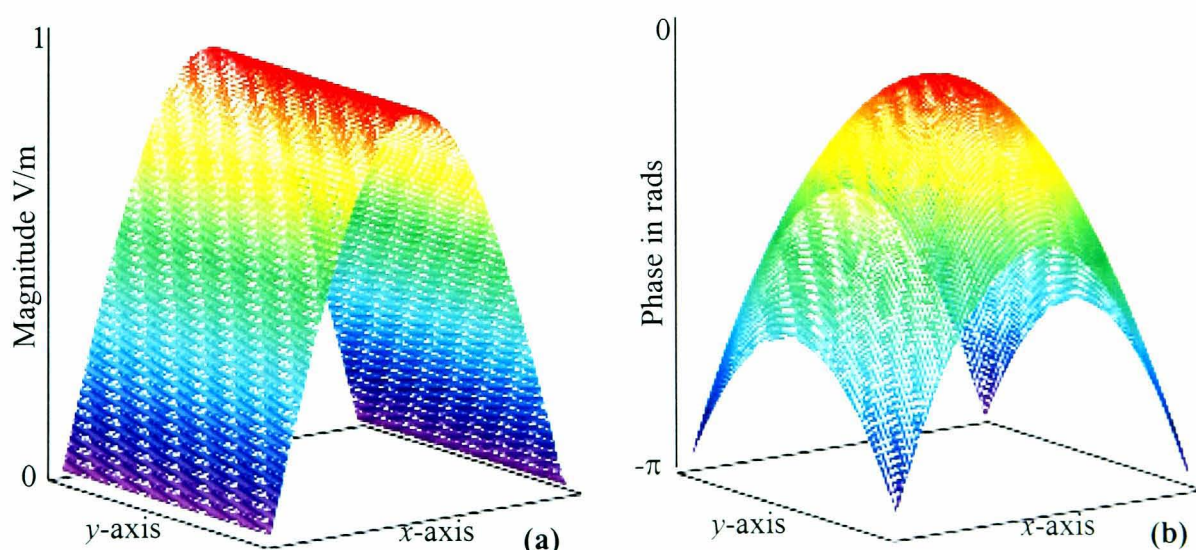
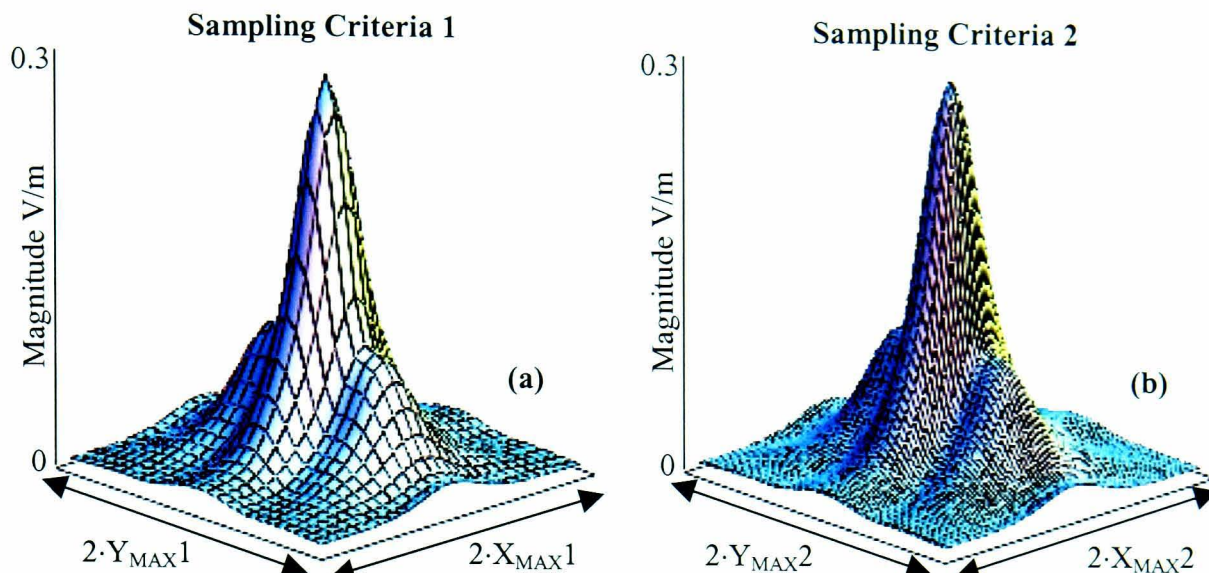
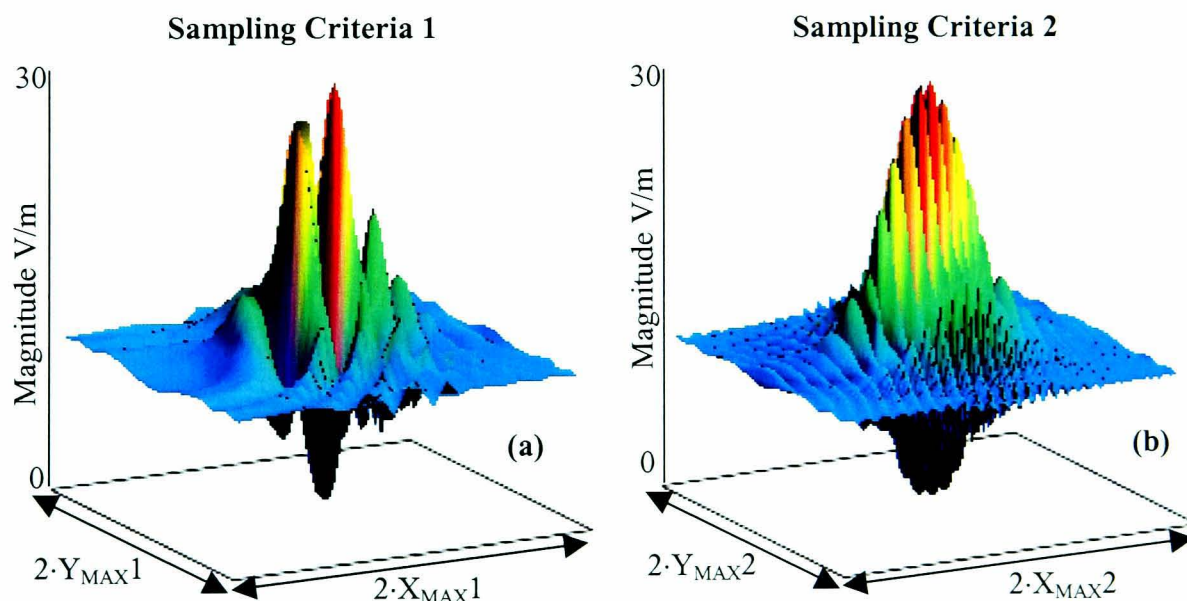


Figure 8.6 Simulated Flann 16240 Pyramidal Horn  $TE_{10}$  Aperture Illumination  
(a) Magnitude And (b) Phase



**Figure 8.7** Flann 16240 Pyramidal Horn Near-Field Magnitude Distribution For (a) Sampling Criteria 1  $\Delta x = \Delta y = \lambda/2$  And (b) Sampling Criteria 2  $\Delta x = \lambda/6$   $\Delta y = \lambda/3$  Calculated From The Aperture Distribution In Figure 8.6

The intensity between the Near-Field of the pyramidal horn and the reference wave for each of the sampling criteria is formed at each point in the sampling plane, these are shown in Figure 8.8. The intensity pattern generated by sampling criteria 1 varies much less rapidly than sampling criteria 2, this should be expected since the phase of the reference is changing three times as fast.



**Figure 8.8** Intensity Patterns Formed Between Simulated Near-Field Of Figure 8.7 And A Reference Wave With  $\theta_{NI} = 120^\circ$  For (a) Sampling Criteria 1  $\Delta x = \Delta y = \lambda/2$  And (b) Sampling Criteria 2  $\Delta x = \lambda/6$   $\Delta y = \lambda/3$

The intensity patterns undergo DC subtraction followed by zero buffering prior to the FT in order to obtain the spectrums of the intensity patterns; as shown in Figures 8.9

and 8.10. The one-dimensional cuts in these two figures show the ability of the two sampling criteria to provide separation of the terms along the  $k_x$  axis in the intensity spectrum. Sampling criteria 1 ( $\Delta x = \lambda/2$ ,  $\Delta y = \lambda/2$ ) fails to provide adequate separation of the terms, however for sampling criteria 2 ( $\Delta x = \lambda/6$ ,  $\Delta y = \lambda/3$ ), three separated regions are clearly observed along the  $k_x$  axis.

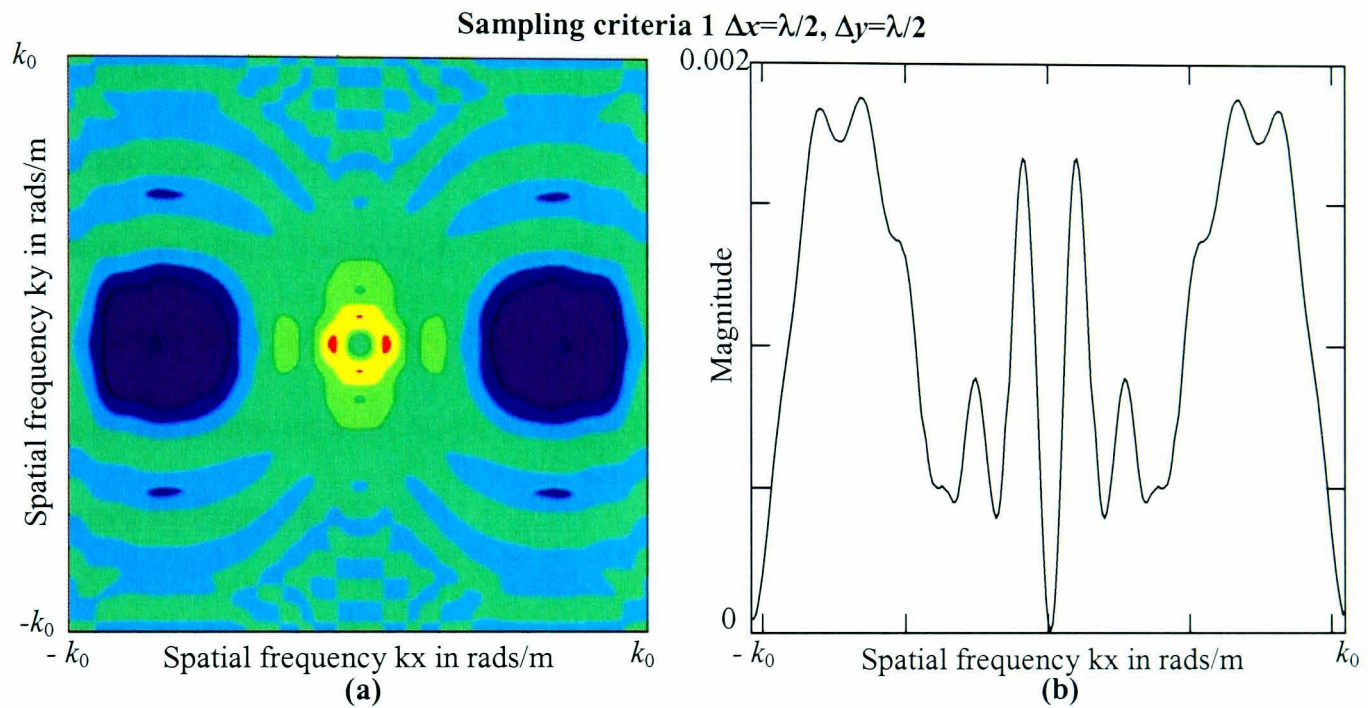


**Figure 8.9 Spectral Distribution Of Figure 8.8(a) Sampling Criteria 1 As (a) Contour Plot And (b) Cut Through The Centre Of The  $y$ -axis**

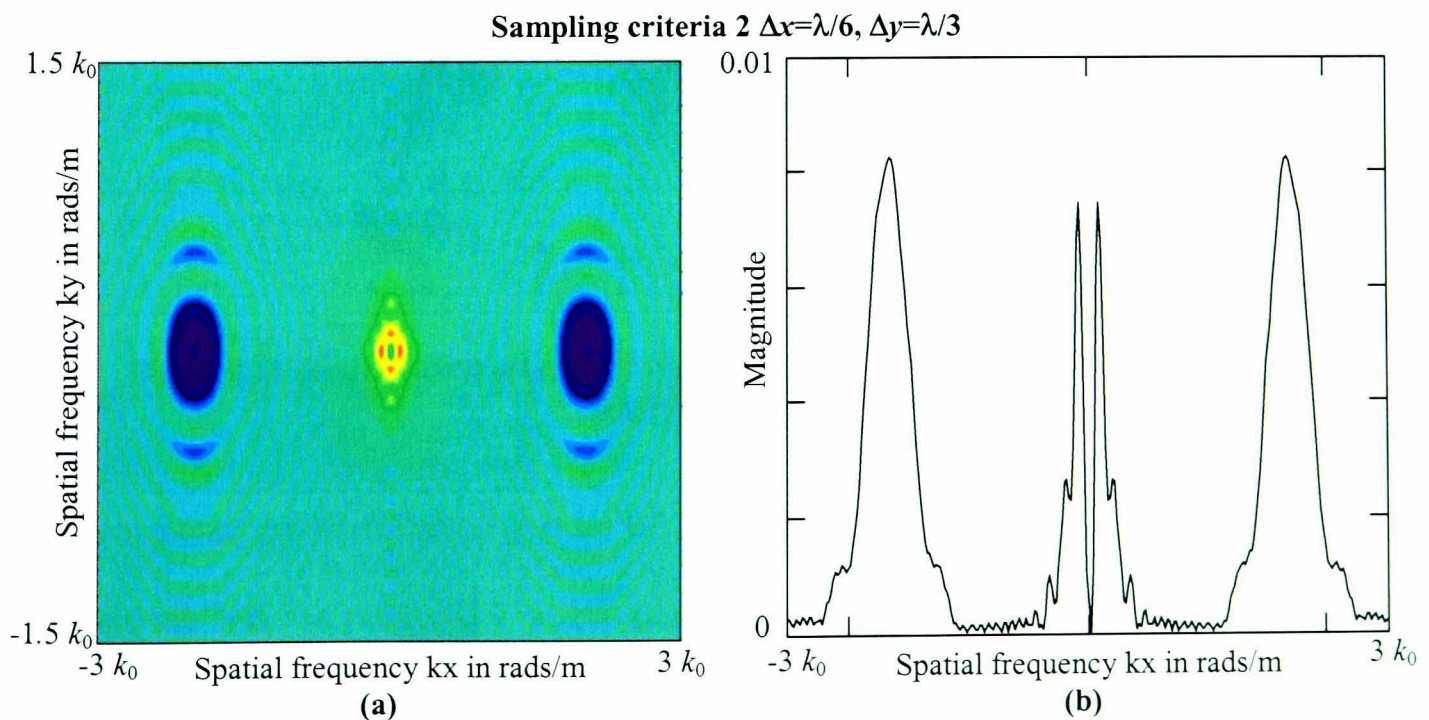


**Figure 8.10 Spectral Distribution Of Figure 8.8(b) Sampling Criteria 2 As (a) Contour Plot And (b) Cut Through The Centre Of The  $y$ -axis**

Having shown the inability of standard  $\lambda/2$  sample spacing in the direction of the phase gradient to provide adequately separated components and hence allow the PWS of the pyramidal horn to be obtained, no further post processing concerning the standard sample spacing will be shown.

To obtain the Far-Field radiation pattern, the PWS is filtered from the intensity spectrum. The reference phase increment angle is  $120^\circ$  and as such it is the lower component in the intensity spectrum, which represents the real AUT PWS image, while the upper component is the conjugate image. The component is filtered from the spectrum at cut-off angles of  $\pm\theta_{XV}$  and  $\pm\theta_{YV}$  and then centred at zero degrees. The Far-Field radiation pattern as in previous chapters is calculated via (3.5), the result is shown in Figure 8.11.

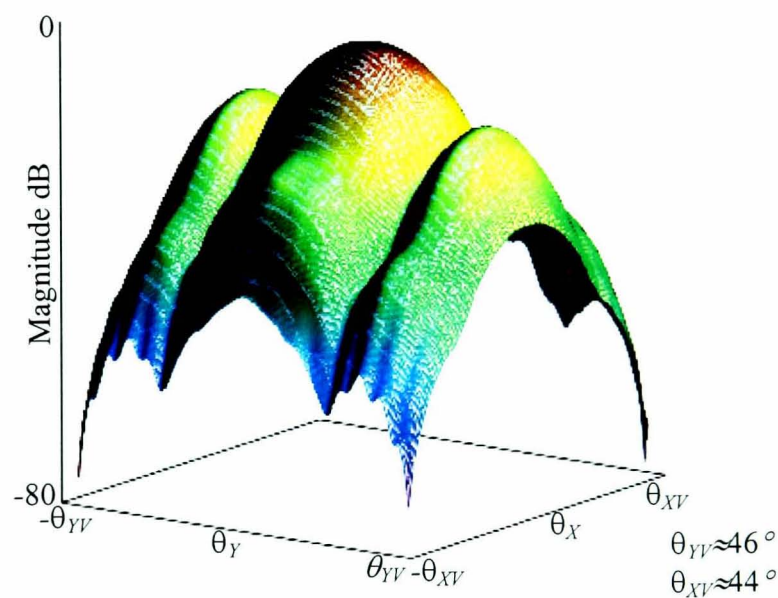


**Figure 8.11 Simulated Far-Field Radiation Pattern Of Pyramidal Horn Obtained Using Sampling Criteria 2**

To evaluate the Far-Field in Figure 8.11 obtained using the indirect holographic slow wave method, the principal E and H planes are shown in Figure 8.12 together with the Far-Field calculated by application of the direct holographic method (Near-Field to Far-Field transform as in Chapter 3) with the same parameters as sampling criteria 1

and the Far-Field obtained by performing Fresnel integrals over the aperture distribution to provide a non-beam limited Far-Field approximation [2].

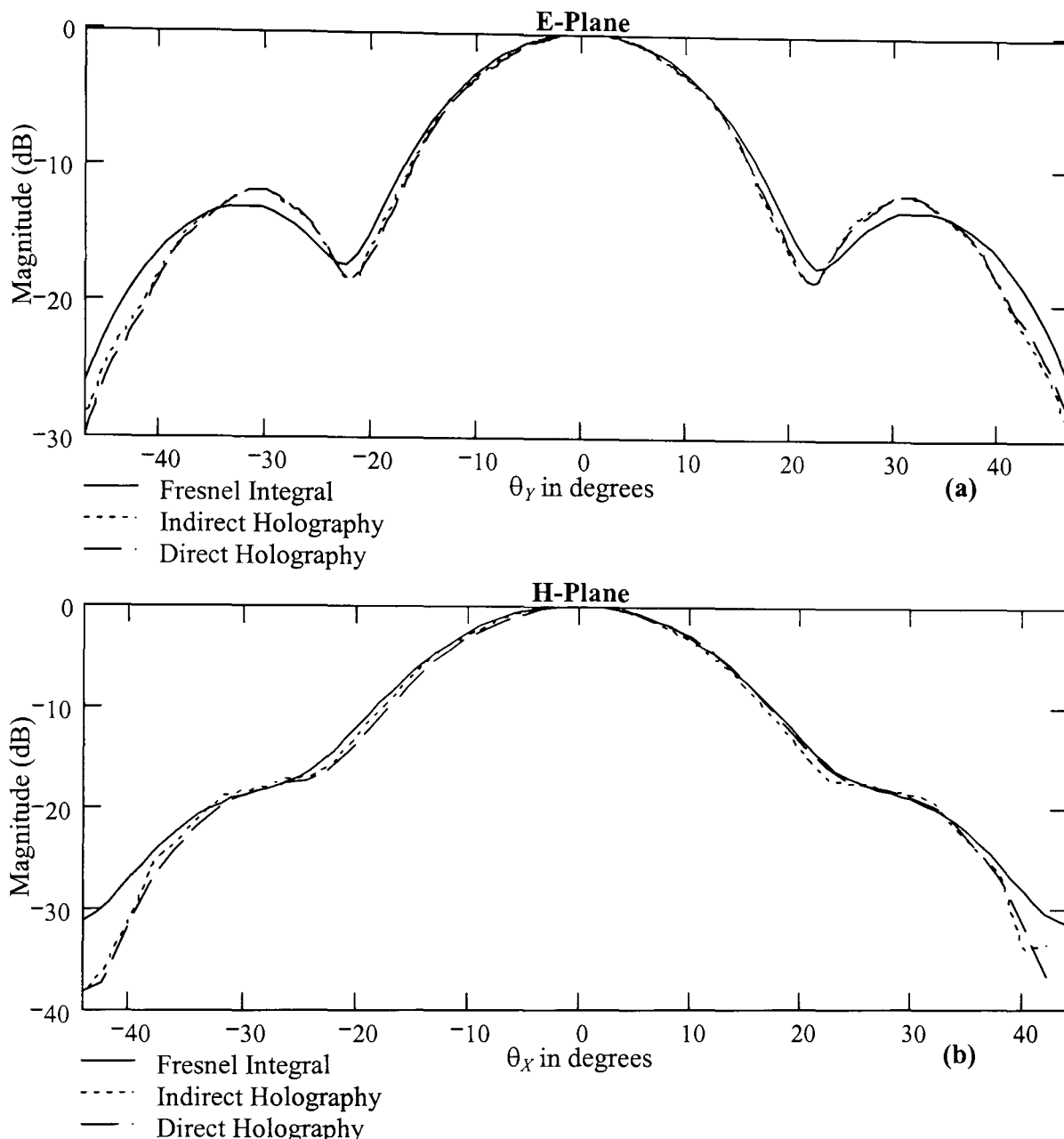


**Figure 8.12 Comparison Of Pyramidal Horn Far-Field Principal (a) E-Plane And (b) H-Plane Produced Through Simulation Using Fresnel Integrals And Direct/Indirect Holography For Sampling Criteria 2**

From the comparisons in Figure 8.12, it is seen that the two holographic methods performed over the same size sampling aperture produce Far-Field results that vary within 0.1 dB over the valid angle in both planes. Although the direct holographic method requires three times less samples than the indirect method this decreased sampling would come at the expense of having to use a VNA. Comparing the two holographic methods to the Fresnel integrals, the effect of beam-limiting on the two

holographic methods due to the size restriction of the sampling plane can be seen. The effect of beam-limiting is more apparent in the E-Plane where the aperture field is uniform producing bigger sidelobes and a wider angular spread than in the H-Plane.

Having obtained the AUT PWS and thereafter the Far-Field using the indirect holographic method and verified it using two further simulations, the original aperture field can also be found by back propagation of the PWS prior to the inverse transform, as per (3.18). A comparison of the defined aperture illumination and the aperture field reconstructed from the indirect holographic technique through the centre of each axis  $(x, y)$ , is shown in Figure 8.13.

The reconstructed aperture field follows the general trend of the initial aperture illumination in both planes. The difference between the two is once again the result of beam-limiting and again the effect is more visible in the  $y$ -axis (E-Plane) due to the initial uniform illumination. Simulations have been performed to show that by extending the sampling plane to encapsulate more of the Near-Field results in the aperture reconstruction get closer to the initial aperture illumination.

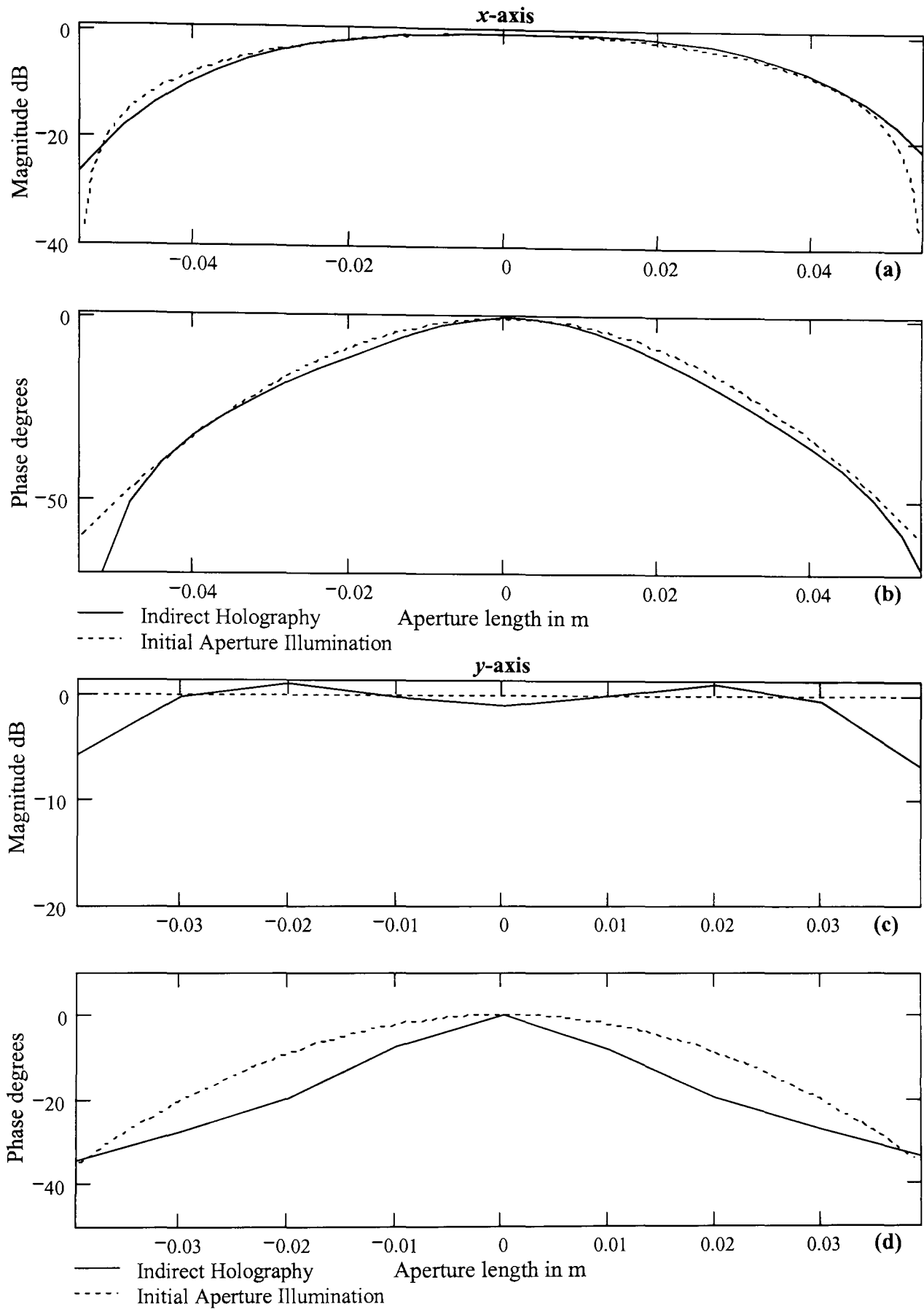


**Figure 8.13 Comparison Of Initial Aperture Illumination and Reconstructed Aperture Field From Indirect Holographic Processing Using  $\lambda/6$  Sample Spacing (a) Magnitude Across Centre Of The x-axis (b) Phase Across Centre Of The x-axis (c) Magnitude Across Centre Of The y-axis (d) Phase Across Centre Of The y-axis**

The process of reducing the sample spacing while maintaining a constant phase gradient to provide better separation of the terms in the intensity spectrum and hence allow medium gain antennas to be measured utilising this ‘slow wave’ technique has now been verified by simulation, for the given system parameters. The process will now be physically implemented to show that it is also possible in practice.

## 8.5 Practical Measurement Of Pyramidal Horn Using Reduced Sample Spacing

The pyramidal horn described above is measured using the novel indirect holographic technique with both standard and reduced sample spacing. The Far-Field radiation pattern is obtained using the indirect holographic technique and then compared with direct Far-Field measurements and direct holographic Near-Field measurement.

The measurement system is the same as that described in section 7.4 and the photograph in Figure 7.8, however a pyramidal horn antenna replaces the parabolic dish. Also the pair of phase shifters used to achieve the linear phase gradient must be re-calibrated to work at the chosen frequency, 10 GHz the phase shifter settings and associated characteristics are given in Table 8.2.

Phase Shifter		Required Phase Angle (degrees)	Actual Phase Angle (degrees)	Attenuation (dB)
A	B			
0	2.98	0°	0.01	-0.614
9	3.94	120°	119.79	-0.629
0	7.96	-120°	-121.08	-0.926

Table 8.2 Phase Shifter Settings At 10 GHz

The indirect holographic measurements performed using both sampling criteria are discussed below followed by a comparison of the Far-Fields obtained using the three techniques as discussed.

### **8.5.1 Indirect holographic measurement of medium gain pyramidal horn antenna (sampling criteria 1)**

The intensity pattern resulting from the application of sampling criteria 1 in Table 8.1 where  $\Delta x = \lambda/2$  is and  $\Delta y = \lambda/2$  is shown in Figure 8.14. The reference wave has been set approximately equal in magnitude to the central Near-Field component to provide a large dynamic range using the third variable phase shifter and variable attenuator.

The intensity pattern is of the form expected, i.e. large and rapid variation in the  $x$ -axis in line with the reference phase variation and slower in the  $y$ -axis with zero reference phase shift. From the intensity pattern it can be seen that in the  $x$ -axis the interference has reduced to almost a constant level towards the edge of the scan plane, identifying that the AUT field has reduced to almost zero, however in the  $y$ -axis the near uniform aperture illumination gives rise to higher sidelobe levels, therefore the Near-Field has not decreased to a negligible level at the extent of the scanning aperture.

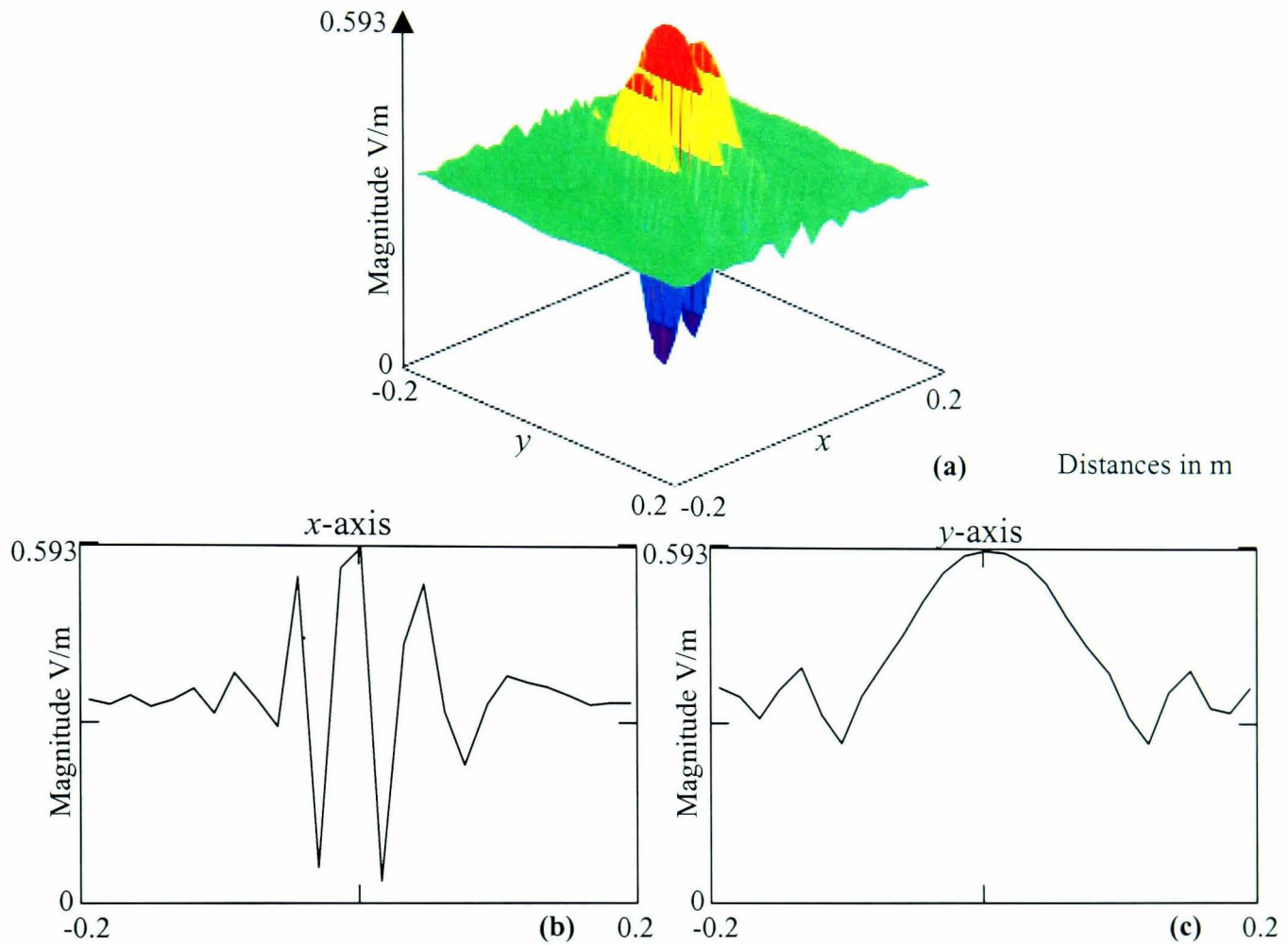


**Figure 8.14 Measured Two-Dimensional Intensity Pattern For Pyramidal Horn For Sampling Criteria 1  $\Delta x = \Delta y = \lambda/2$  and  $\theta_{XI} = 120^\circ$  (a) Surface Plot Of Measured Data, (b) Cut Through Centre Of The x-axis And (c) Cut Through Centre Of The y-axis**

The intensity spectrum of Figure 8.15 is obtained after DC removal and zero buffering.

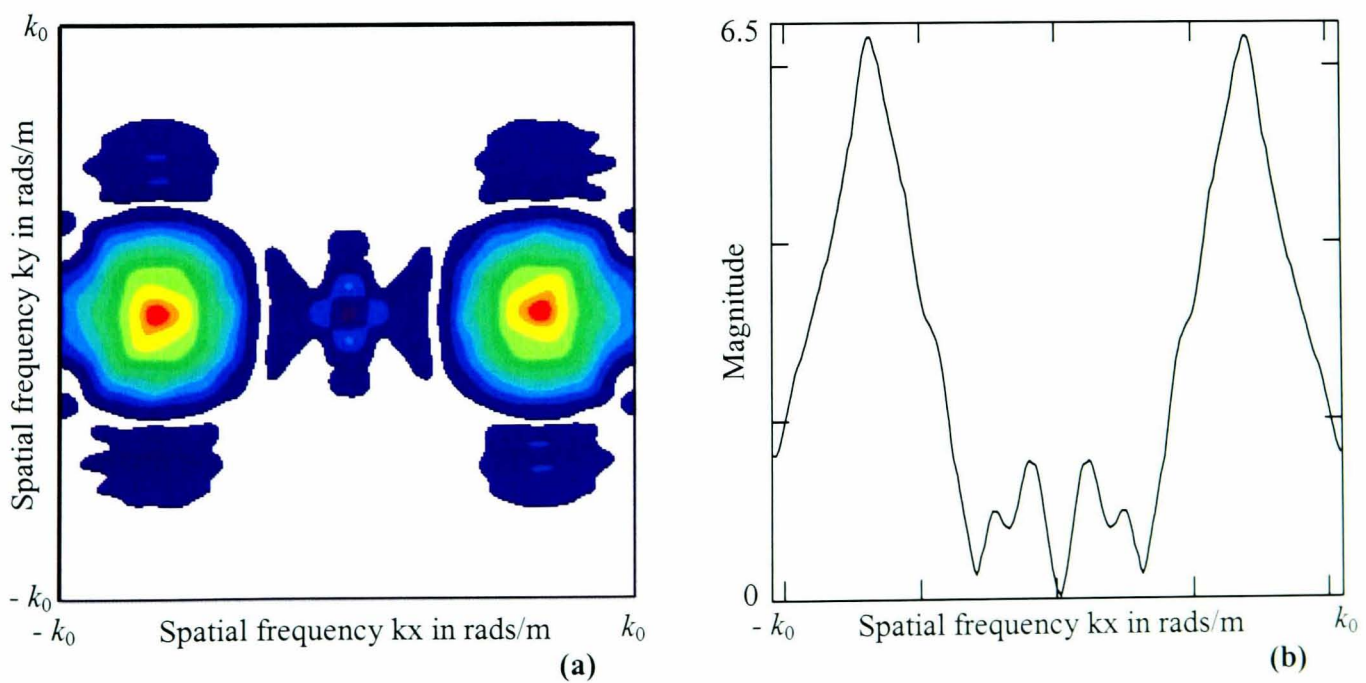


**Figure 8.15 Spectral Distribution Of Intensity Pattern In Figure 8.14 Using Sampling Criteria 1 (a) Contour Plot And (b) Cut Through The Centre Of The y-axis**

Once again, as in the simulation, it is clear from this spectrum that the AUT PWS is not suitably separated and cannot be filtered from the spectrum due to the interference between the components. No further processing will be completed for sampling criteria 1, the reduced sample spacing scheme of sampling criteria 2 in Table 8.1 will now be employed as in the simulation, to show that the AUT PWS can be separated from the other terms in the intensity spectrum.

### **8.5.2 Indirect holographic measurement of medium gain pyramidal horn antenna (sampling criteria 2)**

Having shown both, in practice and through simulation that standard sample spacing of  $\lambda/2$  cannot be implemented here to attain the AUT PWS, sampling criteria 2 from Table 8.1 is now applied in practice;  $\Delta x = \lambda/6$  and  $\Delta y = \lambda/3$ .

The Intensity pattern measured is shown in Figure 8.16 the variation in the  $x$ -axis varies much more rapidly than that seen in Figure 8.14, due to the increased rate of change in reference wave phase across the plane. The  $y$ -axis displays a slower variation, since the reference does not change phase in this direction. It is worth noting at this point that in observing the  $x$ -axis cut through the intensity pattern towards the extents of the sampling plane ripple exists, the effect of this ripple will be seen and discussed later. Also as expected from the simulation the pattern in the  $y$ -axis has not yet converged to the constant value signifying that the sampling plane has not intersected the whole AUT Near-Field.

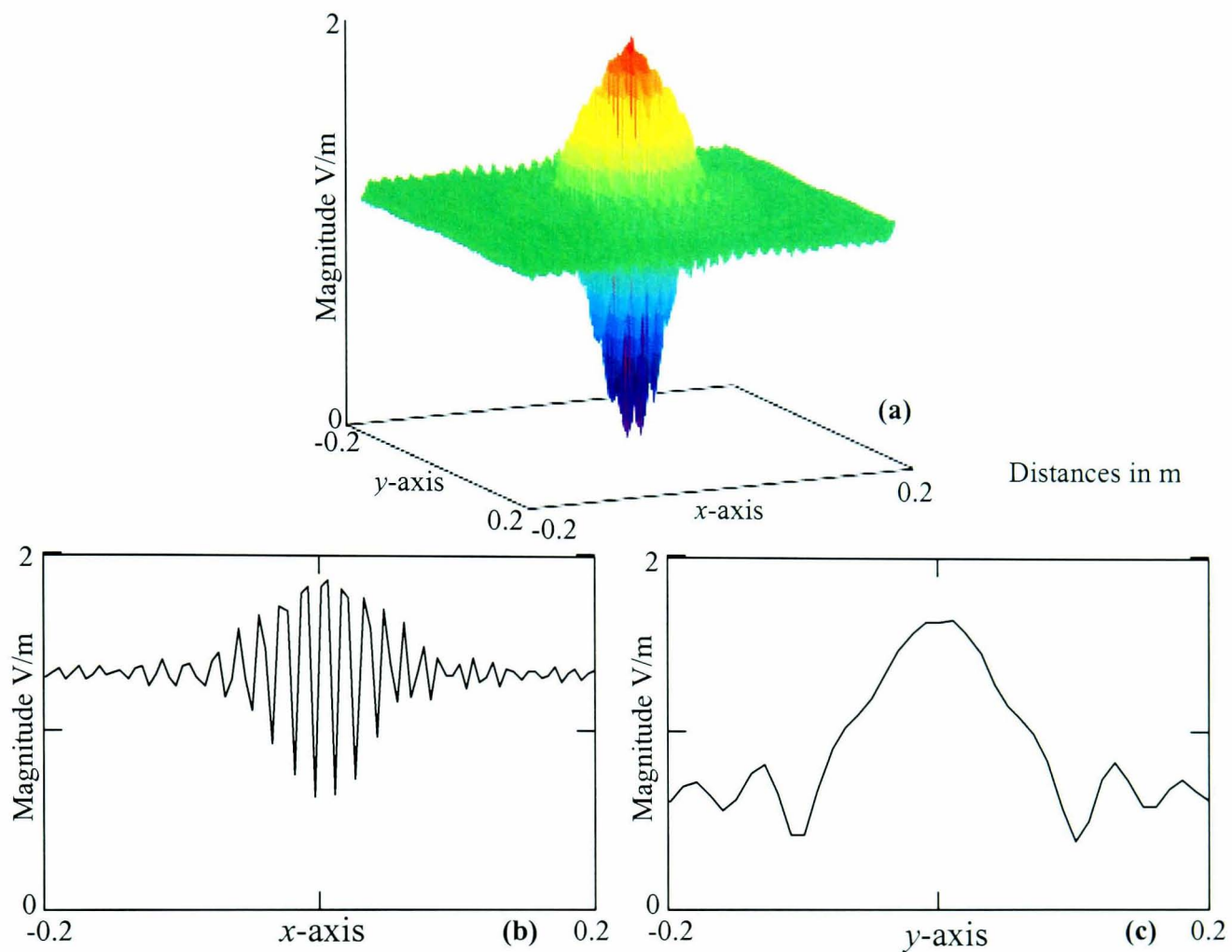


**Figure 8.16 Measured Two-Dimensional Intensity Pattern For Pyramidal Horn For Sampling Criteria  $2 \Delta x = \lambda/6$   $\Delta y = \lambda/3$  and  $\theta_{MI} = 120^\circ$  (a) Surface Plot Of Measured Data, (b) Cut Through Centre Of The  $x$ -Axis And (c) Cut Through Centre Of The  $y$ -axis**

The spectrum obtained after DC removal and zero buffering is shown in Figure 8.17. The reduced sample spacing is seen to provide separation of the components allowing the AUT PWS to be filtered from the spectrum at the valid angles.

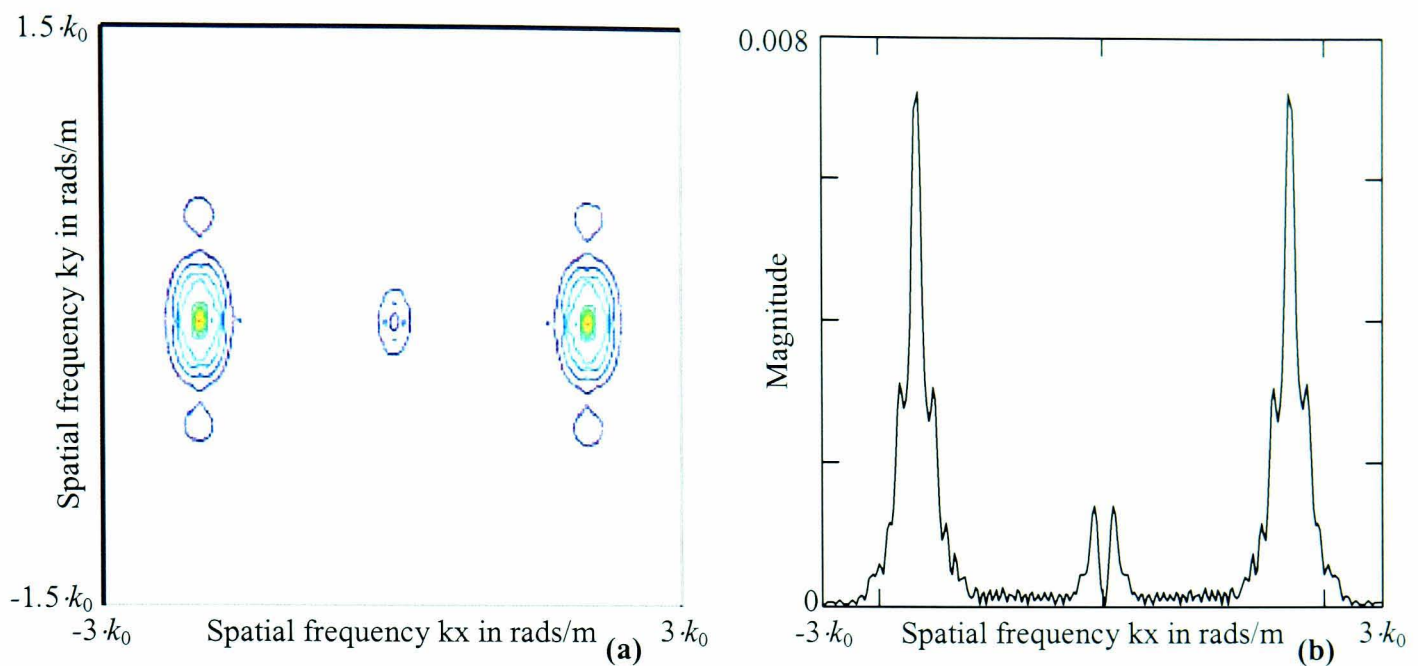


**Figure 8.17 Spectral Distribution Of Intensity Pattern In Figure 8.14 Using Sampling Criteria 2  
(a) Contour Plot And (b) Cut Through The Centre Of The  $y$ -axis**

The Far-Field radiation pattern is shown in Figure 8.18, it is immediately apparent that there is a large ripple component emanating from the centre of the Far-Field pattern. The ripple has a greater effect across the H-Plane in line with the reference phase gradient. The extent of the ripple is more visible in the principal plane cuts of Figure 8.21, where a comparison is made between the three techniques used to obtain the Far-Field of the pyramidal horn.

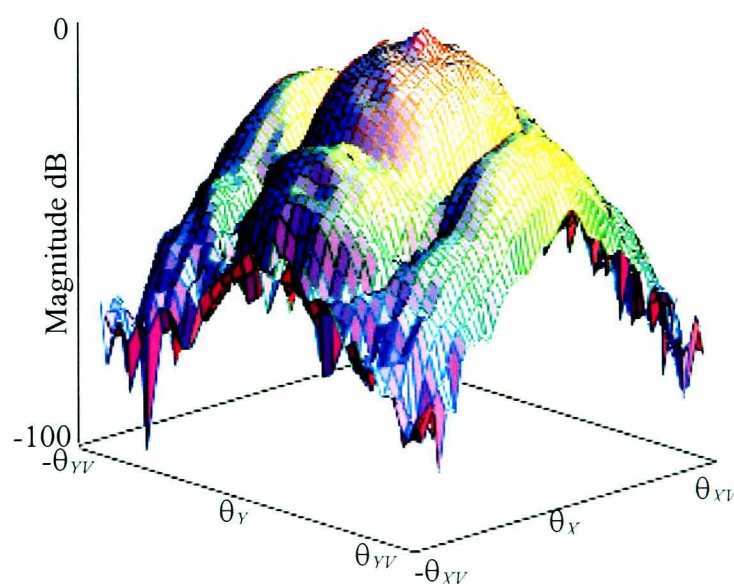


**Figure 8.18 Far-Field From Pyramidal Horn Sampling Criteria 2**

### 8.5.3 Direct holographic measurement of medium gain pyramidal horn antenna

The processing of the direct holographic data is not included here, as it follows the same processing defined in previous chapters. The measurements were recorded as in previous examples with standard sample spacing of  $\lambda/2$  in both axes. The recorded data and Far-Field radiation pattern obtained from the Near-Field Far-Field transform process are shown in Figure 8.19 and Figure 8.20.

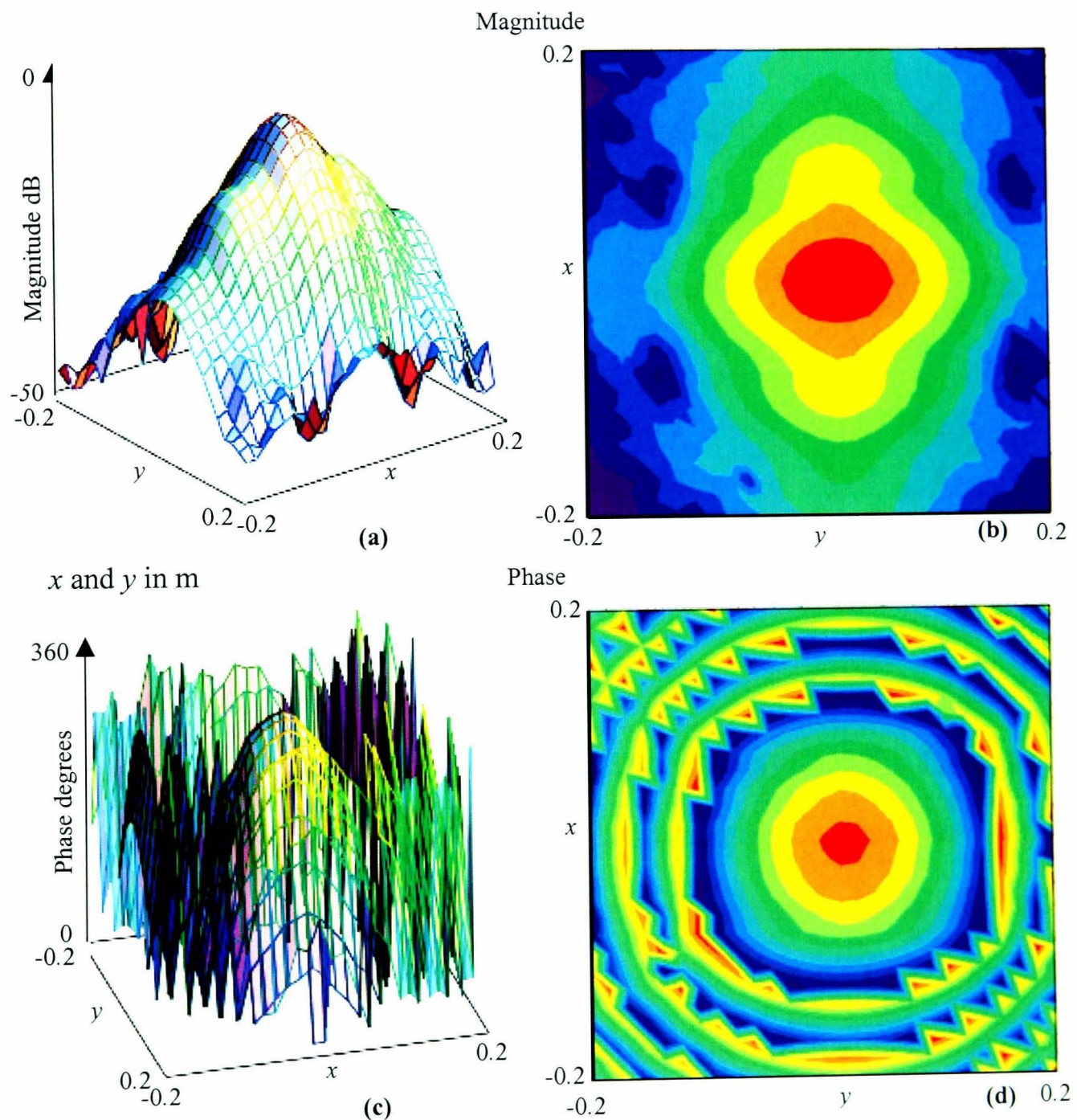


**Figure 8.19 Measured Complex Near-Field Magnitude (a) Surface Plot, (b) Contour Plot And Phase (c) Surface Plot And (d) Contour Plot**

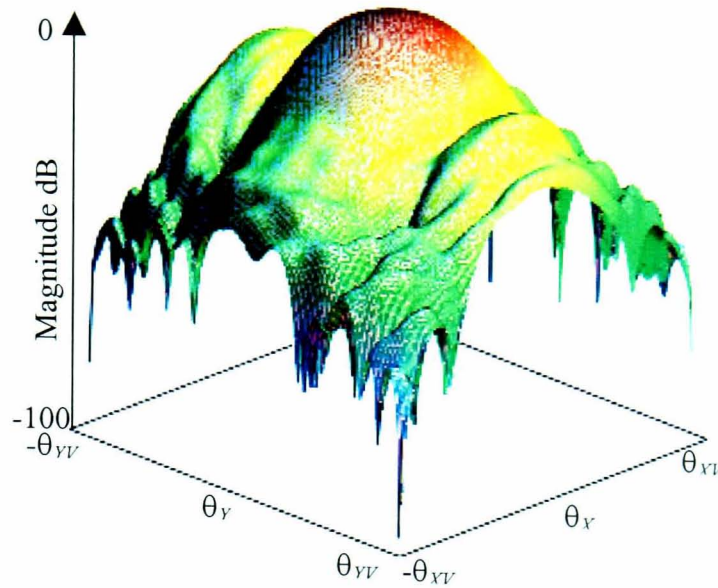


**Figure 8.20 Far-Field Radiation Pattern Of Pyramidal Horn Obtained From Complex Near-Field Measurements**

#### **8.5.4 Comparison of pyramidal horn Far-Field patterns**

The principal planes of the Far-Field radiation patterns obtained through direct Far-Field measurement, Direct Holography and ‘slow wave’ Indirect Holography are compared in Figure 8.21.

The ripple in the Far-Field, obtained via the ‘slow wave’ Indirect Holographic technique is clearly visible when compared to the principal planes obtained using the other two techniques. The ripple is generated because of the variation in attenuation between the three settings on the phase shifters. Due to the technique used, the reference wave appears as a three level step function, periodic with every third sample point in the direction of the phase shift. As a result of this, the magnitude of the reference wave component of the intensity pattern is not uniform. This means that the reference magnitude  $R$  in the third and fourth terms of (5.6) should be changed to represent the stepped function. The consequent FT of these two terms then becomes a convolution of the two functions. The step function generates a *sinc* component in the spectrum centred at the same location as the AUT Near-Field giving rise to the

apparent ripple. This will be discussed further in the next section regarding the system limitations. Due to the contamination of the PWS by the periodic step function, the back propagation of the PWS to find the aperture distribution has not been included.

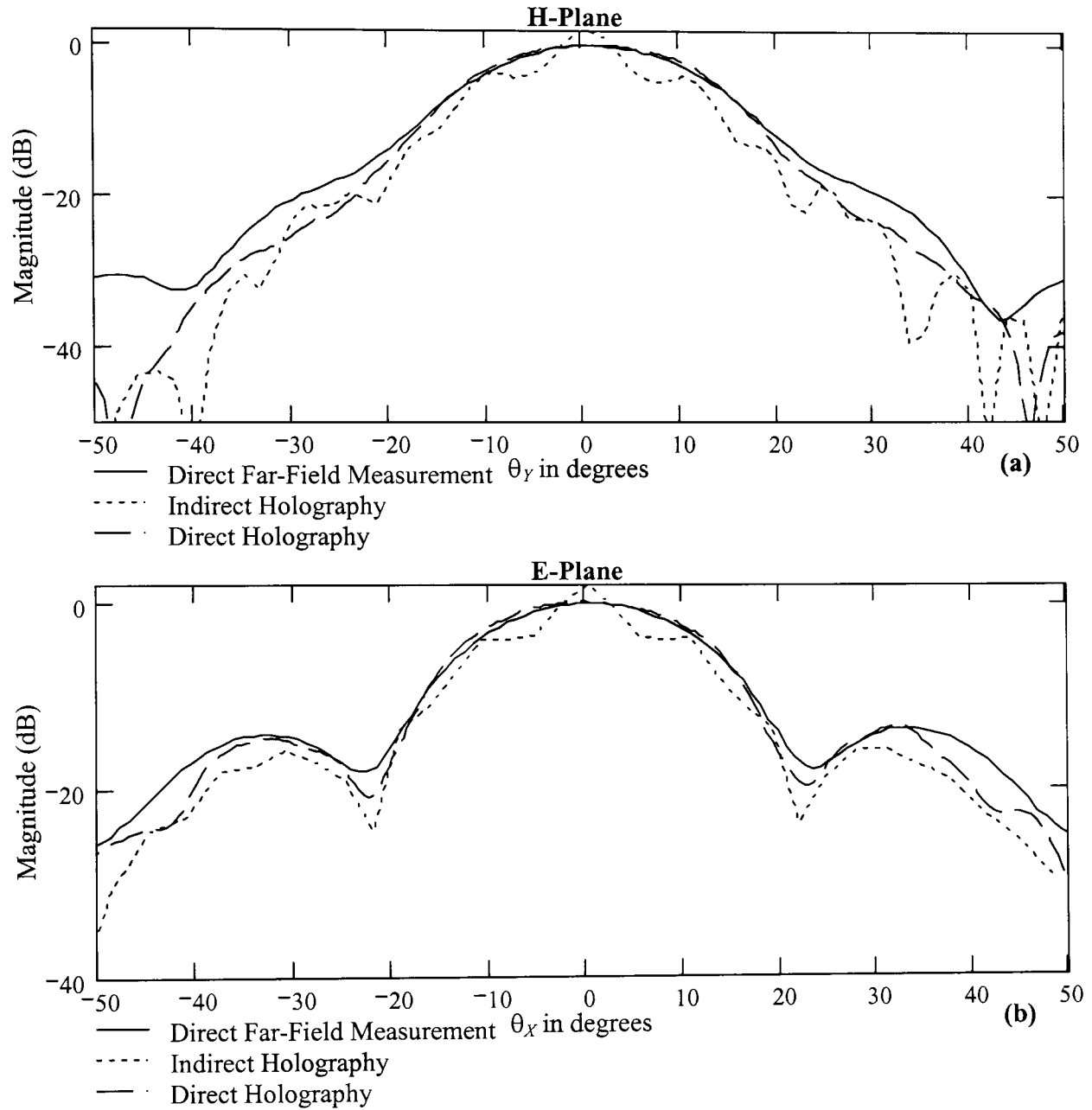


**Figure 8.21 Comparison Of Far-Fields Of Pyramidal Horn In The Principal (a) H-Plane And (b) E-Plane Obtained Using Direct Far-Field Measurement, Direct Holographic Measurement And Indirect Holographic Measurement Using Sampling Criteria 2**

## 8.6 System Limitations

The ability of the process discussed to match standard planar Near-Field antenna measurement techniques (Near-Field to Far-Field transform) for the measurement of a medium gain horn antenna over the same size sampling window has been shown in simulation.

The limitations of the scanning system are the same here as in Chapter 7 for the measurement of the pyramidal horn, the overriding physical limitation still being the size of the scanning plane in relation to the antennas available for test and the inherent beam-limiting this forces on the measurements. In the case of the 'slow wave' reference generation an additional limitation has been introduced which requires further discussion.

As described previously the ripple is introduced into the Far-Field pattern due to the stepped nature of the reference wave. This step is derived from the non-ideal attenuation response of the variable phase shifters used. The magnitude characteristic produced by a traditional radiated reference wave is also non-linear, however providing the radiating element used to produce the off-axis reference wave has been chosen carefully, its magnitude response over the sampling plane will be a slowly varying continuous function. In comparison the stepped response produced by the phase shifters has square edges and a periodicity set by the sample spacing and as such has a more prominent spectral content.

The ripple effect was not apparent in the measurements of the parabolic dish at 12.7 GHz because of the perceived frequency of the step change. The problem is

compounded when moving to smaller sample spacing as the frequency content of the reference step function is increased. At  $\lambda/2$  sample spacing as used at 12.7 GHz the period of the ripple produced is wider than the valid angle observed and so no effect is apparent.

The variation in attenuation across the phase shifters between the three settings used is approximately  $\pm 0.2$  dB. The repeatability of these values was of the order of  $\pm 0.1$  dB, it is envisaged that if improved variable phase shifters or multiple fixed phase shifters were used, this problem could be overcome. An initial study by simulation suggests that the reference could exhibit a total deviation of approximately  $\pm 0.1$  dB, before the effect of the ripple becomes apparent.

## 8.7 Summary

In this chapter the synthetic reference wave technique developed in the previous two chapters has been built on to enable the system to be applied to the measurement of medium gain antenna. The introduction of a so called ‘slow wave’ reference explained in section 8.2 showed that there is no restriction on the AUT in terms of obtaining separation in the intensity spectrum. It was shown that by having direct control of the phase increment per sample of the reference wave  $\theta_{XI}$  and  $\theta_{YI}$  rather than the intercept angle  $\theta_{XR}$  and  $\theta_{YR}$  that the phase offset of the object components can be increased by more than the  $90^\circ$  as would otherwise be the limit. This in turn allows the sample spacing to be used to make the spectrum wider while increasing the perceived intercept angle by maintaining the phase increment per sample.

From the relationships defined a definition for the minimum sample spacing based on the valid angle of the measurement system for a given antenna has been developed alongside an analysis of the optimal phase gradient to provide the best use of the spectrum width.

A simulation based on the available physical system and a medium gain pyramidal horn with standard illumination showed that the same level of information could be obtained using the novel 'slow wave' indirect holographic measurement approach described as was obtained using the standard complex Near-Field measurement theory. Comparison of these two techniques with a direct Far-Field calculation obtained using a standard Fresnel integral evaluation showed that the available measurement plane was not large enough to encapsulate the full energy radiated by the antenna.

The practical evaluation of 'slow wave' generation showed that separation of the three component regions can be physically achieved. However, it also highlighted that the device or devices used to produce the linear phase shift must provide the same attenuation for each of the phases required. If this is not the case then a ripple, induced by the periodic change in reference magnitude, contaminates the desired AUT PWS as was shown. Using fixed true time delays as phase shifters or a controllable variable rotary vane phase shifter could provide a more constant attenuation in the phase shifting. Alternatively a combination of phase shifters and an attenuator could be used to provide a constant level of attenuation.

Despite the inability of the equipment to provide a constant level of attenuation over the reference, it has been shown that the system can produce adequate separation of the terms in the intensity pattern and could be used to obtain the required information as proven by simulation.

# CHAPTER 9 CONCLUSIONS & FURTHER WORK

This aim of this chapter is to amalgamate all of the important findings of this research work, defining what has been gained as a result of the work and to show how the objectives initially identified have been addressed and their outcomes. A discussion of the direction in which this work can be taken forward and where the findings may be applied in other areas is also presented.

## 9.1 Conclusions

The motivation behind this work was derived from the desire to attain the radiation characteristics of microwave antenna, from intensity only Near-Field measurements and in doing so reduce the cost of traditional complex Near-Field measurement by dispensing of the need for an expensive VNA. More specifically, the objectives were focused on the method of antenna metrology concerned with indirect microwave holography via the Off-Axis hologram approach and its adoption from the optical region to the microwave region. The aims were rooted in the development of the mechanisms currently used to generate the Off-Axis reference wave required for an Off-Axis hologram in the microwave frequency region.

A novel system for the measurement of microwave antenna radiation patterns using indirect holography was presented in Chapter 6 after detailing the theoretical basis for the process. This novel technique has disposed of using a cumbersome second antenna that is unable to supply a plane reference wave at an angle to the hologram plane. Instead, waveguide phase shifters and attenuators have been employed to synthetically

generate a reference signal, which these components can directly control to provide the desired reference signal effect. A hybrid-tee is used to sum this synthetic reference wave and the antenna Near-Field signal, which is probed over a rectangular grid of regularly spaced sample points, as in any planar Near-Field measurement system. The interference between the two signals is obtained at each sample point from the output of a square law detector connected to the summation port of the hybrid-tee.

The advantages of utilising a bounded reference wave in this manner are four fold. Firstly, the ability to obtain the radiating characteristics of an antenna from intensity only measurements has been achieved and verified against the traditional complex Near-Field measurement. Showing that it is possible to replace the VNA (costing upwards of £60,000 depending on its frequency range), essential in direct phase measurement and integral to the standard Near-Field measurement technique, by a vastly cheaper square law detector (as simple as a diode), and the same level of information can be attained.

Secondly, the anechoic environment required to house this novel Off-Axis hologram system is attained, as no second radiating source for the reference needs to be present. The format of the system would allow it to be instantly adapted into any current planar Near-Field system as shown in Figure 6.1, all of the reference synthesis takes place separate from the anechoic environment.

Thirdly the reference wave properties over the entire sampling plane are directly controllable in comparison to previous implementations of the same technique. The angle at which the wave appears to be incident on the measurement plane can be

readily adjusted via a pair of phase shifters to provide a reference beam at any desired angle. The magnitude can also be easily adapted to provide the required reference wave amplitude depending on the AUT and with the addition of some extra hardware (to be discussed in further work), the uniformity of the reference wave can be monitored.

Fourthly, the direct control of the phase gradient in this case as opposed to the reference beam insertion angle, affords the opportunity to generate greater separation of the terms produced in the intensity spectrum as was discussed in Chapter 8. This presents the opportunity to apply the measurement technique in the testing of less directive antenna. Where previously due to the restricted spectral separability it had only been applied to large, highly directive antenna, which have narrow beamwidths and as such could be sufficiently separated. This increased separation comes at the expense of increasing the amount of data to be collected. However, the size of the sampling plane does not have to increase in comparison to that used for traditional Near-Field measurements for any given antenna.

The first two advantages listed are created as a direct result of the novel implementation proposed. They are both concerned with the ability to provide antenna designers and developers with a cheaper solution to the planar Near-Field measurement technique by a simple adaptation of their current facilities. The second two are concerned with the further development of the indirect holographic process, in relation to the measurement of antenna radiation patterns. This work has led to the development of a process which enables the technique to be applied to less directive antennas than previously.

The methodology used for data collection, is one of the novel concept of the system. Having restricted the phase gradient to form an integer multiple of a full cycle, therefore needing in this case only three phases to perform the full scan, the time required to first calibrate the phase shifters and second to collect the data is reduced. No time is taken between samples to change the phase as all locations in the sampling plane that exhibit the same reference phase are consecutively. Since the phase shifters are not changed at each sample point, the likelihood of errors occurring to the phase gradient of the synthetic reference wave is reduced. A minimum of three receivers could be used in conjunction with three fixed phase shifters to simultaneously collect all the three phase sets.

The main aim behind the development and implementation of the novel indirect holographic technique for this thesis was to enable the replacement of the VNA as an essential component in antenna Near-Field measurement facilities. To validate that the proposed system could be used to replace this equipment it was necessary to show that the same level of information could be attained. It has been shown through simulation that the two methods provide equivalent results. In the practical domain the both this novel indirect and the standard direct holographic techniques were implemented. The comparisons presented in Chapters 6 and 7, between the various antenna fields attained, from each of the techniques provided confirmation of the simulation results. This was especially true when the valid spectral content was taken of both techniques was taken into account.

In Chapter 8, a novel sampling criteria was derived, allowing the maximum sample spacing required in terms of a priori knowledge of the antenna valid beamwidth. The

ability to surpass what is physically possible by radiating the reference wave by synthesising a ‘slow wave’ through the direct control of the phase gradient was shown in simulation to allow the measurement technique to be applied to medium gain antenna. The practical verification of this ‘slow wave’ technique highlighted the necessity to have well calibrated phase shifters. The variation in attenuation produced by the phase shifters used generated an unwanted *sinc* component within the FT. Despite this the separation of the image component from the other intensity spectral components was successfully achieved.

In conclusion, a novel Off-Axis holographic system has been developed and its ability to produce Off-Axis holographic intensity patterns using the synthetic reference wave has been observed. It has also been shown that from the intensity only data collected in the Near-Field of an antenna, it is possible attain the antennas Far-Field radiation pattern. Verification of this was made by the utilisation of the same scanning system to record complex Near-Field data over the same sampling plane followed by the application of standard Near-Field to Far-Field transformation theory. The verification process confirmed that the novel method could produce the same level of Far-Field information. The capacity of the intensity only data to reconstruct the complex Near-Field and aperture field of the antenna was also demonstrated and verified. The further development of the ‘slow wave’ synthetic Off-Axis reference wave increases the versatility of the measurement technique, leading to the successful culmination of the initial research aim and objectives.

## **9.2 Further Work**

The excellent results presented throughout this thesis and the positive conclusions they have allowed to be drawn, regarding the capabilities of this novel system, have highlighted the importance and value of this work. However, the initial system constructed to perform the measurements has physical limitations, which have been appropriately discussed. One area of further work lies in dealing with these limitations.

As a direct result of the work on the development of this holographic system, a second area of interest has arisen, adopting the synthetic reference wave technique into the area of object imaging.

### **9.2.1 System development**

System developments fall into two three main categories, the first concerns the restricted scanning plane and scanning environment, the second relates to the generation of the synthetic reference wave and the third to the development of the receiver section of the system.

It is clear from the results presented, using both the direct and indirect holographic techniques, that the restricted scanning plane has a significant effect on the ability to construct the various fields of the antenna. The effect of beam-limiting demonstrates the necessity to use a measurement system with a larger scanning plane. To this end a planar measurement system capable of providing a 5 feet square scanning plane has recently been purchased by Northumbria University and will be utilised for, amongst

other things, the application of the novel antenna measurement system developed in this thesis.

Some enhanced environmental control should be applied to minimise noise contributions in to measurements. Although microwave absorber was used to reduce reflections from the immediate surroundings, a well-designed anechoic chamber would provide an added element of noise protection. The chamber should also be fitted with some form of alignment apparatus to ensure that the AUT and probe are located both parallel and square to each other, with the centre of the scanning plane aligned with the centre of the AUT.

The issue regarding the variation of the attenuation across the phase shifters currently utilised to generate the linear phase gradient, needs to be addressed. It could be possible to use an additional variable attenuator in series with the variable phase shifters during calibration in an attempt to produce the desired plane wave characteristic. However, continuing to use manually adjustable components leaves the process open to repeatability errors, and it is envisaged that the calibration process would become long and tedious. Use of a controllable, rotary vane variable phase shifter would be preferred to this. The repeatability of this would be much greater due to the computer control and the rotary vane design is more stable attenuation as the phase is changed. The final and most promising option, would be to manufacture true time delays (lengths of wire) based on the frequency of operation to provide the desired number of phase shifts. In this case where  $120^\circ$  has been used, three fixed phase shifts would be required. The implementation of these into the system, leads neatly into the discussion of receiver development.

To speed up the data collection process it is proposed that a minimum of three receivers should be used to simultaneously collect the three separate reference phase components. This would allow the reference arm of the system to be divided into three equal components with a splitter or coupler each with its fixed phase shifter (time delay). Since the three reference wave components required would be generated simultaneously and continuously, they could be easily adjusted to produce a high quality, Off-Axis plane wave and no problem regarding repeatability exists. This would require a set of time delay elements for each frequency at which testing is performed to maintain the  $120^\circ$  phase gradient.

A possible solution to the removal of the two auto-correlation terms in the Off-Axis hologram is also currently under consideration. Placing a directional coupler in the both reference arm and the arm attached to the probe samples of the magnitude of the two individual signal components (antenna Near-Field and Reference) measured simultaneously, allowing the removal of the auto-correlation terms produced in the intensity spectrum prior to the transform. This would provide more space in the intensity spectrum in which to separate the two object components (the real and conjugate PWS's).

This system has been designed around the measurement of antenna radiation patterns using a planar measurement surface, however the principle can be extended to other standard measurement surfaces as shown in Figure 2.5, this would allow antenna other than omni-hemispherical to be measured using this technique. Mathematical processes, as well as the construction of a measurement system, require investigation prior to the adoption of any further scanning surfaces.

Finally, most antenna manufacturers require not only the Far-Field radiation pattern of the antenna to be acquired, but also the gain of the antenna to be evaluated as part of the measurement procedure. A methodology for the measurement of antenna gain should be incorporated into the Off-Axis holographic measurement system.

### **9.2.2 Microwave imaging**

The area of microwave imaging is currently receiving a lot of attention especially in the areas of concealed weapon detection and medical imaging. A concurrent project to this thesis has been running looking at the application of the Off-Axis holographic technique to the area of object imaging, some initial results based on the system developed here, have been published by Smith and Leach et. al. [68], [69], [83], initial experimentation of imaging the magnitude and phase of various passive objects are highly encouraging.

One of the reasons that microwave imaging is currently receiving much attention, is that microwaves are a non-ionising form of radiation and as such pose no health risk to human tissue cells when used within reasonable power levels. In terms of medical imaging this is very important, as it reduces the risk of exposure to radiation such as X-rays, while maintaining sufficient image resolution due to the relatively short wavelength. One of the specific medical areas of particular interest is early cancer detection. It is known that the dielectric properties of a cancerous tumour even in the early stages are significantly different to those of normal tissues and therefore microwave imaging may provide an earlier detection of such tumours.

In the area of concealed object detection, such as weapons hidden about a body, there are already microwave systems under development by various companies around the globe. To date these systems have mainly concentrated on radiography methods. It is envisaged that in certain situations the phase information produced by an object may be more useful than magnitude information, this system may be able to offer the versatility of attaining both magnitude and phase information with an intensity only measurement instead of using a VNA to measure the phase directly, allowing a more cost effective system to be developed.

## REFERENCES

- [1] J. C. Bennett, A. P. Anderson, P. A. McInnes and A. J. T. Whitaker, 'Investigation Of The Characteristics Of A Large Reflector Antenna Using Microwave Holography', *Int. Symposium On Antennas And Propagation*, New York, U.S., 1973, pp. 298-301.
- [2] C. A. Balanis, 'Antenna Theory Analysis And Design', Second Ed., Wiley, New York, U.S., 1997.
- [3] R. C. Johnson, H. A. Ecker and J. S. Hollis 'Determination of Far-Field Antenna Patterns From Near-Field Measurements', *Proc. of the IEEE*, Vol. 61, No. 12, 1973, pp. 1668-1692.
- [4] 'Introduction To Antenna Measurement Theory' <http://www.orbitfr.com>, *ORBIT/FR Inc.*, 2003.
- [5] P. W. Arnold, 'The Slant Antenna Range', *IEEE Trans. On Antennas And Propagation*, Vol. AP-14, No. 5, 1966, pp. 658-659.
- [6] R. A. Heaton, 'Antenna Gain Calibration On A Ground Reflection Range', *IEEE Trans. On Antennas And Propagation*, Vol. AP-21, No. 4, 1973, pp. 532-537.
- [7] B. J. Kasstan, "The Satellite: "An Ideal Test Range For Accurate Earth Station Antenna Measurements"", *Sixth Int. Conf. On Antennas And Propagation ICAP-89*, Conf. Publ. No. 301, Vol. 1, 1989, pp. 473-477.
- [8] 'IEEE Standard Test Procedures For Antennas', *Publ. By IEEE Inc.*, 1979, distributed by Wiley, New York.
- [9] R. C. Johnson, H. A. Ecker and R. A. Moor, 'Compact Range Techniques And Measurements', *IEEE Trans. On Antennas And Propagation*, Vol. AP-17, No. 5, 1969, pp. 568-576.

- [10] K. S. Farhat and J. C. Bennett, 'A Semi Compact Range Facility For Fast Prediction Of Antenna Far-Field Patterns', *Fourth Int. Conf. On Antennas And Propagation ICAP-85*, Warwick, UK, Conf. Publ. No. 248, Vol. 1, 1985, pp. 199-202.
- [11] C. G. Parini, A. D. Olver, P. McNair and C. J. Prior, 'The Design, Construction And Use Of A Millimeterwave Compact Antenna Test Range', *Sixth Int. Conf. On Antennas And Propagation ICAP-89*, London, UK, Conf. Publ. No. 301, Vol. 1, 1989, pp. 345-350.
- [12] D. C. Chang, Z. X. Liao and C. C. Wu, 'Compact Antenna Test Range Without Edge Treatment And RF Anechoic Chamber' *IEEE Antennas And Propagation Magazine*, Vol. 46, No. 6, 2004, pp. 22-37.
- [13] A. Lonngvist, J. Ala-Laurinaho, J. Hakli, T. Koskinen, J. Mallat, A. V. Raisanen, J. Saily and J. Tuovinen, '*IEEE 34<sup>th</sup> European Microwave Conf. Proc.*', London, UK, Cat.-No. 04EX963, Vol. 2, 2004, pp. 553-556.
- [14] H. G. Booker and P. C. Clemmow 'The Concept Of An Angular Spectrum Of Plane Waves, And Its Relation To That Of Polar Diagram And Aperture Distribution', *Proc. IEE*, Vol. 97, 1950, pp. 11-17.
- [15] J. Brown, 'A Theoretical Analysis Of Some Errors In Aerial Measurements', *Journal Of IEE*, Vol. 105, Pt. C, 1958, pp. 343-351.
- [16] J. Brown and E. V. Jull, 'The Prediction Of Aerial Radiation Patterns From Near-Field Measurements', *Proc. IEE*, Paper No. 3649E, 1961, pp. 635-644.
- [17] D. M. Kerns, 'Analytical Techniques For The Correction of Near-Field Antenna Measurements Made With An Arbitrary But Known Measuring Antenna', *URSI-IRE Meeting*, 1963, pp. 6-7.
- [18] D. M. Kerns, 'Correction Of Near-Field Antenna Measurements Made With An Arbitrary But Known Measuring Antenna', *Electronics Letters*, Vol. 6, No. 11, 1970, pp. 346-347.

- [19] J. E. Hansen and F. Jensen, 'Near-Field Measurements Using Directive Antennas' *Int. IEEE Antennas And Propagation Symposium Digest*, New York, U.S., 1970, pp. 284-287.
- [20] P. F. Wacker, 'Near-Field Antenna Measurements Using A Spherical Scan: Efficient Data Reduction With Probe Correction', *IEE Conf. On Precision Electromagnetic Measurements CPEM-74*, London, UK, 1974, pp. 286-288.
- [21] Y. Rahmat-Samii, L. Williams and R. Yaccarino, 'The Bi-Polar Planar Near-Field Measurement and Diagnostic Facility', *Eighth Int. Conf. On Antennas And Propagation*, Edinburgh, UK, Conf. Publ. No. 370, Vol. 1, 1993, pp. 392-395.
- [22] K. S. Farhat, J. C. Bennet and A. J. T. Whitaker, 'Near-Field Measurements On A Plane Polar Facility', *Int. Conf. On Antennas And Propagation ICAP-87*, York, UK, Conf. Publ. No. 274, Vol.1, 1987, pp. 359-362.
- [23] A. C. Newell, 'Current State-Of-The-Art In Near-Field Antenna Measurements', *IEEE Int. Symposium Of Antennas And Propagation Soc.*, Vol. 4, 2001, pp. 420-423.
- [24] 'Special Issue on Near-Field Scanning Techniques', *IEEE Trans. On Antennas And Propagation*, Vol. AP-36, No. 6, June 1988.
- [25] D. J. van Rensberg, 'Scan-Plane Reduction Techniques For Planar Near-Field Measurements', *IEE Antennas And Propagation Magazine*, Vol. 46, No. 6, 2004, pp. 179-184.
- [26] D. Gabor, 'A New Microscopic Principal', *Nature*, Vol. 161, 1948, pp. 777-778.
- [27] D. Gabor, "Microscopy by Reconstructed Wave-fronts", *Proc. Roy. Soc. A*, Vol. 197, Feb 1949, pp. 454-487.

- [28] D. Gabor, G. W. Stroke, D. Brumm, A. Funkhouser and A. Labeyrie, 'Reconstruction Of Phase Objects By Holography', *Nature*, Vol. 208, 1965, pp. 1159-1162.
- [29] E. N. Leith and J. Upatnieks, 'Wavefront Reconstruction And Communication Theory', *Journal Of The Optical Society Of America*, Vol. 52, No. 10, 1962, pp. 1123-1130.
- [30] E. N. Leith and J. Upatnieks, 'Wavefront Reconstruction With Continuous-Tone Objects', *Journal Of The Optical Society Of America*, Vol. 53, No. 12, 1963, pp. 1377-1381.
- [31] E. N. Leith and J. Upatnieks, 'Wavefront Reconstruction With Diffused Illumination And Three-Dimensional Objects', *Journal Of The Optical Society Of America*, Vol. 54, No. 11, 1964, pp. 1295-1301.
- [32] E. N. Leith and J. Upatnieks, 'Microscopy By Wavefront Reconstruction', *Journal Of The Optical Society Of America*, Vol. 55, No. 5, 1965, pp. 569-570.
- [33] E. N. Leith, J. Upatnieks and A. Haines, 'Microscopy By Wavefront Reconstruction', *Journal Of The Optical Society Of America*, Vol. 55, No. 5, 1965, pp. 981-986.
- [34] A. P. Anderson, 'Microwave Holography' *IEE-Reviews*, Vol. 124, No. 11R, 1977, pp. 946-962.
- [35] J. C. Bennett, A. P. Anderson, P.A. McInnes and A. J. T. Whitaker, 'Microwave Holographic Metrology Of Large Reflector Antennas', *IEEE Trans. On Antennas And Propagation*, AP-24, No. 3, 1976, pp. 293-301.
- [36] J. C. Bennett, 'Investigation Of The Characteristics Of Large Reflector Antennas Using Microwave Holography' PhD. Thesis, University Of Sheffield, UK, 1974.

- [37] T. Huang ‘’, Ph. D Thesis, The University Of Sheffield, England, 1999.
- [38] J. E. McCormack, G. Junkin and A. P. Anderson, ‘Microwave Metrology Of Reflector Antennas From A Single Intensity Scan’, *IEE Proc.*, Vol. 137, Pt. H, No. 5, Oct. 1990, pp. 276-284.
- [39] R. W. Gercheberg and W. O. Saxton, ‘Phase Determination From Image and Diffraction Plane Pictures In The Electron Microscope’, *Optik*, Vol. 34, 1971, pp. 275-284.
- [40] A. Tennant, G. Junkin and A. P. Anderson, ‘Advances In Phase Retrieval Antenna Metrology’, *Eighth Int. Conf. On Antennas And Propagation*, Edinburgh, UK, Conf. Publ. No. 370, Vol. 1, 1993, pp. 323-326.
- [41] R. G. Yaccarino and Y. Rahmat-Samii, ‘Progress In Phaseless Near-Field Measurement Research At the University of California, Los Angeles’, *Int. Symposium Of IEEE Antennas And Propagation Soc. Digest*, New Jersey, U.S., Vol. 4, 2001, pp. 416-419.
- [42] J. E. McCormack, G. Junkin, A. P. Anderson and A. J. T. Whitaker, ‘Microwave Antenna Metrology From A Single Intensity Scan’, *IEE Proc. On Antennas And Propagation*, Pt H, Vol. 137, No. 5, 1990, pp. 276-284.
- [43] A. Tennant, G. Junkin and A. P. Anderson, ‘Advances In Phase Retrieval Metrology’, *Eighth Int. Conf. On Antennas And Propagation*, London, UK, Conf. Publ. No. 370, Vol. 1, 1993, pp. 323-326.
- [44] S. Costanzo, C. Di-Massa and M. D. Migliore, ‘A X-Band Probe For Phaseless Near-Field Measurements’, *Int. Symposium Of IEEE Antennas And Propagation Soc.*, New Jersey, U.S., Vol. 1, 2002, pp. 274-277.
- [45] Y. S. El-Said and A. M. Attiya, ‘Modified Two Probe Approach For Amplitude Only Near-Field Measurements’, 21<sup>st</sup> National Radio Science Conference, Cairo, Egypt, Conf. Proc. Vol. 1, 2004, pp. B2 1-5.

- [46] P. C. Clemmow, 'The Plane Wave Spectrum Representation Of Electromagnetic Fields', Wiley IEEE Press, New York, U.S. 1996.
- [47] D. T. Paris, W. M. Leach Jr. and E. B. Joy, 'Basic Theory Of Probe Compensated Near-Field Measurements', *IEEE Trans. On Antennas And Propagation*, Vol. AP-26, No.3 1978, pp. 373-379.
- [48] J. J. H. Wang, 'An Examination Of The Theory And Practices Of Planar Near-Field Measurement', *IEEE Trans. On Antennas And Propagation*, Vol. 36, No. 6, 1988, pp. 746-753.
- [49] A. D. Yaghjian, 'An Overview Of Near-Field Antenna Measurements', *IEEE Trans. On Antennas And Propagation*, Vol. AP-34, 1986, pp. 30-45.
- [50] E. B. Joy and D. T. Paris 'Spatial Sampling And Filtering In Near-Field Measurements', *IEEE Trans. On Antennas And Propagation*, Vol. AP-20, No. 3, 1972, pp 253-261.
- [51] J. F. James, 'A Student's Guide To Fourier Transforms: With Applications In Physics And Engineering', Cambridge, Cambridge University Press, 1995.
- [52] Y. Rahmat-Samii, L. I. Williams and R. G. Yaccarino, 'The UCLA Bi-polar Planar-Near-Field Antenna-Measurement and Diagnostics Range', *IEEE Antennas and Propagation Magazine*, Vol. 37, No. 6, 1995, pp. 16-35.
- [53] E. B. Joy, W. M. Leach Jr., G. P. Rodrigue and D. T. Paris, 'Applications Of Probe-Compensated Near-Field Measurements', *IEEE Trans. On Antennas And Propagation*, Vol. AP-26, No.3 1978, pp. 379-389.
- [54] C. A. Rose, "Accuracy Estimation Of Microwave Holography From Planar Near-Field Measurements", *Antenna Measurements Techniques Association Proceedings* 2000, 2001, pp. 12-18.

- [55] J. McCormick and E. D. Silva, 'The Use Of An Auxiliary Translation System In Near-Field Measurements', *Tenth Int. Conf. On Antennas and Propagation*, Edinburgh, UK, Conf. Publ. No. 436, 1997, pp. 1.90-1.94.
- [56] M. H. Francis, A. C. Newell, K. R. Grimm, J. Hoffman and H. E. Schrank, "Comparison Of Ultralow-Sidelobe-Antenna Far-Field Patterns Using The Planar-Near-Field Method And The Far-Field Method", *IEEE Antennas And Propagation Magazine*, Vol. 37, No. 6, 1995, pp. 7-15.
- [57] L. E. Correy and E. B. Joy, 'On Computation Of Electromagnetic Fields On Planar Surfaces From Fields Specified On Nearby Surfaces' *IEEE Trans. On Antennas And Propagation*, Vol. AP-29, No. 2, 1981, pp. 402-404.
- [58] C. Huygens, "Traite de la Lumiere", Leyden, 1660. Translated into English by S. P. Thompson, London, 1912, reprinted by the University of Chicago Press.
- [59] R. C. Rudduck, D. C. F. Wu and M. R. Intihar, "Near-Field Analysis By The Plane Wave Approach", *IEEE Trans. On Antennas and Propagation*, Vol. AP-18, 1973, pp. 231-234.
- [60] J. C. Bennett, 'Recent Developments In Near-Field Antenna Measurements', *Fifth Int. Conf. On Antennas And Propagation ICAP-87*, York, UK, Conf. Publ. No. 274, Vol.1, 1987, pp. 467-472.
- [61] P. R. Miller, J. Ward, P. R. Prowting and S. Gregson 'The Implementation And Validation Of A Large 22m By 8m Planar Near-Field Test Range For Space Antenna Systems And Payload Testing', Edinburgh, UK, *Tenth Int. Conf. On Antennas and Propagation*, Conf. Publ. No. 436, 1997, pp. 1.105-1.109.
- [62] D. Slater, 'Near-Field Antenna Measurements', Artech Ho. Publ., Boston, 1991, ISBN:0-89006-361-3.

- [63] P. Hariharan, 'Optical Holography', Second Ed., Cambridge Univ. Press, 1996, ISBN:0-52-131163-2.
- [64] 'History', <http://www.holophile.com/history.htm>, *Holophile Inc.*, 1995-2005.
- [65] R. P. Dooley, 'X-Band Holography', *Proc. IEEE*, 1965, pp. 1733-1735.
- [66] Y. Aoki, 'Microwave Holograms And Optical Reconstruction', *Applied Optics*, Vol. 6, No. 11, 1967, pp. 1943-1946.
- [67] K. Iizuka, 'Making It In Pictures', *Electronics*, Vol. 41, 1968, pp. 130-131.
- [68] D. Smith, M. Leach, M. Elsdon and S. J. Foti, 'Imaging Of Concealed Objects From Scalar Microwave Holograms', *RF and Microwaves Conf.*, RFM-04 Malaysia, Oct. 2004, pp. 127-131.
- [69] D. Smith and M. Leach, '3D Imaging of Antenna Fields and Metal Objects Using a New Indirect Holographic Technique', *Int. Conf. On Electromagnetics for Advanced Applications*, ICEAA-03, Torino Italy, Sept. 2003, pp. 711-714.
- [70] P. F. Checcacci, V. Russo and A. M. Scheggi, 'Holographic Antennas', *Proc. IEEE*, Vol. 56, No. 12, 1968, pp. 2165-2167.
- [71] D. M. Sazonov, 'Computer Aided Design Of Holographic Antennas', *IEEE Int. Symposium On Antennas And Propagation 1999 Digest*, Vol. 2, 1999, pp. 738-741.
- [72] S. R. Thingvold, A. Ittipiboon, A. Sebak and A. Petosa, 'Holographic Antenna Efficiency', *IEEE Int. Symposium On Antennas And Propagation 2003 Digest*, New Jersey, U.S. Vol. 3, 2003, pp. 721-724.
- [73] G. Tricoles and N. H. Farhat, 'Microwave Holography: Applications And Techniques', *Proc. IEEE*, Vol. 65, No. 1, 1977, pp. 108-121.

- [74] D. J. Rochblatt, P. H. Richter and T. Y. Otoshi, 'A Microwave Performance Calibration System For NASA's Deep Space Network Antennas, Part 2: Holography, Alignment and Frequency Stability', *Tenth Int. Conf. On Antennas And Propagation*, Edinburgh, UK, Conf. Publ. No. 436, Vol. 1, 1997, pp. 1.150-1.155.
- [75] P. J. Napier and R. H. T. Bates, 'Antenna Aperture Distributions From Holographic-Type Radiation Pattern Measurement', *Proc. IEEE*, Vol. 120, No. 1, 1973, pp. 30-34.
- [76] T. Huang, J. C. Bennett and G. Junkin, 'A Holographic Technique For Millimeter-Wave Antenna Near-Field/Far-Field Transformation', *Ninth Int. Conf. On Antennas And Propagation*, Eindhoven, Holland, Conf. Publ. No. 407, Vol. 1, 1995, pp. 41-44.
- [77] G. Junkin, T. Huang and J. C. Bennett, 'Holographic Near-Field/Far-Field For Terahertz Antenna Testing', *AMTA-97 19th Meeting And Symposium*, 1997, pp. 419-424.
- [78] D. Smith, M. Leach, A. J. Sambell, 'An Indirect Holographic Method for Determining Antenna Radiation Patterns and Imaging Antenna Fields', *IEEE Int. Symp. Of Antennas and Propagation Soc.*, San Antonio Texas US, Conf. Publ. Vol. 3, 2002, pp. 706-709.
- [79] D. Smith and M. Leach, '3D Imaging Of Antenna Fields From Electronically Synthesised Scalar Intensity Patterns', *Asia-Pacific Conference On Applied Electromagnetics*, APACE-03, Kuala Lumpur Malaysia, Conf. Publ. Vol. 1, Aug. 2003, pp. 50-53.
- [80] D. Smith, M. Leach, A. J. Sambell, 'Microwave Indirect Holographic Imaging using an Adaptation of Optical Techniques', *IEEE Microwave and Wireless Components Letters*, Vol. 13, No. 9, Sept. 2003, pp. 379-381.

- [81] Andrews Corp. 'Test Report VHLP1-130-211 Antenna Serial No. 144372', 2002.
- [82] R. Benjamin and H. D. Griffiths, 'Qualified 'Separability' In The Measurement And Computation Of Antenna Radiation Patterns', *Ninth Int. Conf. On Antennas And Propagation*, Conf. Publ. No. 407, Vol. 1, 1995, pp. 45-48.
- [83] D. Smith, M. Leach, M. Elsdon and S. J. Foti, 'Holographic Reconstruction of Dish Antenna Measurements', *Int. Symp. On Antennas*, JINA-04, Nice France, Nov. 2004, pp. 308-309.
- [84] D. Smith, M. Leach, S. S. Dlay, W. L. Woo, 'A Novel Technique for the Determination of the Radiation Patterns of Medium Gain Antennas from Scalar Intensity Patterns', *Sixth Int. Sym. On Antennas, Propagation and Electromagnetic Theory*, ISAPE-03, Beijing China, Oct. 2003, pp. 373-376.
- [85] D. Smith, M. Leach and A. Kellner, 'Indirect Holographic Imaging Of Antennas Using An Electronically Synthesised Slow-Wave', *IEEE Int. Symp. Antennas And Propagation Soc.*, Monterey California, U.S., June 2004, pp. 703-706.
- [86] D. Smith, M. Leach, M. Elsdon and S. J. Foti, 'Using Invisible Region Wave Vectors For Determining The Properties Of Microwave Antennas And Imaging Fields', *Fourth Int. Symp. On Communication Systems, Networks And Digital Signal Processing*, CSNDSP-04, Newcastle UK, July 2004, pp. 248-251.